UNIVERSITY OF SOUTHAMPTON

Faculty of Engineering and Physical Sciences
School of Engineering

Influence of drift angle on the self-propelled ship's powering performance in waves

by

Yifu Zhang

ORCiD: 0000-0001-6980-3985

A thesis for the degree of
Doctor of Philosophy

October 2023

University of Southampton

Abstract

Faculty of Engineering and Physical Sciences
School of Engineering

Doctor of Philosophy

Influence of drift angle on the self-propelled ship's powering performance in waves

by Yifu Zhang

The ability to accurately predict the ship's powering and manoeuvring performance in waves is of high importance for the design of new vessels. This is closely related to ship safety, reliability, and overall propulsive efficiency. However, it is a challenging task because of the complex interaction among ship motions, wakefield, and hydrodynamic forces exerted on the hull and its appendages. Conventional experimental methods and direct numerical simulation of dynamic manoeuvring in waves can provide valuable results, but both of them are very costly and time-consuming. Besides, the validation of traditional direct ship manoeuvring calculations is still very difficult and expensive. Therefore, a more cost-effective numerical method to accurately predict the powering and manoeuvring performance of ships in waves is still in high demand.

Instead of modelling the complete time-varying manoeuvre, this thesis presents a cost-effective numerical approach for evaluating the fully appended ship under static drift, static rudder and combined drift rudder conditions, representing quasi-static phases of actual ship manoeuvre in waves. A stepwise study procedure is used including the double body method and the Volume of Fluid free surface calculations in calm water and waves. Two body force models are used for propeller modelling in drift conditions and the sectorial approach of Blade element momentum theory is adopted to capture non-uniform wake. The computed results are compared to available experimental and numerical results. The hull forces in some drift computations are validated with EFD data from the Southampton Boldrewood towing tank. This provides a reference for experimental measurements of hull and appendage forces and contributes to future validation of actual dynamic manoeuvring simulation. The presented methodology and results of drift influence on fully appended ships allow for the integration of wind-assist devices on commercial ships and predict the interaction between wind propulsion systems and ship hydrodynamics for wind-assist ships, thereby contributing to reducing fuel consumption and related emissions from ships and realizing the goal of decarbonisation in the maritime sector.

Contents

List of Figures

List of Tables

Listings

Declaration of Authorship

I declare that this thesis and the work presented in it is my own and has been generated by me as the result of my own original research.

I confirm that:

1. This work was done wholly or mainly while in candidature for a research degree at this University;
2. Where any part of this thesis has previously been submitted for a degree or any other qualification at this University or any other institution, this has been clearly stated;
3. Where I have consulted the published work of others, this is always clearly attributed;
4. Where I have quoted from the work of others, the source is always given. With the exception of such quotations, this thesis is entirely my own work;
5. I have acknowledged all main sources of help;
6. Where the thesis is based on work done by myself jointly with others, I have made clear exactly what was done by others and what I have contributed myself;
7. Parts of this work have been published as:

Signed:.. Date:..................

Acknowledgements

Firstly, I would like to express my sincerest gratitude to my supervisors, Prof. Stephen Turnock and Prof. Dominic Hudson, for their unwavering support, invaluable guidance, and constant encouragement throughout my PhD studies and research. Their vast knowledge, insightful feedback, and mentorship have been indispensable to the successful completion of this work.

I would also like to extend my heartfelt appreciation to Dr. Björn Windén for his exceptional support throughout the years. In particular, I appreciate the invaluable contribution of providing the propeller modelling code and the solution to related questions.

Special thanks go to Dr. Héctor Rubén Díaz Ojeda for his continuous support and helpful suggestions throughout this journey.

I would also like to express my gratitude to the University of Southampton for providing the use of the iridis5 High-Performance Computing facility and Boldrewood Towing Tank.

My deepest gratitude goes to my parents and grandparents for their love and support all the time. Their sacrifices and encouragement have been the pillars of my strength and motivation.

Last but not least, I want to express my sincere gratitude to Jingwen Wang for her understanding, encouragement, and companionship during the most challenging times.

Definitions and Abbreviations

a	axial inflow factor
a'	circumferential inflow factor
B	ship breadth (m)
c	blade chord (m)
C_B	block coefficient
C_D	drag coefficient
C_L	lift coefficient
C_F	frictional resistance coefficient
C_T	total resistance coefficient
C_P	pressure resistance coefficient
C_V	viscous resistance coefficient
C_W	wave-making resistance coefficient
D	ship depth (m)
D_P	propeller diameter (m)
$E(\%D)$	error as a percentage of experimental value
Fn	Froude number
F_Y	lateral force (N)
F'_Y	non-dimensionalized lateral force coefficient
J	advance coefficient
K	Goldstein correction factor
K_T	propeller thrust coefficient
K_Q	propeller torque coefficient
L_{PP}	length between perpendiculars (m)
M_Z	yaw moment (Nm)
M'_Z	non-dimensionalized yaw moment coefficient
n	revolutions per second (s^{-1})
p	pressure (Pa)
P/D	pitch diameter ratio
P_D	delivered power (W)
P_E	effective power (W)
P_T	thrust power (W)
Q	torque (Nm)

r	local propeller radius (m)
r_G	mesh refinement ratio
R	propeller radius (m)
RPM	propeller revolution rate per min
Re	Reynolds number
R_{CW}	calm water resistance (N)
R_{AW}	added resistance in waves (N)
R_T	total resistance (N)
S_L	simulation lower bound
S_U	simulation upper bound
S_W	hull wetted surface area (m^2)
t	thrust deduction factor
T	draught (m)
	thrust (N)
U	velocity (m/s)
U_G	grid uncertainty
u_i	Cartesian velocity component (m/s)
u'_i	fluctuating velocity component (m/s)
V	velocity (m/s)
w_T	wake fraction
y^+	non-dimensionalised distance from wall in boundary layer
Z	Number of blades
α	angle of attack (°)
β	ship drift angle (°)
β_r	rudder angle relative to the ship axis (°)
dC_T	augment of total resistance coefficient
dC_D	augment of rudder drag coefficient
dC_L	augment of rudder lift coefficient
dD	local drag (N)
dL	local lift (N)
dT	local thrust (N)
dQ	local torque (Nm)
dK_T	local thrust coefficient
	augment of thrust coefficient
dK_Q	local torque coefficient
	augment of torque coefficient
ϵ	dissipation rate (m^2/s^3)
η	efficiency
η_D	quasi-propulsive efficiency
η_H	hull efficiency
η_O	open water efficiency

η_R	relative rotative efficiency
η_i	ideal efficiency
μ	dynamic viscosity (kg/ms)
ν	kinematic viscosity (m^2/s)
ρ	fluid density (kg/m^3)
Ω	rotational velocity (s^{-1})
λ	wave length (m)
ζ_0	wave amplitude (m)
σ_{AW}	non dimensional added resistance coefficient in wave
2D	Two Dimensional
3D	Three Dimensional
BEMt	Blade Element Momentum theory
CFD	Computational Fluid Dynamics
CPU	Central Processing Unit
EEDI	Energy Efficiency Design Index
EFD	Experimental Fluid Dynamics
FV	Finite Volume (method)
HPC	High-Performance Computing
IMO	International Maritime Organization
ITTC	International Towing Tank Conference
KCS	Korean Container Ship
M	Millions
MULES	Multidimensional Universal Limiter with Explicit Solution
NS	Navier-Stokes
OpenFOAM	Open source Field Operation And Manipulation
PISO	Pressure-Implicit with Splitting of Operators
PIMPLE	Pressure-Implicit with Operator-Splitting Multi-Phase Explicit
RANS	Reynolds Averaged Navier-Stokes
SIMPLE	Semi-Implicit Method for Pressure-Linked Equations
SIMPLEC	Semi-Implicit Method for Pressure Linked Equations-Consistent
SST	Shear Stree Transport
URANS	Unsteady Reynolds Averaged Navier-Stokes
VOF	Volume of Fluid

Chapter 1

Introduction

1.1 Background and motivation

Due to unrestricted emissions of greenhouse gases, global warming poses a considerable threat to our earth. The shipping industry, contributing to approximately 2 to 3 % of the global CO_2 emissions, has to confront this significant challenge of reducing emissions despite the continued heavy reliance on maritime transportation for global trade. According to 2008 CO_2 emission data, the International Maritime Organization (IMO) sets targets of reducing CO_2 emissions by 40% by 2030 and 70% by 2050. Meanwhile, the organization aims to decrease greenhouse gas emissions by 50% by 2050 (MEPC72 2018), with the ambitious objective of entirely decarbonizing the shipping industry within this century. As the emphasis on zero-carbon and green shipping intensifies, the maritime sector strives to achieve the goal of improved efficiency and reduced emissions without compromising the safety and reliability of ships. Therefore, naval architects are always making efforts to find innovative approaches for enhancing vessel efficiency and improving new ship design.

Accurate evaluation of ship manoeuvring and coursekeeping performance in actual seaways is one of the most important indicators in ship design. It is closely related to ship operation safety, reliability and vessel efficiency, especially when ships travelling in adverse wave and wind conditions. IMO released ship manoeuvrability standards in 2002, emphasizing the necessity of checking ship manoeuvring performance during the early ship design stage (International Maritime Organization 2002). Figure 1.1 presents the typical ship manoeuvring when operating in real sea states. Although ship manoeuvring in calm water has been studied widely, the understanding of ship manoeuvrability in real sea states is not well developed and manoeuvring prediction capability is still challenging (ITTC 2021). Experimental model tests involving unconstrained motion are frequently used to examine a vessel's manoeuvrability in a direct manner, which is accurate and reliable, but it is very costly and requires high specifications of models and facilities. In comparison, direct simulation using Computational fluid dynamics (CFD) is a highly promising method, which can accurately resolve local flow characteristics surrounding the hull and its appendages, therefore enhancing comprehension of the hydrodynamic challenges associated with ship manoeuvring. However, this direct dynamic manoeuvring simulation requires extremely high computational costs and an exceedingly long simulation time even when using the high-performance computing cluster, making it unsuitable for the initial ship design. Therefore, there is still a pressing need to find a more cost-effective numerical method to accurately predict the powering and manoeuvring performance of ships in waves.

FIGURE 1.1: Ship manoeuvring in seaways (Caribbean 2017)

In addition, wind-assist devices, as one of the most promising strategies to reduce fuel consumption and greenhouse gas emissions, play a significant role in decarbonising the maritime sector. These systems harness wind power to augment a ship's propulsion, leading to improved energy efficiency and better ship design. One of the common approaches is to use FastRig wing-sail retrofitted on a commercial ship, as shown in Figure 1.2. To ensure the successful integration and application of wind-assist devices on traditional commercial ships, a better understanding of ship manoeuvring in waves is still needed, as wind-assist devices can reduce the required propeller thrust but meanwhile generate the lateral force on the hull, causing the ship to operate at the angle of drift. Therefore, the complex interactions between the hull, propeller, rudder and their surrounding fluid under drift conditions need to be captured with reasonable accuracy.

FIGURE 1.2: FastRig wing-sails developed by Smart Green Shipping (Shipping 2023)

1.2 Aim and objectives

The overall purpose of this work is to contribute to optimizing ship design for better powering performance in real sea states. To achieve this, the aim is to present a cost-effective numerical methodology that can effectively model the propulsion power demand for a specific vessel in waves due to ship manoeuvring and operational wind assist vessels. The development of this methodology requires the completion of the following objectives:

1. to conduct a systematic literature review on the research of the hydrodynamic performance of ships in waves, mainly self-propulsion in waves and ship manoeuvring in waves, and define the associated challenges.
2. to present an open-source numerical towing tank capable of modelling the ship operating under static drift, static rudder and combined drift rudder conditions.
3. to use a cost-efficient propeller modelling method under drift without explicitly resolving propeller geometry.
4. to capture the influence of drift angle on the fully appended ship in waves.
5. to gain a better understanding of forces and moments on the hull, the propeller, the rudder and their interaction effect under drift, subsequently contributing to better ship design.

1.3 Novel contributions

The novel contributions presented in this thesis are listed below:

1. Instead of direct CFD simulations for ship manoeuvring in waves, this thesis presents a cost-effective numerical approach for simulating a fully appended ship in waves under static drift, static rudder and combined drift rudder conditions, which can represent quasi-static phases of an actual ship manoeuvre in real sea states. This kind of approach removes the need for modelling the complete time-varying manoeuvre, which greatly reduces the computational cost. In contrast to the direct simulation of ship manoeuvring, the simulation under static drift and rudder conditions allows for direct validation and contributes to the future validation process of the actual dynamic manoeuvring models and simulations.
2. The impact of both drift and rudder angles on the forces exerted upon the hull and its appendages is a topic frequently acknowledged, yet not extensively studied or discussed. This thesis presents a systematic study of positive and negative drift

and rudder angles' influence on the hull, propeller and rudder performances in both calm water and waves, which effectively provides a reference for how the propeller-rudder unit needs to be designed as a whole with changes in propeller operating conditions strongly influenced by ship orientation, rudder angle and wave phase.

3. In terms of propeller modelling, two body force models are compared in drift conditions with and without the effect of tangential wake. More specifically, the Blade element momentum theory (BEMt), is used to model the action of the propeller at drift, and it can capture the non-uniform wake by adopting the sectorial approach. To ensure the reliability and accuracy of the BEMt code, the Yamazaki model is also employed for comparison and verification purposes.

4. Towing tank experiments are performed in the Southampton Boldrewood Towing tank for CFD validation, including hull forces and wave patterns at drift. This contributes to future experimental measurements of hull and appendage forces when the angle of drift is applied, subsequently ship manoeuvrability assessment.

5. In this work, the investigation of drift's influence on fully appended vessels helps to gain a better understanding of the effects of wind-assist devices on ship powering performance. Wind-assist systems can reduce the propeller-generated thrust and also create lateral forces on the hull, leading the ship to operate at an angle of drift. By examining these relationships, this research aids in the optimization of ship designs that harness wind assistance, thereby contributing to maritime decarbonization efforts.

1.3.1 Publications

1.3.1.1 Conference papers

Zhang, Y., Hudson, D., Windén, B., Turnock, S.R. (2021), Evaluating the effects of drift angle on the self-propelled ship using Blade Element Momentum Theory, in 'Proceedings of the 23rd Numerical Towing Tank Symposium, 11-13 October, Mülheim an der Ruhr, Germany', pp. 162-167.

Zhang, Y., Windén, B., Hudson, D., Turnock, S.R. (2022), Hydrodynamic performance of a self-propelled KCS at angle of drift including rudder forces, in 'Proceedings of the 24th Numerical Towing Tank Symposium, 16-18 October, Zagreb, Croatia, pp. 188-193.

Bowker, J., Buckland, D., Gregory, M., Townsend, N., Zhang, Y., Turnock, S. (2023), A free running instrumented container ship model for investigating energy efficiency in waves, '7th International Conference on Advanced Model Measurement Technology for The Maritime Industry, AMT'23, 24-26 October 2023, Istanbul Turkey', (Abstract accepted).

Zhang, Y., Banks, J., Hudson, D., Turnock, S. (2024), Influence of leeway on hull-propeller-rudder interaction using CFD methods, '8th International Symposium on Marine Propulsors, smp'24, 17-21 March 2024, Hurghada, Egypt', (Abstract accepted).

1.3.1.2 Journal papers

Zhang, Y., Windén, B., Ojeda, H.R.D., Hudson, D., Turnock, S.R. (2023a), 'Influence of drift angle on a fully appended container ship (KCS) using CFD and EFD methods', Ocean Engineering (Under review).

Zhang, Y., Windén, B., Ojeda, H.R.D., Hudson, D., Turnock, S.R. (2023b), 'Influence of combined drift and rudder angles on a fully appended ship in waves ', Ocean Engineering (Pending submission).

1.4 Structure of thesis

In order to understand the state of the art of ship hydrodynamic performance in waves, chapter 2 provides a detailed literature review of ship resistance, propulsion and manoeuvring performance in waves predicted by both experimental and numerical methods. It is found that the experimental method is valuable, but it is also very costly and time-consuming. In comparison, the numerical method based on CFD can provide a more flexible and cheaper alternative. However, direct simulation of conventional dynamic ship manoeuvring still remains computationally expensive and very difficult to validate. Therefore, the focus of this work is to present a cost-effective numerical method for predicting the powering performance of a specific fully appended ship under static drift angles combined with a series of rudder angles, representing quasi-static phases of an actual ship manoeuvre.

Based on the experience of literature in Chapter 2, Chapter 3 introduces the mathematical formulations and numerical techniques adopted for developing the cost-effective numerical method for a stepwise study of estimating the fully appended ship in waves under combined drift and rudder conditions. A Reynolds-Averaged Navier-Stokes (RANS) based CFD method is used for modelling fluid flow around the KCS within the open source code OpenFOAM environment. The stepwise study starts with the double body approach, then the Volume of Fluid (VOF) method for the free surface computations.

Chapter 4 focuses on the numerical framework for simulating ships with the angle of drift and numerical propeller modelling methods used in this thesis. Ship-axis-based and domain-axis-based coordinate systems are introduced, and the force and moment transformation matrix is discussed. Body force propeller models are adopted due to their lower computational cost compared to the fully discretized propeller approach. To capture the non-uniform wake resulting from the presence of drift, rudder angles and propeller operating aft the hull, a sectorial approach of Blade element momentum theory (BEMt) is used. Another body force model, the Yamazaki model, is also employed to compare and verify numerical results obtained from the BEMt.

Chapters 5, 6 and 7 present the numerical simulation results in the order of increasing complexity in the stepwise study mentioned in section 3.1. Chapter 5 studies the static drift angle effects on the interaction between the hull, propeller and rudder of the benchmark KRISO Container Ship (KCS) with using the steady RANS simulation of double body flow in calm water. The computed results show good agreement with EFD data from the 2015 Tokyo CFD workshop and the numerical results of other institutions. It demonstrates that the double body method with body force propeller modelling can be valuable in evaluating the hull propeller rudder interaction at a relatively low computational cost. However, the absence of the free surface model results in a notable underestimation of the KCS longitudinal force.

Chapter 6 provides a numerical methodology for investigating the fully-appended KCS subject to static drift angles in conjunction with a series of drift angles, including free surface modelling. Due to the use of an unsteady CFD analysis method, the associated computational cost is significantly increased compared to the computations in the previous chapter. Both BEMt and Yamazaki models are used to capture the propeller performance under static drift conditions, exhibiting good agreement of propeller forces.

Chapter 7 makes use of the numerical method and experience gained from Chapters 5 and 6 to investigate the impact of drift angle on fully appended KCS's powering performance in regular waves.

Chapter 8 provides a summary of the key findings presented in the preceding sections of this thesis and also mentions the potential future work recommendations.

Chapter 2

Hydrodynamic performance of ships in waves

2.1 Introduction

The shipbuilding industry is constantly exploring more efficient and cost-effective approaches to designing ships in response to the ever-growing needs of the market. Concerns have been expressed about the influence maritime operations, such as the increasing transportation, overexploitation of marine resources, and overfishing, have on the environment due to the worldwide expansion in shipping activities. Because of these factors, naval architects have been compelled to search for innovative and more environmentally responsible ship design methods. There is a growing desire to improve ship designs to ensure vessels are able to adapt to the actual maritime environments they will be operating in, such as when waves, wind, and other real sea states are presented (Taskar, Yum, Steen & Pedersen 2016).

In addition, the operational speed-propulsive power performance and fuel consumption under actual operating circumstances of ships have been the primary focus of study since the establishment of the ship energy efficiency design index (EEDI). Because of this trend, the shipbuilding industry faces formidable challenges. The physical complexity of free-surface flows raises enormous difficulties related to the practical and accurate prediction of the hull resistance, self-propulsion point, manoeuvrability performances, and ship motions, all of which are common issues for a naval architect to solve (Lungu 2020). It is fortunate that with the rapid development of numerical analysis and computer technology, the computational fluid dynamics (CFD) approach is now often employed to estimate the ship performance in real sea states and to advise designers further to optimise hull lines and ship design.

Furthermore, the modelling of ship self-propulsion is undoubtedly one of the most effective and straightforward methods of evaluating different designs. The simulation of self-propulsion in calm water conditions has been well developed over the course of many years of dedicated experience. Nonetheless, accurately predicting the ship's hydrodynamic performance in real seaways remains challenging because of the complexity of ship motions in waves and the hull-propeller-rudder interaction effects. In light of this, academic research has consistently focused on developing more computationally efficient techniques for predicting ship resistance, propulsion and manoeuvrability in actual sea conditions. This chapter will describe the specifics of the literature review on ship hydrodynamic behaviours in waves, focusing on self-propulsion in waves, manoeuvring in waves, and the effects of the hull, propeller, and rudder in combination.

2.2 Basic concepts of ship resistance and propulsion

This section aims to present the fundamental principles and the estimation of the basic components of hull resistance, propulsive power, and propulsion coefficients. It mainly follows the early chapters in Molland et al. (2017) but is summarized for better readability.

2.2.1 Components of Propulsive Power

Early in the design process, it is crucial to estimate the amount of power required to propel a ship at a certain speed. An estimate of the required power for a new design may be derived from either a comparison to an already existing vessel of a similar kind or by conducting model tests. In either case, it is necessary to derive a power estimate for one size of craft from the power requirement of a different size of craft. Figure 2.1 is a simplified representation of the primary factors contributing to the overall ship power: the ship's resistance to motion, the propeller open water efficiency, and the hull-propeller interaction efficiency. Figure 2.2 is a schematic depicting the different parts of the ship power estimate and the steps of the powering process. Due to the limited scope of this thesis, only details of main hull resistance components are introduced here listed in section 2.2.3.

2.2.2 Components of the main hull resistance

Scaling the resistance of one ship to that of a different size, or more typically, scaling the resistance from model-scale to full-scale ship, requires a good understanding of the

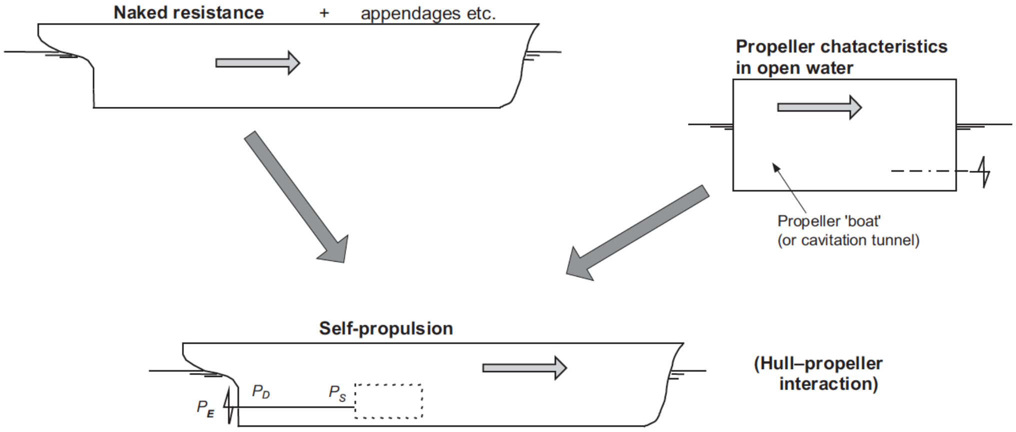

FIGURE 2.1: Components of ship powering–main considerations (Molland et al. 2017).

physical components of ship resistance and their behavior. These resistance calculations are then used to determine how much the required power will be generated from the propulsion system.

Figure 2.3 shows two flow characteristics that can be seen while a ship is traveling through water: a wave pattern that moves alongside the hull and a zone of turbulent flow that builds up along the hull's length and extends as a wake behind the hull.

The hull experiences a resistance force due to the fact that the flow's vortices and waves are absorbing energy from the hull. This force of resistance is transferred to the hull in the form of pressure and shear forces that are distributed along the hull; the viscosity of the water is what causes the shear stress to arise.

This brings about the first probable physical breakdown of resistance which considers the forces acting:

(1) Frictional resistance: the hull's total shear resistance or frictional resistance is determined by summing the forward and aft components of the tangential shear forces acting on each element of the hull's surface.

(2) Pressure resistance: the fore and aft components of the pressure force acting on each element of the hull surface can be summed over the hull to produce a total pressure resistance.

As the pressure resistance is partially caused by viscous effects and by hull wavemaking, whereas the frictional resistance is entirely caused by the viscosity. Therefore, another possible physical breakdown of resistance considers energy dissipation.

(3) Total viscous resistance: both the skin frictional resistance and part of the pressure resistance contributes to the total viscous resistance.

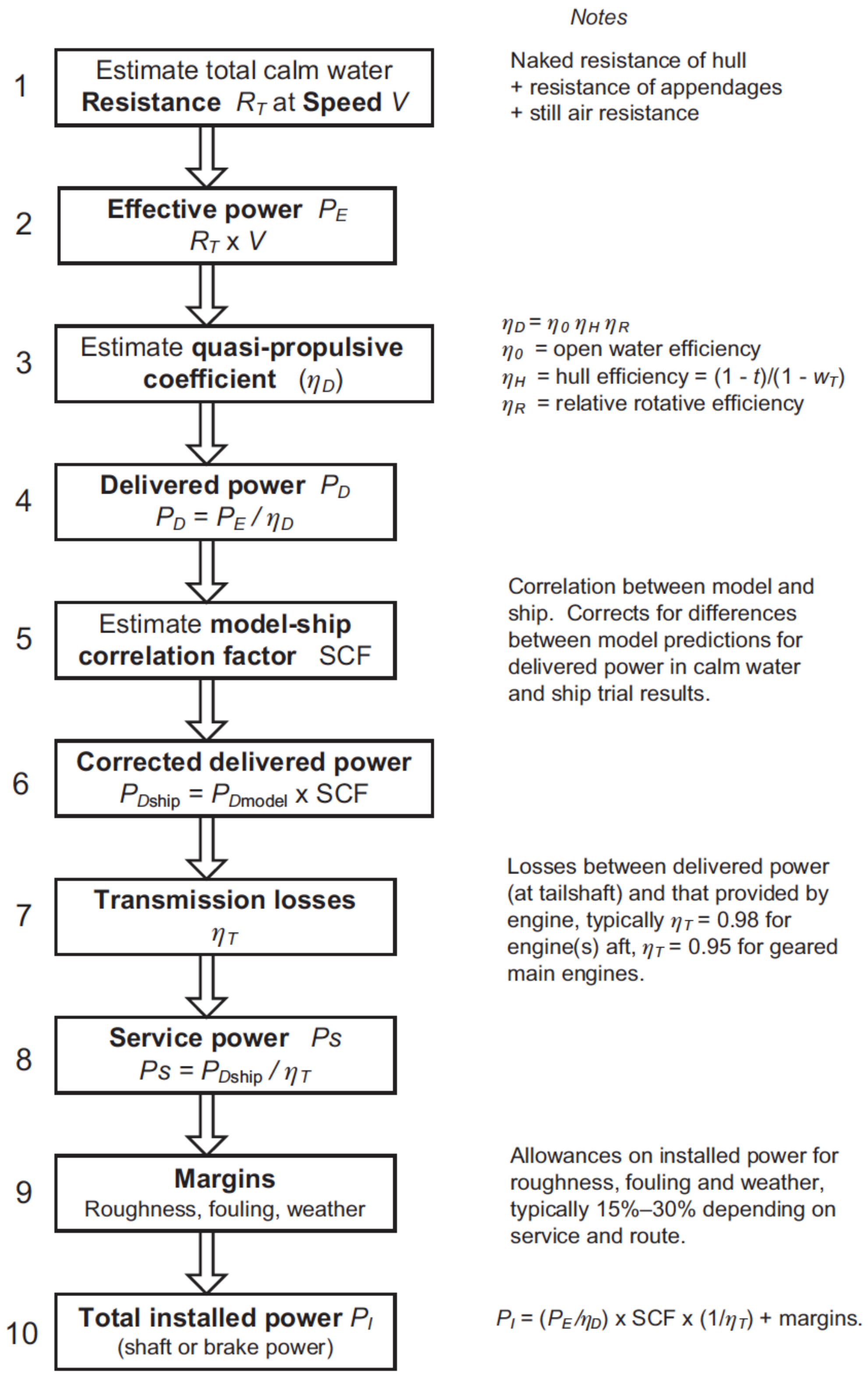

FIGURE 2.2: Components of the ship power estimate (Molland et al. 2017).

(4) Total wave resistance: the hull's wave pattern can be measured and broken down into its constituent waves for analysis. By estimating the energy needed to maintain

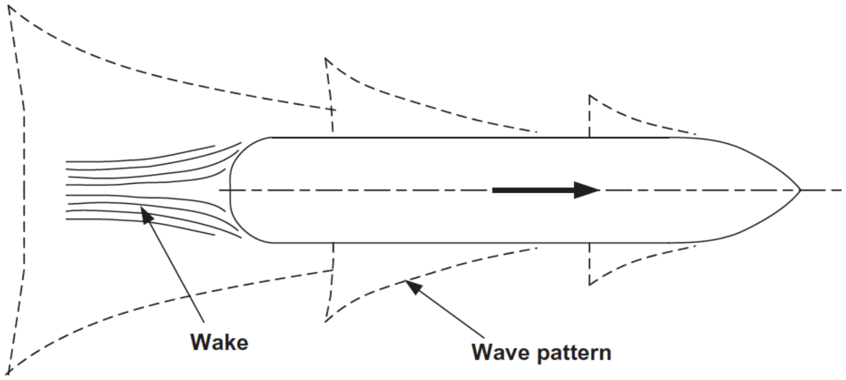

FIGURE 2.3: Waves and wake (Molland et al. 2017).

each wave component, the total wave resistance can be derived.

Therefore, the total ship resistance can be composed of the sum of the tangential shear and normal pressure forces acting on the wetted surface of the vessel in terms of forces acting. Likewise, in terms of energy dissipation, the total resistance is the sum of the energy dissipated in the wake and the energy used in the creation of waves. The calculation of ship resistance follows the manner of forces acting in this thesis.

2.2.3 Ship propulsion and propeller flow physics

The previous two sections provide the fundamentals of propulsive power and ship resistance, which is critical for accurate prediction of a ship's hydrodynamic performance. Likewise, the presence of a propeller aft hull makes the ship's stern and wake flows more complicated, involving the action of propulsor, hull-propeller interaction and etc. Therefore, this section aims to describe the relevant physics for ship propulsion and propeller flow and summarize the basic of propeller flow, and gives an overview of the general terms and parameters.

When designing a ship, the propeller and the ship are often considered in isolation at many phases (both numerical and experimental), but their interaction is crucial for taking into account all essential characteristics and interaction effects. In comparison to the resistance of the bare hull, the presence of a ship's propeller generates extra resistance by increasing the flow velocities and decreasing the pressure on the aft body of the hull. Therefore, the amount of thrust (T) that is produced by the propeller has to be greater than the amount of resistance (R). The difference between them is typically expressed by the thrust deduction fraction:

$$t = \frac{T - R}{T} \tag{2.1}$$

The fluid flow that is directed towards the propeller is greatly impacted by the design of the ship's hull due to the fact that the propeller is normally situated towards the rear of the vessel. The wake that a ship leaves behind is affected by a number of different factors, which may be broken down into three primary categories. Firstly, the potential wake is the wake field that a floating body would form in an inviscid fluid with minor axial velocity components around the stagnation points directly in front of and behind the body. A ship's hull creates a flow acceleration zone laterally. Secondly, the wave system of a ship has an effect on the velocities in the propeller plane because of the orbital velocities and the change in pressure that occurs during a wave crest or a wave trough. But these two impacts are often rather insignificant, and they may also be forecasted using potential flow approaches as state in Carlton (2018). The frictional wake is the most critical part of the total wake. This component takes into account how the flow behaves in the boundary layer area due to the viscous effects. An additional factor that contributes to the frictional wake is the possibility of flow separation as well as the generation of vortices, such as in the bilge area. Because of this, the wake can only be studied using techniques that take into account the viscosity of the fluid.

The nominal wake is that measured in the vicinity of the propeller plane but without the propeller present. The velocities in the propeller plane are altered while the propeller is in operation. Therefore, the effective wake field is the wake measured in the propeller plane with the propeller present. A single parameter, the wake fraction, is used to represent the appropriate non-dimensional mean wake value, and it is computed as follows:

$$\omega_T = \frac{V_S - V_A}{V_S} \tag{2.2}$$

Here, V_A is the average speed of flow into the propeller, and V_S is the speed of advance of the hull. In most cases, the wake fraction is not calculated based on an examination of the velocity distribution in the propeller plane but it is calculated based on the results of the traditional model test procedure. According to the procedure, the propeller will first be tested in open water conditions without the presence of the ship, and it is called the propeller open water test (OWT). Following this, it will participate in a self-propulsion test with the vessel. A propeller is tested in open water by mounting it on an open-water test rig, where the propeller operates in quasi-stationary conditions. In this way, the inflow velocity is stepwise adjusted while the number of revolutions remains fixed. Usually, a cavitation tunnel at cavitation conditions appropriate to the ship or towing tank under cavitation conditions appropriate to the model is used for these kinds of experiments (Molland et al. 2017). Due to enough depth to which the propeller is submerged during the open water test in the towing tank, free surface effects are ignored in both situations.

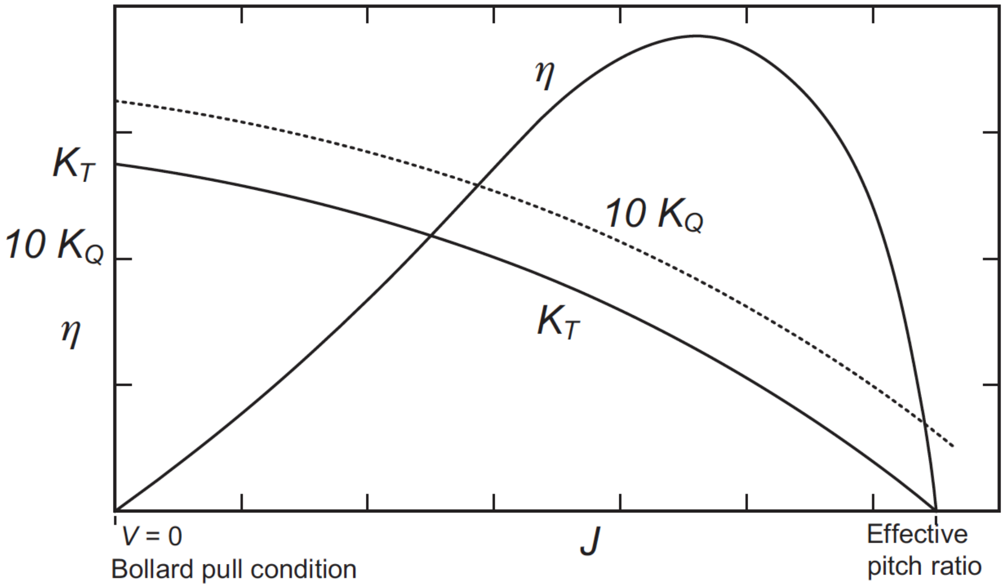

FIGURE 2.4: Open water K_T-K_Q chart (Molland et al. 2017).

Figure 2.4 is a typical open water test diagram, in which the thrust (T) and torque (Q) values of the propeller are plotted in a non-dimensional form over the advance coefficient (J). The thrust coefficient (K_T) and torque coefficient (K_Q) are defined as follows:

$$K_T = \frac{T}{\rho n^2 D^4} \tag{2.3}$$

$$K_Q = \frac{Q}{\rho n^2 D^5} \tag{2.4}$$

Where n refers to the number of revolutions and D is the propeller diameter. Furthermore, the so-called open water efficiency η, which is an important parameter to determine the required power for a certain thrust, can be obtained from such an experiment. This parameter describes the relationship between the thrust power (TV_a) and the delivered power ($2\pi n Q$), which can also be expressed in terms of K_T, K_Q and the advance coefficient J:

$$\eta = \frac{TV_A}{2\pi n Q} = \frac{K_T}{K_Q} \times \frac{J}{2\pi} \tag{2.5}$$

Self-propulsion tests can be used to determine the interaction parameters (thrust deduction and wake fraction) after the resistance test has been completed. This experiment involves a self-propelled ship with a mounted propeller. The number of propeller rotations is varied in the continental approach until the target ship speed is reached. As a result of the greater frictional resistance encountered during model testing, the propeller loading of the model propeller is greater when compared to that of the full scale one.

The comparison of the resistance test to the propulsion test yields the findings that are used to calculate the thrust deduction fraction. The wake fraction, as stated by Equation 2.2, can be found by making a comparison between the working conditions of the propeller while it is behind the hull and when it is operating in open water. Therefore, the principle of thrust identity is often adopted. Following the thrust identity analysis, it is expected that, in the propulsion test, the propeller creates the same thrust as in the open water test. The open water diagram can be used to calculate a corresponding advance coefficient for a given thrust, and from there, the velocity in Equation 2.2 ($V_a = JnD$) can be computed. The final findings from the propulsion test can be expressed in terms of delivered power (P_D) and propulsive efficiency (η_D) using the following formula:

$$P_D = \frac{P_E}{\eta_D} = \frac{R_T V_S}{\eta_D} \tag{2.6}$$

$$\eta_D = \eta_o \eta_H \eta_R = \eta_o \frac{1-t}{1-\omega_T} \eta_R \tag{2.7}$$

For Equation 2.6, P_E represents the necessary power to tow the ship, which is calculated from the resistance test. Three components contribute to the overall propulsive efficiency (η_D): the hull efficiency (η_H), the open water efficiency (η_o), and the relative rotative efficiency (η_R). These components are crucial for extrapolating the results to the full-scale ship. Regarding the importance of the effective wake, It is worth noting that wake fraction (ω_T) is a crucial factor in calculating the required power, yet the effective wake field associated cannot be directly measured. As a result, the influence of the propeller on the wake can, in principle, be computed using numerical approaches that take into account both the ship and the working propeller. Still, it is challenging to separate the approach flow, the induced velocities, and the interaction of the induced velocities. By definition, the induced velocities are not part of the effective wake, but the interaction effects between the ship and propeller are. Therefore, the nominal wake is typically employed to design the propeller blades, although it does not include the effect of propeller on propeller plane's velocities (Wöckner-Kluwe 2013).

In terms of propeller analysis, a propeller's thrust is generated by the local lift forces experienced by each blade. As a result, a ship's propeller can be modelled as a lifting surface with a smaller span-to-chord ratio. However, the ship propeller flow is much more complicated than that of other foils like aviation foils due to the lower span-to-chord ratio (Bertram 2012). Modelling the operation of a marine propeller in two dimensions using techniques like the lifting-line theory may lead to significant errors and uncertainties, which need big corrections. Using a three-dimensional flow approach is an apparent better solution due to the increasing popularity of highly skewed propellers. Lifting surfaces, vortex-lattice approaches, etc. are examples of current three-dimensional methods (Badoe 2015). The following is the overview of different numerical methods for propeller analysis (summarized from Molland et al. (2017)) in ascending order of physical and temporal precision and also in increasing order of computational cost. This is an estimate of how much computational resources each method would cost compared to the baseline blade element-momentum theory (BEMt), which has a cost of one, as presented by Phillips et al. (2009*a*) and Bertram (2000).

(1)**Blade element theory**: The forces and moments acting on the blade are calculated using a series of independent sections represented as two-dimensional aerofoils at an angle of attack to the fluid flow. Lift and drag information for the sections must be provided in advance, and the induced velocities in the fluid caused by the propeller's action are not taken into consideration.

Cost: < 1.

Applications: Benini (2004)

(2)**Momentum theory**: The propeller is modelled as an actuator disc over which there is an instantaneous pressure change, resulting in a thrust acting at the disc. The thrust, torque and delivered power are attributed to changes in the fluid velocity within the slipstream surrounding the disc.

Cost: < 1.

Applications: Phillips (2002), Phillips et al. (2010).

(3)**Blade element Momentum theory**: By combining momentum theory with blade element theory, the induced velocity field can be found around the two-dimensional sections. Corrections can be presented to account for the finite number of blades and strong curvature effects.

Cost: $= 1$.

Applications: Phillips et al. (2009*a*), Badoe et al. (2014), Windén (2014), Zhang et al. (2021).

(4)**Lifting line method**: The propeller blades are represented by lifting lines, which have a varying circulation as a function of radius. This approach is unable to capture stall behaviour.

Cost: ~ 10.

Applications: Flood (2009), Epps et al. (2010).

(5)**Lifting surface method**: The propeller blade is represented as an infinitely thin surface fitted to the blade camber line. A distribution of vorticity is applied in the spanwise and chordwise directions.

Cost: $\sim 10^2$.

Applications: Pien (1961), Kerwin & Lee (1978), Schulten (1996).

(6)**Panel method**: Panel methods extend the lifting surface method to account for blade thickness and the hub by representing the surface of the blade by a finite number of vortex panels.

Cost: $\sim 10^3$.

Applications: Kerwin et al. (1987), Seol et al. (2002), Baltazar et al. (2012).

(7)**Reynolds Average Navier-Stokes method**: Full three-dimensional viscous flow field modelled using a finite volume or finite-element approach to solving the averaged flow field.

Cost: $\sim 10^6$.

Applications: Stanier (1998), Carrica et al. (2010).

(8)**Large eddy simulation**: Has ability to simulate unsteady behavior of propeller flow, especially the size and frequency of turbulent structures but at the most expensive computational cost.

Cost: $\sim 10^8$.

Applications: Bensow & Bark (2010), Balaras et al. (2015), Kumar & Mahesh (2017).

The design objectives of a propeller optimisation are to minimise the required power for delivered thrust with a suitably robust propeller that prevents cavitation erosion in both design and off-design situations. Based on the above overview of different numerical methods of propeller modeling, the computational cost and advantages vary. The physical fidelity of the simulation can be traded against the computational cost if suitable empiricism can be included in interpreting the results of the analysis (Molland et al. 2017). There are two different methods adopted for analyzing propeller flow in this thesis, Blade Element Momentum theory (BEMt) and Yamazaki simplified propeller theory. A detailed description of both methods is presented in later chapter.

Overall, section 2.2 provides details of components of propulsive power, main hull resistance, propeller flow physics and ship propulsion in calm water conditions. Different numerical approaches to analyzing propeller flow are presented with their estimates of relative computational cost. However, when a ship sails in real sea states, its operating conditions are more complicated than in ideal calm water. One of the main differences between real seaway and calm water is the presence of waves, thus the next section provides a summary of the ship's added resistance in waves.

2.3 The added resistance in waves

There is extra resistance caused by the waves and winds when the ship moves forward in a real seaway. The magnitude of this extra resistance, also known as the added resistance, is reportedly up to between 10 and 30 percent of the resistance encountered in still water (Arribas 2007). One of the main factors impacting ship performance in a voyage is the added resistance due to waves. Therefore, it is necessary to accurately anticipate wave-induced additional resistance in the ship design stage, not only help to choose the suitable engine/propulsion system but also to determine the economic service speed in varied sea conditions (Kim & Kim 2011). Studies of the hydrodynamic causes of wave-added resistance date back to the 1920s and accurate estimation of added resistance in waves has been extensively studied both experimentally and numerically, initially with the potential flow approach and more recently using the Computational Fluid Dynamics (CFD) method.

Storm-Tejsen (1973) carried out experiments to determine the specific properties of Series 60 vessels that contribute to the added resistance. Fujii & Takahashi (1975) and Nakamura & Natio (1977) experimentally predicted the added resistance for the S175 container ship at different speeds in the head wave condition and found that the results were consistent with those in the two studies. Besides, an experimental study on the resistance increase of a ship in regular oblique waves was reported in Fujii & Takahashi (1975). Experiments and calculations on 4 Wigley hull forms in head waves were performed by Journee (1992). The effect of various bow-shape configurations on the added resistance of modified KVLCC2 hulls was tested experimentally by Lee et al. (2017). More recently, Stocker (2016) performed a series of experiments to measure added resistance in a variety of conditions, such as calm water, head waves, and oblique waves, with the goal of creating a validation benchmark for CFD codes that calculate added resistance and ship model motions during manoeuvring. Free-running tests of KRISO Container Ship model (KCS) were conducted by Sanada et al. (2017) to gain a better understanding of the added powering in regular variable heading waves. Undoubtedly, the experimental results of added resistance in waves are considered reliable, and the experimental approach has high fidelity (Park et al. 2019). However, the cost of physical tests is high and very time-consuming; therefore, the number of test runs is constrained to a large extent. At the same time, due to the sensitivity of the experimental setup and the uncertainties in the measured data, Hizir et al. (2019) admitted that the accurate measurement of added resistance in short waves is still very challenging. Therefore, more focus has been placed on the prediction of the wave added resistance using a numerical technique.

In addition to the use of experimental approaches, there are generally two numerical methods for predicting added resistance: the far-field formulation using momentum conservation (Newman 1967, Kashiwagi 1992) and the near-field formulation using pressure integration over the wetted hull surface (Gerritsma & Beukelman 1972, Salvesen 1975, Pinkster 1979, Faltinsen et al. 1980, Papanikolaou & Zaraphonitis 1987). At that time, these two formulas using potential flow theory (and very often based on slender body theory assumptions) were widely adopted. It is evident that the main benefit of these inviscid potential flow-based approaches is their low computational cost, which makes such codes appealing for applications like hull form optimizations, where the quick assessment of a large number of design choices is more essential than accuracy (ITTC 2017*a*). Potential flow is better for quick estimates of the added resistance by itself, whereas computational fluid dynamics methods (N-S based techniques) provide a more thorough investigation of self-propulsion in waves (Windén 2014). According to the findings of the 28th ITTC Seakeeping Committee report (ITTC 2017*a*), compared to the potential flow theory, RANSE solvers make it possible to investigate the full physics of added resistance in waves, which includes large amplitude motions, non-linear effects, and the influence of viscosity. Numerical investigations of wave added resistance have become more prevalent because of the widespread availability of computational fluid dynamics (CFD) tools in recent years. Its strengths over potential methods lie in its ability to deal with nonlinear flow phenomena like breaking waves and green water without using explicit approximations and empirical values (Kim et al. 2017). Moctar et al. (2017), Ozdemir & Barlas (2017), Sigmund & El Moctar (2018) presented results of wave added resistance by solving the Reynolds-averaged Navier-Stokes (RANS) equations. Tezdogan et al. (2015) performed fully nonlinear unsteady RANS simulations to predict ship motions and the added resistance of a full-scale KCS model in twelve different regular waves at service and slow steaming speeds. The obtained CFD results were validated with EFD and also compared with calculations using potential flow theory, showing good agreement. Yang et al. (2015) carried out added resistance calculations using a Cartesian grid method-based Euler equation solver. There have also been several research comparing CFD results with potential theory calculations, reported in Seo et al. (2013), Lyu & el Moctar (2017) and Kim et al. (2017). Compared to the potential flow methods, although these computations through CFD approaches require large computational resources, long CPU times, and the setup of the computations in CFD tools requires skills and experience, the N-S based methods in principle provide a more accurate description of the physical phenomena, making them more suitable for the wake and propeller analysis in self-propulsion tests.

In addition, as ship sizes keep increasing to take advantage of economies of scale, the ratio of wave length to ship length, λ/L, which is of practical importance, has changed to lower values, which makes the accurate estimates of added resistance in short waves much more crucial than it used to be. Furthermore, recent targeted experimental investigations (Kim et al. 2014, Valanto & Hong 2015) and time-consuming CFD calculations

(Ley et al. 2014) have indicated that viscous effects, which cannot be well studied by potential flow theory, seem to play a substantial role in the prediction of the added resistance in short wave conditions, particularly when approaching limiting values. However, as shown by the research of Söding et al. (2014), the limitations of both CFD and potential-flow approaches were found when dealing with extremely short waves, since this requires very dense grids/small size panels in order to accurately capture flow changes. Due to the very tiny measured values, obtaining reliable measurements of the added resistance in short waves during towing tank tests is always a big challenge. Because of this, tank operators tend to apply steeper incident short waves for relevant measurements, which may call into question the quadratic dependence of the additional resistance on wave height. Therefore, when developing short wave added residence formulations, it is very necessary to make use of trustworthy experimental data in order to fine-tune the correctly introduced semi-empirical correction coefficients (Liu & Papanikolaou 2016). As a consequence of this, semi-empirical adjustments are often used alongside numerical findings in order to improve the accuracy of predicting the added resistance in short wave scenarios. Both Yang et al. (2018) and Riesner & el Moctar (2018) documented their latest correction schemes. Liu & Papanikolaou (2016) proposed a useful semi-empirical formula for determining the extra resistance encountered by ships travelling in either long or short waves.

2.4 Self-propulsion in waves

To truly predict the ship's actual power requirement, a self propelled ship model test in calm water is a common approach. Apart from the requirements set in the resistance test, the self propulsion tests also involve the presence of the propeller, which makes investigation of self propelled ship more difficult due to the interaction between hull, propeller, rudder and their surrounding fluid. Furthermore, this problem become more complex and more sensitive to errors when considering the self propulsion performance in waves (Windén 2014). Prediction of self-propulsion in waves using experimental methods can provide accurate and reliable estimations of ship powering and experimental results can be used to validate against theoretical and numerical results. However, due to the high cost of the model test setup and the high specification for the hull and propeller models and test facilities, it is necessary to find a more cost-effective alternative. Benefiting from the rapid development of high performance computing, self propulsion model tests can be replicated using a variety of numerical approaches, providing more local details of hull-appendages interaction in stern region, which is less likely to be observed in towing tank or wave basin tests.

2.4.1 Unsteady hydrodynamic performance of propeller in waves

In terms of ship power prediction, the traditional ship self-propulsion test method does not consider the hydrodynamic performance of the propeller under wave conditions unless the coefficient correction is applied later (Zhao et al. 2017). The increase of ship power in waves can be calculated using the direct powering technique, the torque rotational speed method, the thrust rotational speed method, and the resistance equal to thrust method, as outlined by ITTC (2002). All four approaches rely on several assumptions, such as a constant rate of power increase for the vessel, the thrust and torque of the propeller being proportional to the wave height quadratic, etc. None of the aforementioned techniques can offer an accurate assessment of the ship's resistance increase in ballast conditions since they all rely on assumptions that do not accurately represent the actual condition of the ship in the waves. As a result, it is essential to investigate the hydrodynamic performance of the propeller when it is operating under wave conditions, which are closely related to real sea states.

From an experimental perspective, Taniguchi (1961) and McCarthy et al. (1961) presented the open water characteristics of a propeller while it was subjected to waves, where the propeller is attached to the carriage. Nakamura & Naito (1975) conducted research on the open water test of a propeller in both regular and irregular waves, taking into account the influence of heave, pitch, and surge oscillations. They demonstrated that the average characteristics of the propeller in waves are identical to those in calm water conditions. The variation of propeller thrust and torque in wave traces on open-water curves was also clarified. Using open-water characteristics curves and the assumption that the input velocity, thrust, and torque changed sinusoidally, Natio & Nakamura (1979) estimated the fluctuation thrust of the propeller under wave circumstances. Nakamura et al. (1975) and Tsukada et al. (1977) made the wake flow measurement in waves at the propeller position with the use of towed model ships without a propeller and concluded the average wake coefficient in regular waves varies depending on wavelength. However, the average wake in irregular waves is similar to the one in calm water (Nakamura S, Hosoda R, Naito S 1975). In addition, the linear superposition of the thrust and torque variations reported in regular waves agrees with those in an irregular composite sea (Aalbers & Gent 1985, Sluijs 1972). Besides, Nakamura & Natio (1977) demonstrated experimentally that pitch motion has a significant effect on wake velocities, especially close to the pitch natural frequency. Lee (1983) studied the performance of a propeller under racing conditions through experiments and presented the variations of propeller loading in waves together with blade stress and hull pressure fluctuations in waves. Paik et al. (2005) conducted experiments in a circulating water channel to study the influence of a free surface on the wake behind a rotating propeller and indicated the effects of free surface on the axial velocity component and vortex structure behind the propeller. Amini & Steen (2011) carried out a series of model experiments on an azimuth thruster model under oblique inflow circumstances in pushing and pulling modes with various heading angles and advance coefficients and the load at the shaft-bearing points was discovered to be nearly three times more than when simply the propeller weight was taken into account because the propeller shaft lateral force and bending moment were fairly considerable. Guo, Zhao, Wang & Chang (2012) tested a certain propeller in the condition of identical regular waves but varied depths of propeller shaft, finding the influence of waves on propulsive coefficients and unsteady performance of the propeller. In order to determine the unsteady inflow velocity to a propeller in waves, Ueno et al. (2013) performed a free running model test. The unsteady inflow velocity using these direct techniques, which were initially for steady calm water conditions, was analysed by using a standard thrust and torque identification approach. Zhao et al. (2017) performed experimental analysis of propeller's hydrodynamic behaviours in waves and summarized that it is not accurate to simply conclude that the propeller propulsive efficiency reduces in waves compared with calm water, as the main reason for propeller performance changes is the effluent and spatter phenomenon caused by the decreased shaft of shaft.

It is apparent that experimental testing can offer an accurate estimation of the unsteady performance of propellers in waves, which is one of the most important phases in the evaluation of ship self-propulsion in waves. However, given the high costs and time commitments associated with conducting experimental trials, numerical methods have been receiving a greater amount of focus as of late. Tasaki (1957) analyzed the impact of surge motion and the orbital motion of waves on the effective inflow velocity. Faltinsen et al. (1980) stated that pitch motions have a significant impact on wake owing to the pressure shifts caused by the oscillatory vertical motion. The pressure variations cause a pressure gradient along the hull, which alters the nature of the boundary layer and speeds up the flow toward the stern. This has an effect not only on the water flow into the propeller but also on the viscous drag and stern flow separation. Cao (1988) studied the open water properties of a propeller with varying depths of the shaft and in wave conditions, which was necessary for predicting self-propelled ships in waves. Wang & Jia (1989) presented a quasi-steady lifting surface method for estimating a propeller immersed near the water surface with the vortex lattice method applied. Tao & Zhang (1991) investigated the open water propeller behaviors with heaving and pitching in regular waves by adopting the 3D Green function method where the propeller was replaced by a sink disk. Lee et al. (2010) carried out a computational fluid dynamics analysis (CFD) study of the propeller in waves using an overset grid approach in order to determine how wave conditions affect the performance of a propeller while it is running behind a stationary hull. Califano & Steen (2011) conducted numerical simulations of a fully submerged propeller subject to ventilation and found that the tip vortex has a dominant role in the ventilation of conventional propellers. In order to forecast the forces and moments acting on the propeller shaft under oblique flow circumstances, a basic blade element momentum technique (BEMt) was adopted (Amini

& Steen 2011), and good agreements were found between experimental and BEMt results. Guo, Steen & Deng (2012) indicated that axial velocities at the propeller disk could reach as high as 35 percent of the ship's forward speed in the presence of waves by performing unsteady RANS simulations. Taskar, Steen, Bensow & Schröder (2016) and Taskar et al. (2017) investigated how waves affect the operation of propellers, focusing on cavitation, hull pressure changes, and effectiveness. Results showed that the main causes of performance variation are wakefield fluctuations over time, differences in shaft depth, variations in propeller speed, and reduced speed compared to calm water conditions. Zhao et al. (2017) numerically simulated the unsteady performance of the propeller in waves and demonstrated that the changing amplitude of propeller forces is much larger than those in calm water. Therefore, the unsteady features of propellers in waves cannot be neglected when assessing the actual propeller propulsive efficiency in real sea states. Saettone et al. (2020) compared the performance of a full-scale KVLCC2 propeller in waves using both the quasi-steady and fully unsteady approaches and he comparison was based on differences in unsteady propeller forces, cavitation volume, and hull pressure pulses. Eom, Jang & Paik (2021) examined how the propeller performance changes in calm water and waves by altering the immersion depth for four advance ratios of $J = 0.1–0.7$ and it was shown that each of the relative immersion depths and advance ratios might be impacted by the wave phase. The behavior of a propeller with motion in waves was then predicted using a prediction approach. In calm water, a function of the advance ratio (J) and immersion depth (h/D), taking into account the impacts of waves and motion, was used to determine how the propeller performance varied owing to the immersion depth and tilt angle (Eom, Paik, Jang, Ha & Park 2021).

2.4.2 Propeller modeling using numerical methods

The challenge of self-propulsion encompasses determining the self-propulsion coefficients required for calculating power and designing propellers, as well as delving into the transient effects caused by the rotation of the propeller, such as its interaction with the rudder (Durasević et al. 2022). Accurate prediction of self propulsion in waves is important in the ship's hydrodynamic performance and it also provides sound knowledge for assessing the actual ship propulsion power requirements in real seaways. Estimating the hydrodynamic performance of self-propelled ships in waves is often achieved using experimental or empirical approaches. However, they are either excessively costly or incapable of adequately capturing the fluid-structure interaction. Because of the growing availability of computational resources, numerical methods are becoming a more popular and cost-effective method to model the performance and hydrodynamic characteristics of a propeller. Accurate modeling of the propeller is essential for the reliable prediction of self-propulsion characteristics. Section 2.2.4 summarizes brief descriptions of various propeller numerical modeling approaches. The choice of propeller numerical methods depends on the level of accuracy required and the computational resources available. In this section, a detailed literature review of different numerical propeller modeling methods will be presented.

In terms of numerical approaches for marine propeller modeling, the most commonly used techniques in CFD for calculating self-propulsion are the body force method and the fully discretized propeller approach. The two most widely adopted approaches for fully discretized propeller modeling are the sliding interface method and the dynamic overset grid method (Gatin et al. 2018, Senjanović et al. 2020). With the application of dynamic overset grids, a novel approach was proposed using a PI speed controller and discretized propellers to predict self-propulsion performance for three ship geometries: the KVLCC1 tanker, the ONR Tumblehome surface combatant, and the KCS container ship (Carrica et al. 2010). The sliding mesh technique for a rotating propeller was utilized by Seo et al. (2010) to conduct the three primary tests for ship resistance and propulsion performance, including resistance, open water propeller, and self-propulsion tests. Shen et al. (2015) presented the implementation of the dynamic overset grid technique in OpenFOAM, with a focus on its application to the self-propulsion and maneuvering of the KCS. Because the flow around a rotating propeller is complicated and always changing, a discretized propeller model needs a higher mesh resolution and a smaller time step to capture the flow patterns around the propeller blades accurately. However, this results in more complex meshes, increased simulation time, and higher costs. Carrica et al. (2010) admitted that the computational demands of fully discretized propeller simulation are quite substantial and can consume a significant amount of resources. It can take approximately one month of wall-clock time using 50 to 160 processors to complete these calculations. In comparison, the body force model for self-propulsion is relatively simple and requires less computational resources when a detailed capture of the propeller flow is not essential, making it well suited for initial ship design studies and early-stage marine propeller performance predictions.

Based on the approach used to determine the body force source term, body force methods are typically categorized into: iterative body force method and descriptive body force method (Kawamura et al. 1997, El Moctar 2001). The descriptive body force model, firstly proposed by Hough & Ordway (1964), is based on the propeller open water curve and propeller forces distributions. Self propulsion simulation can be carried out using the descriptive body force model as listed in Choi et al. (2010), Ohashi et al. (2018), and Jin et al. (2019). However, velocity correction is normally required. The descriptive body force approach is relatively straightforward and convenient, but it lacks the capability to accurately perform calculations for propeller performance and it cannot directly calculate the force and pressure distribution of a propeller operating behind a ship hull (Guo et al. 2020). The iterative body-force method uses local instantaneous velocity as the advance velocity in each iteration, allowing the virtual propeller and RANS simulation codes to interact and work towards a solution. This approach also allows for the two-way interaction between the local flow field and the virtual propeller to be considered (Feng et al. 2020*b*). Therefore, the RANS coupled with the potential flow approach is a type of iterative body-force method, which is more complex than descriptive methods. This approach is capable of calculating propeller performance by using potential flow methods, with the calculated propeller loads (pressure and force distribution) serving as input for the RANS computation (Guo et al. 2020, Durasević et al. 2022). Yamazaki (1977) developed a simplified theory of a finitely bladed propeller and wave resistance theory, in which the line integral component was omitted and replaced by a theory that considers the impact of the nonlinear free surface. A simple, infinite-bladed propeller model based on potential theory is combined with the Reynolds-averaged Navier-Stokes (RANS) simulation code CFDSHIP-IOWA to produce a model that can interactively assess the interaction between the propeller, hull, and rudder, without the need for a detailed representation of the propeller's geometry (Simonsen & Stern 2005). Vaz & Bosschers (2006) employed Boundary Element Techniques to calculate the forces and moments exerted on the cavitating propeller operating in the ship's wake and the resulting pressure fluctuations on the hull. Tokgoz (2015) proposed a new body-force propeller model that utilizes a simplified quasi-steady Blade Element Theory (BET) to calculate the thrust and torque distributions by utilizing the total velocity field obtained from a Computational Fluid Dynamics (CFD) code. Villa et al. (2012) combined the panel method for propeller modeling with the Reynolds Averaged Navier-Stokes (RANS) equation to calculate the self-propulsion performance of the KCS, taking into account the detailed induced velocity and volume force information from the propeller. Further research was carried out by Gaggero et al. (2017) by coupling Boundary Elements Method (BEM) with the RANS to predict the self propulsion coefficients of the typical benchmarking hull type KCS. Villa et al. (2019) proposed an effective and reliable method for estimating the ship self-propulsion coefficients by coupling Reynolds-averaged Navier–Stokes (RANS) with potiential flow method BEM. Durasević et al. (2022) conducted a comprehensive numerical analysis of global and local self-propulsion characteristics of a model-sized KRISO container ship using both discretized propeller (DP) and actuator Disc (AD) approaches. Two different (AD) methods were tested: the first method only models the axial effect of the propeller while the second one models both axial and tangential influences.

In self propulsion simulations, the interaction between the propeller and the hull also affects the accuracy of propeller modeling because the Reynolds number and local length scales for a propeller and a hull differ, the challenge of finding a model that can accurately predict both remains unresolved (Windén 2014). Therefore, separating the modeling of the propeller flow and the flow around the hull offers numerous advantages, as it permits the use of methods better suited to the local flow conditions in each part of the simulation (Molland et al. 2017). Badoe et al. (2014) combined the Blade

Element Theory and Momentum Theory (BEMt) with RANS calculations in OpenFOAM. The coupling process was achieved by transforming local thrust and torque into momentum sources, which were incorporated into the equations until convergence was achieved. The effective wake field was determined by subtracting the propeller-induced velocities calculated from the BEMt code from the total wake field. An example of how the BEMt modeling method for the propeller can be integrated with a RANS solver was given in Windén (2014). Badoe (2015) evaluated the ability of three different propeller models and the coupling process within a RANS environment, including the Hough and Ordway Prescribed Body Force Propeller (RANS-HO), a propeller performance code based on the Blade Element Momentum Theory (RANS-BEMt), and a discretized propeller approach utilizing the Arbitrary Mesh Interface Model (RANS-AMI). The interaction between the hull on the propeller and the rudder on the propeller is not captured by RANS-HO because it assumes a constant circumferential distribution of propeller forces. This approach provided a fair estimate of the resistance but performed poorly in simulating the swirl effect, which produced a distinct flow field. The thrust and torque can be calculated as part of the simulation using RANS-BEMt, and the simulation can provide good estimates of the interaction between the hull, propeller and rudder. Swirl effect replication is substantially improved over RANS-HO using this method. AMI provides a high level of accuracy in theory, but results could have been even better with finer mesh resolution near the propeller blades and in the boundary layer. To resolve the full transient propeller flow, AMI requires smaller time steps and a higher level of mesh cells to provide accurate estimates of resistance and propulsion parameters, which makes AMI the most computationally demanding approach among these three methods. The axial velocity field at the propeller plane using these three propeller modeling methods is shown in Figure 2.5.

2.5 Ship manoeuvring in waves

High-accuracy prediction of ship manoeuvring and coursekeeping in actual seaways is one of the essential requirements in ship design. It is closely related to ship navigation safety, especially in adverse wave and wind conditions. International Maritime Organization (IMO) released ship manoeuvrability standards in 2002, emphasizing the necessity of checking ship manoeuvring during the early ship design stage (International Maritime Organization 2002). Although ship manoeuvring calculations in calm water have been studied widely, the understanding of ship manoeuvrability in real sea states is still not well established (ITTC 2021). Compared to resistance, propulsion, and seakeeping, the ability to anticipate how a ship will manoeuvre in waves remains a significant challenge because of the complex fluid-structure interaction between hull, rudder, propeller, and their surrounding fluid (Sanada et al. 2021).

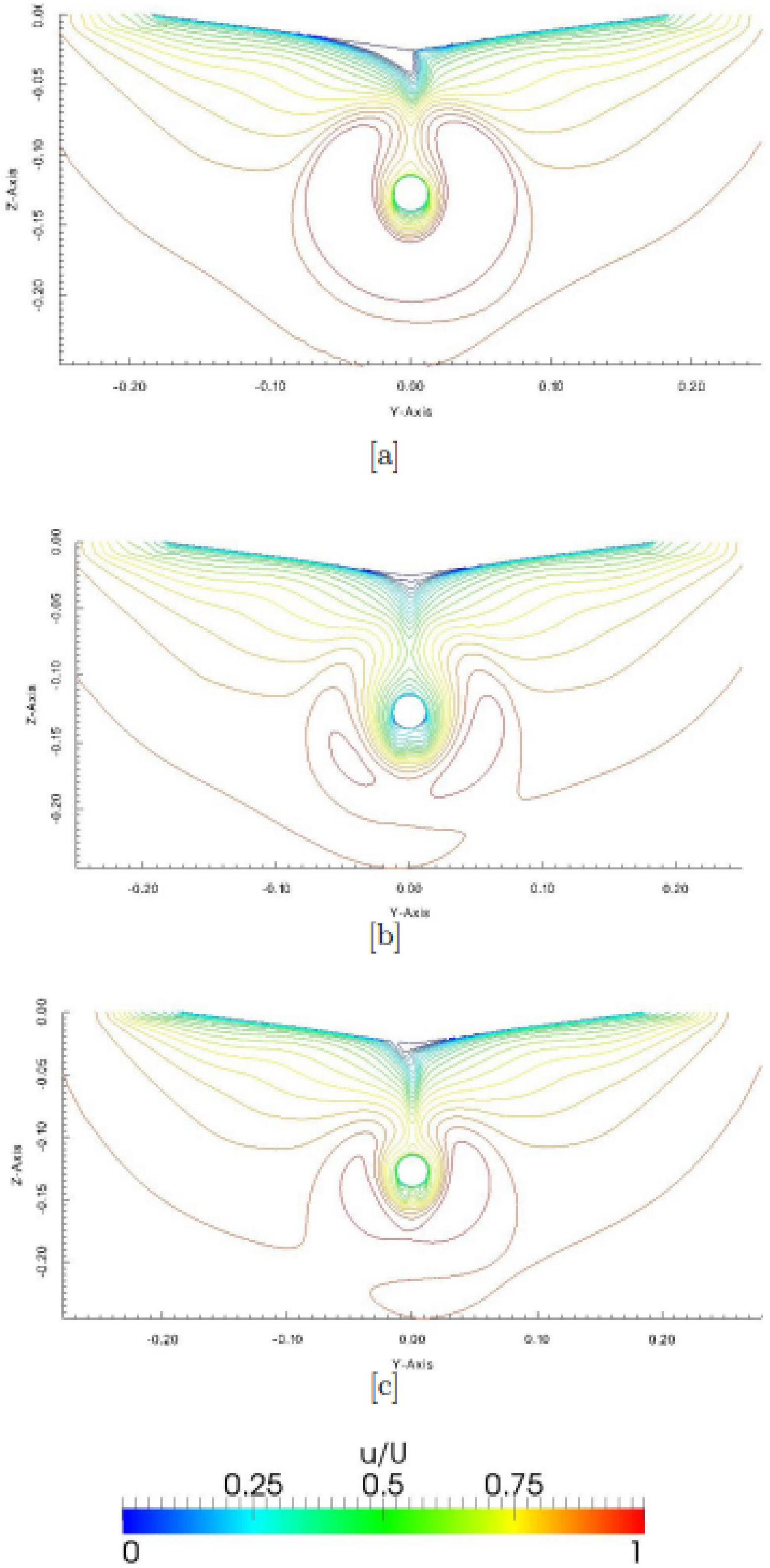

FIGURE 2.5: Axial velocity field at propeller plane using double body computations with Fn=0.202: [a] RANS-HO, [b] RANS-BEMt, [c] AMI (Badoe 2015).

2.5.1 Hull propeller and rudder interaction

In order to truly assess the self propelled ship powering performance in waves, the details of hull-propeller-rudder interaction effects are needed. However, the manouvring characteristics of self propelled ships in realistic sea states have not been clarified completely due to the complicated flow field around the stern. The rudder is a widely used steering device and its ability to control ship manoeuvrability is greatly impacted by the wake, as well as the action of the upstream hull and propeller. Therefore, to improve understanding of a ship's maneuverability in actual sea conditions, it is crucial to clarify the interaction mechanism between the hull, propeller, and rudder. Free-running model testing and captive model tests in a towing tank or wave basin are two standard experimental methods for assessing a ship's manoeuvrability. Manoeuvrability is evaluated in a straightforward manner during free-running model testing by performing a prescribed turning or zigzag test. Captive tests, on the other hand, are used to estimate hydrodynamic forces and moments by solving ship motion equations using the derived hydrodynamic derivatives (manoeuvring coefficients) (Jiang et al. 2022). Molland & Turnock (1992), Molland & Turnock (1995) and Molland & Turnock (2002) conducted a series of wind tunnel experiments to examine the impact of hull length, drift angle, and propeller loading on rudder performance, using various configurations of the hull, propeller, and rudder. Atsavapranee et al. (2010), Khanfir et al. (2011) and Dubbioso et al. (2015) conducted a set of experiments on a ship model with a twin-rudder design to examine the hydrodynamic properties of the propeller and rudder during specific manoeuvring motions. Kim et al. (2019) performed tests of the turning circle for a KVLCC2 ship model while it was freely turning in multi-directional regular waves and a systematic investigation was conducted to examine the impact of regular wavelength, height, and direction on the turning paths. Although relatively accurate and reliable manoeuvring assessments can be obtained by the conventional model test, it is still costly and has a high specification for the ship model and test facilities. The rapid advancement of high-performance computing has allowed numerical methods to provide a potentially more cost-effective method of determining the ship's manoeuvring performance, with greater fidelity of hull-appendages interaction in the stern region, which is less likely to be captured in towing tank tests (Zhang et al. 2021).

Given its potential as a promising alternative for gaining insight into the interaction between the hull and its appendages, a large number of studies have been conducted using Computational Fluid Dynamics (CFD) to simulate the flow around hulls, propellers, and rudders. This approach enables a more detailed understanding of the flow field and hydrodynamic characteristics of ship manoeuvring. Liu et al. (2015) investigated the hydrodynamic properties of an isolated rudder with varying geometries in open water conditions and the influence of rudder profiles on ship manoeuvrability was presented. Phillips et al. (2010), Krasilnikov et al. (2011) and Sánchez-Caja et al. (2015) explored the interaction between the propeller and rudder, including the flow field and performance of the rudder, by simulating the flow around a fully appended ship model, thereby gaining a more comprehensive understanding of the interaction mechanism. Lee et al. (2008) studied the flow characteristics around a type of high-lift rudder as it interacts with the upstream hull and propeller. Jamali (2011) investigated the impact of varying the longitudinal and transverse positions of the rudder on the performance of the propeller and rudder interaction, showing that the optimum rudder location regarding delivered power was determined at b/D=0.2 for model scale while at b/D=0.1 for full scale. Badoe et al. (2015) examined the interaction effects in a hull-propeller-rudder configuration at varying drift angles and hull lengths and found that Positioning the compact board upstream of the propeller while at drift significantly enhances the straightening effect on the flow. Muscari et al. (2017) presented the study of the asymmetrical behaviour of the propeller-rudder system and the load on the bearings of the propeller for twin-screw ships during manoeuvres. The in-house CFD solver naoe-FOAM-SJTU was employed by Wang & Wan (2018) to directly simulate the performance of ship manoeuvring in waves with rotating propellers and turning rudders, providing good local flow characteristics of hull, propeller, and rudder. Woeste et al. (2022) investigated the hull-propeller-rudder interaction in head sea conditions using CFD only and a hybrid CFD and potential flow method and found hull-propeller interaction in waves, nonlinear hydrodynamic and viscous effects have a significant role in added power. The added power coefficient exhibits a non-linear dependence on the square of the wave elevation. Furthermore, as the model size diminishes, there is a marked increase in the overprediction of the added power coefficient.

2.5.2 Importance of rudder forces determination

When determining the characteristics of a ship's manoeuvring and coursekeeping in real sea states, it is important to acquire accurate estimates of the forces and moments acting on both the hull and the rudder. This is especially true when the ship is operating at the angle of drift, as the influence of rudder angle could be significant in assessing the ship resistance, propulsion coefficients, and overall efficiency of a self propelled ship manoeuvres in waves. Molland & Turnock (2007) indicated that the forces exerted by the rudder are significantly impacted by the interaction of the forces and moments generated by the hull and propeller upstream of the rudder. The effective rudder angle is one of the main criteria that determines how the hull and rudder forces behave (Molland & Turnock 2002). When a non-zero rudder angle is applied to alter the ship's course, the ship develops a yaw or drift angle and the flow is no longer aligned with the vessel, and a crossflow is formed across the propeller plane. Therefore, the actual propeller performance, such as thrust, torque and effective direction of the propeller race, will be changed due to the asymmetry fluid. The propeller sideforce will not keep constant as that in straight-head conditions, leading to a decrease in the effective inflow angle to the rudder (Badoe et al. 2015). Additionally, the effective inflow angle to the rudder is recovered or increased due to the existence of the hull and propeller upstream of the rudder, which straightens the flow. Therefore, the flow straightening effect due to the hull and propeller is important in the precise determination of rudder forces during a ship manoeuvre. Studies of Yumuro (1974), Yumuro (1975) and Yumuro (1978) has been conducted to investigate the impact of the drift angle and the flow-straightening influence of the combined hull and propeller on the rudder. Molland & Turnock (1995) used wind tunnel tests to examine the flow straightening influence of the propeller on the effective drift angle and how it affects the rudder performance. Longo & Stern (2002) investigated the effect of drift angle on forces and moments of Series 60 CB=0.6 cargo/container model ship through towing tank tests. El Moctar (2001) calculated the hull forces as a function of drift angle by applying a finite volume method to viscous flow computations. Phillips et al. (2009*b*) coupled a Reynolds averaged Navier Stokes (RANS) solver with Blade Element Momentum Theory (BEMt) to study self-propelled KVLCC2 hull's manoeuvring coefficients at drifted conditions. Badoe et al. (2015) numerically replicated the previous study of Molland & Turnock (1995), providing a detailed understanding of the interaction between the propeller and rudder, including information about the flow field, pressure distributions on the rudder surface, and the impact of thrust and torque augmentation on the propeller blades. It was found that the lift force of rudders placed behind a propeller increases with increasing propeller load. The effect of drift tends to change the direction of the forces associated with the rudder, but it does not completely alter them, and this shift is dependent on the angle of drift. More recently, Sanada et al. (2021) combined experiments and CFD to explore the physics of KCS hull-appendages interaction for turning circles and the reason for differences between port and starboard turning. Sumislawski et al. (2022) examined the JBC hull and propeller interaction under static positive and negative drift conditions, and detailed properties of the fore-body vortex were presented.

2.5.3 Numerical ship manoeuvrability in waves

As mentioned in section 2.5.1, evaluating the manoeuvrability of a ship in waves through experimental methods is costly and highly demanding for test facilities including free-running models, wave basins and etc. Therefore, there is only a limited number of institutions able to perform ship manoeuvring in waves tests such as the Iowa Institute of Hydraulic Research (Sanada et al. 2019) and Hiroshima University (Yasukawa et al. 2021). In addition to experimental approaches, the estimation of a ship's manoeuvring behaviour in waves can also be achieved through the application of theoretical methods, which involve the integration of mathematical models and the potential flow theory. However, due to the fact that complexities of fluid-structure interactions cannot be precisely resolved by the simplified mathematical model and potential flow theory neglects the effect of viscosity, theoretical methods have certain limitations and are not appropriate for predicting a ship's behaviour during manoeuvring in waves (Kim et al. 2021).

In comparison, numerical methods (mainly CFD) using free-running simulations (e.g. turning and zigzag manoeuvres) can provide better ship manoeuvrability in waves assessment because it includes the viscous and rotational effects, and it can capture the interaction between the hull, propeller, rudder and waves. Mofidi & Carrica (2014) conducted the two types of zigzag manoeuvres (the standard 10/10 zigzag manoeuvre and the modified 15/1 zigzag manoeuvre) of the Korean container ship (KCS) model including the moving rudder and rotating propeller. A dynamic overset technique utilizing a hierarchy of bodies was utilized to tackle the difficulties in simulating the motion of the semi-balanced horn rudder. The obtained results demonstrate that direct Computational Fluid Dynamics (CFD) simulations of manoeuvring with a moving rudder and rotating propeller are viable, and the comparisons between the simulations and experiments are highly satisfactory in both cases. Broglia et al. (2015) accomplished the simulation of the turning circle manoeuvre of a naval supply vessel by combining the unsteady Reynolds-Averaged Navier Stokes equations with the equations of rigid body motion that have six degrees of freedom. The validation of the simulation was established through comparison with experimental data obtained from free-running tests, which shows good agreement. Shen et al. (2015) showed the capabilities of Dynamic overset grids in OpenFOAM with application to KCS zig-zag manoeuvre and good agreement was found with experimental data even though relatively coarse grids are adopted. Wang et al. (2017) presented the numerical analysis of the free-running ONR Tumblehome ship model under course keeping control in both calm water and regular waves using naoe-FOAM-SJTU, a CFD solver developed on open source platform OpenFOAM. The predicted trajectory for all cases showed exceptional agreement with the results from the free-running tests, further confirming the applicability of the implemented course-keeping controller. The numerical computations of the ship manoeuvring in waves were further reported in Wang & Wan (2018). Jin et al. (2019) investigated the ship manoeuvrability in waves by coupling body force propeller Todel and the discretized propeller model with unsteady RANS equations. the comparison between the experimental and numerical results showed mostly an agreement of around 10 percent for the analyzed turning circle and zig-zag manoeuvres. Kim et al. (2021) performed a fully nonlinear unsteady RANS simulation to forecast the manoeuvring behaviour of a KRISO Container ship (KCS) model under various wave conditions. The simulation incorporated a course-keeping and manoeuvring control module based on a feedback control system, which controlled rudder deflection according to established manoeuvring procedures. The simulation results were compared with available experimental data and demonstrated good consistency.

It is true that direct CFD simulation using dynamic overset mesh can provide the most accurate prediction of ship manoeuvring in waves with the highest fluid dynamic fidelity. However, the computational cost of using such methods is extremely intensive. Mofidi & Carrica (2014) stated that conducting end-to-end manoeuvring simulations for a new geometry requires approximately 4 months of work from a highly skilled trained engineer, which is too time-consuming and money-consuming. Therefore, a more cost-effective numerical method for ship manoeuvring in waves prediction is still in great need.

2.6 Chapter summary

This chapter provides a thorough literature review that systematically analyzes the hydrodynamic performance of ships in waves, mainly including both historical developments and state of the art in experimental as well as numerical approaches for evaluating a vessel's resistance, propulsion and manoeuvring performance in realistic sea states. It is found that both experimental tests and numerical computations are of high importance in better understanding of resistance and powering capabilities of vessels. The literature reveals that experimental approaches, while valuable, can be very costly, time-consuming, and fraught with uncertainties. Additionally, the completion of experiments often requires high-specification test facilities, accurate ship models and well-trained technicians. In contrast, numerical methods are widely regarded as a more cost-effective alternative. A significant advantage of employing numerical methods lies in their ability to offer detailed insights into the local flow field, particularly regarding hull-appendage interactions in the stern region. Such specific information is often difficult to obtain from experimental tests.

While numerical methods can provide considerable benefits, conventional dynamic ship manoeuvring calculations remain resource-intensive. This is primarily due to the complex interactions among the ship's motion, the wake field, and the hydrodynamic forces exerted on the vessel and its appendages. Furthermore, a key challenge associated with numerical simulations of ships manoeuvring in waves is the validation process. Ensuring the accuracy and reliability of these simulations requires high-quality experimental data, which, however, is very difficult and costly to obtain due to the complexities in testing environments and measurement uncertainties. Therefore, the focus of this work is to numerically simulate a specific fully appended vessel under a series of fixed drift angles, which represents quasi-static phases of an actual ship manoeuvre. This allows for the direct validation of some of these computations and contributes to the future validation of the actual manoeuvring models and manoeuvring simulations. Even though this kind of calculation is cheaper than actual manoeuvring simulations, the computation of considering fully hull-propeller-rudder interaction still requires high computational costs. Therefore, it is still in high demand to find a cost-effective method to model the fully appended ship under drift, which can reasonably capture the interaction effect between the hull, propeller and rudder.

The next chapter will introduce the mathematical formulation and numerical methodology used in this thesis. Chapter 4 will present the sectorial approach of Blade element momentum theory (BEMt) for modelling propeller in drift conditions, which is cost-efficient as body force models in contrast to the fully discretized propeller. Progressive methodology development for studying the fully appended vessel under drift is structured as follows: initially, the double body model is used to capture the hydrodynamic interactions of submerged bodies, shown in Chapter 5, followed by the implementation of the VOF model in calm water to simulate free surface flows, presented in Chapter 6, and finally, the integration of the VOF model in wave scenarios, illustrated in Chapter 7.

Chapter 3

Mathematical formulation and numerical methodology

3.1 Introduction

Understanding the manoeuvring performance of a self-propelled ship in waves, as discussed in Chapter 2, and the hydrodynamic interaction between the hull, propeller, rudder, and surrounding fluid, particularly in the stern area, is a complex matter. Effective and accurate prediction of this requires a clear understanding, which in turn facilitates estimation of the actual resistance and powering performance in real seaways. However, undertaking an initial investigation of a fully integrated system consisting of the propeller, a series of rudder angles, and the hull with different drift angles in wave conditions is too complicated. As a result, it was determined that the complexity should be reduced by modeling one or two of the components at a time. This approach facilitates a better understanding of the interaction effects and allows for the acquisition of experience with the modeling techniques. Subsequently, the knowledge and experience gained can be applied to comprehensively investigate the hydrodynamic performance of self-propelled ships in waves. Therefore, the following stepwise procedure is used:

1. Investigation of the interaction between the hull and the propeller in calm water with different drift angles applied using double body approach.

2. Investigation of the interaction between the hull, propeller, and rudder in calm water with a series of rudder angles using double body approach.

3. Investigation of resistance, propulsion and manoeuvring characteristics of a fully appended ship with a series of rudder angles and drift angles in calm water using the VOF approach.

4. Investigation of resistance and powering performance of a fully appended ship with a series of rudder angles and drift angles in different wave conditions using the VOF approach.

The primary focus of this chapter is to demonstrate the numerical approach used in this thesis. Mathematical derivation of governing equations, Reynolds Averaged Navier-Stokes (RANS) equations, is described and it has been confirmed that the RANS method performed well in ship flow modelling (Larsson et al. 1991, Ferziger et al. 2002) due to its balance between accuracy and computational cost, ability to handle a wide range of turbulence scales, and extensive validation against experimental data. After the RANS equations are derived, an appropriate RANS solver is necessary to solve the problem. In this regard, the open-source software OpenFOAM is introduced and compared with other academic and commercial solvers that are available for simulating ship flow problems. Besides, the free surface modelling, turbulence model choice, and uncertainty analysis are included.

3.2 Reynolds Averaged Navier-Stokes (RANS) equations

The equations describing the motion of incompressible viscous fluids were developed by Navier (1823) and then correctly derived by adding the term for viscosity to Navier's equations (Stokes et al. 1851). The Cartesian tensor form of the continuity equation for the conservation of mass in a fluid, where the fluid is considered to be incompressible, can be expressed as follows:

$$\frac{\partial u_i}{\partial x_i} = 0 \tag{3.1}$$

The equation of incompressible momentum for a Newtonian fluid can be expressed as:

$$\rho\left(\frac{\partial u_i}{\partial t} + \frac{\partial u_i u_j}{\partial x_j}\right) = -\frac{\partial p}{\partial x_i} + \frac{\partial}{\partial x_j}\left(\mu\left(\frac{\partial u_i}{\partial x_j} + \frac{\partial u_j}{\partial x_i}\right)\right) + f_i \tag{3.2}$$

where i and j represent the spatial dimension 1, 2, and 3. ρ is the fluid density, p is the pressure, and μ is the dynamic viscosity.

The Reynolds-averaged Navier-Stokes equations are derived by applying Reynolds averaging to the Navier-Stokes equations, which involves decomposing the velocity and pressure fields into mean and fluctuating components. The resulting equations contain additional terms that represent the effects of turbulence, which are modeled using turbulence closure models. The details of deriving the RANS equations can be found in Versteeg & Malalasekera (2007). Here is a brief derivation of RANS:

Reynolds averaging involves decomposing the velocity and pressure fields into mean and fluctuating components as follows:

$$u_i = \overline{u_i} + u_i' \tag{3.3}$$

$$p = \overline{p} + p' \tag{3.4}$$

where $\overline{\mathbf{u}}$ and $\overline{p}$ are the mean velocity and pressure fields, and $\mathbf{u}'$ and p' are the fluctuating velocity and pressure fields.

Substituting these decompositions into the Navier-Stokes equations and performing some algebraic manipulations, the incompressible RANS equations are expressed as:

$$\frac{\partial \overline{u}_i}{\partial x_i} = 0 \tag{3.5}$$

$$\rho \frac{\partial \overline{u}_i}{\partial t} + \rho \frac{\partial \overline{u}_i \overline{u}_j}{\partial x_j} = -\frac{\partial \overline{p}}{\partial x_i} + \frac{\partial}{\partial x_j}\left[\mu\left(\frac{\partial \overline{u}_i}{\partial x_j} + \frac{\partial \overline{u}_j}{\partial x_i}\right)\right] - \rho \frac{\partial \overline{u_i' u_j'}}{\partial x_j} + \overline{F_i} \tag{3.6}$$

By comparing equation (3.2) and equation (3.6), two equations exhibit identical formats, however, the latter includes an extra term $\frac{\partial \overline{u_i' u_j'}}{\partial x_j}$ known as the Reynolds stress tensor, which represents a momentum transfer caused by turbulent fluctuations. The Reynolds stress tensor is a symmetric second-order tensor that consists of six independent components, which include three normal stresses and three shear stresses. The presence of these six additional terms in the Reynolds stress tensor means that the system is not closed. Therefore, a crucial challenge in turbulence modeling using the RANS equation is to derive six additional equations that can close the system of equations (3.6) (Ferziger et al. 2002).

3.3 OpenFOAM

3.3.1 Introduction

Selecting an appropriate RANS solver is necessary once the RANS equations are derived. Currently, there are various solvers accessible for simulating ship flows, such as ANSYS CFX, ANSYS Fluent, StarCCM+, ReFRESCO, and OpenFOAM. The comparison of these RANS solvers is presented in Table 3.1 with their own features.

TABLE 3.1: Comparison of different available RANS solvers

Solver	**Pros**	**Cons**	**License**	**Type**
ANSYS CFX	Transient simulations, multiphase flows	Proprietary, Limited turbulence models	Proprietary	Commercial
ANSYS Fluent	Advanced turbulence models, multiphase flows	Proprietary, High cost	Proprietary	Commercial
StarCCM+	Automated meshing, CAD import, wide range of turbulence models	High cost, Steep learning curve	Proprietary	Commercial
ReFRESCO	High accuracy, parallel computing	Limited user community, Limited turbulence models	GPL	Open-source
OpenFOAM	Large user community, extensive customization options	Steep learning curve, Limited technical support	GPL	Open-source

The choice of RANS solver indeed depends on the specific needs and goals of the study. After evaluating the advantages and disadvantages of each solver, OpenFOAM was chosen for this study over the other options for the following reasons (OpenFOAM Foundation 2023):

Unlike commercial CFD vendors, OpenFOAM provides a fully customizable and extensible software platform specifically designed for research use. Its object-oriented design and extensive modelling capabilities in library form allow for complete flexibility and add-on development to meet the specific needs of the study. OpenFOAM also offers advanced features for complex geometry handling and model development without any licensing restrictions or costs. Furthermore, developers provide a range of commercial support and training options that are informative and useful for users (OpenFOAMFoundation 2019).

While OpenFOAM is a piece of popular and versatile software, it does have some limitations. One such limitation is its lack of an integrated graphical user interface, though stand-alone open-source and proprietary options are available. Additionally, the Programmer's guide may not provide sufficient detail, which can make progress slow when adding new functionality or developing new applications. Furthermore, due to the lack of maintained documentation and extensive code verification, some new users may prefer to choose a commercial solver such as StarCCM+ for their simulations.

While it is not without its limitations, OpenFOAM's approach can provide a reliable numerical solution for problems in continuum mechanics through a set of highly customizable C++ libraries (Jasak et al. 2007). These libraries allow users to build complex and abstract physical models using high-level mathematical expressions. OpenFOAM's structure is built around a large base library that provides core capabilities such as tensor and field operations, discretization of partial differential equations using a human-readable syntax, and more. These capabilities are then used to develop applications. The syntax used in OpenFOAM's applications aims to reproduce conventional mathematical notation, making it easier for users to work with and understand.

3.3.2 OpenFOAM discretization method

When the mathematical model (RANS) has been chosen, the next step is to select an appropriate discretization method. This involves approximating the differential equations by a system of algebraic equations for the variables at a set of discrete locations in space and time (Ferziger et al. 2002). The general discretization process is shown in Figure 3.1, and it can be grouped into two categories:

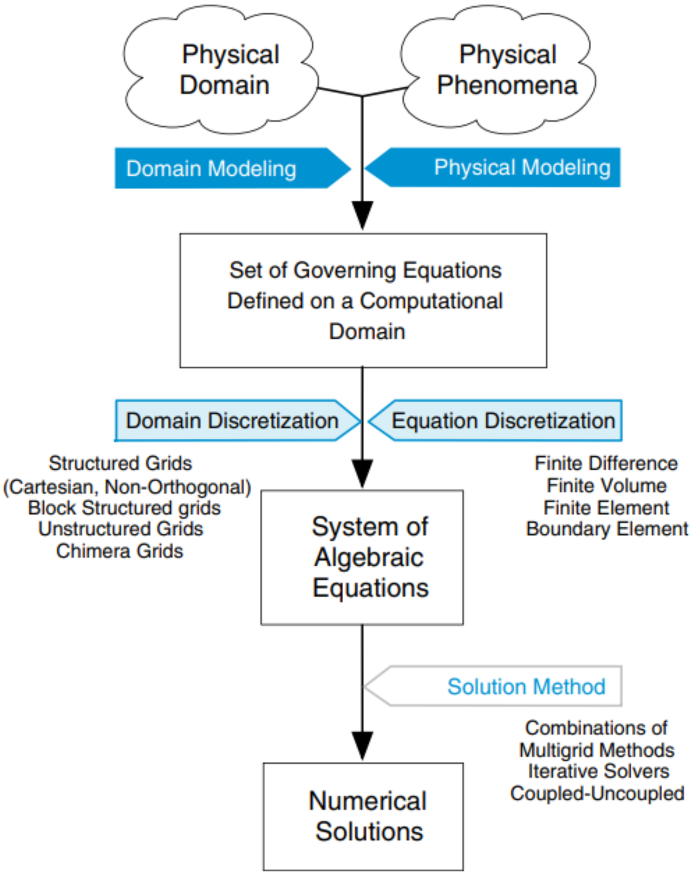

FIGURE 3.1: The general discretization process (Moukalled et al. 2016)

- Domain discretization: the process of dividing the computational domain of the system into a finite number of smaller subdomains or control volumes.
- Equation discretization: the process of approximating the governing equations of a continuous system with a finite set of discrete algebraic equations that are needed to be solved in an iterative way.

There are many commonly used discretization methods, such as the Finite difference method (FDM), the Finite element method (FEM), the Finite volume method (FVM), and etc. The choice of discretization method depends on the problem being solved and the available computational resources, and the comparison between them is shown in Table 3.2. Most CFD codes today use the Finite volume method to solve the RANS equations (Tu et al. 2018). Similarly, FVM is also used in OpenFOAM. As the focus of this thesis is limited, a comprehensive explanation of the OpenFOAM discretization method can be found in Greenshields & Weller (2022). The Finite volume discretization is briefly presented here for better readability.

TABLE 3.2: Comparison of different available discretization methods

Method	Basic Idea	Advantages	Disadvantages
FDM	Discretizes the derivatives of the governing equations	Simple and easy to implement; can be used for a wide range of problems, including complex geometries; relatively low computational cost	Can be inaccurate for complex geometries; prone to numerical instability; requires structured grids
FEM	Discretizes the variational form of the governing equations	Handles complex geometries well; allow for different types of meshes, including unstructured meshes; can provide high accuracy with proper choice of basis functions	Can be computationally expensive; may require additional efforts to satisfy conservation laws; difficult to implement for some types of problems
FVM	Discretizes the integral form of the governing equations	Conserves mass, momentum, and energy; can handle non-uniform and unstructured grids; suitable for problems with shocks or discontinuities; relatively simple to implement	Can be computationally expensive; can be sensitive to grid quality; may require special treatment for advection-dominated problems

The Finite Volume Method (FVM) directly discretizes the governing equations in the physical space without requiring any conversion between physical and computational coordinate systems. FVM also utilizes a collocated arrangement, making it ideal for solving flow problems in complex geometries. Another important characteristic of FVM is that its numerical scheme reflects the underlying physics and conservation principles of the modeled system, including the integral properties of the governing equations and the characteristics of the discretized terms (Moukalled et al. 2016).

The core of the Finite Volume Method is the discretization of the governing equations in the integral form, which ensures the conservation of fundamental variables. The process of spatial discretization involves representing each discrete control volume individually, as illustrated in Figure 3.2. The face area vector, denoted by **S**, is perpendicular to the face it belongs to, with a magnitude equal to the area of the face. The normal vector on the face f, denoted by **n**, is obtained by dividing the face area vector by its magnitude, so that $\mathbf{n} = \frac{S}{|S|}$. The normal vector points from the control volume of interest, P, to its neighboring volume, N. The centers of P and N are joined by a vector **d**. The discretization process will be described using the standard transport equation. The general transport equation in its integral form by integrating in space over an arbitrary control volume can be expressed as Equation (3.7):

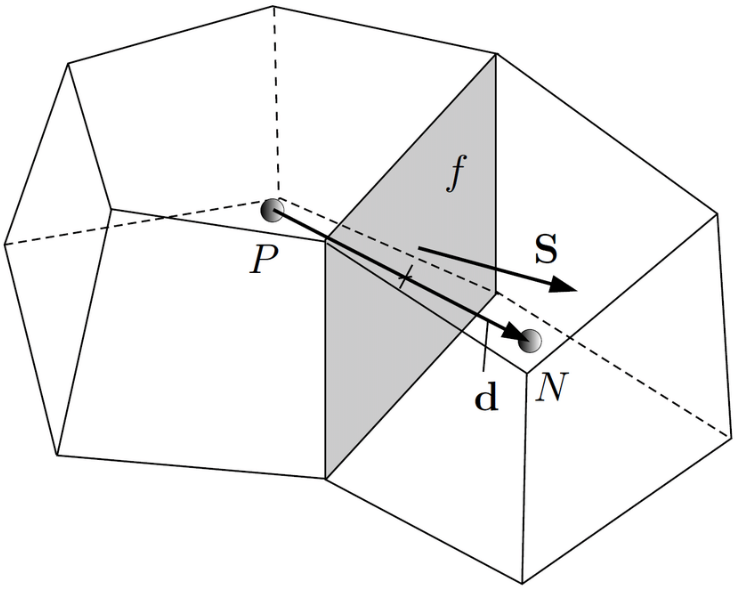

FIGURE 3.2: Parameters for finite control volume discretization (Rusche 2003)

$$\frac{\partial}{\partial t}\int_V \rho\phi\, dV + \int_V \nabla\cdot(\rho\mathbf{U}\phi)\, dV = \int_V \rho S_\phi(\phi)\, dV + \int_V \nabla\cdot(\rho D\nabla\phi)\, dV \tag{3.7}$$

$$\int_V \nabla\phi\, dV = \int_S \phi\, dS \tag{3.8}$$

where D is the diffusion coefficient, ∇ is the gradient operator, ρ is the density of the fluid, ϕ is the transport quantity such as velocity and **U** is the velocity. Gauss's theorem, shown in Equation (3.8), is used to reduce volume integrals to surface integrals, where S represents the surface that encloses the volume V, and dS is an infinitesimal surface element with an outward pointing normal on the surface S.

In equation (3.7), $\frac{\partial}{\partial t}\int_V \rho\phi \, dV$ is the time derivative; $\int_V \nabla \cdot (\rho\mathbf{U}\phi)\, dV$ is the convective term; $\int_V \rho S_\phi(\phi)\, dV$ is the source term and $\int_V \nabla \cdot (\rho D \nabla\phi)\, dV$ is the diffusive term.

Assuming the discretization is second-order accurate in both space and time, each term of the general transport equation can be obtained by integrating the transport equation in space over the control volume Vp and using Gauss's theorem to transform volume integrals into surface integrals. This process involves integrating each term in space to obtain their respective surface integrals.

- **Temporal derivative**

The time derivative $\frac{\partial}{\partial t}\int_V \rho\phi \, dV$ is discretized by integrating it over the control volume. For incompressible flow, assuming the linear variation of ϕ over the time step given by:

$$\frac{\partial}{\partial t}\int_V \rho\phi \, dV \approx \rho \frac{\phi_P^n - \phi_P^o}{\Delta t} V_P \tag{3.9}$$

Where $\phi^n \equiv \phi(t + \Delta t)$ is the new value at the new time step while $\phi^o \equiv \phi(t)$ is the old value from the previous time step.

- **Convective term**

The convective term $\int_V \nabla \cdot (\rho\mathbf{U}\phi)\, dV$ is discretized in the following form using Gauss's theorem

$$\int_V \nabla \cdot (\rho\mathbf{U}\phi)\, dV = \int_S (\rho\mathbf{U}\phi) \cdot \, dS = \sum_f \mathbf{S} \cdot (\rho\mathbf{U})_f \phi_f \tag{3.10}$$

Where $\mathbf{S} \cdot (\rho\mathbf{U})_f$ is the mass flux through the face f. The value of face field ϕ_f can be calculated using Central Differencing, Upwind Differencing, and Blended Differencing schemes.

- **Diffusive term**

A similar procedure to the one used for the convective term $\int_V \nabla \cdot (\rho D \nabla\phi)\, dV$ is used to discretize the diffusion term. The diffusion term can be written after applying Gauss's theorem.

$$\int_V \nabla \cdot (\rho D \nabla \phi)\, dV = \int_S (\rho D \nabla \phi) \cdot\, dS \approx \sum_f \rho D_f (\mathbf{S} \cdot \nabla \phi)_f \tag{3.11}$$

The face gradient of ϕ can be calculated as:

$$\mathbf{S}(\cdot \nabla \phi)_f = |\mathbf{S_d}| \frac{\phi_N - \phi_P}{|\mathbf{d}|} + \mathbf{S_\Delta} \cdot (\cdot \nabla \phi)_f \tag{3.12}$$

The vector $\mathbf{S_d}$ represents the component parallel to d, while $\mathbf{S_\Delta}$ represents the remaining component that needs to be calculated using a non-orthogonality treatment to preserve second-order accuracy. This study employs the over-relaxed approach proposed by Jasak (1996).

- **Source term**

Similarly, the source term $\int_V \rho S_\phi(\phi)\, dV$ can be expressed as:

$$\int_V \rho S_\phi(\phi)\, dV = \rho S_\phi V \tag{3.13}$$

- **Temporal discretization**

Applying temporal discretization to Equation (3.7) leads to:

$$\int_t^{t+\Delta t} [\frac{\partial}{\partial t} \int_V \rho \phi\, dV + \int_V \nabla \cdot (\rho \mathbf{U} \phi)\, dV]\, dt \;= \int_t^{t+\Delta t} [\int_V \rho S_\phi(\phi)\, dV + \int_V \nabla \cdot (\rho D \nabla \phi)\, dV]\, dt \tag{3.14}$$

By applying Equations (3.9 - 3.13) to evaluate Equation (3.14) for all control volumes, a semi-discrete equation can be obtained:

$$\int_t^{t+\Delta t} [\rho \frac{\phi_P^n - \phi_P^o}{\Delta t} V_P + \sum_f \mathbf{S} \cdot (\rho \mathbf{U})_f \phi_f]\, dt \;= \int_t^{t+\Delta t} [\sum_f \rho D_f (\mathbf{S} \cdot \nabla \phi)_f + \rho S_\phi V]\, dt \tag{3.15}$$

Once the spatial and temporal discretization has been performed for all control volumes in the domain, a set of equations can be obtained for the field variable. These equations can then be solved using any iterative method.

3.3.3 Pressure velocity coupling

When solving the RANS equations for an incompressible fluid, a challenge arises because pressure does not have an independent transport equation. The momentum equation (Equation 3.5) indicates that the velocity field is driven in part by the pressure gradient $\frac{\partial p}{\partial x_i}$. The continuity equation (Equation 3.6) governs the velocity field as well. Although this creates a self-contained system of equations (with four unknowns in $u_1, 2, 3$ and p and four equations), the continuity equation only constrains the velocity field and does not incorporate pressure. Thus, coupling the pressure and velocity fields is not a straightforward task because there is no independent way to verify that the pressure gradient is driving the velocity field correctly (Windén 2014). To solve this problem, an equation for pressure calculation is derived from the continuity equation using the momentum conservation equation. OpenFOAM offers a range of pressure-velocity coupling algorithms, including but not limited to, SIMPLE, SIMPLEC, PISO, and PIMPLE.

- **SIMPLE algorithm**

SIMPLE (Semi-Implicit Method for Pressure-Linked Equations), originally proposed by Patankar & Spalding (1983), adopts the iterative way to achieve velocity pressure coupling. To apply the SIMPLE algorithm, an initial estimate for the pressure field is required to solve the momentum equations for the velocities. However, the resulting velocities do not necessarily satisfy the continuity equation. To address this, pressure and velocities are adjusted through pressure correction equations, ensuring the modified velocities meet the continuity equation. In OpenFOAM, the SIMPLE algorithm is implemented in a steady-state solver for incompressible, turbulent flow, named ”simpleFoam”. The main steps of SIMPLE are summarized as follows:

a) Initialization: Set the initial boundary conditions.

b) Pressure correction: Solve a pressure correction equation to obtain a corrected pressure field.

c) Velocity correction: Correct the velocity field using the corrected pressure field.

d) Convergence check: Evaluate the solution convergence by comparing the residual values against a specified tolerance.

e) Field update: If not converged, update the velocity and pressure fields and return to the pressure correction step. If converged, the simulation ends.

- **SIMPLEC algorithm**

The SIMPLEC (Semi-Implicit Method for Pressure Linked Equations-Consistent) algorithm, developed by Van Doormaal & Raithby (1984), is a modified version of SIMPLE algorithm. It follows the same procedures of SIMPLE, but it modifies the momentum equations in such a way that the velocity correction equations can exclude terms that are deemed less significant compared to those omitted in SIMPLE. This alteration is made with the aim of reducing the impact of removing neighbor correction terms for velocity, thus attempting to mitigate their effects. It exhibits superior performance compared to the SIMPLE algorithm.

- **PISO algorithm**

PISO algorithm (Pressure-Implicit with Splitting of Operators) was proposed by Issa (1986) and it is an extension of SIMPLE shceme with the main difference being the inclusion of an extra pressure correction step that is updated iteratively until convergence is found and no under-relaxation is conducted. Two pressure correction steps enhance the solution's stability and accuracy in situations where the pressure field undergoes significant changes over time. However, it has the disadvantage of a smaller time step and a Courant number of fewer than 1 requirement. PISO is implemented in OpenFOAM by transient or unsteady solvers, icoFoam, and pisoFoam.

- **PIMPLE algorithm**

The PIMPLE (Pressure-Implicit with Operator-Splitting Multi-Phase Explicit) is a combination of PISO and SIMPLE. The PIMPLE includes both velocity correction and under-relaxation without the Courant number restraint in PISO, which makes PIMPLE more suitable for unsteady flow simulation, especially ship stern flow where the unsteady fluid-structure interaction is prominent. In OpenFOAM, the PIMPLE algorithm is implemented by interFoam solver. The general procedures of PIMPLE are as follows:

a) Initialization: Specify the initial boundary conditions.

b) PISO loop: Predict the velocity field, correct the pressure field, and obtain the final velocity field.

c) Inner loop: Update the velocity and pressure fields using an implicit method until a convergence criterion is met.

d) Boundary condition correction: Correct the boundary conditions for the velocity and pressure fields.

e) Convergence check: Check for convergence by comparing the residual values with a specified tolerance level.

f) Field update: If not converged, update the velocity and pressure fields and return to the PISO loop. If converged, increase the time step and return to the PISO loop.

g) End: Output the final fields for analysis.

The SIMPLE and PIMPLE algorithms are adopted for ship flow simulation in this thesis.

3.4 Turbulence model

As mentioned in section 3.2, a model that describes the Reynolds stress is necessary to close the Reynolds-Averaged Navier-Stokes (RANS) equations and obtain the time-averaged flow properties. This is essential as the Reynolds stresses depend on the instantaneous fluctuations in the flow, which cannot be directly computed in a RANS simulation. Therefore, the Reynolds stresses are modeled using an eddy viscosity model, which relates the Reynolds stresses to the mean velocity and strain rate tensors. Typically, the Boussinesq assumption serves as the foundation for most eddy viscosity models utilized in RANS simulations. This assumption presumes that the eddy viscosity is proportional to both the turbulent kinetic energy and the length scale of the turbulent eddies. The length scale is frequently associated with the grid size or the distance from the flow's wall, whereas the turbulent kinetic energy is obtained from an equation that is resolved in conjunction with the RANS equations. There are various eddy viscosity models, such as the k-ϵ model, k-ω model, and Reynolds stress models and each model has its own assumptions and limitations.

In the application of ship hydrodynamics, the k-ϵ model (Launder & Sharma 1974) assumes that the turbulence can be described by two separate transport equations. The first equation accounts for the transport of turbulent kinetic energy, k, while the second equation deals with the dissipation of turbulent kinetic energy, ϵ. It was found good to predict the features of the ship's viscous wake but one of the limitations of the k-ϵ model is its inability to accurately model turbulence in the boundary layer close to a wall, which can result in inaccurate predictions of separation in the flow. To solve its stability issues, Wilcox (1988) proposed the k-ω model by accounting for the near wall grid spacing and its performance in estimating the near field turbulence and separation is greatly improved. To obtain an accurate prediction of the ship hydrodynamics problem, a combination of k-ϵ and k-ω models is required because the turbulence characteristics of both the near-wall and free-stream regions are needed to be captured.

Menter (1994) developed the k-ω Shear Stress Transport (SST) model, which includes a blending function that smoothly transitions between the k-ω and k-ϵ models. The k-ω SST model was further updated by Menter et al. (2003) and it is the most suitable model for simulating the ship's performance in waves (Windén 2014). This model has been shown to be able to provide a good estimation of ship flow simulation and it was adopted by 80 percent of submissions in the 2010 Gothenburg workshop on numerical hydrodynamics (Larsson et al. 2013). Therefore, the k-ω SST model is adopted for all calculations in this thesis.

3.5 Free surface modeling

In the simulation of a ship sailing in real sea states such as waves, the fluid domain is a two-phase mixture of air and water. In order to simulate ships' real hydrodynamic performance in waves, a multiphase flow model is required for modeling the free surface. In this thesis, the Volume of Fluid (VOF) method, a fixed grid technique designed for two or more incompressible, isothermal, and immiscible fluids, is adopted to capture the effect of free surface and to represent the dynamic behaviors of the interface between water and air. In VOF method, the volume fraction α is governed by:

$$\frac{\partial \alpha}{\partial t} + \nabla \cdot (\alpha \mathbf{U}) = 0 \tag{3.16}$$

In this equation, α represents the volume fraction of one phase in a two-phase flow, and $\mathbf{U}$ is the velocity vector of the flow. A cell with a volume fraction value of $\alpha = 1$ represents a cell that is completely filled with water, while a value of $\alpha = 0$ indicates a cell that is completely filled with air. Therefore, the interface between the two phases, or the free surface, is formed by the cells that have intermediate values of α, with $0 < \alpha < 1$. These cells contain a mixture of water and air, and the distribution of α values across the cells is used to track the location and shape of the free surface accurately. Besides, the local density ρ and viscosity μ can be determined by the following equations based on the corresponding α value:

$$\rho = \alpha \rho_{water} + (1 - \alpha) \rho_{air} \tag{3.17}$$

$$\mu = \alpha \mu_{water} + (1 - \alpha) \mu_{air} \tag{3.18}$$

The Multidimensional Universal Limiter with Explicit Solution (MULES) method (Ubbink & Issa 1999) is adopted to ensure a sharp resolution of the free surface.

3.6 Near wall treatment

When simulating the ship's hydrodynamic performance using gridwise methods, the presence of the hull and its appendages' walls alters the flow of fluids and turbulence characteristics in the thin layer of fluid near a solid boundary, which is known as the boundary layer. The velocity of the fluid near the boundary is much smaller than that of the fluid further away from the boundary due to viscous effects. This results in the development of a velocity gradient from the wall of the boundary layer to the outer flow, which is characterized by the thickness of the boundary layer. Accurately resolving the boundary layer requires good command of the grid resolution in the near-wall region. A non-dimensional parameter is often employed to characterize the near-wall region, y^+ is defined as:

$$y^+ = \frac{y u_\tau}{\nu} \tag{3.19}$$

$$u_\tau = \sqrt{\frac{\tau_\omega}{\rho}} \tag{3.20}$$

y^+ is the dimensionless distance from the wall, u_τ is the friction velocity, y is the distance from the wall, ν is the kinematic viscosity, τ_ω refers to the wall shear stress and ρ is the density.

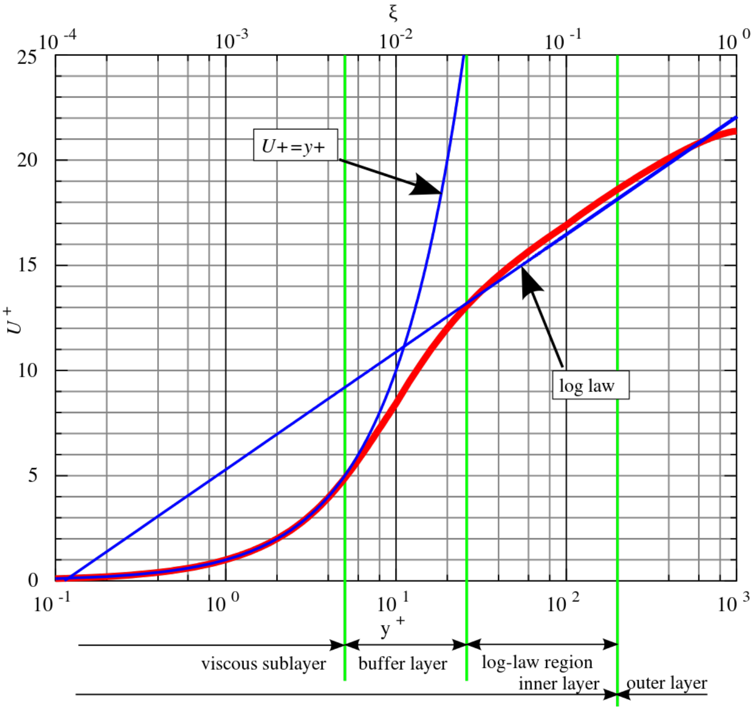

FIGURE 3.3: law of the wall, horizontal velocity near the wall with mixing length model (Kundu et al. 2015)

Experiments show that boundary layer region consists of four layers, viscous sub-layer, buffer layer, log-law layer and outer layer, shown in Figure 3.3 (Kundu et al. 2015).

- The viscous sub-layer: is a thin region, the value of y^+ about up to 5, close to the wall and dominated by viscous effects.
- The buffer layer: $5 < y^+ < 15$, is the region that the laminar wall law blends to turbulence wall law.
- The log law layer: $15 < y^+ < 500$, fully turbulent region and the turbulence stress dominate the flow.
- The outer layer: can be described as a ”free stream” region in some cases and inertia dominates the flow and free from direct viscous effect.

OpenFOAM provides two methods for determining the viscous shear stress near a solid wall. One method involves directly solving for the viscous sub-layer, while the other involves using empirical wall functions. The choice of approach depends on the value of y^+. A comprehensive description of the implementation of wall functions in OpenFOAM can be found in Liu (2016). Selecting the appropriate wall function in OpenFOAM depends on several factors, including the type of flow, the Reynolds number, the type of turbulence model, and the solver. Besides, the implementation of wall functions in an OpenFOAM simulation is conducted through the boundary conditions, which will be covered in later chapter.

3.7 Convergence criteria

3.7.1 Residual

Solving the ship hydrodynamics problems using the CFD method means that a discrete domain with a gridwise approach replaces a continuous problem domain. Every flow variable is defined within the continuous domain at each point, while the discrete system comprises a vast collection of interconnected, algebraic equations that pertain to the discrete variables (Ali 2020). The system of equations can be addressed by characterizing it as a matrix operation. Solving the equation system for minuscule matrices can be accomplished using Gauss elimination, for instance, but this approach is computationally inefficient for significant matrices. Therefore, the usual technique for dealing with large matrices is to resolve the equation system through iterative methods, employing the previous outcome as a starting guess for the next iteration. Convergence of the solution is achieved when the variations in values between iterations become less than a specified lower threshold value. At this point, the equation system can be regarded as resolved. The divergence found for a given variable in each iteration during the iterative resolution of the algebraic equations is referred to as a residual (Windén 2014).

Employing iterative methods to solve discretized governing equations as a vast system of linear equations can be articulated in the following matrix form:

$$\mathbf{AX} = \mathbf{B} \tag{3.21}$$

And the residual can be expressed as:

$$\mathbf{R} = \mathbf{B} - \mathbf{AX} \tag{3.22}$$

A normalizing factor is utilized to normalize the residuals:

$$n = \sum(|\mathbf{AX} - \mathbf{A}\overline{\mathbf{X}}| + |\mathbf{B} - \mathbf{A}\overline{\mathbf{X}}|) \tag{3.23}$$

Here, $\mathbf{X}$ denotes the solution vector, and $\overline{\mathbf{X}}$ represents the average of the solution vector.

The normalized residuals are subsequently represented as follows:

$$R = \frac{1}{n}\sum|\mathbf{B} - \mathbf{AX}| \tag{3.24}$$

As the CFD solution is attained through iterative means, achieving precisely zero residuals is not feasible. Nevertheless, a more numerically precise solution corresponds to a lower residual value. The solution is considered to reach the convergence period when the residuals remain relatively stable throughout the simulation period.

3.7.2 Time marching

When employing iterative method to solve the RANS equations, the residuals should be minimised, and the convergence of fields needs to be also checked. The temporal derivative of velocity field $\frac{\partial \overline{u}_i}{\partial t}$ contained in the RANS equations means it is a unsteady process. As a result, it is necessary to employ an appropriate method for progressing the solution over time by solving the governing equations at discrete time steps, which is commonly referred to as a time marching technique. The time marching algorithms used in OpenFOAM for solving ship flow problems, especially seakeeping, can be found in Monroy & Seng (2017). The general procedure is to employ an outer time loop, within which an inner process is executed in each time step to achieve convergence of the residuals. In cases where a steady equilibrium can be reached, such as in calculating the calm water resistance of a ship, the value of $\frac{\partial \overline{u}_i}{\partial t}$ is considered zero, and the outer loop continues until the field variables reach a steady state. In the case of a steady average solution, the time step is less important, as the flow conditions at intermediate time steps are only necessary to maintain stability. However, in the case of an unsteady process, such as in waves where the time history of the flow is critical, greater attention must be paid to the approach used to advance time in the solver (Windén 2014). In this thesis, implicit time-marching schemes are employed, with the local Euler scheme utilized for steady cases and the Euler scheme used for unsteady cases.

3.8 Numerical solvers

OpenFOAM provides a multitude of solvers for steady and unsteady simulations. In this thesis, steady and unsteady simulations were conducted using the simpleFoam and interFoam solvers, respectively. A brief description of these solvers is provided below.

- simpleFoam: a steady-state solver designed to calculate steady-state solutions for incompressible, turbulent flow, single phase flow. The solver is based on the SIMPLE (Semi-Implicit Method for Pressure Linked Equations) algorithm and can also utilize the SIMPLEC (Semi-Implicit Method for Pressure Linked Equations Consistent) algorithm in newer releases. It is used in this thesis for simulation in chapter 5.
- interFoam: a solver within the OpenFOAM toolbox for simulating two-phase flows. Specifically, it is designed to calculate the interactions between two immiscible, incompressible fluids, such as water and air. interFoam is a finite volume solver that utilizes the Volume of Fluid (VOF) method to track the interface between the two fluids and the Navier-Stokes equations to solve for the velocity and pressure fields of the fluids. The solver also includes models for surface tension and gravity effects. interFoam is mainly used for computations in chapter 6 and 7.

In addition to the above two standard solvers for ship resistance simulation in calm water and wave conditions, a customized package selfPropFoam is also used for computing ship self-propulsion tests. The selfPropFoam package, initially developed by Windén (2014) and Windén et al. (2014), provides a modular approach for coupling any OpenFOAM Finite Volume solver with an arbitrary model for body force or momentum source. This coupling enables greater flexibility and customization in simulations of self-propelled ship in waves, and its detailed features can be found in Winden (2021*b*). Based on this package, another two custom solvers are employed in this thesis for self-propulsion:

- selfPropsimpleFoam: A modified version of the basic OpenFOAM SIMPLE solver simpleFoam. It utilizes the propeller library to compute the body force distribution and incorporates this information into the momentum equation.
- selfPropinterFoam: Coupling the selfPropFoam with the standard interFoam solver. The basic idea is similar to selfPropsimpleFoam. This allows to account for the action of propeller effects in multiphase fluid flow simulations.

3.9 Uncertainty analysis

When using CFD methods to simulate ship hydrodynamics performance in waves, uncertainty and error cannot be avoided. Uncertainty can source from the accuracy of the boundary conditions, the quality of the mesh, or the modeling assumptions and error can arise from various sources, such as discretization errors, truncation errors, or round-off errors. Therefore, to ensure the accuracy of numerical simulations and boost confidence in CFD, carrying out the the validation and verification anaylysis for the used codes to ensure their consistent performance is necessary (Islam & Soares 2019). The widely accepted terminologies are expressed as follows (ITTC 2017*b*):

- Verification: is the process of determining that a model implementation accurately represents the developer's conceptual description of the model and the solution to the model.
- Validation: is the process of determining the degree to which a model is an accurate representation of the real world from the perspective of the intended uses of the model.

3.9.1 Validation

The validation error (or comparison error) E can be defined as:

$$E = S - D \tag{3.25}$$

Where S is the numerical solution and D is the experimental data. The uncertainty of validation error E is shown as:

$$U_E^2 = U_D^2 + U_{SN}^2 + U_{SM}^2 \tag{3.26}$$

U_D is the experimental uncertainty, U_{SN} is the numerical uncertainty and U_{SM} is the simulation modelling uncertainty. The modelling uncertainty can be decomposed into modelling assumptions and the use of previous data (ITTC 2017*b*). Hence, the validation uncertainty U_V is introduced rather than U_E and the U_V can be expressed as:

$$U_V^2 = U_D^2 + U_{SN}^2 \tag{3.27}$$

When $|E| \leq U_V$, the validation is acheived at U_V level, while $|E| \geq U_V$, the simulation modelling still requires further improvement.

3.9.2 Verification

Stern et al. (2001) defined verification as a process for assessing simulation numerical uncertainty and, when conditions permit, estimating the sign and magnitude of the simulation numerical error itself and the uncertainty in that error estimate. The detailed verification procedures can be found in Stern et al. (2001), ITTC (2017*b*) and Islam & Soares (2019). The verification procedures are briefly introduced here for better readability and applied to this work. Since 2008, the ITTC Resistance Committee has recognized the value of this verification methodology and recommended it as a standard practice (Procedures & Guidelines 2008). Consequently, this analysis technique has become widely utilized in ship flow simulation.

3.9.2.1 Convergence study

A convergence study in CFD involves varying the numerical parameters of a simulation, such as grid size or time step, to determine the impact on the accuracy and stability of the results. Here the methodology is presented using grid convergence study. To ensure an accurate solution, it is recommended to conduct computations to evaluate the mesh generated. This involves creating at least three meshes, refining them systematically in all directions with the same refinement ratio r_G, and then comparing the solution variations among these meshes. The mesh convergence ratio for the input parameter can be defined as the ratio of these solution variations:

$$R_G = \frac{\epsilon_{21}}{\epsilon_{32}} = \frac{S_2 - S_1}{S_3 - S_2} \tag{3.28}$$

Where S_1, S_2, S_3 represent three different solutions obtained using fine, medium and coarse meshes, respectively. Based on the sign and magnitude of R_G, three convergence conditions can be listed:

- Monotonic convergence: $0 < R_G < 1$
- Oscillatory convergence: $R_G < 0$
- Divergence: $R_G > 1$

3.9.2.2 Monotonic convergence

For monotonic convergence, the order of convergence rate or accuracy p_G is given by:

$$p_G = \frac{In(\epsilon_{32}/\epsilon_{21})}{Inr_G} \tag{3.29}$$

Then Richardson extrapolation is adopted to estimate normalized discretization error for the fine mesh $\delta_{RE,G1}$:

$$\delta_{RE,G1} = \frac{\epsilon_{21}}{r_G^{p_G} - 1} \tag{3.30}$$

Based on the theoretical order of accuracy p_{th} of the applied method, a correction factor C_G is proposed as (Wilson & Stern 2002, Wilson et al. 2004):

$$C_G = \frac{r_G^{p_G} - 1}{r_G^{p_{th}} - 1} \tag{3.31}$$

If the correction factor → 1, the mesh uncertainty can be expressed as:

$$U_G = |(1 - C_G)\delta_{RE,G1}| \tag{3.32}$$

Otherwise, the uncertainty is estimated using the following:

$$U_G = |(1 - C_G)\delta_{RE,G1}| + |C_G\delta_{RE,G1}| \tag{3.33}$$

3.9.2.3 Oscillatory convergence

To evaluate oscillatory convergence, the error is bounded within the average of the maximums (S_U) and minimums (S_L) of the oscillations to estimate the uncertainties (Islam & Soares 2019):

$$U_G = \frac{1}{2}(S_U - S_L) \tag{3.34}$$

3.9.2.4 Divergence

In terms of diverging results, errors and uncertainties cannot be estimated. Therefore, the mesh quality needs further improvement to realize monotonic or oscillatory convergence.

3.10 Chapter summary

This chapter discusses the mathematical formulation and numerical techniques used in this thesis for developing the numerical approach for a stepwise study of simulating a fully appended ship in waves under drift. A Reynolds-Averaged Navier-Stokes (RANS) based method is employed to simulate fluid flow surrounding the fully appended hull in the presence of drift conditions. The $k - \omega$ Shear Stress Transport (SST) turbulence model is selected for achieving turbulence closure, as it demonstrates a strong capability to accurately represent wakefield phenomena and the complex interaction effects between the hull, propeller, and rudder (Larsson et al. 2015).

An open-source code OpenFOAM is chosen as the RANS solver, allowing for the execution of ship flow simulations at the angle of drift conditions and also with the high flexibility of coupling propeller modelling. Pressure-velocity coupling is achieved through the use of the SIMPLE algorithm in double body simulations, whereas the PIMPLE algorithm is employed for the Volume of Fluid (VOF) free surface calculations. Besides, numerical solvers for steady and unsteady simulation are also described, along with the used uncertainty analysis methods.

The next chapter is dedicated to introducing the basic setup for vessels operating under drift in a numerical towing tank environment. The presence of drift and rudder angles and the propeller working behind the hull results in a non-uniform wake field. Therefore, a sectorial approach of the body force propeller model, Blade element momentum theory (BEMt), is used for modelling the action of propeller under static drift.

Chapter 4

Numerical setup for drift angle and propeller modelling

4.1 Introduction

In assessing the hydrodynamic performance of a vessel manoeuvring in waves, it is crucial to accurately predict the forces and moments acting upon the manoeuvring ships. As discussed in Section 2.5.3, direct simulations of ship manoeuvres, including zigzag and turning circle tests, require substantial computational resources. Although numerical simulations employing direct methods can yield exceptional fluid fidelity and satisfactory accuracy, their considerable time and financial costs make them impractical for initial evaluations in ship manoeuvring studies. Consequently, there is still a pressing need for a cost-effective approach that maintains reasonable accuracy in order to study the performance of ship manoeuvres in real sea states.

To facilitate a ship's turning during the manoeuvring process, the rudder must effectively position and sustain the vessel at an angle of attack relative to the water flow along the hull. This action generates hydrodynamic forces on the hull, thereby inducing the ship's turn, with the rudder contributing minimally to the turning effect (Molland & Turnock 2007). The drift angle is defined as the angle between the ship's longitudinal axis and the actual tangent to the path, as illustrated in Figure 4.1.

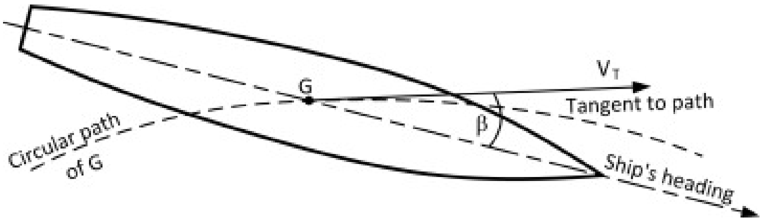

FIGURE 4.1: The angle of drift β (Molland & Turnock 2007)

Instead of studying the complete time varying manoeuvre, a methodology of adopting static drift angles combined with a series of rudder angles to represent quasi-static phases of an actual ship manoeuvre is presented in this thesis. The proposed innovative methodology eliminates the necessity to model the entire transient manoeuvre, substantially decreasing computational expenses and offering a valuable reference for experimental calculations of hull and appendage forces when the angle of drift is applied. This chapter aims to present the basic setup for a ship operating at the angle of drift in a numerical towing tank. In addition, to accurately capture the interaction between the hull with its appendages, two body force propeller models are used in this thesis, namely Blade Element Momentum Theory (BEMt) and the Yamazaki model. In contrast to fully discretized propellers, body force models eliminate the requirement for generating a rotating sub-domain or mesh with complicated propeller blade resolution. This approach not only reduces computational expenses but also mitigates geometric complexities, particularly for propellers operating near, or even within, stationary structures such as rudders, ducts, and energy-saving devices (Winden 2021*b*).

4.2 Coordinate systems for drift simulation

The simulation of a ship operating under drift conditions necessitates the consideration of two different coordinate systems, as the ship's longitudinal and transverse axes deviate from alignment with those of the computational domain. Consequently, two coordinate systems are employed in this thesis incorporating both the computational domain system and the ship-fixed system. Adhering to the right-hand rule, these coordinate systems are illustrated in Figure 4.2. In this thesis, the majority of hydrodynamic forces and moments calculations are based on the ship-fixed coordinate system O-XYZ unless otherwise stated. This system features an x-axis directed towards the bow, a y-axis pointing towards the starboard, and an origin situated at the mid-ship. β is the angle of drift of the ship, β_r represents the rudder angle relative to the ship axis. The drift angle, β, is defined as positive when the ship deviates towards the starboard side. This convention is also applied to the rudder angle β_r, ensuring a consistent explanation within the analysis.

As depicted in Figure 4.2, the ship's resistance is denoted by R, while F_Y represents the lateral force exerted on the hull, and M_Z signifies the yaw moment. Regarding the rudder force, D corresponds to the rudder drag, and L refers to the rudder lift. These parameters are evaluated within the ship's coordinate system.

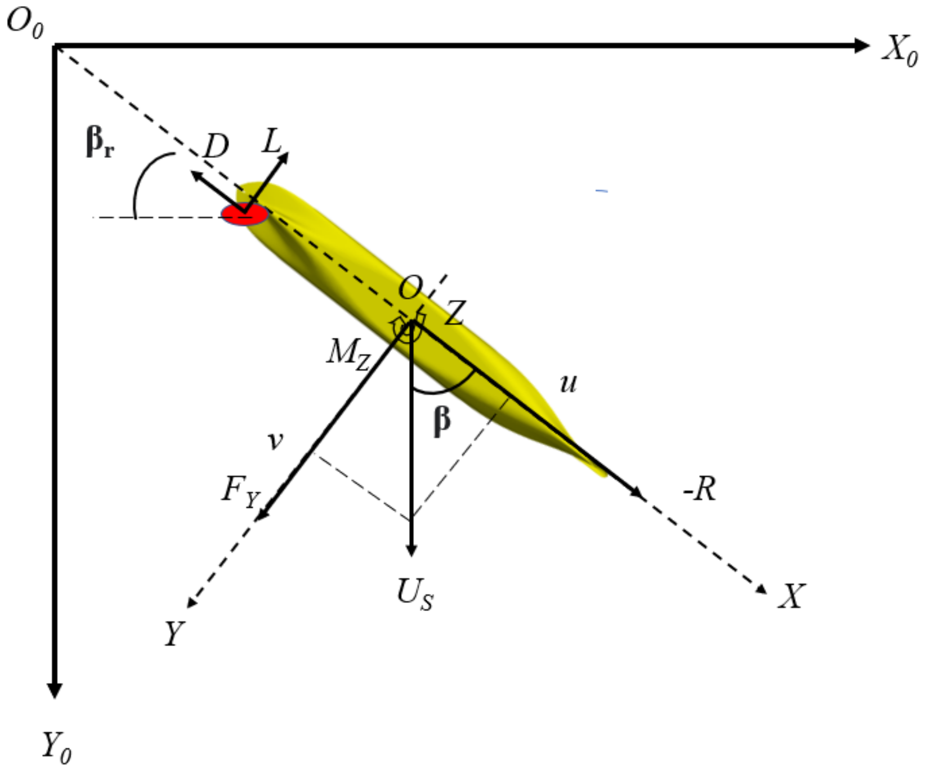

FIGURE 4.2: Coordinate systems and variables

4.3 Data recording and calculation

When a static drift angle is imposed on a vessel, its longitudinal axis deviates from the computational domain axis. Forces and moments computed by OpenFOAM are derived from the computational domain axis. To accurately determine the resistance, lateral force, and yaw moment along the vessel's axis, a transformation matrix is employed to facilitate the conversion between the two coordinate systems.

$$\begin{bmatrix} R \\ F_Y \\ M_Z \end{bmatrix} = \begin{bmatrix} cos\beta & sin\beta & 0 \\ -sin\beta & cos\beta & 0 \\ 0 & 0 & 1 \end{bmatrix} \times \begin{bmatrix} X \\ Y \\ N \end{bmatrix} \tag{4.1}$$

In Equation 4.1, the variables on the left side are based on the ship's coordinate system, while those on the right side originate from the computational domain coordinate system. The physical meaning of each variable can be found in Table 4.1. To compute the resistance and side force exerted on the hull, the subsequent equations are used:

$$LongitudinalPressureForce = P_X * cos\beta - P_Y * sin\beta \tag{4.2}$$

TABLE 4.1: Physical meaning of variables in ship and domain axis systems

Physical Meaning of Variables	
Ship Axis System	Domain Axis System
F_Y: Side Force	Y: Transverse force
R: Resistance	X: Longitudinal force
M_Z: Yaw moment	N: Yaw moment

$$LongitudinalViscousForce = V_X * cos\beta - V_Y * sin\beta \tag{4.3}$$

$$TransversePressureForce = P_X * sin\beta + P_Y * cos\beta \tag{4.4}$$

$$TransverseViscousForce = V_X * sin\beta + V_Y * cos\beta \tag{4.5}$$

The ship resistance is the sum of the pressure force and viscous force in the longitudinal direction, combing equations 4.2 and 4.3:

$$R = Resistance = P_X * cos\beta - P_Y * sin\beta + V_X * cos\beta - V_Y * sin\beta \tag{4.6}$$

Likewise, the ship side force is the sum of the pressure force and viscous force in the transverse direction, combing equations 4.4 and 4.5:

$$F_Y = SideForce = P_X * sin\beta + P_Y * cos\beta + V_X * sin\beta + V_Y * cos\beta \tag{4.7}$$

Where the P_X is the pressure force in the domain x (longitudinal) direction, P_Y is the pressure force in the domain y (transverse) direction, V_X is the viscous force in the domain x direction, V_Y is the viscous force in the domain y direction. $Y = P_Y + V_Y$, $X = P_X + V_X$ and the values of P_X, P_Y, V_X, V_Y can be derived from OpenFOAM directly.

In OpenFOAM's force and moment calculation, the default reference frame is the computational domain axis. The direct computed forces from OpenFOAM should apply the above equations to generate the ship resistance and side force if a non-zero drift angle β is presented. In terms of the yaw moment, it is independent of the axis systems. Therefore, the yaw moment is identical in both the ship and computational domain axes.

4.4 Body force propeller models

The primary objectives of propeller optimization involve minimizing the power necessary to generate a given thrust and meanwhile preventing cavitation erosion during both design and off-design operating conditions. Section 2.2 provides a comprehensive examination of diverse numerical methods for simulating propellers, along with the corresponding computational costs. Considering the focus of research objectives and the desired level of accuracy in simulation, a balance between physical fidelity and computational expense may be achieved by incorporating appropriate empirical insights when interpreting the analytical outcomes (Molland et al. 2017).

In the current study, the simulations primarily concern the interaction effects among the hull, propeller, and rudder under drift conditions, rather than directly focusing on the propeller itself. As a result, the decision is made to forgo directly replicating the propeller flow and its complex geometry. Moreover, taking into account the trade-off between computational requirements and the precision of numerical fluid dynamics, body force propeller models are chosen for the propeller analysis in this thesis. The propeller's influence on the flow is represented through the incorporation of momentum source terms.

4.4.1 Blade Element Momentum theory

Owing to its ability to capture the interaction among the hull, propeller, and rudder, the Blade Element Momentum theory (BEMt) is chosen for the propeller modelling. Initially proposed by Burrill (1944), the Blade Element Momentum theory integrates 2D blade element theory with axial momentum theory, making it well-suited for evaluating marine propellers operating near their design conditions (Benini 2004) and facilitates the investigation of propeller-hull interactions (Molland et al. 2017). Implementing the BEMt employed in this study adheres to the methodology outlined by Windén (2014), but it is described for better readability. The distance from the centerline is normalized using the propeller radius R, such that the local radius r can be expressed as $r = xR$, where x represents the dimensionless radius.

4.4.1.1 Momentum theory

The momentum theory or disk actuator theory, first proposed by Rankine (1865), describes a mathematical model of an ideal actuator disk, such as a propeller. The rotor is represented as an infinitely thin disk, which causes a uniform velocity along the rotation axis. The fluid flow within a stream tube that passes through the propeller disk is illustrated in Figure 4.3, which assumes there is no friction within the tube, and the power generated by the engine can be transmitted to the fluid via a discrete pressure jump at the plane of the propeller.

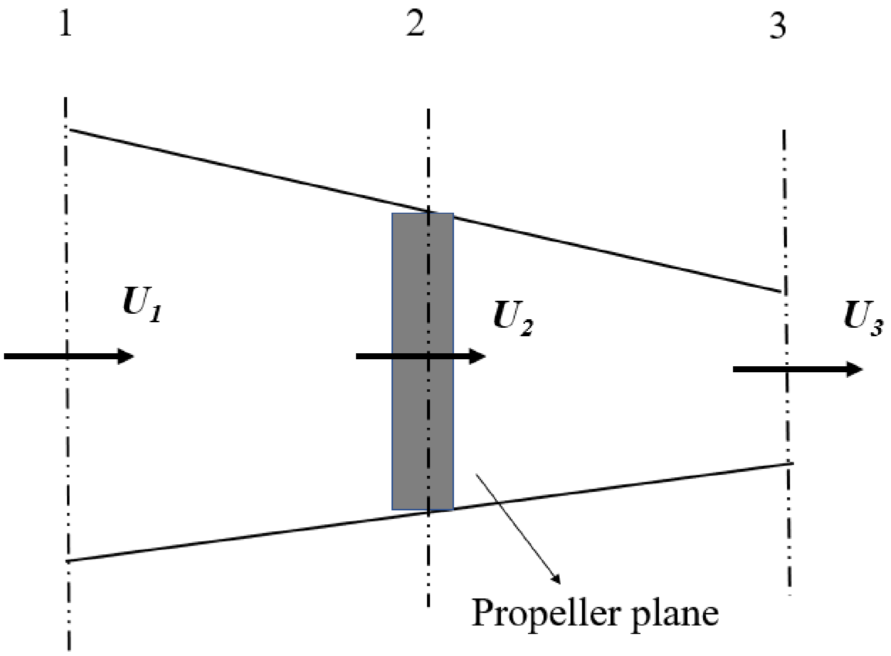

FIGURE 4.3: Momentum representations of propeller plane

Considering the fluid flow within an annular region of radius r and thickness dr in the stream tube, the mass flow rate traversing the respective section at the propeller plane can be described as follows:

$$\dot{m} = 2\pi r dr \rho U_2 \tag{4.8}$$

Assuming the pressure jump at the propeller plane to be discrete, the axial change in momentum rate within the annular region equals the thrust produced by the propeller:

$$dT = \dot{m}(U_3 - U_1) \tag{4.9}$$

Velocities at planes 2 and 3, U_2 and U_3, can be expressed with far upstream velocity and the axial inflow factors, shown as:

$$U_2 = U_1(1 + a_{2\infty}) \tag{4.10}$$

$$U_3 = U_1(1 + a_{3\infty}) \tag{4.11}$$

Carlton (2018) indicates U_2 is the average of U_3 and U_2 in open water flow, therefore:

$$a_{3\infty} = 2a_{2\infty} \tag{4.12}$$

Then the thrust generated by the propeller can be written as:

$$dT = 4\pi r \rho U_1^2 a_{2\infty}(1 + a_{2\infty})dr \tag{4.13}$$

Nonetheless, equation 4.13 is only applicable when interference between blades is disregarded. When dealing with a finite number of blades, an averaging factor, K, known as the Goldstein factor, is incorporated to adjust the thrust and torque expressions, initially proposed by Goldstein (1929). In this study, a curve is fitted to the experimentally established correction factor K, as presented by Molland et al. (2017).

$$K = \frac{2}{\pi}\cos^{-1}\left(\frac{\cosh\left[x\left(\frac{Z}{2x\tan\phi} - 0.5\right)\right]}{\cosh\left[\frac{Z}{2x\tan\phi} - 0.5\right]}\right) \tag{4.14}$$

Z is the number of blades, and ϕ is the hydrodynamic pitch. By employing the dimensionless radial position, the formulas for both the thrust and torque coefficients can be written as:

$$\mathrm{d}K_T = \pi x J^2 K a(1 + a)\mathrm{d}x \tag{4.15}$$

$$\mathrm{d}K_Q = \frac{1}{2}\pi x^3 J K a'(1 + a)\mathrm{d}x \tag{4.16}$$

a is now the inflow factor and a' is the circumferential inflow factor at the blade location. The local efficiency η can be derived by

$$\eta = \frac{P_E}{P_D} = \frac{TU_1}{2\pi n Q} = \frac{TU_1}{\Omega Q} \tag{4.17}$$

$$\eta = \frac{U_1\frac{\mathrm{d}T}{\mathrm{d}r}}{\Omega\frac{\mathrm{d}Q}{\mathrm{d}r}} = \left(\frac{U_1}{r\Omega}\right)^2\frac{a}{a'} \tag{4.18}$$

4.4.1.2 Blade element theory

An alternative approach to evaluating propeller performance is Blade Element Theory, which divides the propeller blade into smaller sections. The lift and drag of each portion are then examined independently, assuming a two-dimensional flow. The lift dL and drag dD for a element with span dr can be written as:

$$\mathrm{d}L = \frac{1}{2}\rho Z c(r) U_{\mathrm{foil}}^2 C_L(\alpha)\mathrm{d}r \tag{4.19}$$

$$\mathrm{d}D = \frac{1}{2}\rho Z c(r) U_{\mathrm{foil}}^2 C_D(\alpha)\mathrm{d}r \tag{4.20}$$

$c(r)$ is the local chord of the blade. The angle of attack α and the local inflow velocity U_{foil} remain unknown. Figure 4.4 depicts a velocity vector diagram that incorporates the inflow velocity components resulting from the propeller's operation, in which V is the same as U_1 of Figure 4.3.

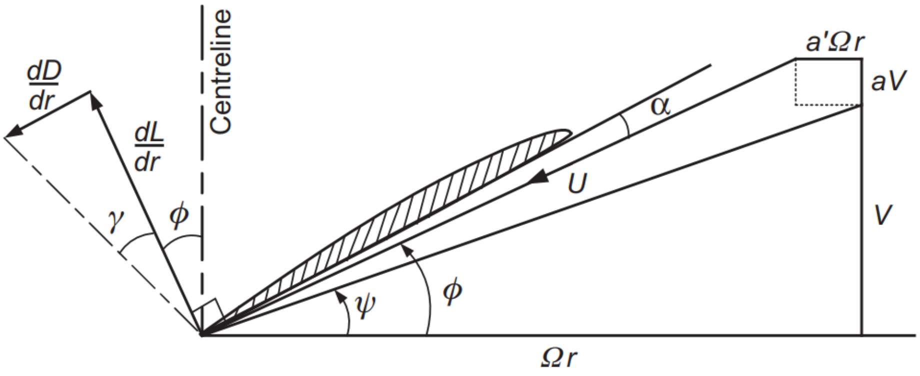

FIGURE 4.4: Blade element diagram (Molland et al. 2017)

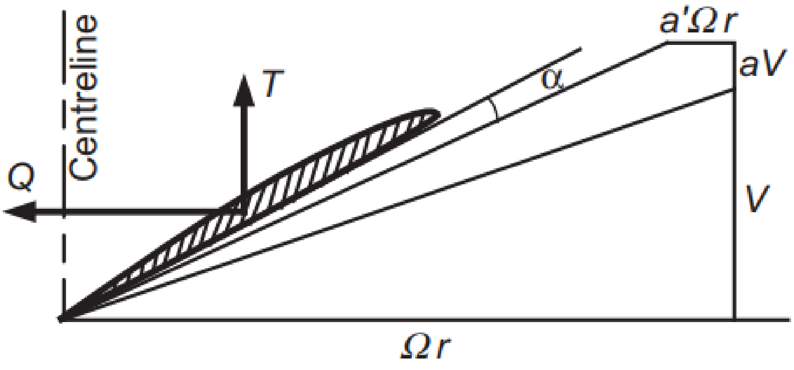

FIGURE 4.5: Blade element representations of propeller action (Molland et al. 2017)

The local section pitch P is the sum of the induced flow angle ϕ and the effective angle of attack α, thereby

$$\tan(\phi + \alpha) = \frac{P}{2\pi r} = \frac{P/D}{\pi x} \tag{4.21}$$

The thrust and torque shown in Figure 4.5 can be obtained from lift and drag, written as:

$$\mathrm{d}T = \mathrm{d}L \cos\phi - \mathrm{d}D \sin\phi = \mathrm{d}L \cos\phi(1 - \tan\phi \tan\gamma) \tag{4.22}$$

$$\mathrm{d}Q = r(\mathrm{d}L \sin\phi + \mathrm{d}D \cos\phi) = r\mathrm{d}L \cos\phi(\tan\phi + \tan\gamma) \tag{4.23}$$

And

$$\tan\gamma = \frac{\mathrm{d}D}{\mathrm{d}L} = \frac{C_D(\alpha)}{C_L(\alpha)} \tag{4.24}$$

Substituting dT, dQ into equation 4.18 and the local efficiency of the section is:

$$\eta = \frac{U_1}{\Omega r} \frac{1}{\tan(\phi + \gamma)} \tag{4.25}$$

From the geometry, it is also found that

$$\tan\psi = \frac{U_1}{\Omega r} \tag{4.26}$$

$$\tan\phi = \frac{U_1(1 + a)}{\Omega r(1 - a')} \tag{4.27}$$

Equation 4.25 becomes:

$$\eta = \frac{\tan\psi}{\tan(\phi + \gamma)} \tag{4.28}$$

4.4.1.3 Coupling of Blade element and momentum theories

Both blade element and momentum theories provide two separate equations for the local efficiency η; combining these two equations is essential for determining the solution within the framework of the blade element-momentum theory.

- Momentum theory:

$$\eta = \tan^2\psi \frac{a}{a'} \tag{4.29}$$

- Blade element theory:

$$\eta = \frac{\tan\psi}{\tan(\phi+\gamma)} \tag{4.30}$$

The ideal efficiency is given by:

$$\eta_i = \frac{\tan\psi}{\tan\phi} = \frac{(1-a')}{(1+a)} \quad (\text{assuming } C_D = 0 \text{ and } \gamma = 0) \tag{4.31}$$

Combining the above equations, the axial and circumferential inflow factors can be expressed as:

$$a' = 1 - \eta_i(1+a) \tag{4.32}$$

$$a = \frac{1-\eta_i}{\eta_i + \frac{1}{\eta}\tan^2\psi} \tag{4.33}$$

The equations of BEMt are solved in an iterative process and follow the steps shown in Figure 4.6. As C_L and dKT/dx are relatively insensitive to drag, it is common to begin by assuming $C_D = 0$, which results in $\gamma = 0$ and $\eta = \eta_i$ for the initial iteration. Using equation 4.33, an initial solution for α can be obtained, which can then be used to derive dKT/dx from equation 4.15 and subsequently C_L from equations 4.19 and 4.22. Introducing C_D allows for calculating $\gamma = tan^{-1}(C_D/C_L)$ and the actual value of η. This iterative process is then repeated until convergence for η is achieved (Molland et al. 2017). The propeller operates at the rear of the hull, resulting in a non-uniform wake. Consequently, the solution can be separated into various circumferential segments, each having its own radial distribution of J. The procedure depicted in Figure 4.6 is performed for every segment, with θ representing the angle of each individual segment.

4.4.1.4 Validation of Blade element momentum theory

The sections outlined above provide a detailed description of the BEMt coupling methods and the steps involved in their implementation. In order to obtain confidence in the accuracy of BEMt, it is initially employed to predict the open water curves for the KCS propeller. The KCS propeller geometry definition is listed in Table 4.2, which uses 11 reference radii and the blade area ratio is 0.8, and the number of blade Z is 5.

The computed values of K_T, K_Q and η are compared with the experimental data from Hino et al. (2020), as shown in Figure 4.7. Overall, good agreement is found between BEMt's open water curve and the experimental data, which indicates the robustness of

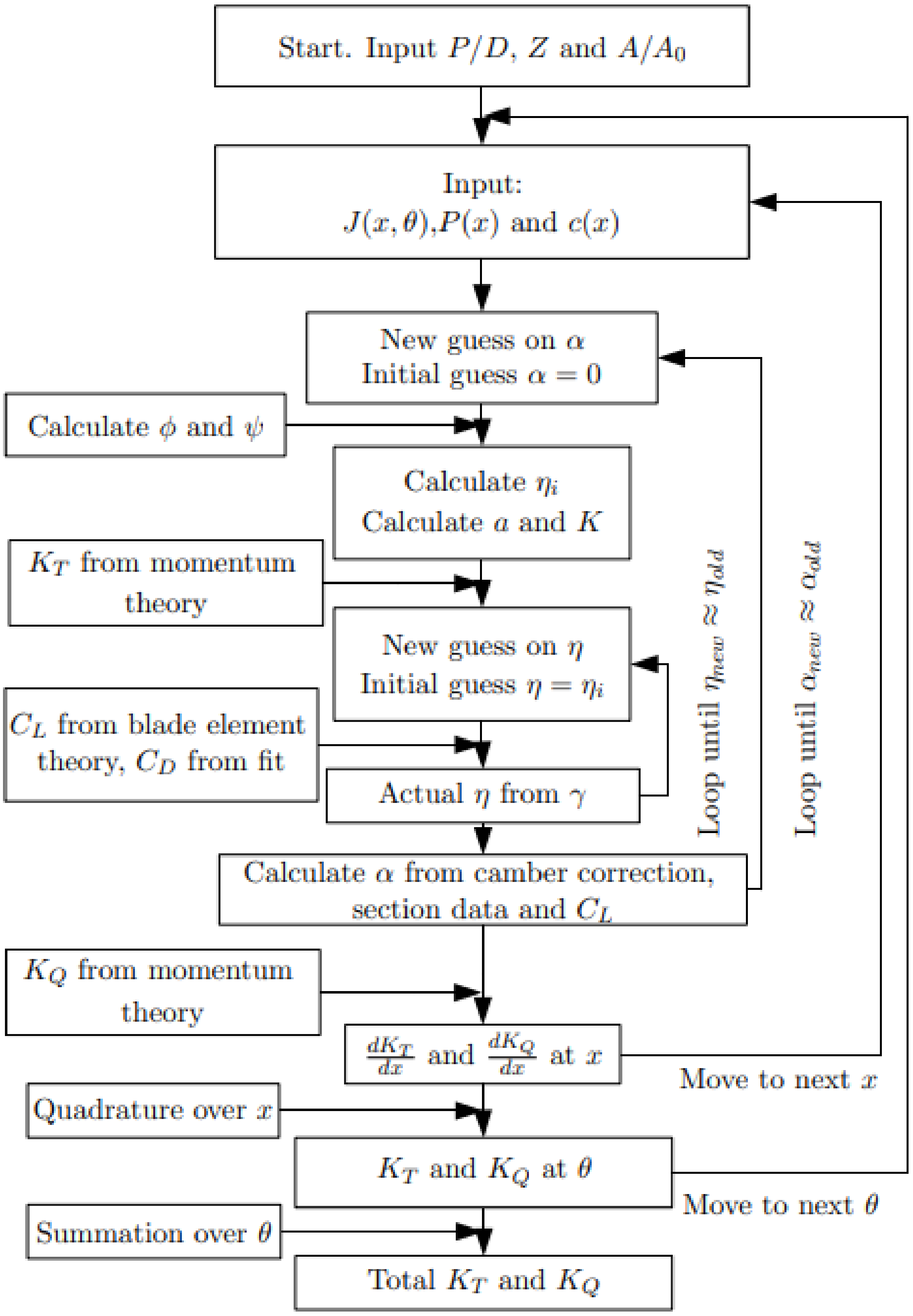

FIGURE 4.6: Iterative steps of the BEMt algorithm (Windén 2014)

the BEMt code for propeller modelling even though the actual propeller geometry is not taken into account.

TABLE 4.2: The KCS propeller geometry definition in BEMt code

Reference radii, r/R	Pitch distribution, P/D	Chord distribution, c/D	Thickness distribution, t/c
0.18	0.8347	0.2313	0.198227
0.25	0.8912	0.2618	0.1555
0.3	0.9269	0.2809	0.132147
0.4	0.9783	0.3138	0.0971
0.5	1.0079	0.3403	0.07226
0.6	1.013	0.3573	0.054492
0.7	0.9967	0.359	0.04156
0.8	0.9566	0.3376	0.031783
0.9	0.9006	0.2797	0.024777
0.95	0.8683	0.2225	0.02373
1.00	0.8331	0.0001	0.0001

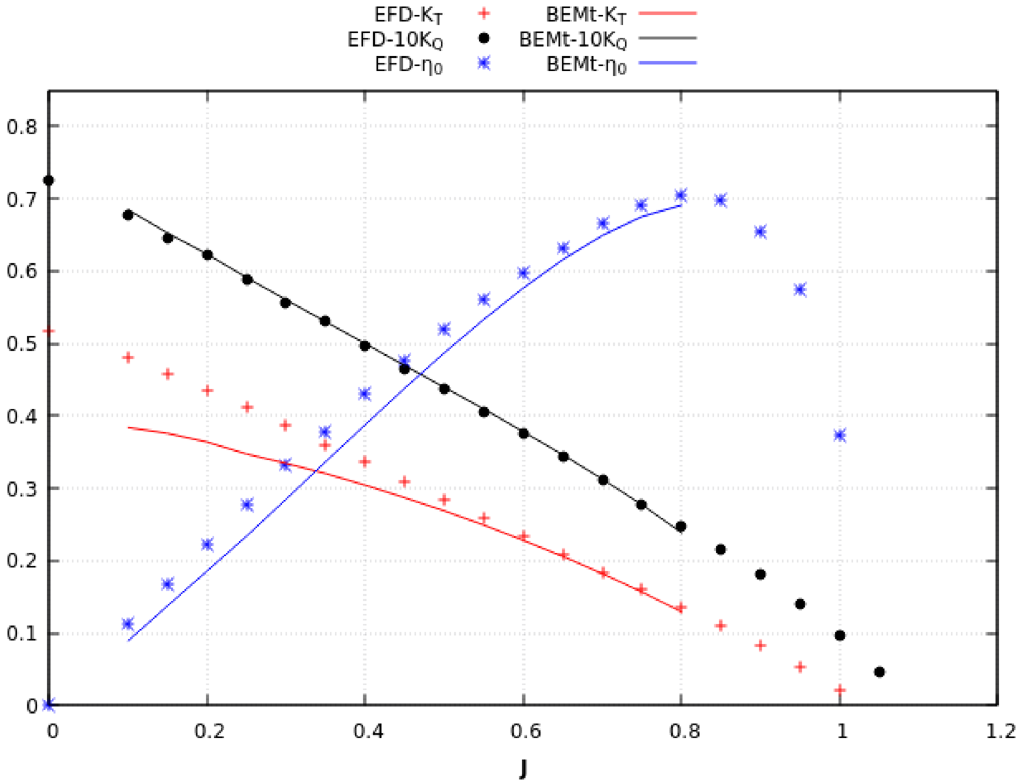

FIGURE 4.7: Open water curve of the KCS propeller predicted by the BEMt and compared with EFD data obtained from Hino et al. (2020)

4.4.2 Yamazaki model

A description of the Yamazaki model is made here based on Windén (2021*a*) and Windén (2021*c*). It was originally developed by Yamazaki (1968) and improved on by Moriyama (1979) and Yamazaki (1998). It depicts the propeller's interaction with the fluid by distributing bound vortices with a strength of Γ as a substitute for the propeller blades, and a free vortex with a pitch of h to symbolize the trailing wake. The strength $\Gamma(\mathrm{r}, \theta)$ is discretely distributed over a concentric grid [r, θ] that is centered around the propeller's center of mass. This forms a combined theory that integrates elements from both lifting line and lifting surface theories.

- The calculation of propeller flow

$\Gamma(r, \theta)$ and $h(r)$ are determined iteratively by blending 2D airfoil theory, potential flow, propeller inflow, and the interaction between the free vortex and the blades at the propeller's plane. The propeller-induced velocity disturbance is represented by the velocity potential $\varphi_{Pf\infty}$, which is derived from the Green's function G_P. This Green's function captures the cumulative effect of $\Gamma(r', \theta')$ from every grid-panel on the overall disturbance at $[r, \theta]$. In this context, r_0 represents the propeller's radius while r_h signifies the hub's radius.

$$\varphi_{\mathrm{Pf}\infty} = \frac{1}{4\pi} \int_{r_h}^{r_0} r' dr' \int_0^{2\pi} \Gamma(r', \theta') G_p d\theta' \tag{4.34}$$

$$G_p = \frac{r'}{h(r') R_{20}} - \frac{r \sin(\theta' - \theta)}{r'^2 + r^2 - 2rr' \cos(\theta' - \theta)} \left(1 + \frac{x}{R_{20}}\right) \tag{4.35}$$

The disturbance is inversely proportional to the distance R_{20} from the source where

$$R_{20} = \sqrt{x^2 + r'^2 + r^2 - 2r'r \cos(\theta' - \theta)} \tag{4.36}$$

Given the disturbed velocity, the wake velocity, the propeller geometry, the strength of bound vortices, and the pitch of the free vortex, the boundary condition for the propeller, which defines the velocity at its blades, can be established as:

$$\begin{aligned} &\left(\frac{2\sqrt{r^2 + a(r)^2}}{Zk_1 c(r)} + \frac{r^2 + h(r)^2}{2rh(r)\kappa_N(r)} \right) \Gamma(r, \theta) \\ &+ \left[\frac{\partial \phi_{\mathrm{Pf}\infty}}{\partial x_p} \right]_P - \frac{h(r)}{r} \left[\frac{\partial \phi_{\mathrm{Pf}\infty}}{\partial \theta} \right]_P \\ &= \frac{a(r)}{r} \left(\Omega r + [u_{p\theta}(r, \theta)]_P \right) - [u_{px}(r, \theta)]_P \end{aligned} \tag{4.37}$$

Where $a(r)$ and $c(r)$ describe the blade pitch and chord distributions. Z is the number of propeller blades and Ω is rotation rate of propeller. The index $[]_P$ indicates values on propeller disk $(x = 0)$ and $u_{px}(r,\theta)$, $u_{p\theta}(r,\theta)$ are the undisturbed axial and tangential velocity distributions in the nominal wake. $\kappa_N(r)$ is the Prandtl tip correction factor and k_1 is an empirical correction for lift slope by Yamazaki (1968), defined as:

$$\kappa_N(r) = \frac{2}{\pi}\cos^{-1}\left(e^{-Z\left(1-\frac{r}{r_0}\right)\frac{\sqrt{r^2+h(r)^2}}{h(r_0)}}\right) \qquad k_1 = \left[1.07 - 1.05\frac{c(r)}{r_0} + 0.375\left(\frac{c(r)}{r_0}\right)^2\right]_{r=0.7r_0} \tag{4.38}$$

The undisturbed velocities, $u_{px}(r,\theta)$ and $u_{p\theta}(r,\theta)$, necessitate a clear understanding of the propeller's total induced velocities for effective coupling with a RANS solver. By subtracting these from the velocities presented on the propeller plane by RANS, the undisturbed wake can be identified. Additionally, these total velocities aid in calculating the momentum transferred to the fluid, which subsequently helps determine the thrust and torque. The induced velocities in both axial and tangential directions are described as:

$$V_{Px} = \frac{r\Gamma(r,\theta)}{2h(r)\kappa_N(r)} + \left[\frac{\partial\varphi_\infty}{\partial x}\right]_P \qquad \overline{V_{Px}} = \int_0^{2\pi} V_{Px}d\theta \tag{4.39}$$

$$V_{P\theta} = -\frac{\Gamma(r,\theta)}{2\kappa_N(r)} + \left[\frac{\partial\varphi_\infty}{r\partial\theta}\right]_P \qquad \overline{V_{P\theta}} = \int_0^{2\pi} V_{P\theta}d\theta \tag{4.40}$$

The definition specifies that both the induced velocity in the radial direction and the radial force are zero. Using these velocities, the pitch of the free vortex can be determined as:

$$h(r) = k_2 r\frac{\overline{V_{Px}}}{\overline{V_{P\theta}}} \qquad k_2 = 1 + 0.625\left(\frac{c_{\max} - 0.84}{r_0}\right) \tag{4.41}$$

Equations (4.34)-(4.41) are solved iteratively until convergence of h is found.

- The calculation of forces

By integrating the pressure and viscous force components deriving from the vortex strength and the induced momentum, the total thrust T and total torque Q can be calculated:

$$T = -F_{Px} = -\rho\int_{r_h}^{r_0} dr\int_0^{2\pi}\frac{d^2F_{px}}{rdrd\theta}rd\theta + \frac{dF_{fx}}{dr} \tag{4.42}$$

$$Q = M_{Px} = \rho \int_{r_h}^{r_0} rdr \int_{0}^{2\pi} \frac{d^2F_{p\theta}}{rdrd\theta} rd\theta + \frac{dF_{f\theta}}{dr} \tag{4.43}$$

The pressure force components are defined as:

$$\frac{d^2F_{Px}}{drd\theta} = \Gamma(r,\theta)V_{P\theta} \qquad \frac{d^2F_{P\theta}}{drd\theta} = \Gamma(r,\theta)V_{Px} \tag{4.44}$$

The viscous force components are defined as:

$$\frac{dF_{Px}}{dr} = -\frac{1}{2}C_{PD}Zc(r)\sqrt{1+\frac{h(r)^2}{r^2}}\overline{V_{Px}}\,\overline{V_{P\theta}} \qquad \frac{dF_{P\theta}}{dr} = -\frac{1}{2}C_{PD}Zc(r)\sqrt{1+\frac{h(r)^2}{r^2}}\overline{V_{P\theta}}^2 \tag{4.45}$$

By applying the forces determined from Equations (4.44) and (4.45) as momentum sources in the RANS simulation via Equation (6), and employing the thrust and torque derived from Equations (4.42) and (4.43) to control the rotation rate, the Yamazaki model is established that can predict the performance of a certain hull/propeller combination.

The open waver performance of the KCS propeller is predicted by the Yamazaki model and compared with the EFD results, as shown in Figure 4.8. The primary purpose of the Yamazaki model is to provide numerical verification in conjunction with the BEMt code, which in turn ensures the accuracy and reliability of the calculated outcomes.

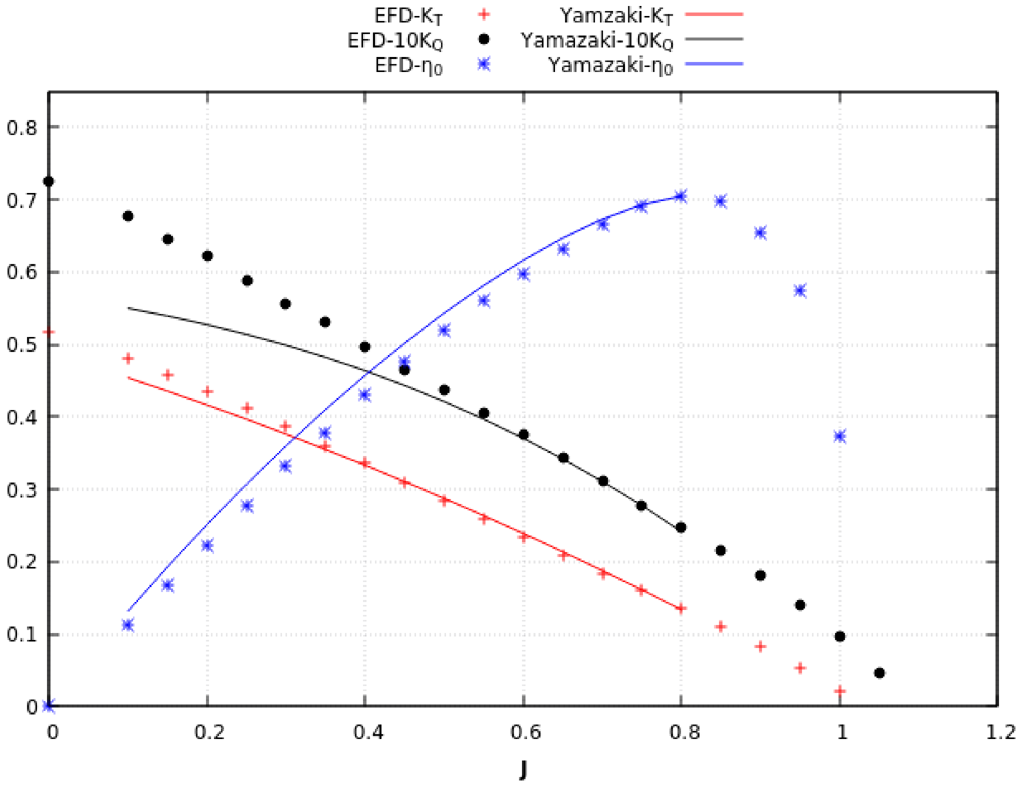

FIGURE 4.8: Open water curve of the KCS propeller predicted by the Yamazaki model and compared with EFD data obtained from Hino et al. (2020)

4.5 RANS-Body Force Models coupling

The coupling between the RANS solver and body force models (BEMt and Yamazaki model) is achieved using a two-way coupling. Initially, the velocity derived from the RANS solution is utilized to generate a wakefield, which directly impacts how propeller thrust and torque are distributed within the propeller code. Subsequently, these propeller thrust and torque variations are reintroduced into the RANS domain, reflecting the shifts in velocity and pressure stemming from the propeller's presence. The mapping of velocity u and body force Fv between RANS (hull-rudder) and concentric (propeller) meshes is illustrated in Figure 4.9. The equations coupling is also demonstrated in Figure 4.10.

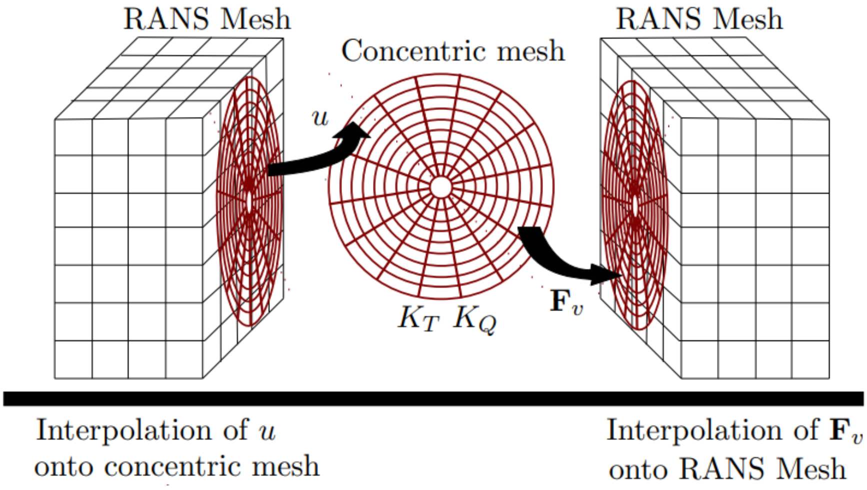

FIGURE 4.9: Mapping of velocity u and body force Fv between RANS and concentric meshes Windén (2014)

4.6 Chapter summary

This chapter primarily focuses on the numerical framework employed for simulating a ship with the angle of drift and the numerical propeller modelling methods selected in this thesis. Two coordinate systems, namely, the ship-axis-based and domain-axis-based systems, are introduced. Section 4.3 describes the transformation matrix, which facilitates the conversion of longitudinal and transverse forces from the domain to the ship axis.

In terms of the propeller modelling approaches, this thesis adopts two body force propeller models to analyze the propeller's action rather than utilizing a discretized propeller with detailed blade geometry. A fully discretized propeller and rotating geometry, such as one using an AMI, requires a significantly smaller time step and extended simulation time to fully resolve the flow field surrounding the propeller geometry, thus

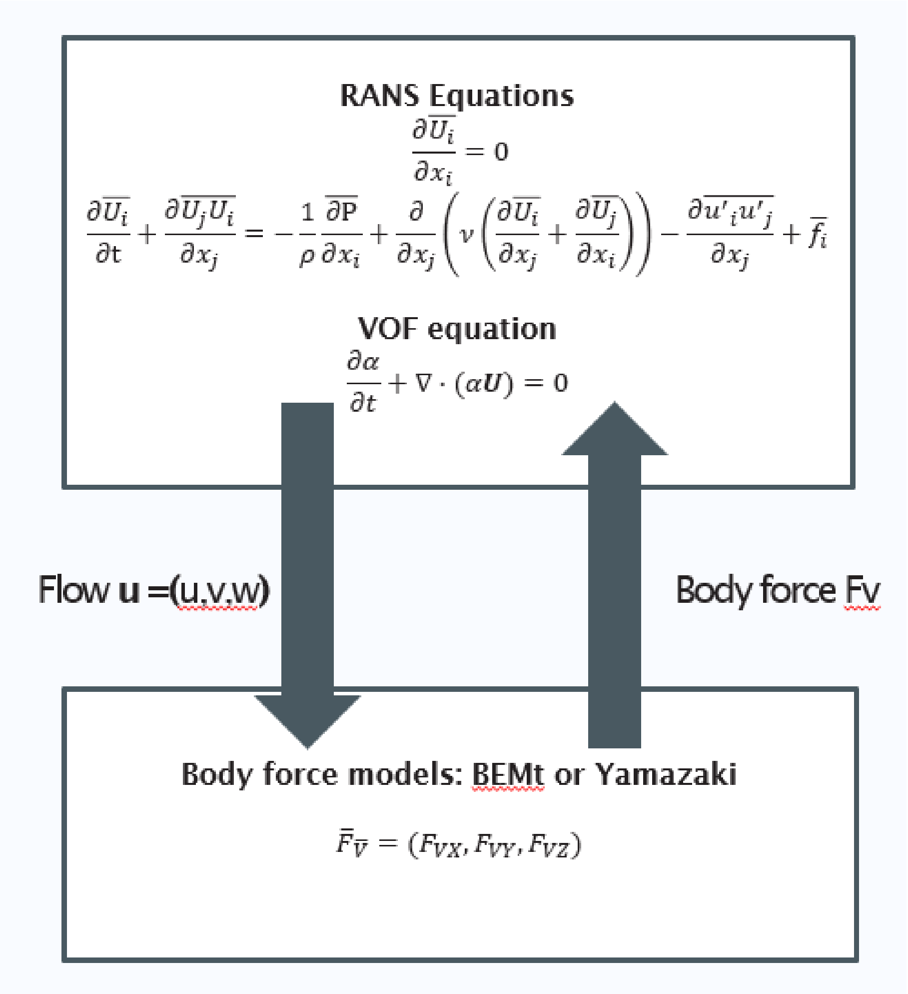

FIGURE 4.10: Equations coupling between RANS and body force models

resulting in substantial computational expenses. Moreover, this study primarily focuses on the interplay between the hull, propeller, and rudder in drift angle conditions rather than exclusively concentrating on the propeller itself. Consequently, body force models provide more advantages when the local flow details at the stern are not the focus of the study.

The Blade Element Momentum theory (BEMt) is selected as the primary propeller modelling method due to its successful prior applications such as ship self-propulsion in waves (Windén 2014), resistance and powering performance prediction (Badoe 2015), and vessel manoeuvring performance (Phillips et al. 2009*b*). Section 4.4.1 offers a comprehensive explanation of the momentum theory, blade element theory, and their coupling procedures for analyzing the propeller action. The BEMt proves to be able to accurately predict the KCS propeller open water curve, demonstrating overall good agreement with available experimental open water data. To ensure the accuracy and reliability of the BEMt code, another body force model, the Yamazaki model, is also briefly introduced and will be employed in Chapter 6 for comparative analysis and verification alongside the BEMt.

Chapter 5

Influence of drift angle on KCS using double body

5.1 Introduction

Ship designers and operators consider accurate estimation of ship manoeuvring in real sea states as an essential requirement. This holds particularly true when ships navigate through adverse weather conditions. Nevertheless, comprehending the ship's manoeuvrability in actual sea conditions is not adequately established (ITTC 2021). Compared to traditional experimental methods of assessing ship manoeuvring performance in towing tank or wave basin, numerical approaches can provide a more cost-effective way to determine a ship's manoeuvrability and course keeping ability. Nonetheless, performing CFD simulations for the complete time varying manoeuvre in waves can demand significant computational resources. This is mainly due to the substantial computational effort involved in accurately modeling the unsteady flow around the moving hull, the rotating propeller and the turning rudder. Therefore, an innovative approach is proposed in this thesis, simulating the self-propelled ship at different drift angles combined with a series of rudder angles to represent quasi-static phases of an actual ship manoeuvre.

As mentioned in section 3.1, the stepwise procedure is used to fully understand the influence of drift angle on the hydrodynamic performance of the self-propelled ship in waves. This chapter aims to provide an understanding of the interaction between the hull, the propeller, and the rudder in different drift scenarios using a double body approach. The double body approach involves using a symmetry boundary condition at the waterplane to represent the free surface without including any above-water geometry and without modelling the dynamics of the free surface. The main content of this chapter includes the resistance and propulsion characteristics of a self-propelled ship with different angles of drift and rudder angles in calm water conditions. Most of this chapter is also included in Zhang et al. (2021) and Zhang et al. (2022).

5.2 Influence of drift angle on hull-propeller interaction

5.2.1 Hull geometry

The KCS (KRISO Container Ship) is the selected ship model for this research due to its extensive experimental and computational studies. The vessel offers comprehensive insights into flow physics and serves as a modern container ship for numerical validation and verification purposes. Information on the KCS's self-propulsion performance was made available through the Tokyo 2015 workshop on numerical hydrodynamics as experimental data (Hino et al. 2020). The model's body plan and profile for the KCS are illustrated in Figure 5.1 and Figure 5.2. Table 5.1 presents the main particulars of the KCS, including the propeller.

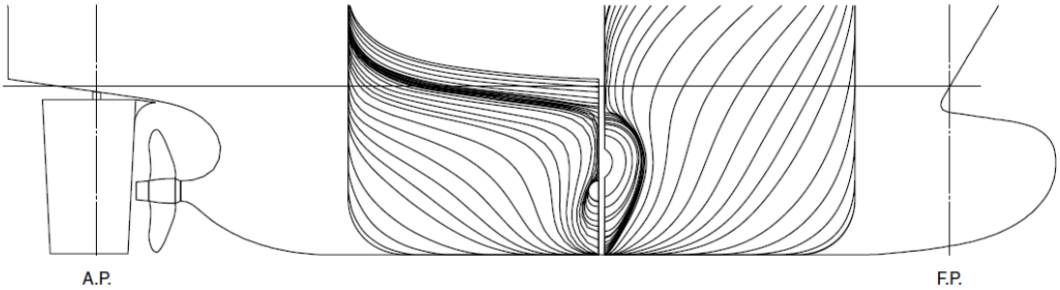

FIGURE 5.1: Body plan and profile elevation of KCS

FIGURE 5.2: KCS bare hull geometry used for CFD workshops (Larsson et al. 2013, Hino et al. 2020)

5.2.2 Simulation conditions

Seven cases are simulated in calm water conditions, with drift angles of β = -15 °, -10 °, -5 °, 0 °, 5 °, 10 °and 15 °using OpenFOAM version 7. The RANS equations are iteratively solved in all cases through the use of the SIMPLE algorithm, divided into two iteration sets. Initially, the simpleFoam solver is deployed for 1000 iterations for the resistance test of the bare hull, excluding propeller modeling. This process produces

TABLE 5.1: Main Particulars of KCS

Parameter	Model Scale	Full Scale	Unit
Length between perpendicular, L_{pp}	7.2786	230	m
Maximum beam of waterline, B_{WL}	1.0190	32.2	m
Depth, D	0.6013	19	m
Draft, T	0.3418	10.8	m
Displacement, ∇	1.6490	52030	m^3
Wetted surface area w/o rudder, S_W	9.4379	9424	m^2
Froude Number, Fn	0.26	0.26	-
Design speed, U	2.196	12.35	m/s
Propeller diameter	0.25	7.9	m
The number of propeller blades	5	5	-
Propeller rotation direction (view from stern)	clockwise	clockwise	-

the towed resistance of the hull, represented as R_{tow}. This value serves as a reference to determine the self-propulsion point of the ship. Following that, the next 1000 iterations are carried out as a self-propulsion test using the custom solver selfPropsimpleFoam, which is included in the open source framework for ship performance analysis called SHORTCUt (Winden 2021*b*). This results in the self-propulsion resistance R_{prop} and the propeller thrust and torque.

5.2.3 Computational domain and boundary conditions

In accordance with the CFD guidelines established by the ITTC (2014), a computational domain was constructed for the numerical simulation of the KCS bare hull. Figure 5.3, and Figure 5.4 display a schematic representation of this computational domain from the side and top views, respectively. The inlet boundary was established $2.5Lpp$ ahead of the FP of KCS, while the outlet boundary was located $5Lpp$ behind the AP of KCS. In order to avoid any wall effects on the numerical simulation, the side boundaries were placed $1.5Lpp$ away from the central plane. The depth of the domain was also set to $1.5Lpp$. The entire flow field is analyzed due to the asymmetry of the flow, which is brought about by both the propeller-induced rotation and the non-zero drift angle.

The boundary conditions used in every case are listed in Table 5.2. The volumeForce parameter is used to calculate the propeller forces, thrust and torque for the self-propulsion test as the propeller modeling is achieved using body forces without meshing the propeller geometry. As mentioned in section 3.6, wall functions in OpenFOAM are implemented through boundary conditions. Therefore the adopted wall functions are also included in Table 5.2:

- kqRWallFunction: The wall function for turbulent kinetic energy k.
- omegaWallFunction: The wall function for the specific dissipation rate ω.

- nutkRoughWallFunction: The rough wall function for the turbulence kinetic eddy viscosity ν_t.

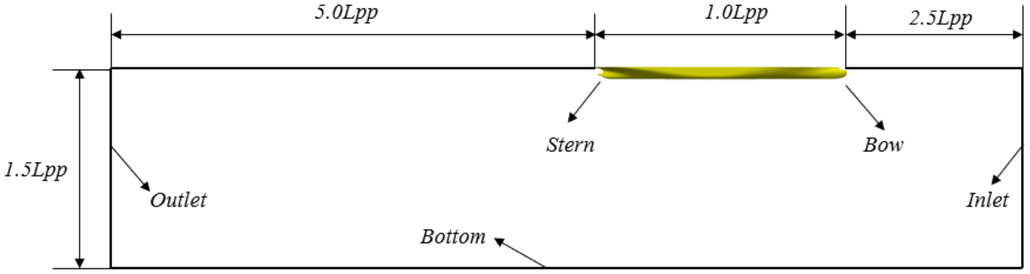

FIGURE 5.3: Dimensions of the computational domain from the side view

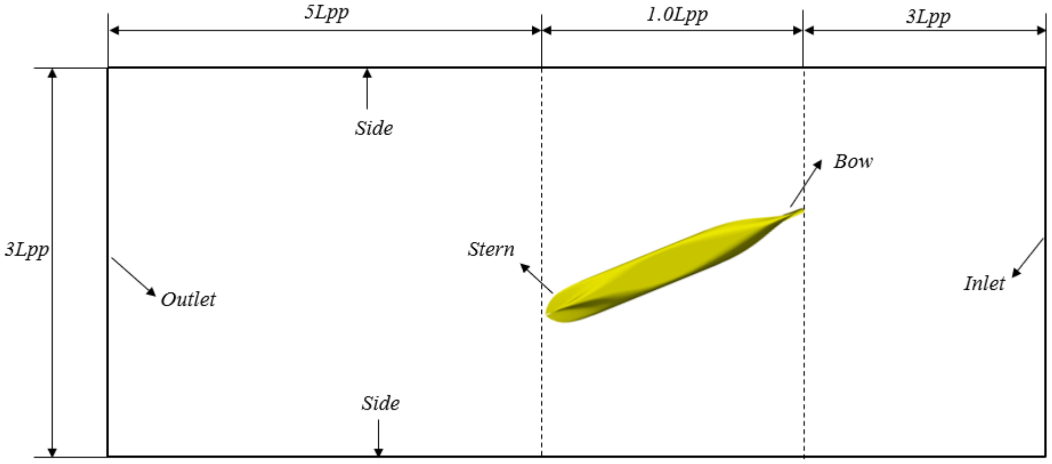

FIGURE 5.4: Dimensions of the computational domain from the top view

TABLE 5.2: Boundary conditions for double body simulations

Parameter	Inlet	Outlet	Top/Side/Bottom	Hull
U	fixedValue	inletOutlet	symmetry	movingWallVelocity
p	zeroGradient	fixedValue	symmetry	zeroGradient
k	fixedValue	inletOutlet	symmetry	kqRWallFunction
ω	fixedValue	inletOutlet	symmetry	omegaWallFunction
ν_t	fixedValue	zeroGradient	symmetry	nutkRoughWallFunction
volumeForce	fixedValue	fixedValue	symmetry	fixedValue

5.2.4 Mesh generation

The same meshing approach (Windén 2021*c*) is applied to all cases by adopting blockMesh and snappyHexMesh utilities in OpenFOAM version 7 and the main steps of meshing and refinement are shown as follows:

- The background mesh: The blockMesh is used to generate the initial structured hexahedral background mesh. The size of the largest cell in the background mesh is $0.075L_{pp}$.
- A refinement region that surrounds the entire hull: a rectangular refinement box that spans 25 % of the vessel's length (L_{pp}) forward and aft of FP and AP, respectively, 25 % of the vessel's beam on both sides, and 50 % of the vessel's draft below.
- Two further refinement boxes surrounding the bow and stern region: enclose the high curvature areas near the bow and stern of KCS, another two refinement boxes are employed that extend 25 % of L_{pp} behind AP and 10 % of L_{pp} in front of FP, as well as a certain distance towards the middle of KCS.
- A refinement cylinder enclosing the propeller and its surrounding region: The cylinder is positioned at the centre of the propeller axis and extends far enough aft to cover the entire KCS rudder. Its forward extent reaches into the stern of the KCS vessel. The cylinder's radial extent is 120 % of the propeller radius.
- Surface refinement on KCS and its appendage: The refinement level of KCS hull is 5, and the rudder refinement is level 8 if the rudder is considered.
- Boundary layer of KCS and its appendages: The initial height of the first cell is determined by targeting a y_1^+ value of approximately 1, and the number of prism layers is set to 25. This ensures that the size of the outermost layer matches the cell size of the surrounding cells from the previous step, with an expansion ratio of 1.2.

For the above meshing steps, the blockMesh is only used in step 1, while steps 2-6 are achieved by the snappyHexMesh utility. The total mesh sizes for cases with different drift angles are listed in Table 5.3. It is evident that the mesh size gradually increases with the increment of the magnitude of the drift angle as the bigger the drift angle magnitude, the larger the refinement boxes needed.

TABLE 5.3: Total mesh sizes for cases with different angles of drift

The angle of drift β (°)	Total mesh size (Million)
0	6.70
±5	9.78
±10	12.59
±15	15.34

5.2.5 Mesh independence study

To ensure the reliability and accuracy of simulation, a mesh independence study is carried out to evaluate the influence of grid spacing on the numerical prediction of hull propeller interaction at zero drift angle condition ($\beta = 0°$) for the bare KCS resistance test and self-propulsion test. Three different grids are created using the grid refinement ratio $\sqrt{2}$ of the structured background blockMesh, representing coarse, medium, and fine resolutions. Table 5.4 presents the grid system employed for the independence analysis. The total number of cells in the coarse, medium and fine grids are 2.59M, 6.70M and 16.83M. Computational costs are given in Table 5.4 and are obtained using S2 Viglen Medium Tower Workstation with Ubuntu 18.04.6 LTS system, Intel Core i7-7700 CPU @ 3.60GHz × 8, and 32GB memory, and with four cores.

TABLE 5.4: Grid system for mesh independence study

Parameter	Coarse grid	Medium grid	Fine grid
blockMesh refinement	$80 \times 28 \times 14$	$113 \times 40 \times 20$	$160 \times 56 \times 28$
Total mesh size	2.59M	6.70M	16.83M
Computational expense (Resistance test)	87mins	226mins	580mins
Computational expense (Self-propulsion test)	74mins	189mins	501mins
Computational expense (Total)	161mins	415mins	1081mins

The computation results obtained from three grids are listed in Table 5.5 and compared with EFD data, which is sourced from Hino et al. (2020) and Feng et al. (2020*a*). Since the simulations are carried out without consideration of the free surface, and the KCS is known to have a significant proportion of wave-making resistance due to its low block coefficient, hence an empirical value of $C_W = 0.467$ from Windén (2021*c*) is added to yield the total resistance coefficient C_T when performing the thrust/resistance calculation for the KCS. More specifically, CFD simulation computes pressure and viscous resistance coefficients, C_P and C_V, hence C_T=C_P+C_V+C_W.

TABLE 5.5: The predicted resistance and self-propulsion coefficients using three grids and compared with EFD obtained from Hino et al. (2020) and Feng et al. (2020*a*)

Parameter	Coarse grid	Medium grid	Fine grid	EFD
$C_T \times 10^{-3}$ (Resistance test)	3.348	3.356	3.366	3.55
$C_T \times 10^{-3}$ (Self-propulsion test)	3.672	3.675	3.682	3.966
K_T	0.139	0.143	0.143	0.170
$10K_Q$	0.265	0.272	0.273	0.29
$n(rps)$	9.98	9.84	9.84	9.50

As mentioned before, a possible explanation for the discrepancy between CFD results and EFD data may be attributed to the increased importance of the free surface in relation to the KCS, which is relevant concerning the pressure distribution on both the hull and the propeller. Based on the results and comparisons shown in Table 5.5, the medium grid is considered the optimal mesh resolution by balancing the trade-off between computational cost and numerical accuracy. Therefore, the medium grid is employed for most simulations in this chapter unless otherwise stated.

5.2.6 Results and discussion

5.2.6.1 Resistance, side force, yaw moment

The hull drag force can be calculated by integrating the pressure and shear stress acting on the hull surface over the entire hull area. The pressure resistance coefficients C_P, the viscous resistance coefficients C_V and the total resistance coefficients C_T are summarized in Table 5.6 for each drift angle scenario, and the wave making resistance coefficient $C_w = 0.467$ is added to the value of C_T.

TABLE 5.6: Resistance coefficients for each drift angle scenario

	Resistance test			Self-propulsion test		
Drift angle β °	$C_P \times 10^{-3}$	$C_V \times 10^{-3}$	$C_T \times 10^{-3}$	$C_P \times 10^{-3}$	$C_V \times 10^{-3}$	$C_T \times 10^{-3}$
-15	0.371	2.951	3.789	0.9	2.971	4.338
-10	0.399	2.859	3.725	0.787	2.871	4.125
-5	0.315	2.693	3.475	0.63	2.703	3.8
0	0.25	2.639	3.356	0.56	2.648	3.675
5	0.316	2.695	3.478	0.65	2.75	3.867
10	0.399	2.855	3.721	0.788	2.89	4.145
15	0.373	2.953	3.793	0.92	2.978	4.365

The time history plots of hull components coefficients (C_P, C_V, and C_T vs iteration numbers) are plotted in Figures 5.5, 5.6 and 5.7 for positive drift angle cases. The variation trend is similar for the negative drift cases, which can be observed from Table 5.6. Overall, as the magnitude of the static drift angle increases, there is a corresponding increase in the resistance coefficients for the ship and the largest increment can be found from $\beta = 5$ °to $\beta = 10$ °.

Once the viscous resistance component reaches the convergence period at approximately 500 iterations, the pressure resistance and total resistance trend follow a similar variation trend. The addition of propeller forcing from iteration 1000 does not cause a substantial change in the value of the viscous resistance component. Obviously, the larger the drift angle, the longer simulation takes to reach the convergence period, especially for the resistance test. Due to the unavailability of experimental data for the drag force of drift cases, comparisons have been made with numerical simulation results from Sun et al. (2018) shown in Figure 5.8. Although good agreement can be found between the two simulation results, there is still some discrepancy due to the fact that Sun et al. (2018) considered the different wetted hull surface areas (S_w) for each drift angle while the constant experimental value of wetted surface is used in the current study. Also, Sun et al. (2018) found that the wet surface area increases with the increment of drift angle magnitude, which explains the possible reason why significant discrepancies are found on large drift angles such as 10 °and 15 °.

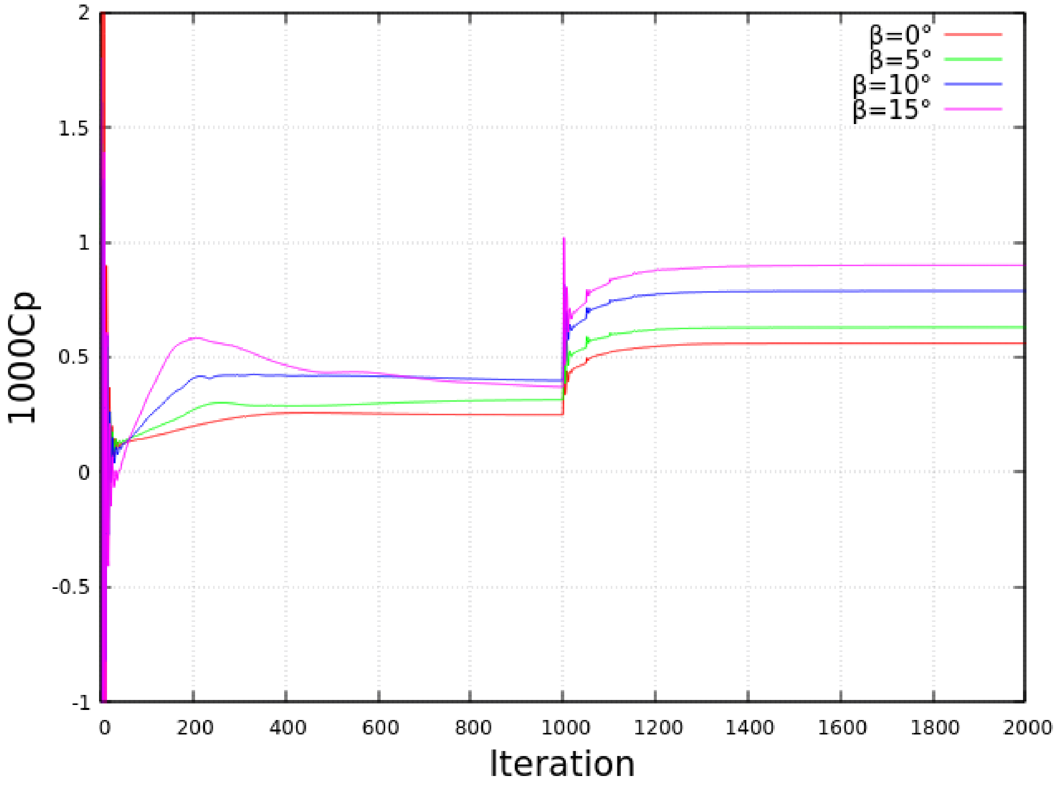

FIGURE 5.5: Pressure resistance coefficient variations with iterations for different drift angles

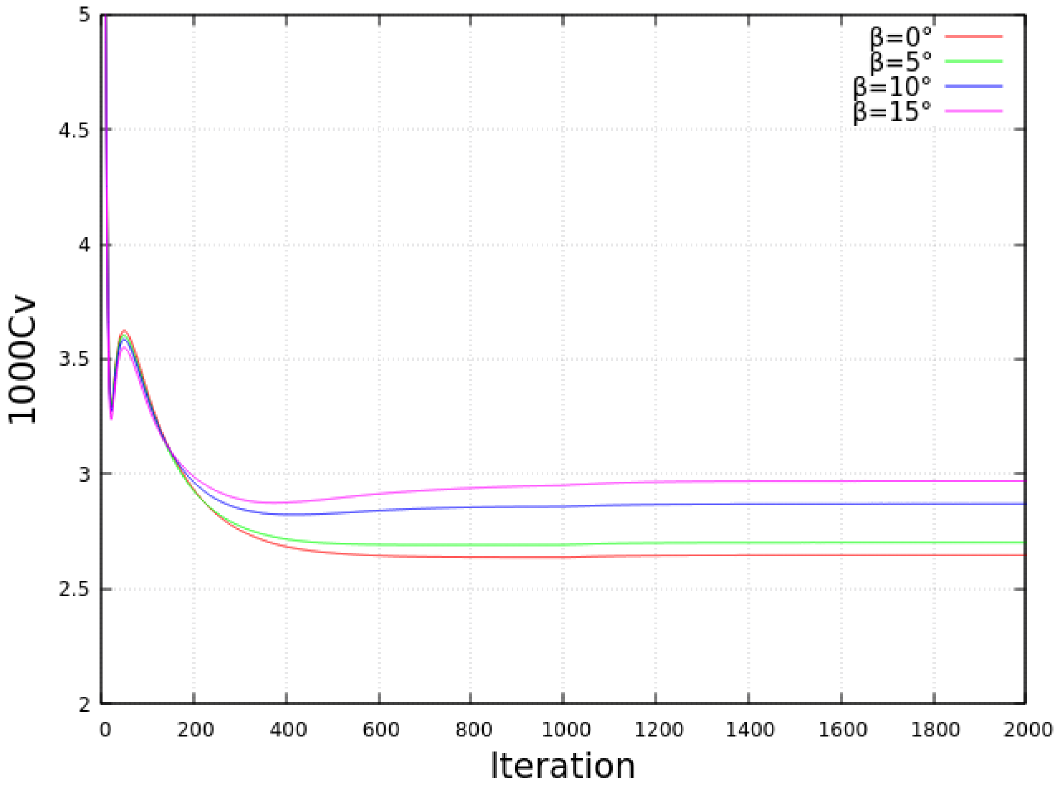

FIGURE 5.6: Viscous resistance coefficient variations with iterations for different drift angles

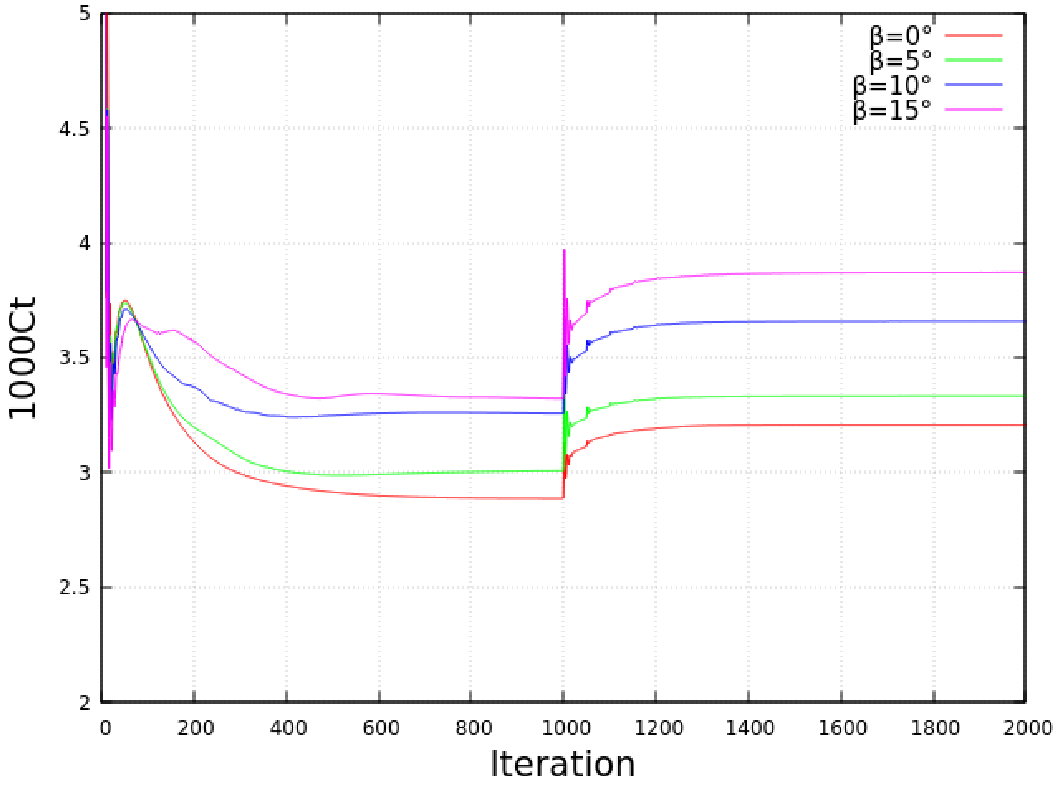

FIGURE 5.7: Total resistance coefficient variations with iterations for different drift angles

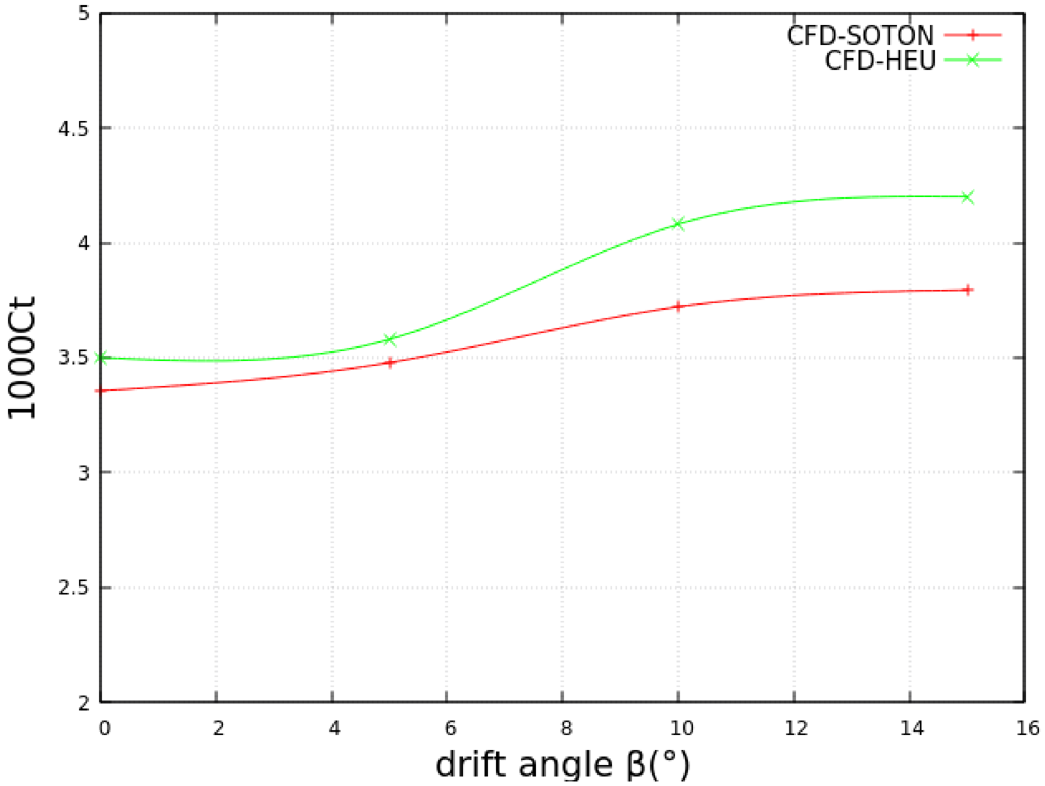

FIGURE 5.8: The comparison of total resistance coefficients of calm water resistance test

In addition to the drag coefficients, the side force and yaw moment generated on the hull are calculated for every drift angle. Side force and yaw moment are non-dimensionalized as the corresponding coefficients, $F_Y^{'}$ and $M_Z^{'}$ using the following equations:

$$F_Y^{'} = \frac{F_Y(N)}{\rho \times U^2 \times L_{pp}^2} \tag{5.1}$$

$$M_Z^{'} = \frac{M_Z(Nm)}{\rho \times U^2 \times L_{pp}^3} \tag{5.2}$$

The values of $F_Y^{'}$ and $M_Z^{'}$ for each drift angle are summarized in Table 5.7. The variations of side force and yaw moment with iterations are also shown in Figures 5.9 and 5.10. In order to ensure the accuracy of the computational results, two sets of experimental data and one set of numerical results are compared, these are presented by Kim et al. (2015) and Islam & Soares (2018), whose results are obtained by the bare hull in different static drift angle conditions without the rudder.

According to Figures 5.11 and 5.12, the simulations are able to capture the variation trend of the side force and yaw moment for different angles of drift. Although two sets of experimental data display slight disagreement with each other, this could be attributed to the application of different scales of KCS models and test facilities. The present findings, obtained through OpenFOAM, reveal a slightly lower side force and yaw moment in comparison to the other results. However, the trend is similar and the deviation is less than 10%. The probable reason for that difference could be the exclusion of the free surface effect in the current study. In general, the simulations indicate that as the static drift angle increases, both lateral force and yaw moment encountered by the KCS model also increase as expected.

TABLE 5.7: KCS's side force and yaw moment coefficients for each drift scenario

	Resistance test		Self-propulsion test	
Drift angle β °	$F_Y^{'} \times 10^{-3}$	$M_Z^{'} \times 10^{-3}$	$F_Y^{'} \times 10^{-3}$	$M_Z^{'} \times 10^{-3}$
-15	1.7987	0.7244	1.8210	0.7101
-10	0.9288	0.4694	0.9584	0.4550
-5	0.3243	0.2390	0.3479	0.2283
0	-0.0004	0.0001	0.0048	-0.0019
5	-0.3288	-0.2397	-0.3465	-0.2390
10	-0.9284	-0.4687	-0.9572	-0.4544
15	-1.7998	-0.7267	-1.8307	-0.7099

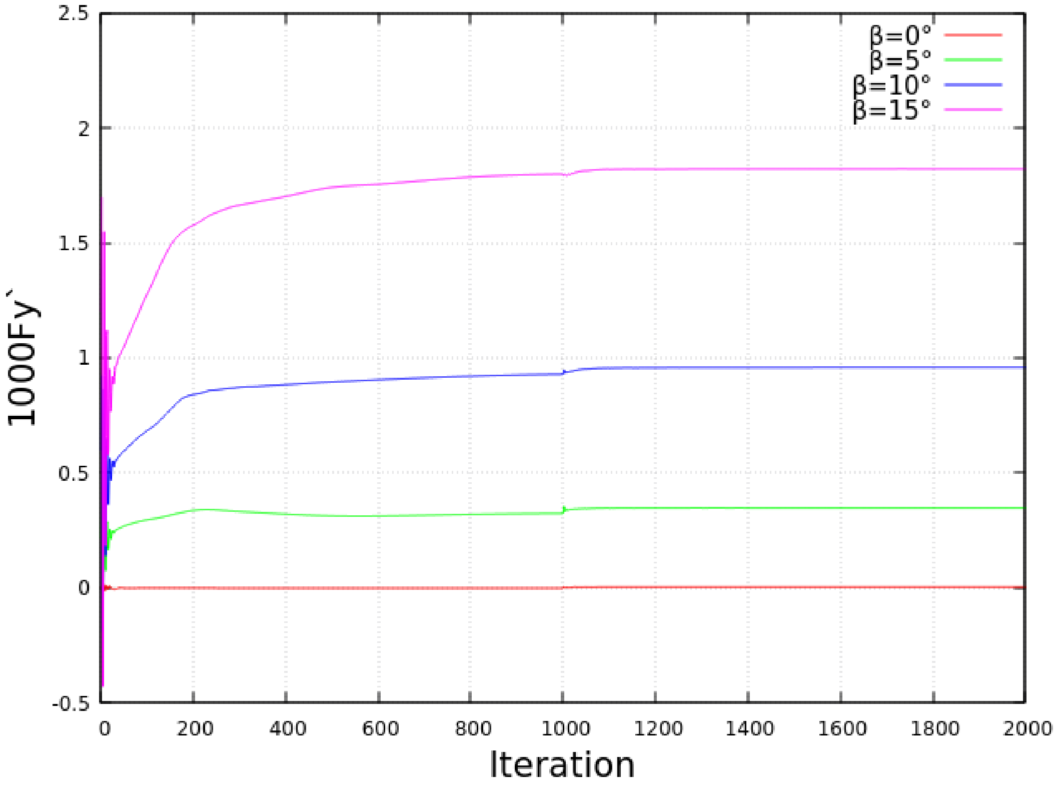

FIGURE 5.9: Side force coefficients variations with iterations for different drift angles

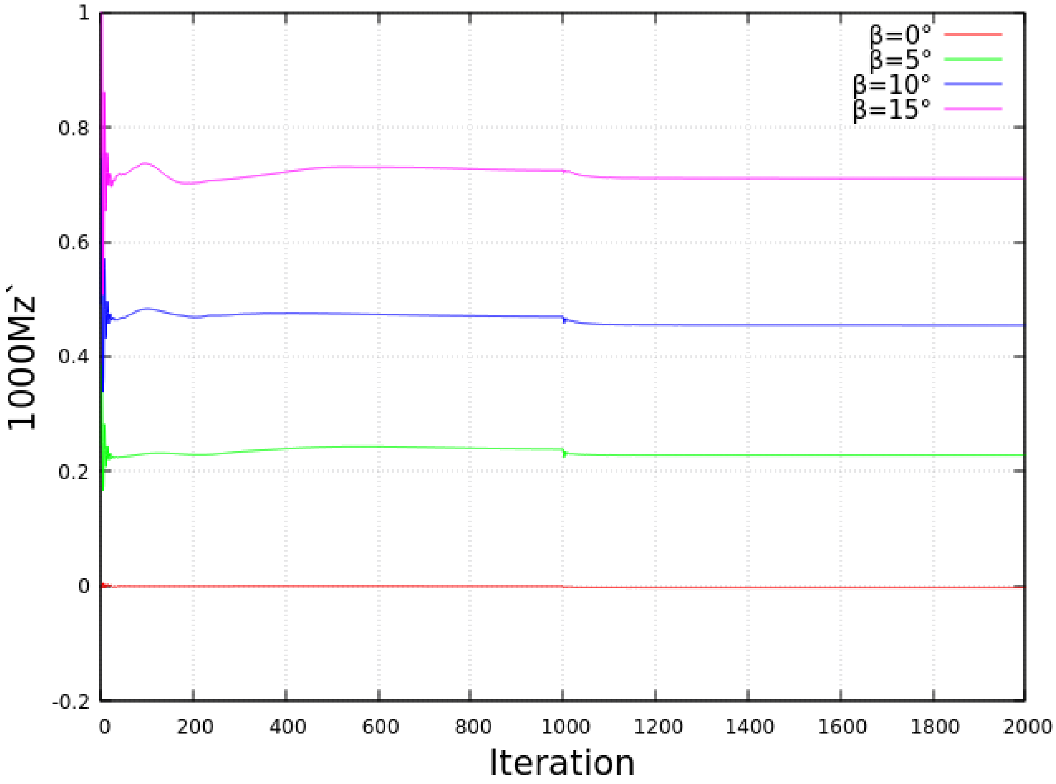

FIGURE 5.10: Yaw moment coefficients variations with iterations for different drift angles

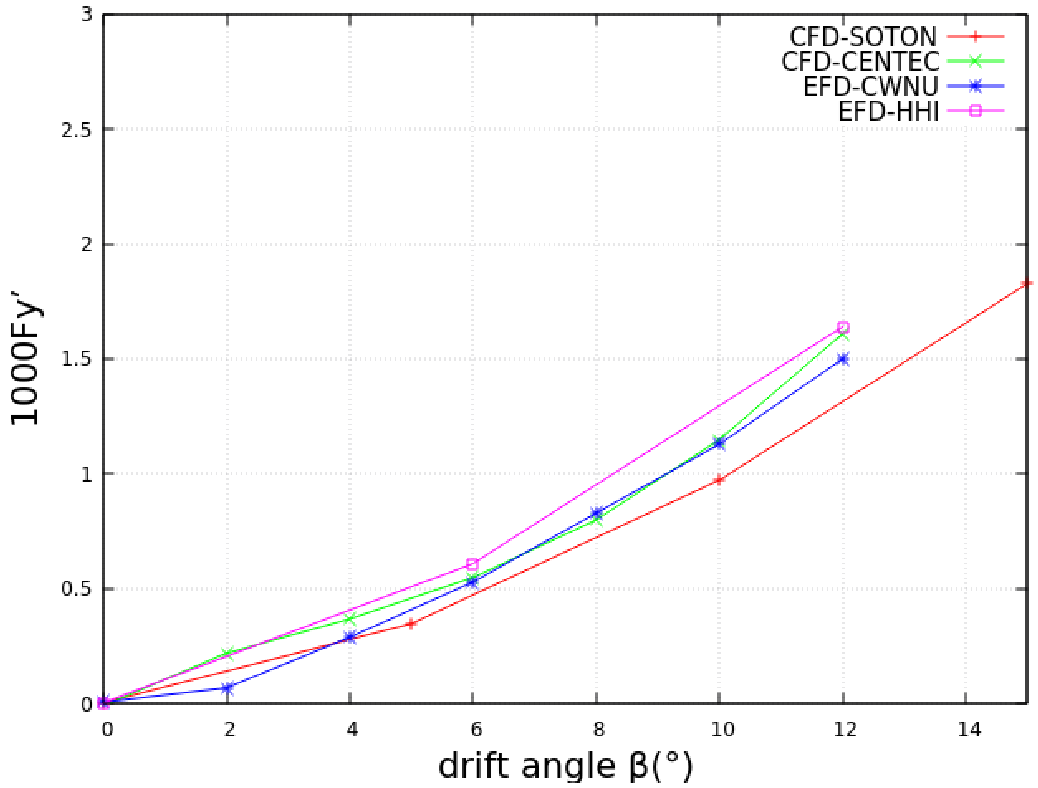

FIGURE 5.11: Non-dimensional side force experienced by KCS for different drift angles

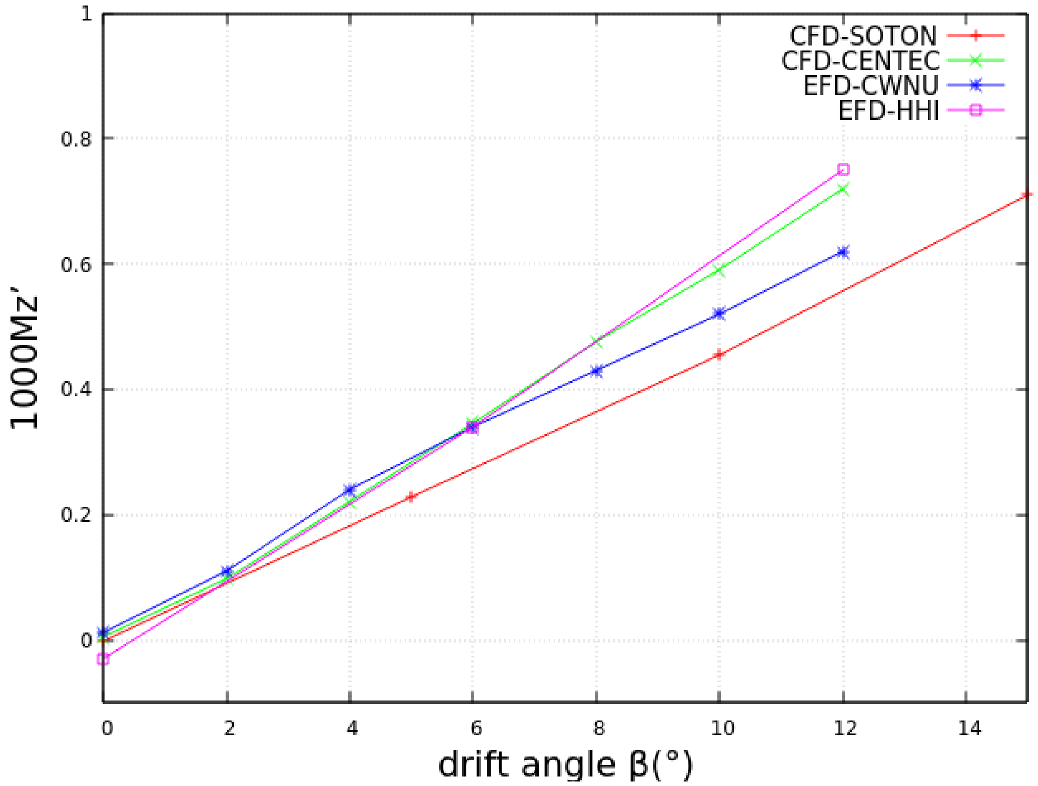

FIGURE 5.12: Non-dimensional yaw moment experienced by KCS for different drift angles

5.2.6.2 Velocity profiles and self-propulsion parameters

The velocity contours and velocity distribution behind the KCS's propeller plane are presented as part of the benchmarking data in the 2015 Tokyo CFD workshop on ship hydrodynamics. In this section, the velocity contours in x, y and z directions, the cross flow vectors and the velocity profiles are presented for three drift cases: β = -10 °, 0 °and 10 °. The zero drift angle case has the same conditions as case 2.7 of the 2015 Tokyo workshop for the KCS model. Therefore, the zero drift case's self-propulsion coefficients are validated with the experimental data and verified with many leading institutions' numerical results, representing the state of the art of ship hydrodynamics in CFD. Both EFD and CFD results presented in the 2015 workshop are summarized and discussed in detail by Hino et al. (2020).

- Zero angle of drift $\beta = 0$ °

The comparisons of axial flow contour downstream of the propeller plane between EFD and CFD are plotted in Figure 5.13 and Figure 5.14. Overall good agreement can be found between experimental data and numerical results obtained from BEMt, which indicates the body force model BEMt is a promising approach for propeller modeling. The main difference between EFD and CFD is the moon-crescent-like region located on the right side of the propeller plane. The axial contours obtained by CFD are more symmetrical compared to EFD, which indicates the need for actual geometry of the propeller may be required if the representation of the local wakefield profile is essential.

In addition to the axial velocity contours, the local flow contours in the y and z direction (U_y and U_z) are also generated by CFD, as shown in Figure 5.19 and Figure 5.20 although there is no available EFD data to compare with. The positive and negative velocity components of U_y can be seen upstream and downstream of the propeller centre axis ($z/Lpp = -0.03$) respectively. Similarly, U_z's positive and negative components are located on the left side and the right side of the propeller centreline ($y/Lpp = 0$).

Furthermore, because of the addition of the angular momentum term from the propeller presence, the dominant velocity component can be observed at the left-hand side of the cross-flow vector graphs in both experimental and numerical results, which are shown in Figure 5.15 and Figure 5.16. And the main vortex induced by the propeller's clockwise rotation can be seen in both EFD and CFD plots.

Velocity profiles downstream of the propeller plane $x/Lpp = -0.9911, z/Lpp = -0.03$ are presented in Figure 5.17 and Figure 5.18. CFD results underpredict the value of u/U close to the plane $y/Lpp = 0$: the experimental u/U value is about 0.6 while the numerical value is around 0.5. Besides, CFD overestimates the value of u/U on the left side of the propeller plane centre, near $y/Lpp = -0.01$: the peak of EFD is approximately 1.05 while the CFD gives the value of 1.15. For the right side of the propeller center, a good agreement can be found between EFD and CFD. This corresponds to the axial velocity contours difference shown in Figure 5.13 and Figure 5.14. For local velocity profiles in y and z directions as presented in Figure 5.19 and Figure 5.20 respectively, CFD results generally agree well with EFD data, indicating the body force propeller model can successfully replicate the asymmetry of w/U and w/U velocity profiles and can capture the changes from positive to negative velocity components across the vertical plane smoothly.

In the 2015 Tokyo workshop, only four submissions were made regarding the calculated self-propulsion point of the KCS while the remaining participants choose the fixed propeller revolution with the use of the experimental data of 9.5 rps. The present CFD study displays the self-propulsion results in conjunction with the submission that involved varying the RPM, as shown in Figures 5.21 to 5.23. From the comparison, other simulation results from the 2015 Tokyo workshop (Hino et al. 2020) seem to outperform slightly against the results in the current study. The major reason for this discrepancy is probably because the modeling of the free surface plays an increasingly significant role in the KCS hull shape in terms of the pressure distribution on the hull and the propeller. The current study is carried out using double body simulation excluding the effect of the free surface while all other results include the free surface modeling in their numerical computations. Besides, the different complexity levels of propeller modeling also influence the results of the KCS self-propulsion prediction. The body force model BEMt is employed in this study to compute the self-propulsion characteristics of KCS after balancing the trade-off between numerical accuracy and computational cost.

The overall prediction of self-propelled KCS in the current study is very competitive and good agreement is found when comparing to EFD data and also other numerical simulation results, which demonstrates that the double body simulation with the body force propeller model can be valuable in assessing the hull propeller interaction for the KCS at a lower computational cost.

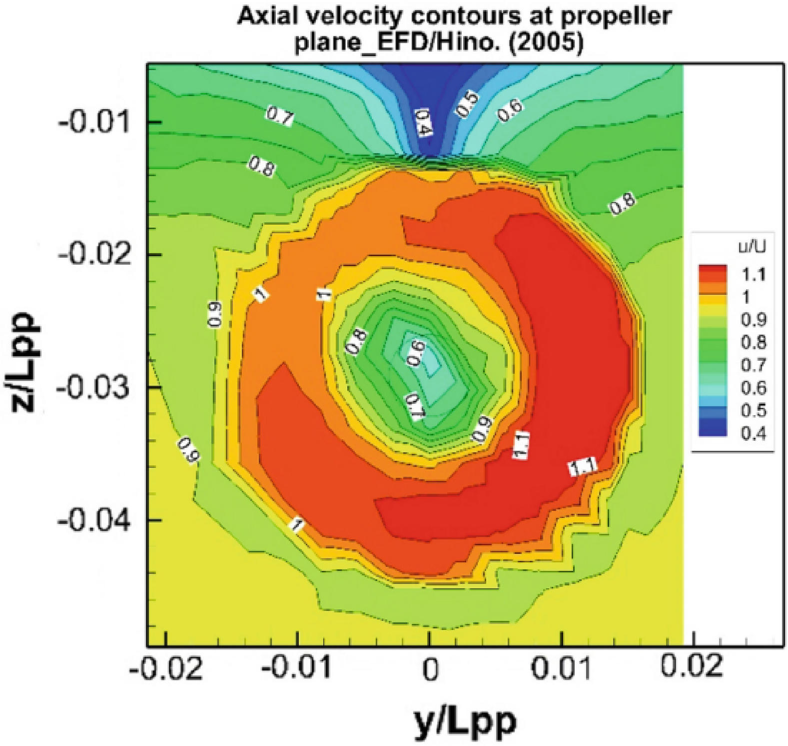

FIGURE 5.13: Experimentally measured axial velocity contours at $x/L_{pp} = 0.9911$ (Hino et al. 2020)

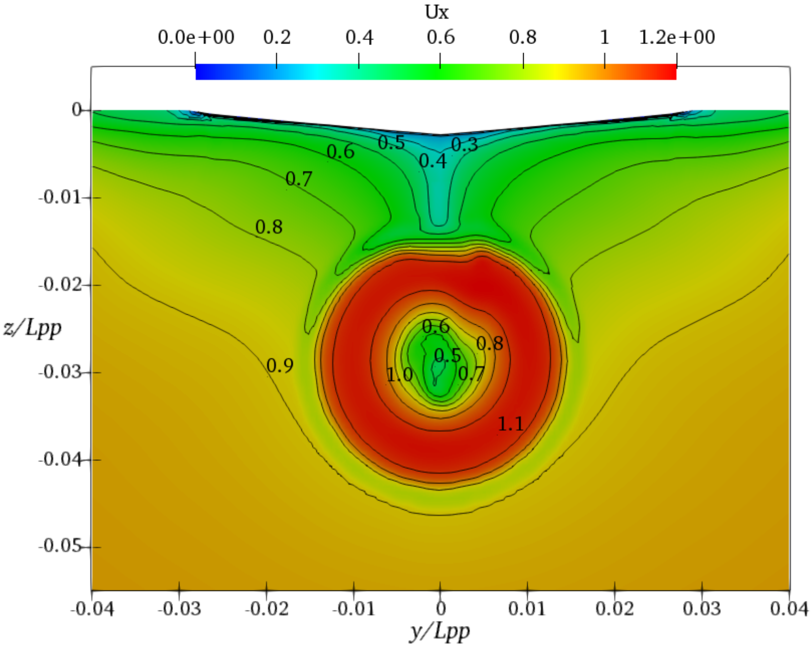

FIGURE 5.14: Axial velocity contours at $x/L_{pp} = 0.9911$ obtained from BEMt

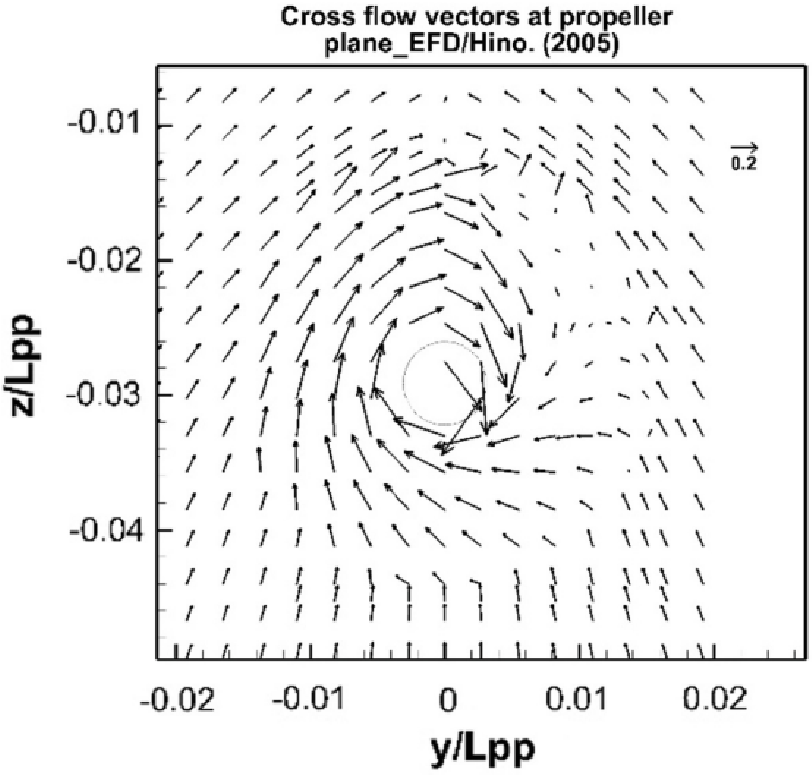

FIGURE 5.15: Experimentally measured cross flow vectors at $x/L_{pp} = 0.9911$ (Hino et al. 2020)

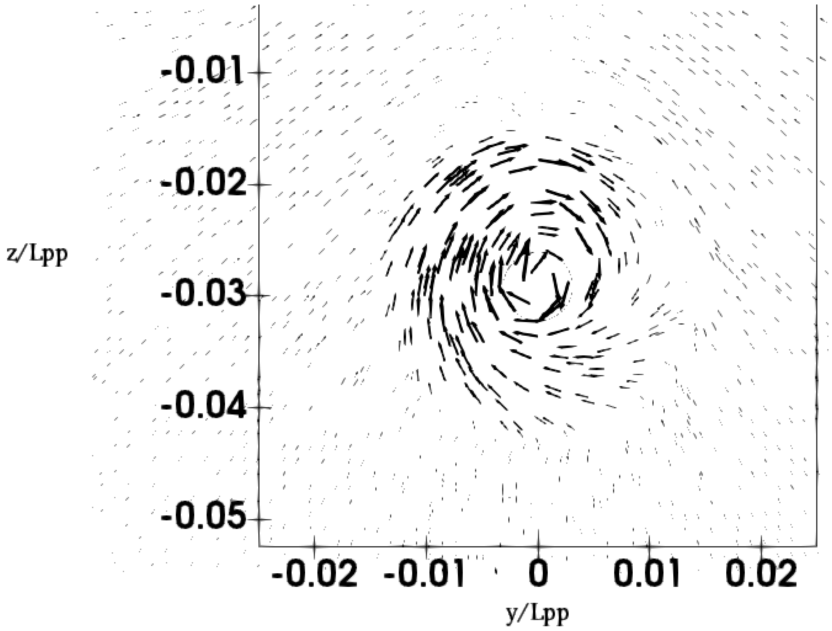

FIGURE 5.16: Cross flow vectors at $x/L_{pp} = 0.9911$ obtained from BEMt

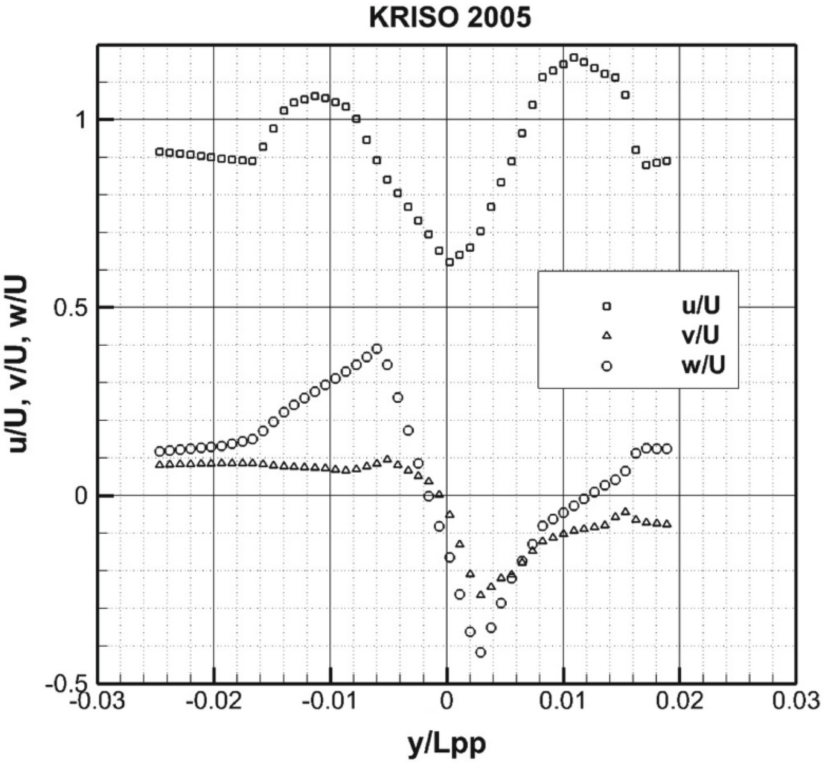

FIGURE 5.17: EFD results of velocity profiles downstream at propeller plane (x/L_{pp} = 0.9911) at z/L_{pp} = -0.03 (Hino et al. 2020); u, v and w are local velocities in x, y and z directions

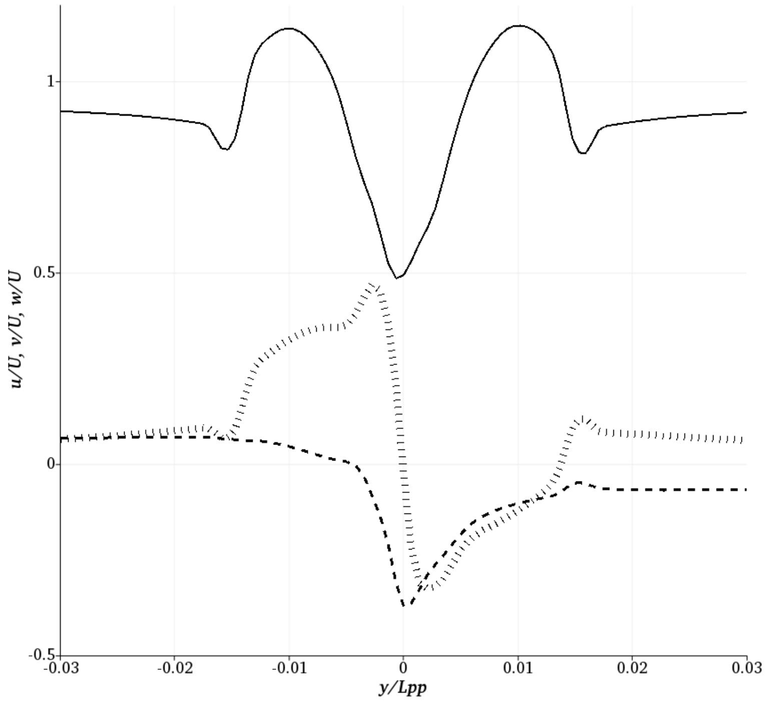

FIGURE 5.18: CFD results of velocity profiles downstream at propeller plane (x/L_{pp} =0.9911) at z/L_{pp} = - 0.03

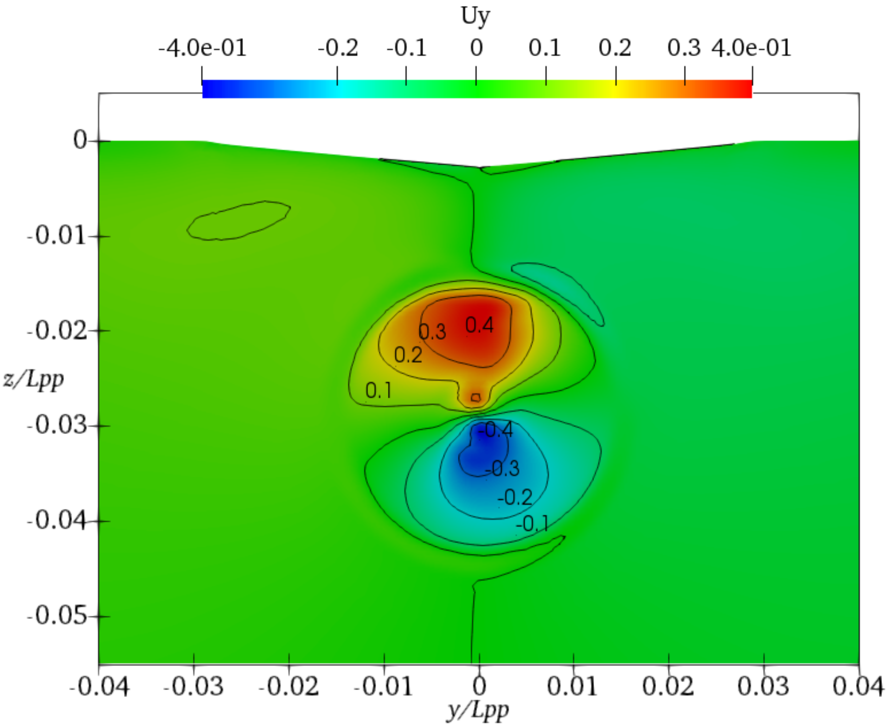

FIGURE 5.19: Local flow contours (U_y) at $x/L_{pp} = 0.9911$ predicted by BEMt

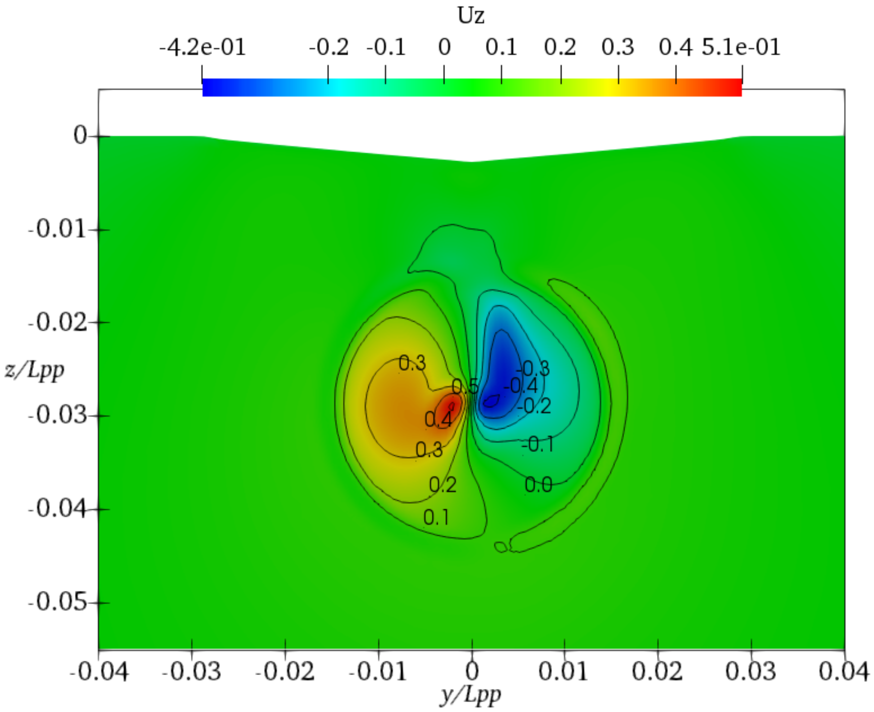

FIGURE 5.20: Local flow contours (U_z) at $x/L_{pp} = 0.9911$ predicted by BEMt

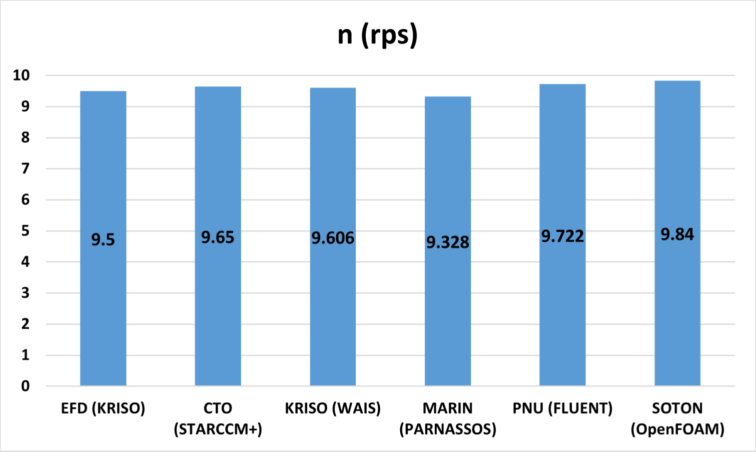

FIGURE 5.21: Comparison of predicted propeller revolution for KCS self-propulsion

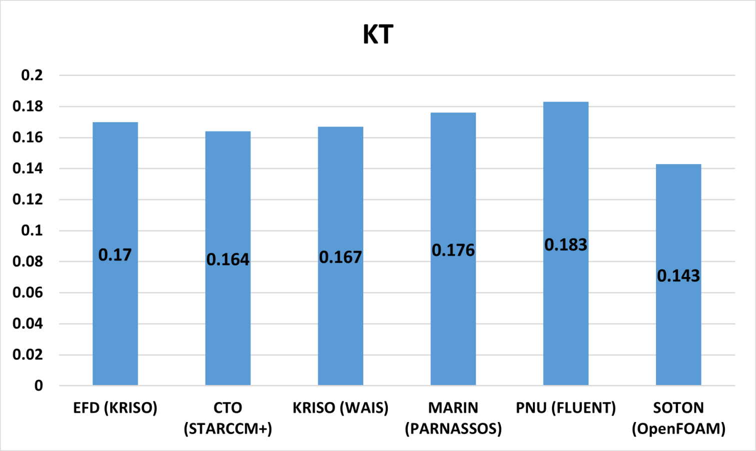

FIGURE 5.22: Comparison of predicted propeller thrust coefficient for KCS self-propulsion

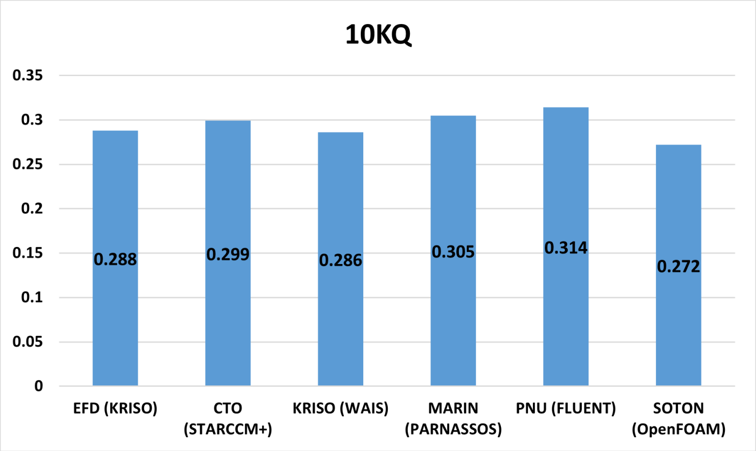

FIGURE 5.23: Comparison of predicted propeller torque coefficient for KCS self-propulsion

- Non-zero angles of drift β= -10 °, 10 °

Due to the fact of unidirectional rotation of the KCS propeller (clockwise), positive and negative angles of drift should be considered separately, in order to predict the influence of drift angle on the performance of the ship's self-propulsion and also manoeuvring, even though the magnitude of the drift angle is the same. The velocity profiles on the propeller plane for two drift angles, β= -10 °, 10 °are presented as the following Figures 5.24 to 5.31.

The contours of axial velocity U_x for β= -10 °, 10 °are shown in Figures 5.24 and 5.25. Compared with the straight-ahead conditions (no applied angle of drift), the asymmetric wake profile is more obvious. The maximum value of U_x in both drift cases is up to 1.3 while it is 1.1 in the zero-drift scenario, which indicates higher propeller revolution is required to compensate for the extra drag in the self-propulsion test when the non-zero drift angle is applied. Besides, the moon-crescent-like region can be found in both drift cases and the maximum velocity value is located in this area. For the U_y velocity component, positive and negative velocity regions are found upstream and downstream of the propeller centre axis $z/Lpp = -0.03$ for β= -10 °, but the negative velocity region is more dominant compared to that of the straight ahead case. However, multiple positive and negative velocity regions are found for β= 10 °, shown in Figure 5.27, the positive velocity components dominate in the propeller plane while the negative velocity is more prevailing outside this region, mainly located on the upper right corner of the plot. The value of U_y ranges from -0.6 to +0.6 for β= -10 °, while from -0.3 to +0.4 for β= 10 °although the same U_x value ranges (0 to +1.3) are found for both β= -10 °and β= 10 °. For the local U_z components, the positive and negative velocity regions are located on the left and right sides of the plane $y/Lpp = 0$ respectively for β= -10 °, which is the similar trend of zero drift case, but the contours extend more, shown in Figure 5.28. For β= 10 °case, another positive velocity region is found on the right side of Figure 5.29, which also dominates the entire U_z profile. Velocity profiles downstream of the propeller plane ($x/Lpp = -0.9911$, $z/Lpp = -0.03$) for β= -10 °and β= 10 °are presented in Figures 5.30 and 5.31. A similar variation of u/U is found for two drift cases and the trend is quite symmetric about the center of plane $y/Lpp = 0$. However, the obvious difference between β= -10 °and β= 10 °cases in terms of v/U and w/U can be observed. The values of v/U are all negative for β= -10 °and all positive v/U are found for β= 10 °, while changes of velocity sign are found in β=0 °case. For w/U components, although the minimum value of approximately -0.8 occurs at around $y/Lpp = 0.01$ for both β= -10 °and β= 10 °, the maximum w/U value of around 0.5 occurs at $y/Lpp = -0.015$ for β= -10 °and $y/Lpp = 0.015$ for β=10 °. This indicates that even though the same magnitude of drift angle is applied, the different signs of drift angle can greatly influence the velocity distribution especially v/U and w/U components when simulating the KCS self-propulsion test in drift conditions.

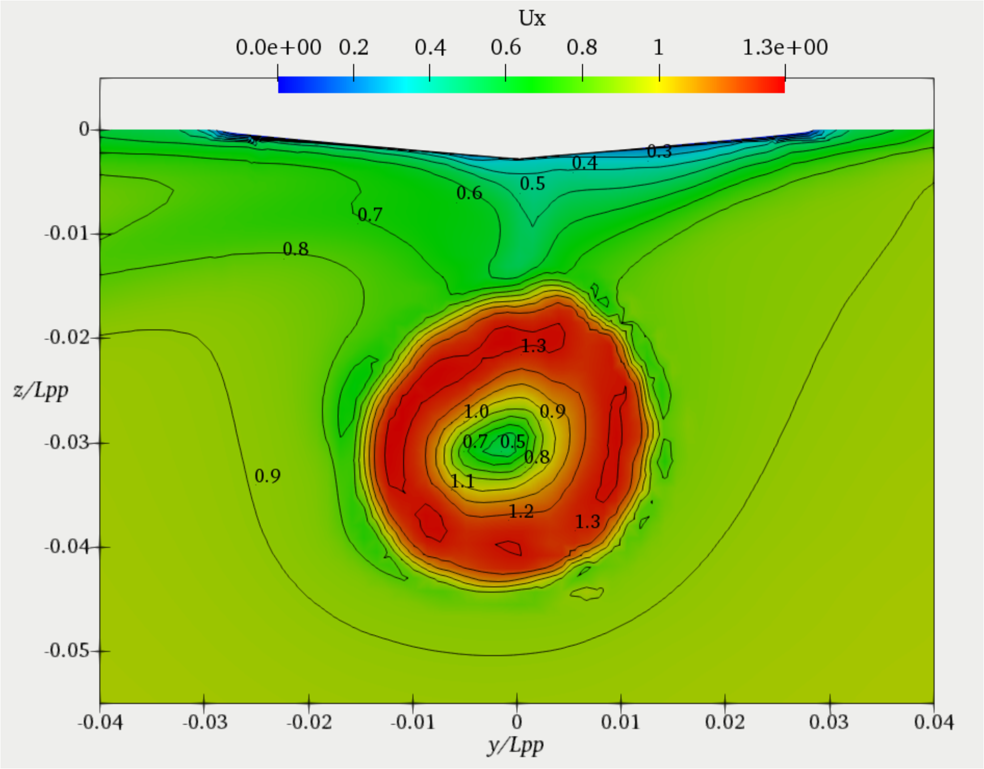

FIGURE 5.24: Axial velocity contours at $x/L_{pp} = 0.9911$ for β= -10 °

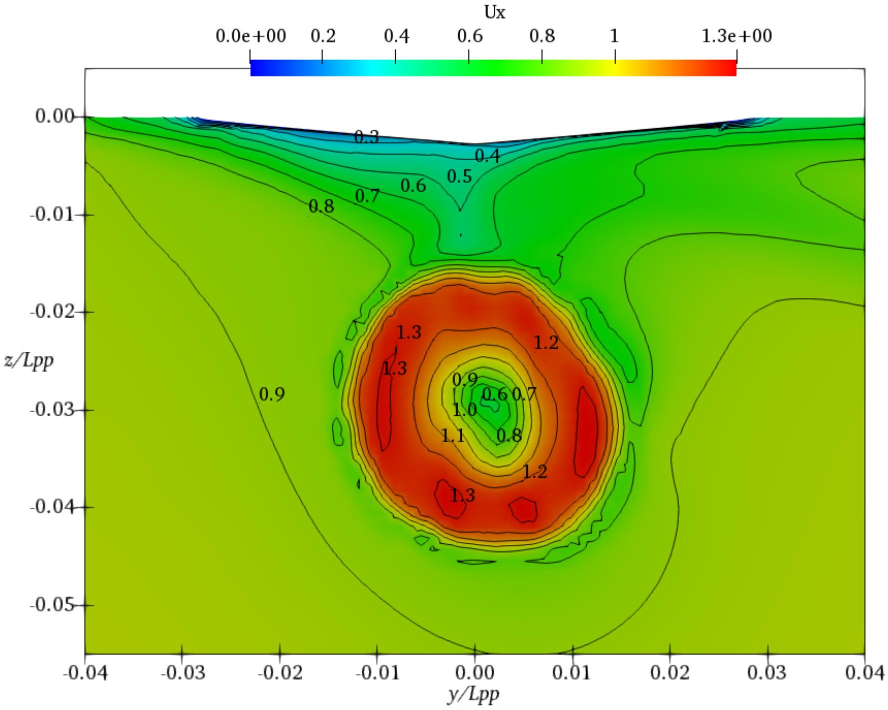

FIGURE 5.25: Axial velocity contours at $x/L_{pp} = 0.9911$ for β= 10 °

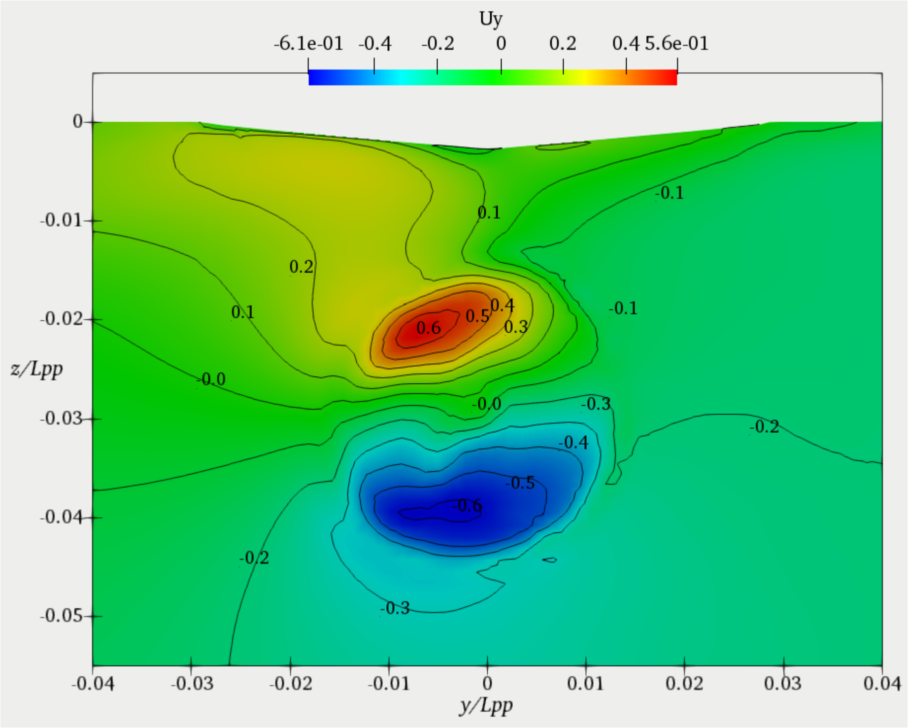

FIGURE 5.26: Local flow contours (U_y) at $x/L_{pp} = 0.9911$ for β= -10 °

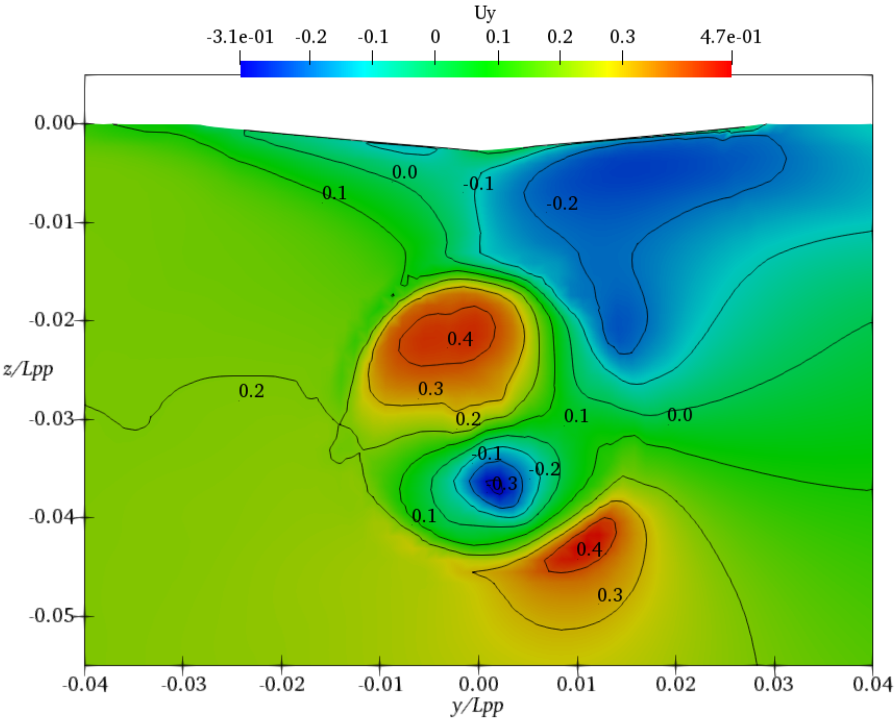

FIGURE 5.27: Local flow contours (U_y) at $x/L_{pp} = 0.9911$ for β= 10 °

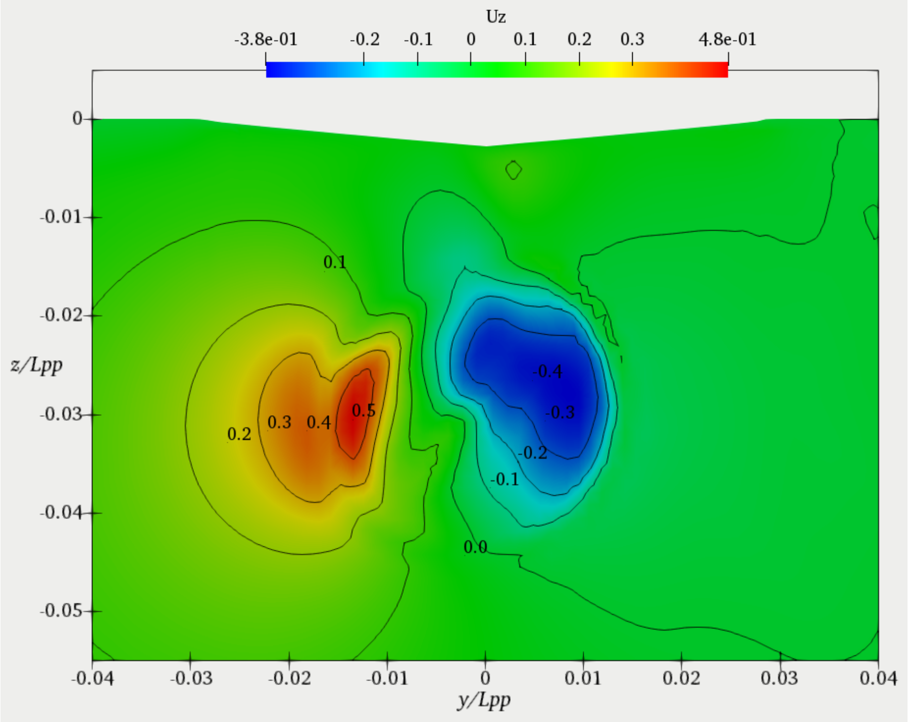

FIGURE 5.28: Local flow contours (U_z) at $x/L_{pp} = 0.9911$ for β= -10 °

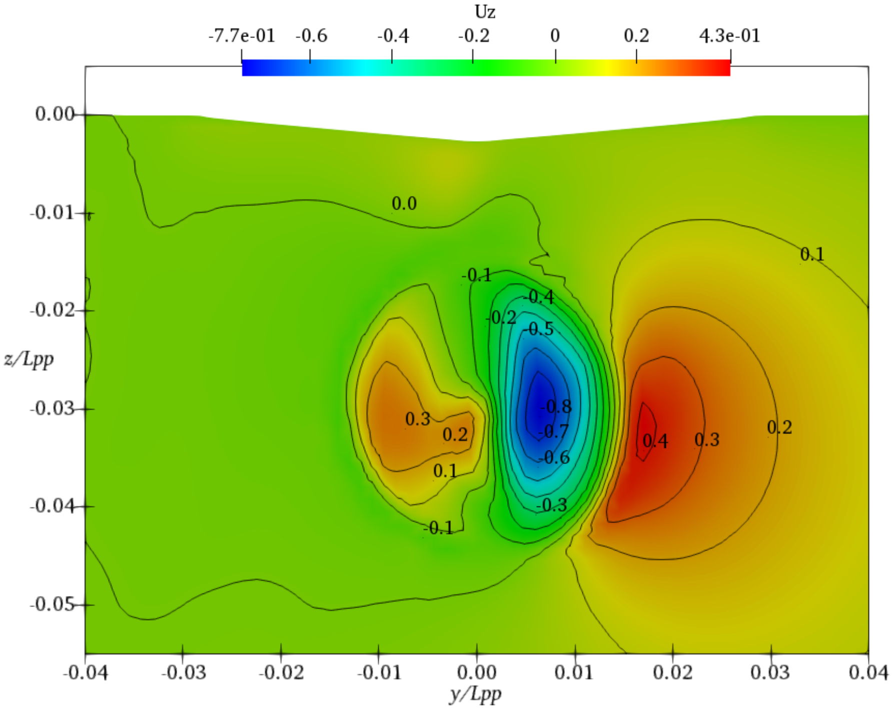

FIGURE 5.29: Local flow contours (U_z) at $x/L_{pp} = 0.9911$ for β= 10 °

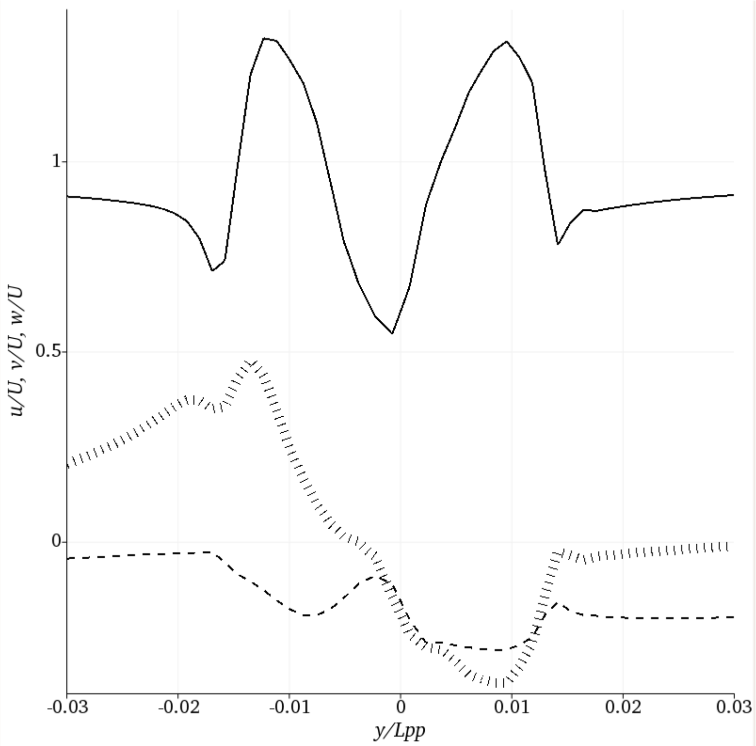

FIGURE 5.30: Velocity distribution downstream at propeller plane (x/L_{pp} =0.9911) at z/L_{pp} = - 0.03 for β= -10 °

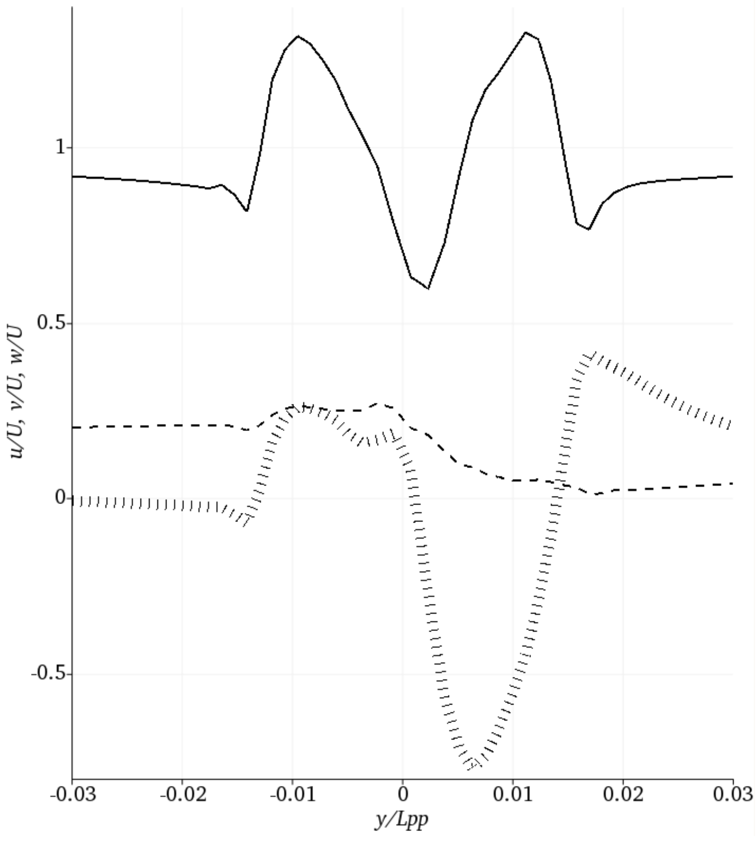

FIGURE 5.31: Velocity distribution downstream at propeller plane (x/L_{pp} =0.9911) at z/L_{pp} = - 0.03 for β= 10 °

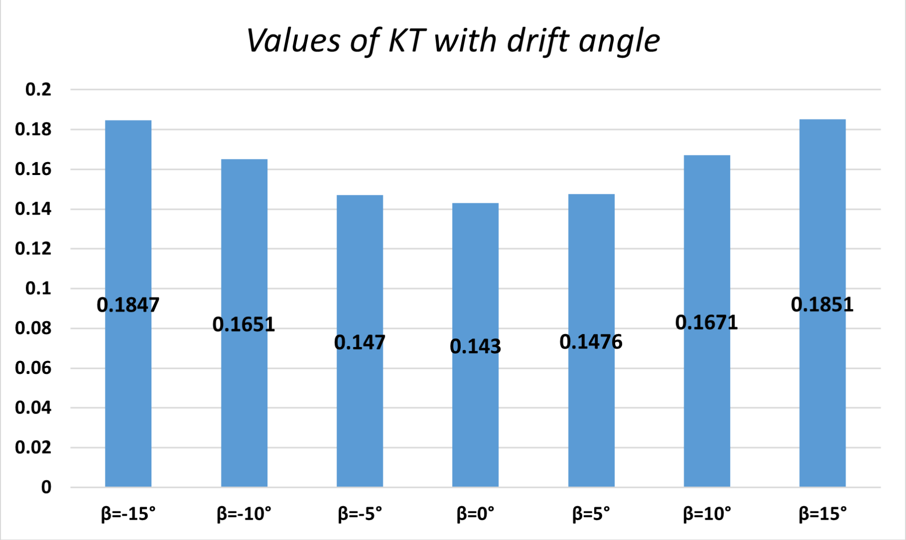

FIGURE 5.32: Propeller thrust coefficients with different angles of drift

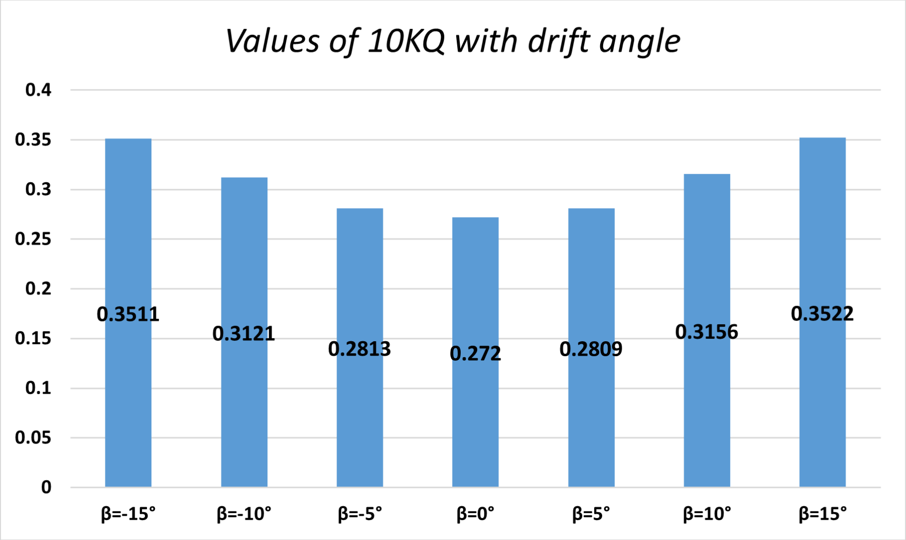

FIGURE 5.33: Propeller torque coefficients with different angles of drift

The propeller thrust and torque coefficients of the self-propulsion test for each drift angle are shown in Figures 5.32 and 5.33. It is clear that as the magnitude of the drift angle increases, both the thrust and torque also increase, which is corresponding to the variation of the total resistance encountered by KCS in static drift conditions, as shown in Table 5.6. However, even though the same magnitude of drift angle is applied, the sign of drift also influences the self-propulsion parameters. Positive drift angles tend to yield higher values of K_T and K_Q than the equivalent magnitude of negative drift cases. This is because more pressure resistance is experienced by the KCS when the positive drift angle is applied; therefore the propeller needs to generate more thrust to balance the extra resistance.

5.3 Influence of drift angle on hull-propeller-rudder interaction

Section 5.2 details how the drift angle affects the hull-propeller interaction in calm water conditions with numerical analysis of global and local resistance and self-propulsion characteristics, mainly including resistance, lateral force, yaw moment, self-propulsion parameters, and velocity profiles downstream of the propeller plane. To truly predict the performance of a fully appended ship during a manoeuvre, the accurate estimation of rudder forces, when ships operate at an angle of drift, is essential. Meanwhile, the interaction between the forces and moments yielded on the hull and propeller upstream of the rudder can significantly affect rudder forces (Badoe et al. 2015). Therefore, this section will include the action of KCS's rudder based on the understanding of the previous section. The self-propelled KCS is simulated at static drift angles combined with a series of rudder angles. Most of the numerical setups are the same as in section 5.2. Still, there are some differences in mesh generation due to the inclusion of a rudder and also, in simulation conditions, because of the applications of a series of rudder angles. The following sections will demonstrate details of mesh and simulation conditions of the hull-propeller-rudder interaction study.

5.3.1 Simulation conditions and mesh

Two different values of drift angles are chosen: β = 0 °and β = -7.5 °. Seven different rudder angles are applied to every drift case: -10 °, -7.5 °, -5 °, 0 °, 5 °, 7.5 °and 10 °. The RANS equations are solved iteratively for each case by adopting the SIMPLE algorithm. The first 1000 iterations are carried out for the resistance test (the hull with the rudder). This yields the towed resistance of the KCS hull with the rudder, which also provides a reference to find the KCS's self-propulsion point. The resistance test also initializes the flow field for the following self-propulsion test. When the resistance test is completed, another 1000 iterations are conducted with the BEMt propeller model switched on. This generates self-propelled KCS parameters. In addition, three sets of fixed RPM tests are performed for all cases.

TABLE 5.8: Main Particulars of KCS rudder

Parameter	Model Scale	Full Scale
Type	All movable rudder	Semi-balanced horn rudder
S of rudder (m^2)	0.1152	115
Lat. area (m^2)	0.0545	54.45

In terms of mesh generation, the same procedure is adopted for studying the hull-propeller-rudder interaction, as explained in section 5.2.4. In addition, another mesh refinement step is executed to refine the KCS rudder surface. The main particulars of the adopted KCS rudder are listed in Table 5.8. Instead of using a semi-balanced horn rudder, the type of all-movable rudder is chosen for this section's simulation. This means that the rudder skeg and blade are fixed together and will rotate together upon application of a non-zero rudder angle. In comparison, for the semi-balanced horn rudder of KCS, the rudder skeg is fixed with the hull, and only the rudder blade is movable. The semi-balanced horn rudder will be applied in the simulation of later chapters. Compared to the KCS hull surface refinement, three higher levels' refinements are conducted for the KCS's rudder, which is realized through the snappyHexMesh utility. The grid distribution around the -7.5 °drift KCS with 0 °rudder angle is shown in Figure 5.34. The total mesh sizes for β = 0 °drift and β = -7.5 °drift KCS are approximately 7.2M and 11.7M respectively. Due to the application of different angles of the rudder, each case's mesh size is slightly different.

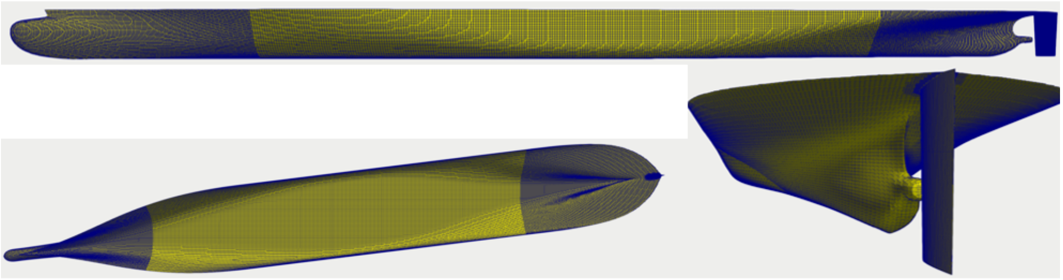

FIGURE 5.34: Mesh distribution around -7.5 °drift KCS with 0 °rudder angle (side, top, rear views)

5.3.2 Results and discussion

5.3.2.1 Forces and moments

As presented in Figure 5.35, when there is no drift angle applied (β= 0 °), the total resistance coefficients (C_t) of both the hull and rudder increase with the increment of rudder angle. It is evident that the C_t lines of resistance and self-propulsion tests are almost axisymmetric around the zero rudder angle (β_r =0 °). On the other hand, when the KCS is operating at a -7.5 °drift angle, increasing the rudder angle from -10° to +10° results in a consistent decrease in the total resistance. The variation in C_t is more noticeable during the self-propulsion test than during resistance tests under the two different drift scenarios.

Non-dimensionalized lateral force (F_y')and yaw moment (M_z') on the bare hull are shown in Figure 5.36 and Figure 5.37 respectively. It is observed that for both drift scenarios, the variations in the hull side force and yaw moment are nearly linear as the rudder angle is adjusted between -10 °and 10 °. The plots of hull side force and yaw moment almost coincide with each other for resistance and self-propulsion scenarios when no drift angle is present. In comparison, in -7.5 °drift cases, the hull's F_y' is slightly higher in the self-propulsion tests compared to the resistance tests, while this variation trend is reversed in hull's $M_z^{'}$ for the corresponding rudder angles.

The drift angle influence on rudder forces (drag and lift) is shown in Figure 5.38 and Figure 5.39. For drift angle β= 0 °, the rudder drag is almost axisymmetric around β_r= 0 °for resistance and self-propulsion tests. In comparison, the rudder drag in the self-propulsion test is higher than that in the resistance test because the presence of the propeller accelerates the fluid passing through the rudder. However, when the drift angle -7.5 °is applied, the rudder drag of the resistance test is higher than that of zero drift KCS for all rudder angles. For self-propulsion tests, the rudder drag varies along with different rudder angles, and the rudder drag is not symmetric anymore due to the unidirectional rotation of the propeller. Meanwhile, as the propeller operates at a much higher rate in the self-propulsion test compared to the fixed RPM test, which leads to a lower value of J, and subsequently higher thrust loading, therefore it is more likely to generate positive thrust on the rudder, which can be observed between β_r=-5 °and β_r=0 °from Figure 5.38. The rudder lift varies almost linearly with the changes in rudder angle for both resistance and self-propulsion tests of both drift scenarios. The influence of the applied -7.5 °drift angle leads to a downward shift of the lift curve for both the resistance and self-propulsion tests, but the lift cure slope does not change significantly.

The resistance coefficient variation with the rudder angles of three fixed RPM tests is shown in Figure 5.40. The fixed RPM values of 1900, 2400, and 3000 were selected as 1900 and 2400 RPM are close to the RPM values at the self-propulsion point when the drift angle is 0° and -7.5°, respectively. Additionally, 3000 RPM represents a 25 % increase over 2400 RPM. Overall, as the RPM value increases, there is a corresponding increase in C_t for both drifting conditions. In the zero drift scenario, the KCS's resistance values for +β_r and -β_r are similar, and this trend is also demonstrated in Figure 5.35. In terms of -7.5 °cases, the resistance variation is more significant when the rudder angle varies from -10 °to +10 °. The C_t value at β_r=-10 °is approximately 1.45 times of that at β_r=10 °when RPM=3000. This indicates that the drag is more sensitive to the rudder angle changes when the KCS sails at a non-zero drift angle.

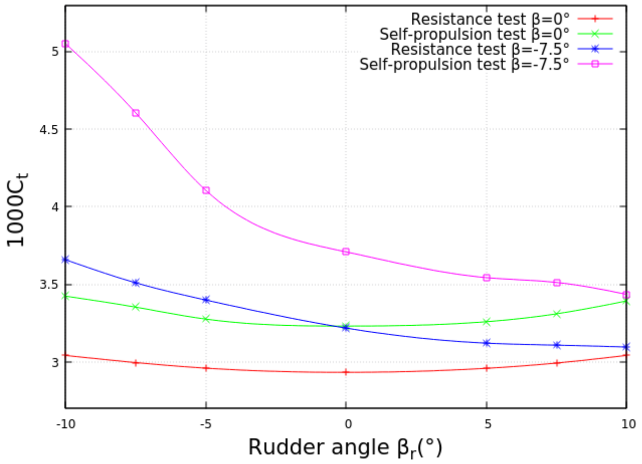

FIGURE 5.35: Drift angle and rudder angle influence on the total resistance coefficients

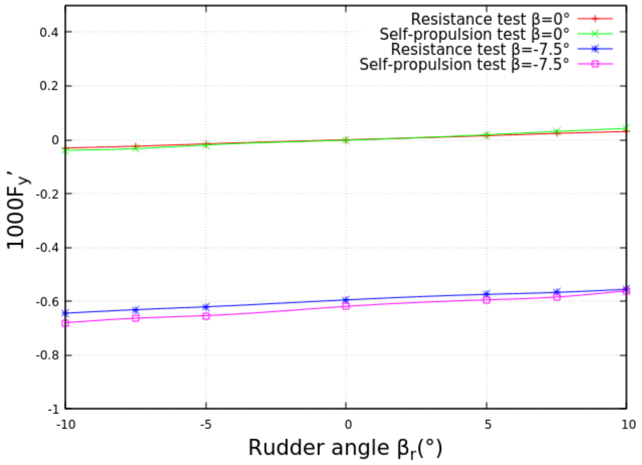

FIGURE 5.36: Drift angle and rudder angle influence on the side force of hull

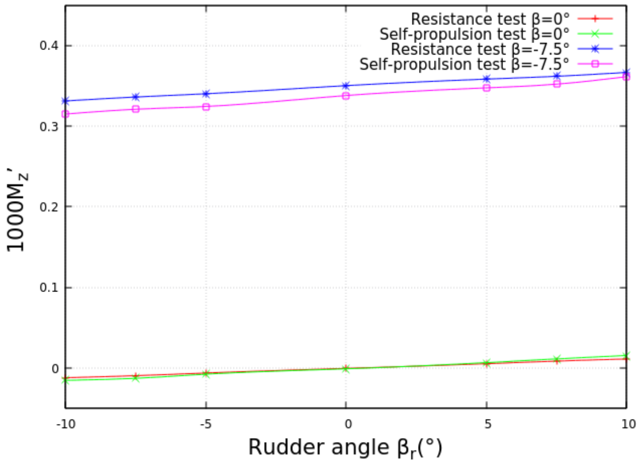

FIGURE 5.37: Drift angle and rudder angle influence on the yaw moment of hull

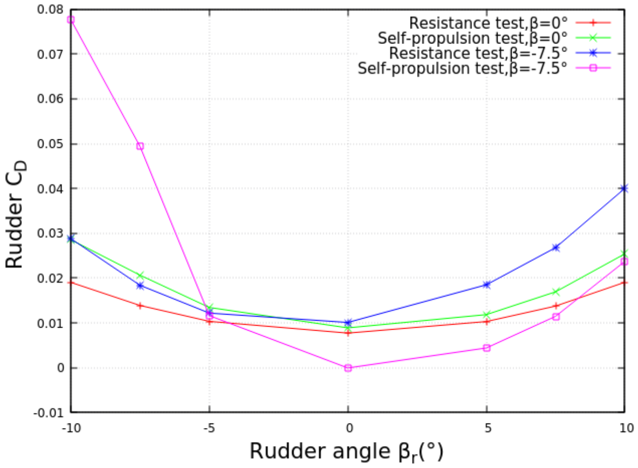

FIGURE 5.38: Drift angle and rudder angle influence on the rudder drag coefficients

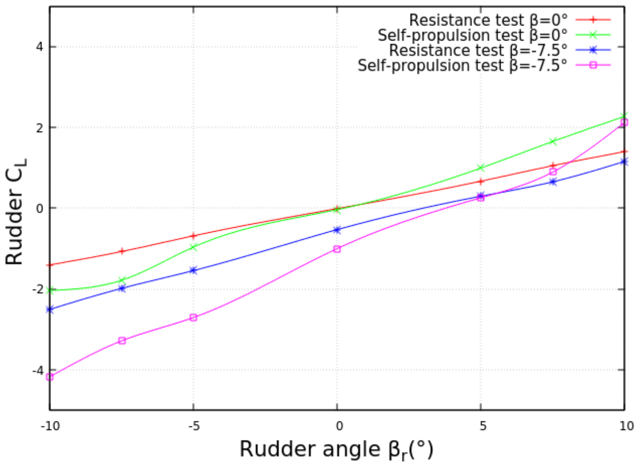

FIGURE 5.39: Drift angle and rudder angle influence on the rudder lift coefficients

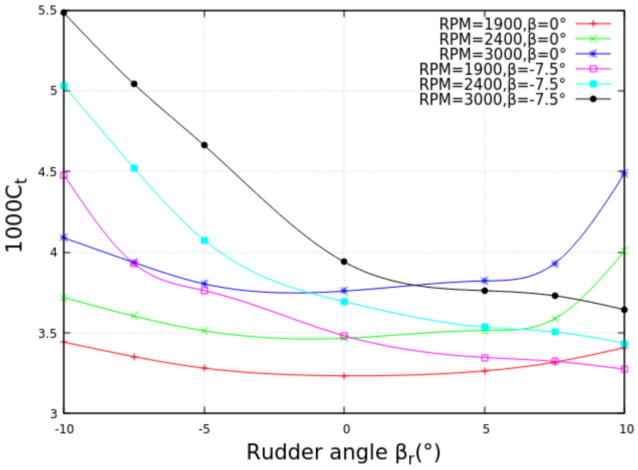

FIGURE 5.40: Drift angle and rudder angle influence on the total drag coefficients of fixed RPM test

5.3.2.2 Propulsive performance

The self-propulsion and fixed RPM cases' propulsive characteristics are presented in accordance with the ITTC 1978 performance prediction approach. The augment delta is defined as the following equation:

$$\textbf{Augment delta (\%)} = \frac{A_n - A_0}{A_0} \times 100 \tag{5.3}$$

Where A_0 is the variable value for 0 °rudder in each scenario, and it is used as a benchmark. A_n is any arbitrary point of variable value, n is the rudder angle annotation and n ranges from -10 °to +10 °. The augment delta can be positive and negative, which means increment and decrement respectively compared to the benchmarking point.

Figure 5.41 depicts the variation of the propeller rotation rate (rps) n during the self-propulsion tests, where the augment delta is negative for all rudder angles when the drift angle is 0 °and the plot is axisymmetric around the β_r =0 °line. A noticeable reduction in the propeller rotation rate is observed in rudder angles that are farther away from 0°. When -7.5 °drift is applied to the KCS, the augment delta is positive for the negative rudder angles while it is negative for positive rudder angles. The maximum difference is found between -5 °rudder angle and +10 °rudder angle, approximately 2 %.

The propeller thrust and torque coefficients' augment deltas for the self-propulsion tests are presented in Figure 5.42. At a zero drift angle of the hull, the maximum thrust and torque can be observed at a rudder angle of β_r =0 °. The remaining scenarios with non-zero rudder angles exhibit a similar trend for both thrust and torque: $K_{T_{-\beta_r}}$ = $K_{T_{+\beta_r}}$ and $K_{Q_{-\beta_r}}$ = $K_{Q_{+\beta_r}}$. However, in cases of -7.5 °drift, the thrust coefficient augment delta is negative for positive β_r while it is positive for negative β_r. In comparison, almost all torque coefficients have positive augment delta for all non-zero rudder angles except for β_r= 7.5 °, whose augment delta is about -0.1 %.

In addition, Figure 5.43 shows the plot of wake fraction and thrust deduction augment delta for all rudder angles. The wake fraction exhibits similar variation for both 0 °and -7.5 °: axisymmetric about β_r= 0 °, and it can be seen that the rudder angle effect does not change wake fraction significantly, within 3 % but wake fraction augment delta is negative for all cases. In terms of thrust deduction, the increment delta is all negative for 0 °drift cases. In contrast, the augment delta is positive for positive rudder angles and negative for negative rudder angles when -7.5 °angle of drift is applied. The maximum decrement delta is about 20 % at -10 °rudder angle.

For fixed RPM tests, the variation plots of thrust and torque with different rudder angles are shown in Figures 5.44 and 5.45. When zero drift angle is applied, both thrust and torque coefficients have a positive augment for all rudder angles in the fixed RPM

1900 and 2400 tests. The maximum increment occurs for RPM=1900 at β_r= -10 °while for RPM=2400 at β_r= +10 °. For cases of RPM=3000, both plots of thrust and torque exhibit central symmetry. The coefficients' augment deltas of -β_r and +β_r almost have the same magnitude but with opposite signs. The largest augment delta points occur when β_r = -5 °and +5 °. For fixed RPM tests with -7.5 °drift, all thrust and torque coefficients have positive increments in addition to -5 °and -7.5 °rudder angles when RPM is set to 1900. The largest increment deltas are found for thrust at β_r =-10 °while for torque at β_r= +10 °.

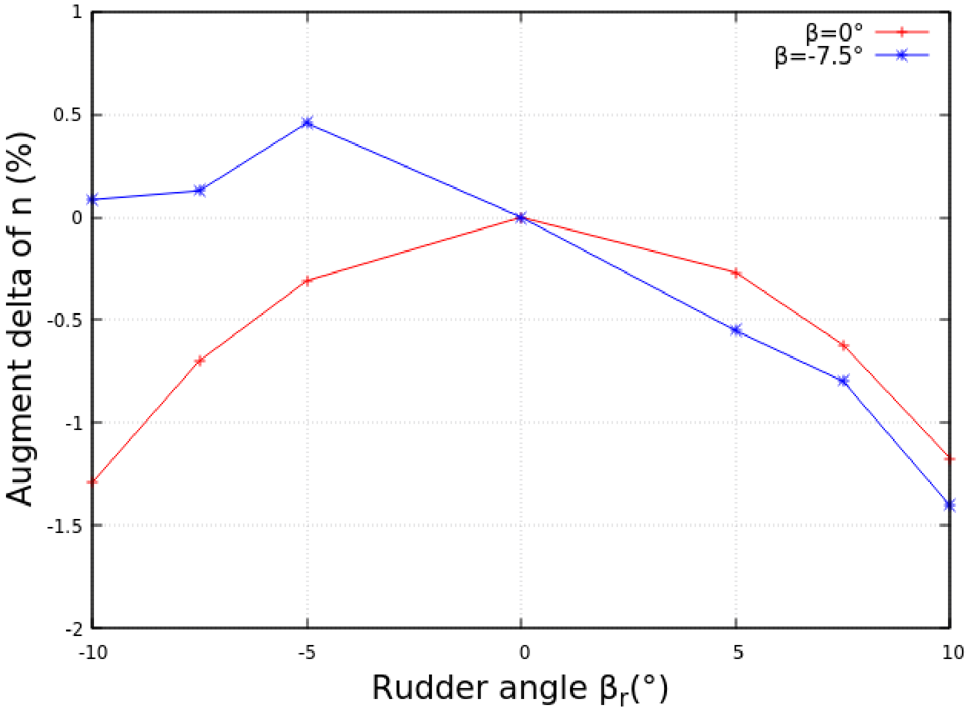

FIGURE 5.41: Drift angle and rudder angle influence on the propeller rotation

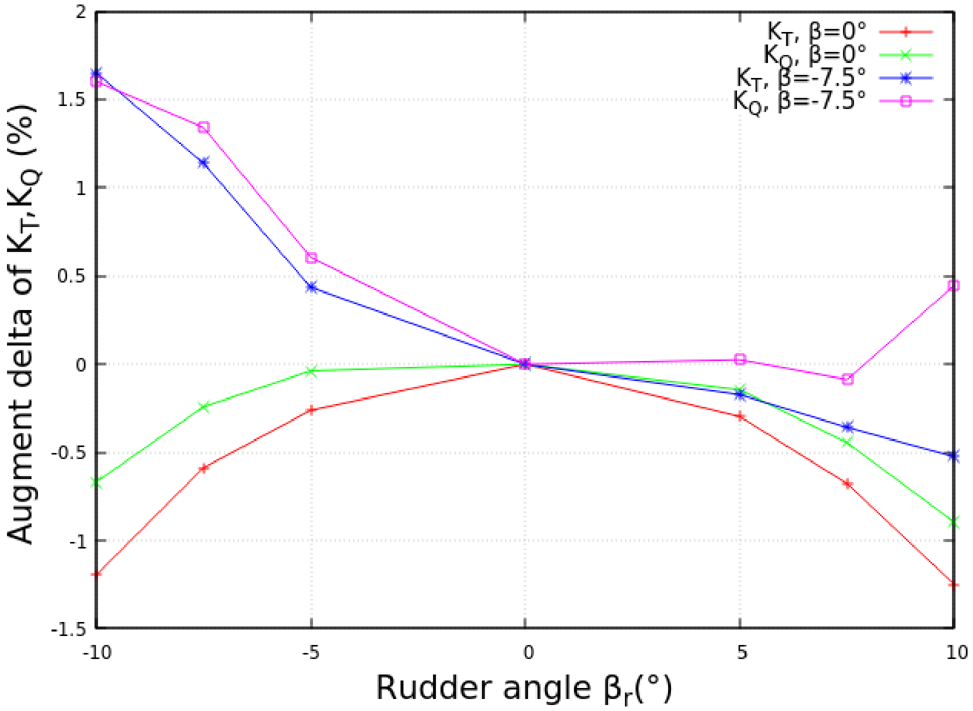

FIGURE 5.42: Drift angle and rudder angle influence on thrust and torque

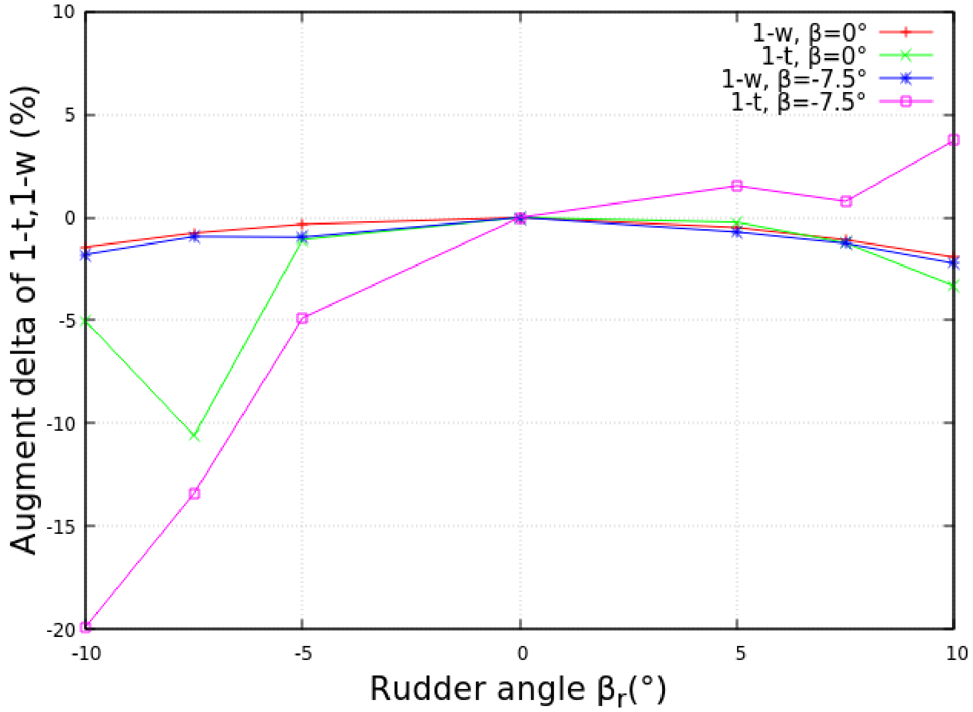

FIGURE 5.43: Drift angle and rudder angle influence on the wake fraction and thrust deduction

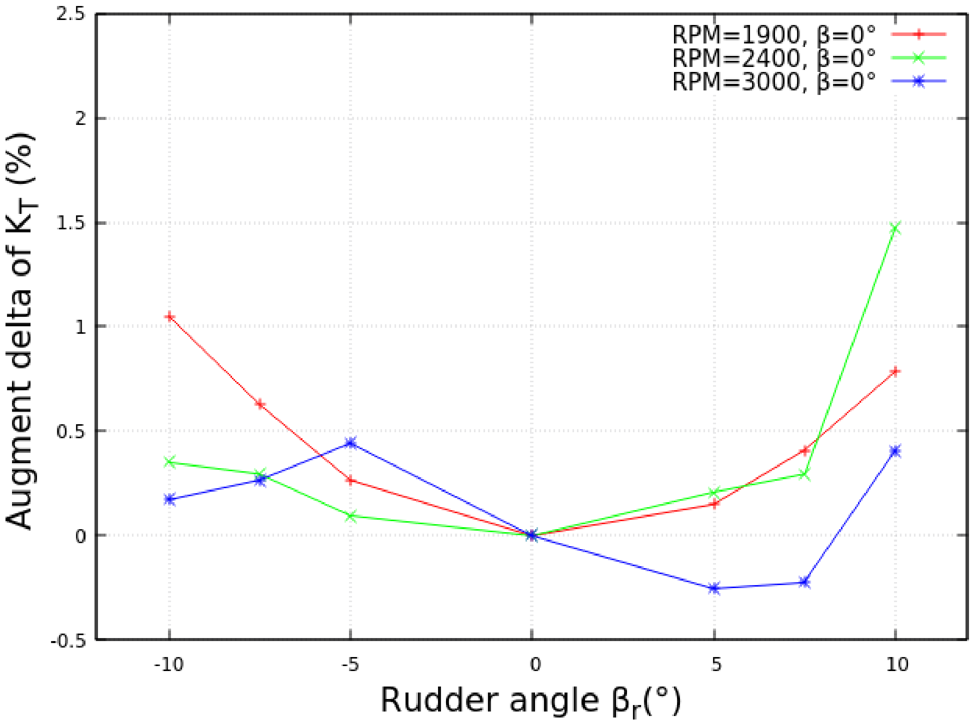

(A) Drift angle β=0 °

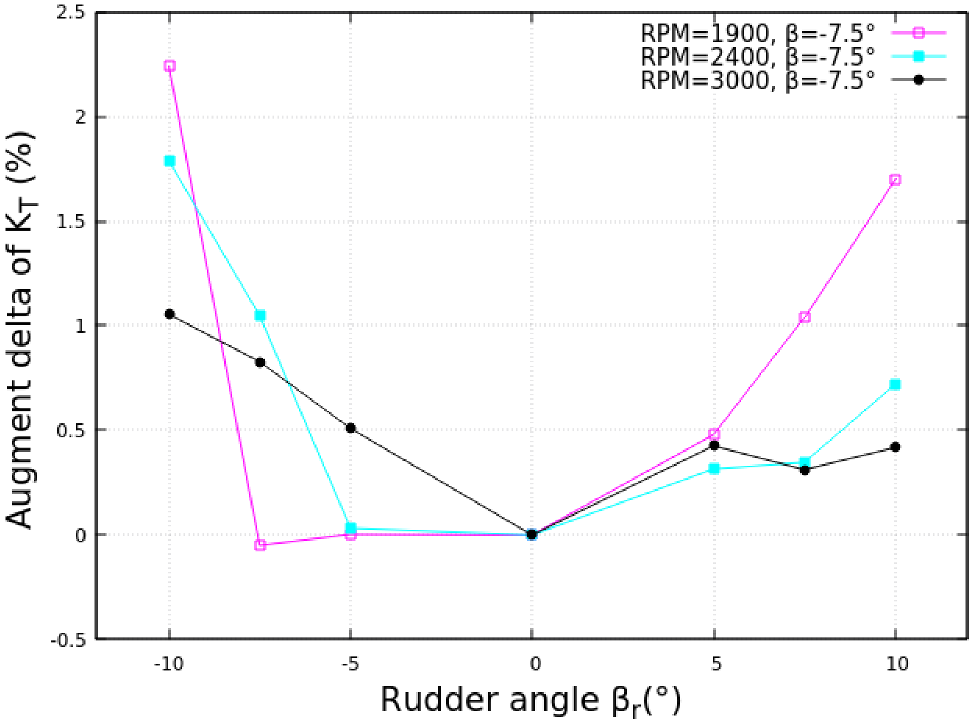

(B) Drift angle β=-7.5 °

FIGURE 5.44: Drift angle and rudder angle influence on the propeller thrust of fixed RPM tests

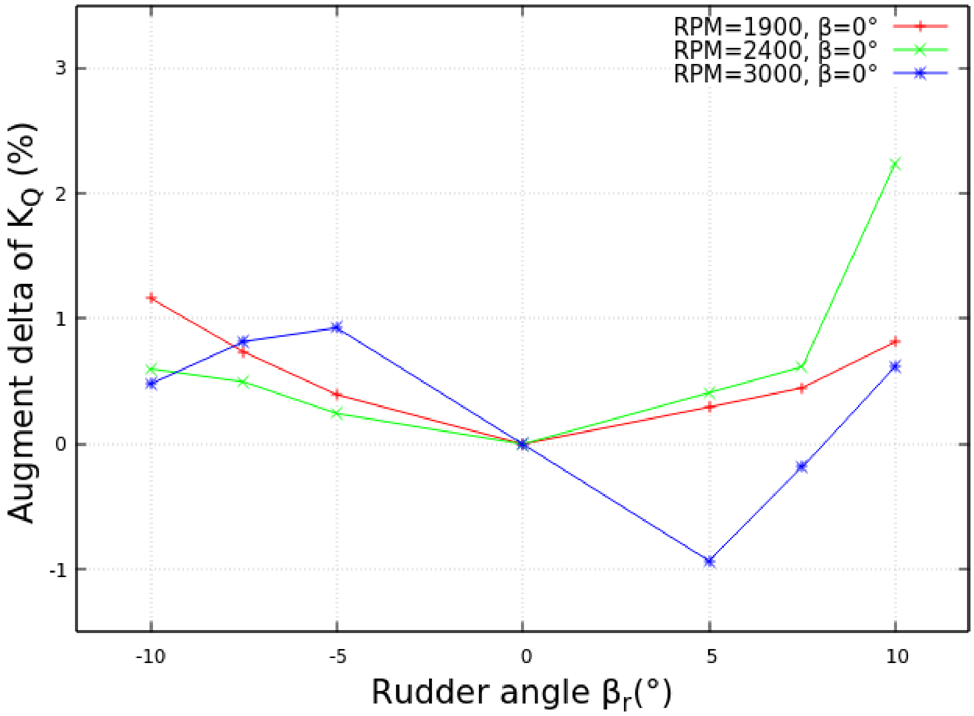

(A) Drift angle β=0 °

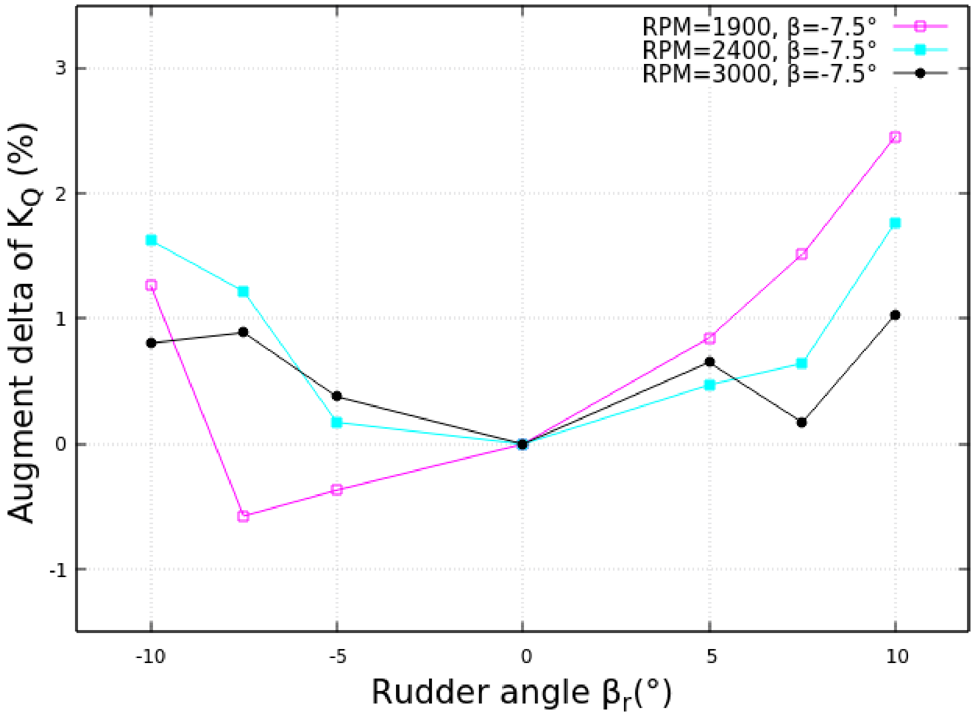

(B) Drift angle β=-7.5 °

FIGURE 5.45: Drift angle and rudder angle influence on the propeller torque of fixed RPM tests

5.3.2.3 Velocity profiles

Figures 5.46 - 5.48 present the local axial velocity (U_x) contours behind the propeller plane of the self-propelled zero drift KCS for three different rudder angles: 0 °,-5 °and -7.5 °. It is evident that the presence of a rudder significantly changes the axial velocity distribution shown in Figure 5.46 compared to Figure 5.14, which has the same simulation conditions but is absent of the rudder. The action of the rudder obstructs and alters the upstream fluid flow into the operating propeller, subsequently influencing the actual velocity distribution on the propeller plane. The moon crescent-like regions can be observed on both sides of the rudder blade shown in Figure 5.46, and the maximum value of U_x is approximately 1.4, which is higher than that in the case without the rudder (U_{xmax}=1.1). The region of U_{xmax} is close to the right side of the rudder blade surface and located at the approximately middle position of the rudder span. When the rudder angle of -5 °is applied, the velocity contour is altered but not significantly and the U_{xmax} is around 1.3, located at the left side of the blade, bottom of span. The moon crescent-like region at the left part of the propeller plane disappears when the rudder angle reaches -7.5 °, but the overall axial velocity on the propeller plane is higher than previous two cases, which indicates the propeller operates at a higher revolution rate to propel the ship. This corresponds to the green line of Figure 5.35, showing the resistance encountered by the KCS increases with the increment of rudder angle magnitude.

In addition, velocity profiles downstream of the propeller plane x/L_{pp}=0.9911 at Z/L_{pp}=-0.03 for the self-propelled zero drift KCS are presented for three different rudder angles. All plots are not continuous around the y/L_{pp}=0 due to the presence of the rudder. The axial velocities (u/U) variation is shown in Figure 5.49. There is no big difference between the three cases when the y/L_{pp} is in the range of -0.03 to -0.015 and 0.015 to 0.03. However, in the range of -0.015 to -0.005, u/U plots of β_r = -5 °and 0 °are almost the same while β_r = -7.5 °case shows an evident increment and the maximum point occurs at y/L_{pp}=-0.01. A similar trend can also be observed for the range 0.005 to 0.015. It is interesting to note that the value of u/U increases with the rudder angle increment when y/L_{pp} is from -0.005 to 0, corresponding to the left side of the rudder blade surface. The tangential velocities (v/U) are presented in Figure 5.50 and the main differences are located in the range -0.01 to 0.01 of y/L_{pp}. The effect of the rudder angle results in a downward shift of tangential velocity plots: the larger magnitude of the rudder angle, the farther the downward shift. In terms of the local velocity in z-direction (w/U) presented in Figure 5.51, the overall trend is similar for all rudder angles, and the plots of 0 °and -5 °agree with each other with minor differences around y/L_{pp} =0. In comparison, the -7.5 °rudder angle leads to the most significant value range, approximately -0.3 to +0.7.

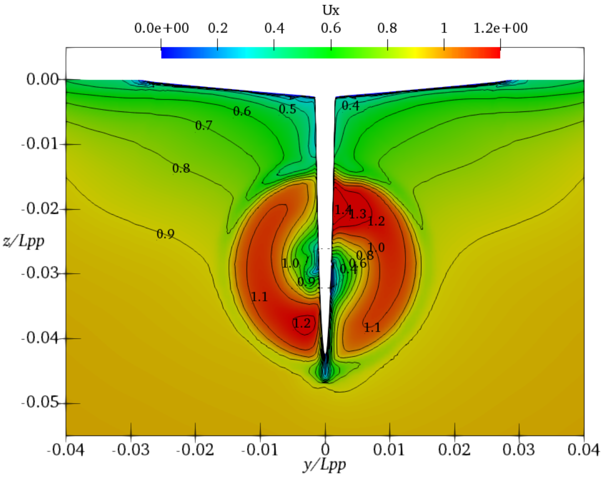

FIGURE 5.46: Local axial flow U_x at x/L_{pp}=0.9911 at zero drift with 0 °rudder angle

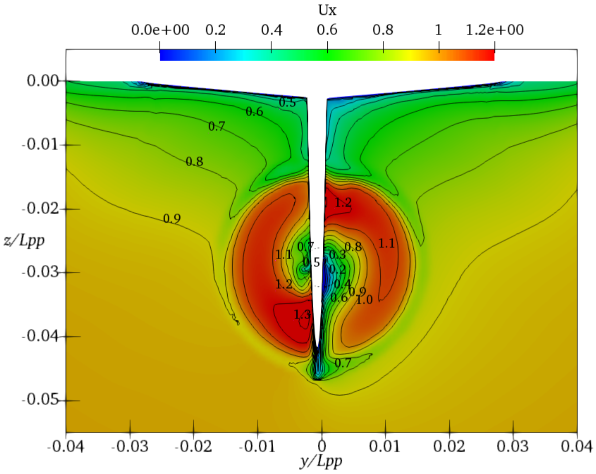

FIGURE 5.47: Local axial flow U_x at x/L_{pp}=0.9911 at zero drift with -5 °rudder angle

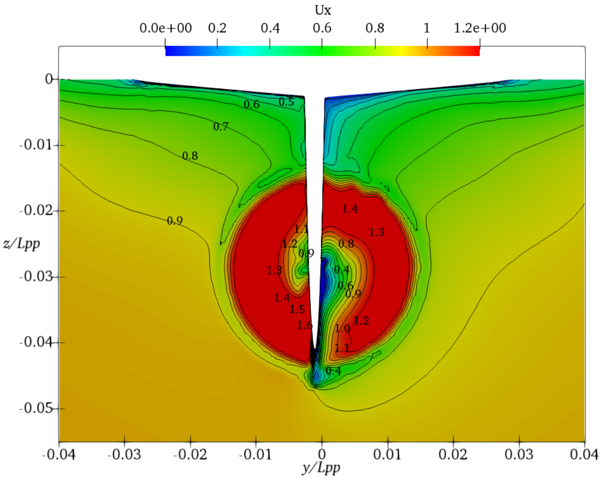

FIGURE 5.48: Local axial flow U_x at x/L_{pp}=0.9911 at zero drift with -7.5 °rudder angle

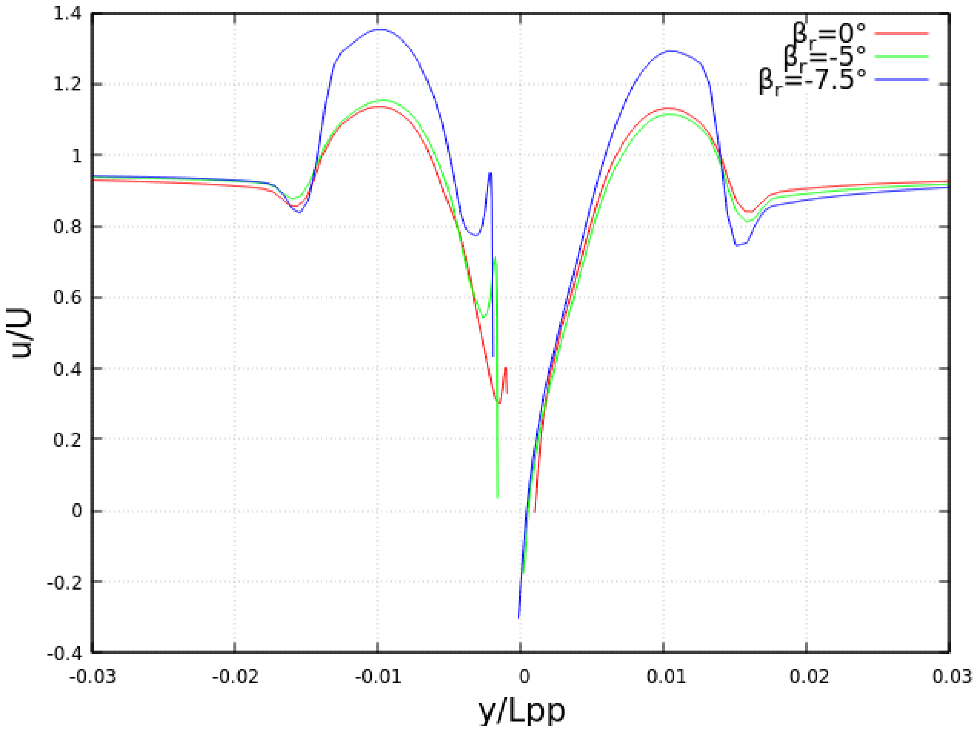

FIGURE 5.49: Local velocity u/U downstream of the propeller plane x/L_{pp}=0.9911 at Z/L_{pp}=-0.03, β = 0 °for three rudder angles

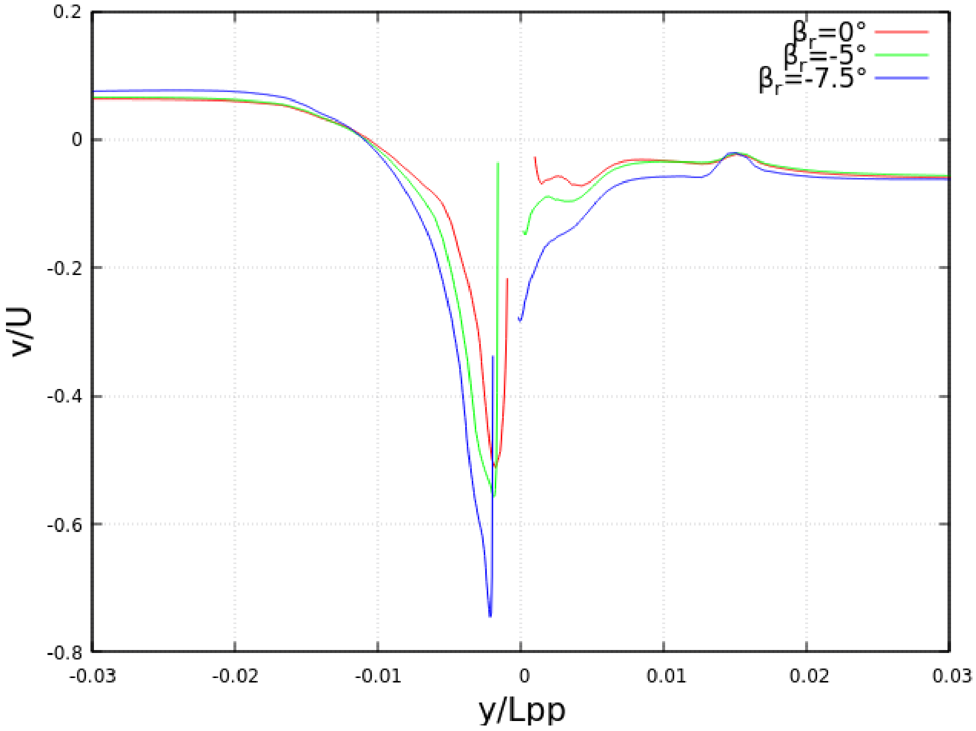

FIGURE 5.50: Local velocity v/U downstream of the propeller plane x/L_{pp}=0.9911 at Z/L_{pp}=-0.03, β = 0 °for three rudder angles

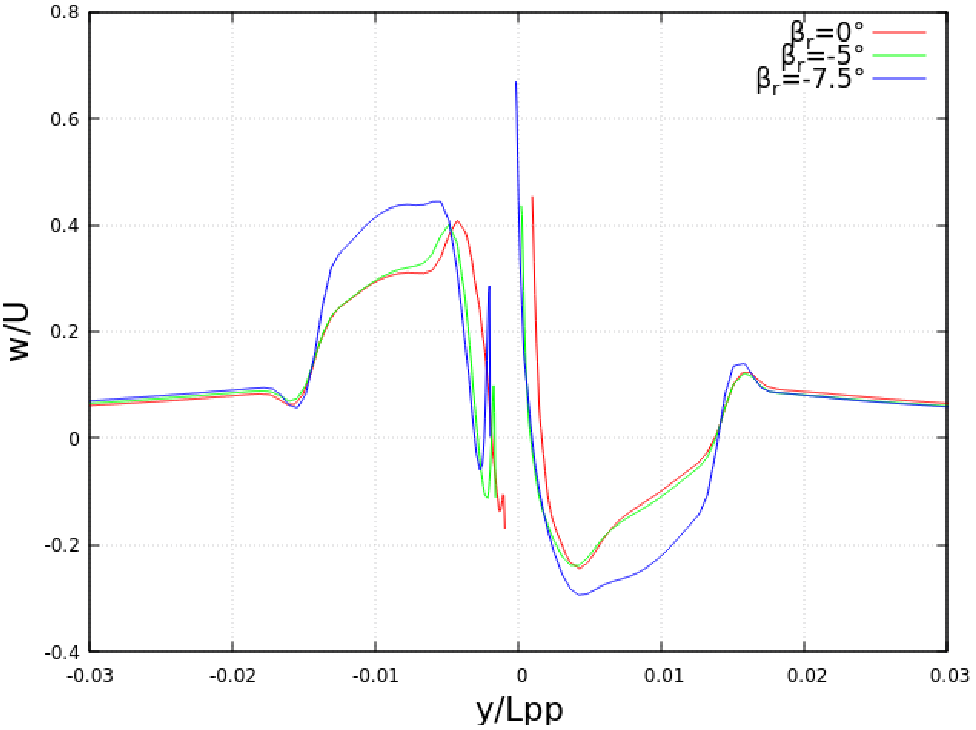

FIGURE 5.51: Local velocity w/U downstream of the propeller plane x/L_{pp}=0.9911 at Z/L_{pp}=-0.03, β = 0 °for three rudder angles

5.4 Chapter summary

This chapter investigates the drift angle effect on the hull propeller rudder interaction of the benchmark KRISO Container Ship (KCS) using the RANS simulations of double body flow in calm water conditions. The computed results include the resistance, lateral force, yaw moment, velocity contours and self-propulsion coefficients in drifting scenarios. In general, the results obtained in this study show good agreement with EFD data from the 2015 Tokyo CFD workshop and numerical results of other institutions, particularly the lateral force, yaw moment and self-propulsion characteristics. However, the absence of free surface modelling results in an underestimation of the KCS longitudinal force prediction, which is consistent with the findings of Jiang et al. (2022).

In Section 5.2, a comprehensive array of drift angles is systematically applied to the KCS in the absence of a rudder. The detailed resistance components of both resistance and self-propulsion tests are presented, indicating the total drag experienced by KCS increases with the increment of drift angle magnitude. Besides, the side force and yaw moment predictions for the KCS across various drift angles exhibit an almost linear fluctuation pattern, demonstrating good consistency with the EFD and CFD results of other research institutions. A comparison of the computed velocity profiles and propeller force coefficients of straight-ahead KCS is made with experiments, and four numerical submissions of the Tokyo workshop and overall satisfactory alignment suggests that the double body methodology is able to provide a relatively accurate prediction of local flow characteristics and provide a reasonable estimation of the hull-propeller interaction at an affordable computational expense.

Section 5.3 involves the action of the all-movable rudder in a double body simulation based on the previous section's experience. The influence of varying rudder angles on hull and propeller performance is presented, including longitudinal, lateral forces on the hull, propeller thrust, torque coefficients and thrust deduction, wake fraction obtained from self-propulsion and fixed rpm tests. The applied drift angle intensifies the variation trend of the above parameters and shifts rudder forces but does not change them totally. In addition, the effect of the rudder angle on the velocity profiles downstream of the propeller plane is shown. It is found that the main differences in wake profiles due to the effect of rudder angles occur near the rudder boundary layer. These need to be accurately captured to estimate the forces on a downstream rudder effectively and the interaction between the propeller and the rudder during ship manoeuvring.

The computed findings presented in this chapter offer a valuable understanding of hull-appendage interplay and facilitate ship manoeuvrability investigations. It is concluded that the method based on an OpenFOAM RANS solver with coupling to Blade Element Momentum theory can predict ship manoeuvring performance in a reasonably accurate and cost-effective way. The capability of the RANS-BEMt propeller modelling approach for capturing hull-propeller-rudder interaction in drifting conditions has been demonstrated. However, the free surface modelling should be included to obtain a more accurate prediction of the hull-propeller-rudder interaction in static drift scenarios.

Chapter 6

The effect of drift on the hull-propeller-rudder interaction

6.1 Introduction

To accurately predict a self-propelled ship's powering and manoeuvring performance in actual sea states, it is essential to have a good understanding of the hydrodynamic interactions between the hull, propeller and rudder and also to model these components with reasonable accuracy. However, this is usually a complicated and challenging task because these interactions involve fluid flow, pressure, and force distributions, which in turn affect the actual hydrodynamic behaviours of these components, manoeuvrability, and the efficiency of the vessel. The complexity of these interactions can be attributed to the following main factors:

- The presence of strong pressure gradients and curvature of the hull, particularly at the stern region of the ship, would lead to flow separation, and it can significantly influence the actual resistance and powering of the ship.
- The operating propeller accelerates the flow ahead of itself, leading to the increase of the shear rate in the boundary layer and the decrease of pressure over the rear of the hull (Molland et al. 2017), which also influences the flow around the upstream hull and the downstream rudder.
- The rudder blocks and diverts the upstream flow into the propeller, changing the thrust and torque developed on the propeller (Badoe 2015). The rudder's movement alters the flow pattern around itself and the hull, further complicating the interactions.

- The nonlinear behaviours of hydrodynamic interactions mean the consequence of interactions cannot be simply determined by analysing each component in isolation or by summing up their individual effects.
- Viscous properties of fluid result in boundary layer development along the hull, propeller and rudder surfaces, leading to drag and flow separation. These viscous effects are difficult to model and capture accurately, adding to the overall complexity.

With the rapid development of computer technology and numerical analysis, studying the complex hull-propeller-rudder interaction is attainable through Computational Fluid Dynamics (CFD) techniques. There are various numerical methods available and the choice of method depends on the specific focus and objectives, available computational resources and the level of accuracy. Although higher fluid dynamics fidelity can be achieved by adopting the higher complexity level of the numerical methods such as fully discretized propeller modelling methods, the overset grid approach for capturing the dynamic motion of the hull, the rudder and etc, the computational cost involved in these methods is extremely high due to the fact that fully unsteady flowfield has to be resolved. Therefore, a more cost-effective approach is still in great demand for studying the self-propelled ship's powering and manoeuvring performance.

The content presented in this chapter adopts the numerical techniques and experience gained from the previous chapter to study the hydrodynamics interactions between the hull, the propeller and the rudder in calm water conditions including the effect of free surface modelling because the results from the Chapter 5 indicate that the wave-making resistance component of the KCS is significant. Three different drift angles combined with a series of rudder angles are applied to the fully appended KCS, representing the quasi-static phases of an actual ship manoeuvre in reality. The semi-balanced horn rudder type is chosen in this chapter. Two different body force models are employed for propeller modelling and a comparison is made for studying the resistance and propulsion capabilities of KCS.

The main focus of this chapter is a detailed analysis of the force and moment prediction of the hull, propeller and rudder in different drift scenarios, which provides a reference for experimental measurements of the hull and appendage forces when the angle of drift is applied, subsequently the ship manoeuvrability assessment. The computed hull longitudinal and transverse forces in straight-ahead and positive drift conditions (β=0 °, +10 °) are validated with the experimental data from the Southampton Boldrewood towing tank. The effect of drift on the hull-propeller-wake interaction is also discussed using thrust deduction and wake fraction, thereby the hull efficiency in all considered scenarios.

6.2 Numerical configurations

The objective of this section is to expound on the numerical setup of fully appended KCS, with specific emphasis on the differences between the present and previous chapters.

6.2.1 Hull and appendages geometry

The KRISO Container Ship (KCS) is again selected as the vessel model, with the KCS geometry conforming to that of the 2015 Toyko CFD workshop (Hino et al. 2020), encompassing the forecastle region, which is not accounted for in the last chapter's simulation due to employment of the double body technique. In addition, the hull geometry is augmented by the inclusion of the propeller hub and cap (the propeller minus the blades), thereby ensuring its congruity with the geometry when the propeller is attached. The geometry of the used KCS is shown in Figure 6.1.

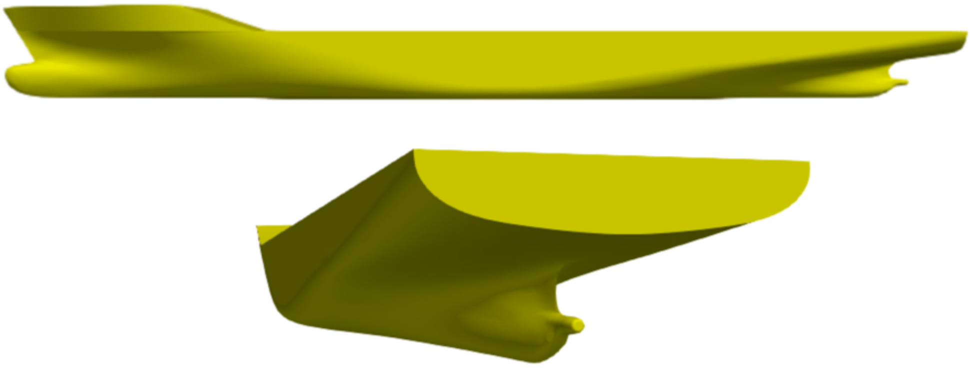

FIGURE 6.1: The geometry of the KCS hull with forecastle and the propeller hub, cap (side, rear views)

In terms of the KCS rudder, the semi-balanced horn rudder configuration is selected, which comprises the rudder blade and the rudder skeg. Notably, the skeg segment is immovably attached to the hull, and only the rudder blade undergoes rotation in response to the application of a non-zero rudder angle. The KCS rudder geometry is presented in Figure 6.2.

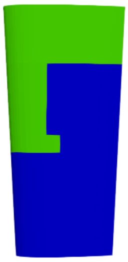

FIGURE 6.2: The geometry of KCS rudder (Green is rudder skeg, blue is rudder blade)

6.2.2 Simulation conditions

Three sets of simulations are carried out on the KCS hull with the rudder considering the effect of the free surface. Three different angles of drift are chosen: β= -10 °, β= 0 °, β= +10 °. For each drift case, a series of static rudder angles are applied. The calm water resistance test is conducted for all cases initially. Subsequently, five sets of fixed RPM tests are performed with RPM values = 600, 720, 900, 1200, and 1500. The specifics of the simulation conditions are presented in detail below.

- KCS at drift angle, β= 0 °, with eleven static rudder angles, β_r= -35 °, -30 °, -20 °, -10 °, -5 °, 0 °, 5 °, 10 °, 20 °, 30 °, 35 °.
- KCS at drift angle, β= -10 °, with seven static rudder angles, β_r= -20 °, -10 °, -5 °, 0 °, 5 °, 10 °, 20 °.
- KCS at drift angle, β= +10 °, with seven static rudder angles, β_r= -20 °, -10 °, -5 °, 0 °, 5 °, 10 °, 20 °.

6.2.3 Computational parameters

The primary distinction between the current and preceding chapters is the incorporation of free surface modelling, achieved through the utilization of the two-phase volume of fluid technique (VOF), as discussed in section 3.5. While Chapter 5 employs steady state double body computations, this chapter conducts transient calculations for all cases utilizing unsteady RANS equations. Specifically, the interFoam and selfPropinterFoam solvers are used for the resistance test and self-propulsion or fixed RPM tests, respectively. Table 6.1 presents the main computational parameters adopted in Chapters 5 and 6.

TABLE 6.1: Computational parameters

Parameter	Steady double body	Transient VOF
Computing	S2 Viglen Medium Tower Workstation	Iridis5 Linux Cluster
Mesh type	Unstructured hexahedral	Unstructured hexahedral
Fluid flow modelling equations	steady RANS	unsteady RANS
Pressure-velocity coupling	SIMPLE	PIMPLE
Solvers	simpleFoam, selfPropsimpleFoam	interFoam, selfPropinterFoam
Ship motion	Fixed	free to heave and pitch
Rudder type	All movable	Semi-balanced horn
Propeller modeling	BEMt	BEMt and Yamazaki

For all transient VOF simulations, the Iridis5 Linux cluster is selected due to the considerable computational expense incurred by the inclusion of free surface modelling when compared to double-body calculations. Indeed, it has been reported that free surface simulations require a computational time that is typically 100-1000 times longer than that of double-body simulations (Turnock et al. 2008).

6.2.4 Model domain and boundary conditions

The computational domain for numerically simulating the KCS hull with rudder is established according to the CFD application guidelines set forth by the ITTC (ITTC 2014). The inlet boundary is situated at 1.0 L_{pp} forward of KCS FP, and the outlet boundary is positioned at 3.0 L_{pp} aft of the KCS AP. To mitigate the wall's impact on the numerical simulation, both side boundaries are established 1.5 L_{pp} apart from the centre of the KCS hull. The bottom boundary is positioned 1.5 L_{pp} below from the free surface, whereas the top boundary is positioned 1.0 L_{pp} above the free surface.

In addition, the KCS rudder is modelled into two distinct segments, namely the rudder skeg and the rudder blade components. In VOF simulation, the top boundary is referred to as the atmosphere. Its properties differ from those in double body simulations, as detailed in the boundary conditions section. As a result, Table 6.2 presents the main boundary conditions specific to VOF simulation.

TABLE 6.2: Boundary conditions for VOF simulations

-	Inlet	Outlet	Atmosphere	Hull/Rudder
U	FV	outletPhaseMeanVelocity	pressureInletOutletVelocity	movingWallVelocity
p	fixedFluxPressure	ZG	totalPressure	fixedFluxPressure
k	FV	inletOutlet	inletOutlet	kqRWallFunction
ω	FV	inletOutlet	inletOutlet	omegaWallFunction
ν_t	FV	ZG	ZG	nutkRoughWallFunction
Fv	FV	FV	FV	FV
alpha	FV	variableHeightFlowRate	inletOutlet	ZG

As shown in Table 6.2, in the first column, Fv denotes volume force, which is utilized in the computation of propeller forces in body force models. FV refers to fixed value, and ZG refers to zero gradient. It is noteworthy that the sides and bottom are not presented in this table since all parameters are treated as symmetry planes and are thus analogous to those employed in the double body simulation.

6.2.5 Grid generation

In a similar manner to the double-body mesh generation, the mesh utilities blockMesh and snappyHexMesh are utilized for grid generation in VOF cases. Furthermore, the topoSet and refineMesh utilities from OpenFOAM v7 are incorporated for local mesh refinement in the vicinity of the hull and rudder. Four refinement boxes are created to facilitate the local mesh refinement, as shown in Figure 6.3, encompassing the entirety of the KCS hull and rudder. The grid generation process is outlined as follows:

- The generation of the computational domain mesh comprised of hexahedral structured mesh and the definition and refinement of the free surface region is achieved by implementing the blockMesh utility.
- Four refinement boxes are employed to gradually refine the grid to enhance the resolution of the structured mesh surrounding the KCS hull and rudder. Specifically, the cells within these boxes are partitioned in both horizontal and vertical directions. In order to ensure smooth transitions between regions with varying mesh densities, a gradual reduction of the refinement zone is implemented during each level of refinement, which can be seen in Figure 6.3.
- After performing mesh refinement with the aforementioned four boxes, a smaller box is utilized to provide an additional refinement to the mesh in the stern region, which encloses the aft part of the KCS hull, the KCS rudder, and also the propeller region.
- To accurately capture the dynamics of the boundary layer, the first cell height is determined based on a target value of y^+=1. The snappyHexMesh utility is employed to add eight prism layers to the KCS hull, KCS rudder blade, and KCS rudder skeg, using an expansion ratio of 1.2 as recommended by ITTC (2014).

It should be noted that in cases involving non-zero drift, the aforementioned mesh generation procedures are modified accordingly. The primary adjustments involve rotating the refinement boxes to an angle equal to the degree of drift to make sure that they are aligned with the longitudinal axis of the hull. This can save the total mesh sizes and the associated computational costs compared to the grid generation approach in the previous chapter.

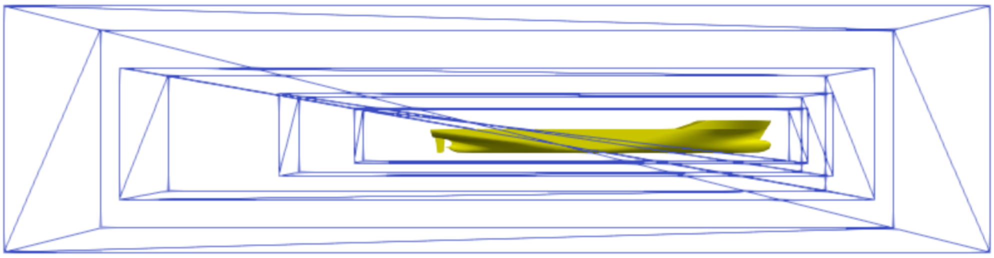

FIGURE 6.3: Four refinement zones enclosing the KCS hull and the rudder.

Table 6.3 displays the average values of y^+ for each component and the corresponding total mesh sizes for three different cases of drift. It is important to note that these values are obtained for the drift KCS with a rudder angle of zero degrees ($\beta_r = 0$ °). However, the actual values may vary for cases with non-zero rudder angles, although the differences are not expected to be significant. The final mesh of zero drift KCS with zero-degree rudder angle is shown in Figures 6.4 to 6.6. Besides, mesh details of +10 °drift KCS and + 30 °rudder are also presented in Figure 6.7 and 6.8.

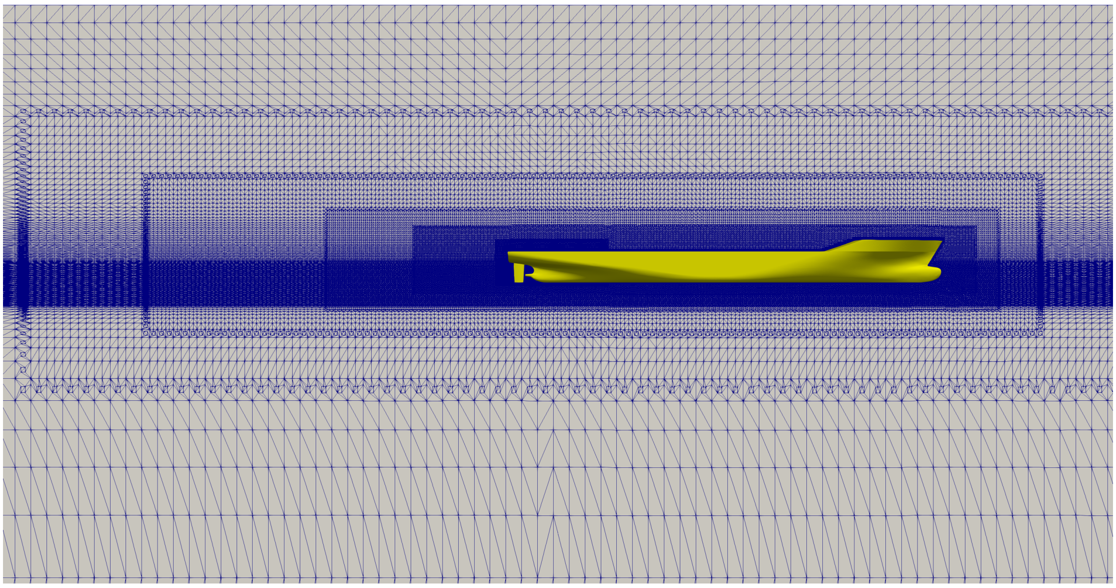

FIGURE 6.4: Grid distribution around the KCS hull from side view

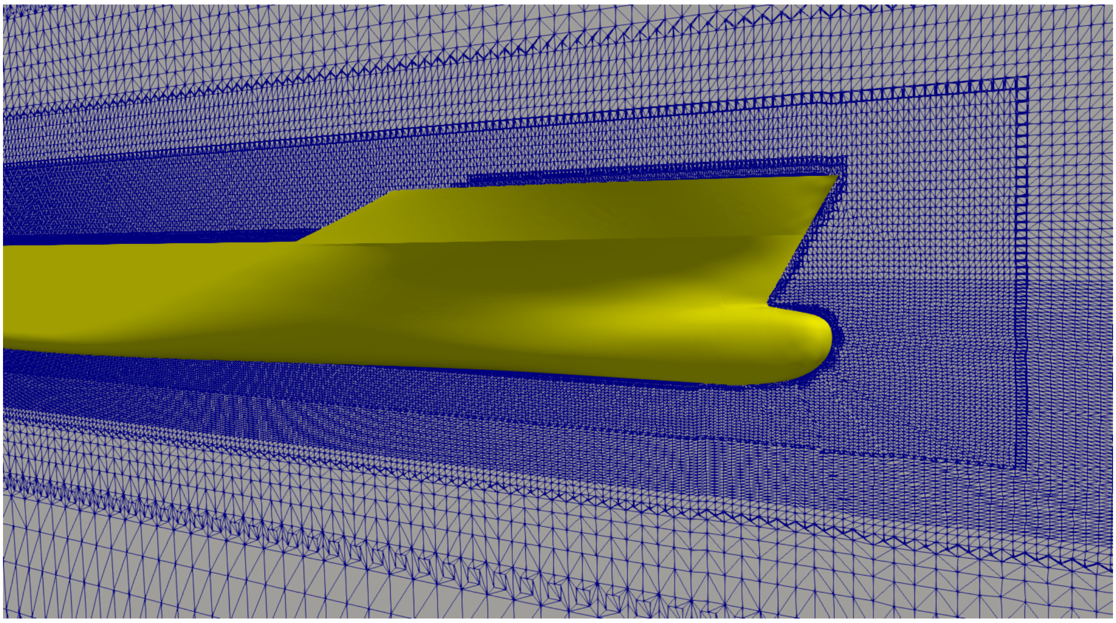

FIGURE 6.5: Mesh details of the KCS bow region from side view

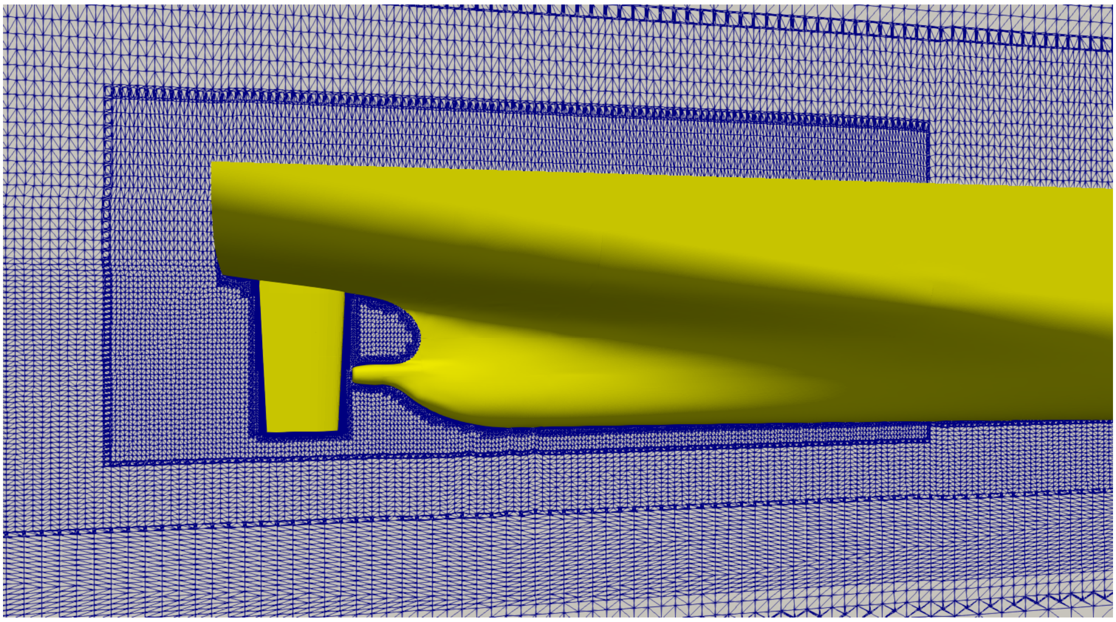

FIGURE 6.6: Mesh details of the KCS stern region from side view

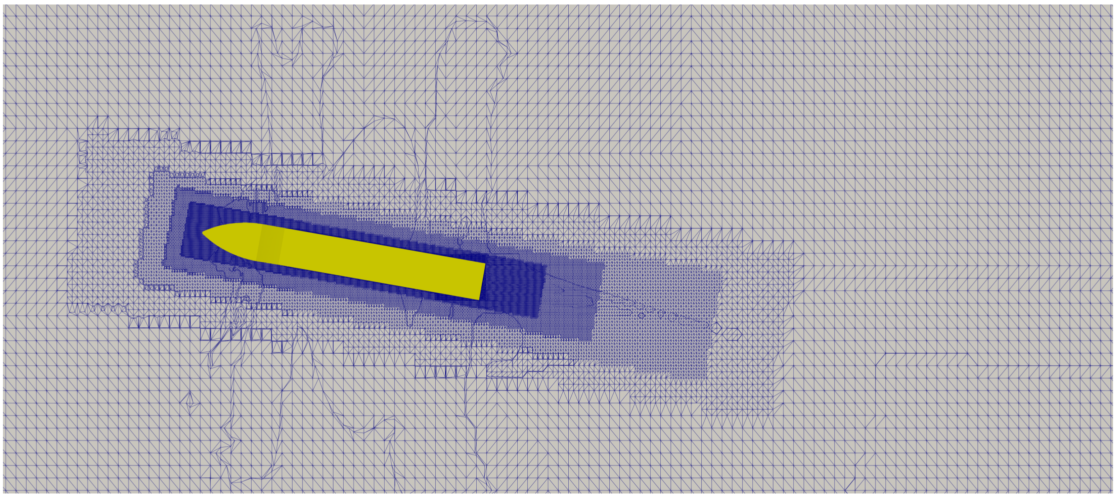

FIGURE 6.7: Mesh details of the 10 °drift KCS from top view

TABLE 6.3: Average y^+ and total mesh size for different drift cases

Parameter	$\beta = -10\,^\circ$	$\beta = 0\,^\circ$	$\beta = +10\,^\circ$
y^+ of hull	1.13	1.05	1.13
y^+ of rudder blade	0.33	0.42	0.34
y^+ of rudder skeg	0.40	0.59	0.39
Total mesh size	15.37M	16.25M	15.32M

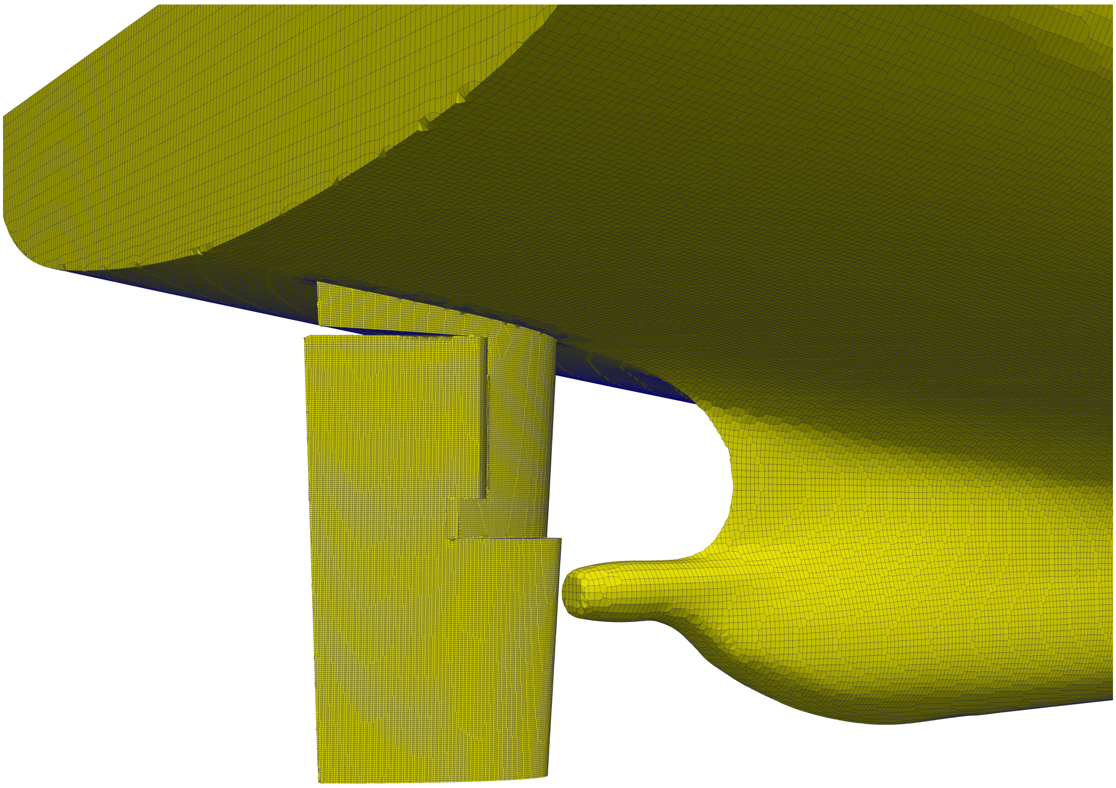

FIGURE 6.8: KCS rudder grid distribution of +30 °rudder angle in stern region

6.2.6 Validation and verification

In order to guarantee the credibility of numerical simulations, a verification and validation study is carried out for the straight-ahead KCS (zero drift angle) with a zero rudder angle at the ship design Froude number (0.26) under calm water conditions with the freedom to heave and pitch. This scenario aligns with Case 2.1 from the 2015 Tokyo Computational Fluid Dynamics (CFD) Workshop. An analysis is conducted to assess the sensitivity of grid spacing and time step, employing a methodology based on the works of Stern et al. (2001) and ITTC (2017*b*), which have been discussed in Section 3.9.

To assess grid sensitivity, three grids are generated, namely, Mesh 1, Mesh 2, and Mesh 3, using a structured background mesh with a systematic refinement factor of 1.1 for the same geometry definition. Table 6.4 below summarizes the grid distribution in x, y z directions and the total mesh size for each grid, along with relevant simulation parameters such as time step, simulation time, and computational costs. Table 6.5 presents the results obtained by the different grid cases. Table 6.6 lists the numerical uncertainties of the KCS total resistance coefficient, indicating the simulation results are valid. Figure 6.9 shows total resistance variation with time history for three grids.

TABLE 6.4: Grid system for mesh sensitivity study

Parameter	Mesh1	Mesh2	Mesh3
blockMesh refinement	133x31x48	121x28x44	110x26x40
Total cell numbers	26.3M	20.5M	16.3M
Time step	0.002s	0.002s	0.002s
Simulation Time	35s	35s	35s
Computatioanl cost	75-80hrs	60-65hrs	50-55hrs
Computing system	Iridis 5 Linux Cluster of HPC Facility at the University of Southampton		
CPUs	Two full nodes with 40 cores per node with 192GB of DDR4 memory		

TABLE 6.5: Total resistance coefficients of different grids

Case	$C_T/10^{-3}$	Diff.
Mesh1	3.666	-1.2 %
Mesh2	3.643	-1.8 %
Mesh3	3.613	-2.6 %
EFD	3.711	-

TABLE 6.6: The numerical uncertainties of resistance coefficients of different grids

Parameter	r_G	R_G	Convergence conditions	C_G	U_{SN} (%D)	E(%D)
Grid	1.1	0.76	monotonic convergence	1.5	3.9	1.2

Similar procedures are also carried out for the time step sensitivity study with three different time steps, 0.002s, 0.001s and 0.0005s for Mesh 3 and the results remain validated. Figure 6.10 shows total resistance variation with time history for three time steps with Mesh3. Due to the significant increase in computational cost related to finer mesh and smaller time step, thus Mesh 3 and the time step of 0.002s is chosen for most aspects of this work unless otherwise stated.

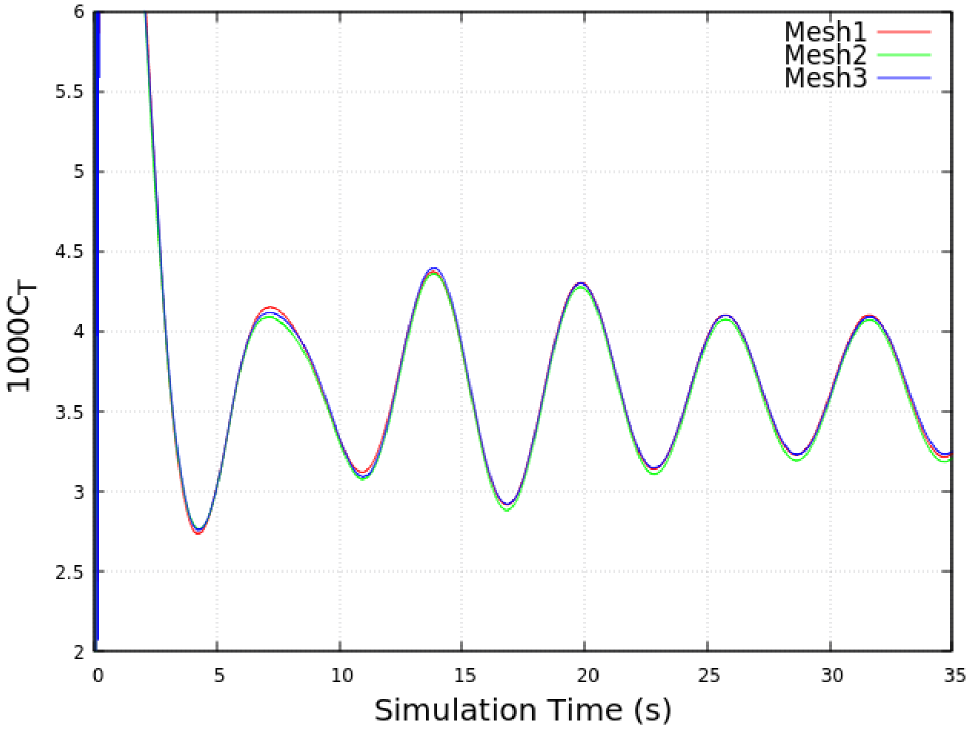

FIGURE 6.9: KCS total resistance coefficient variation with time history for three grids

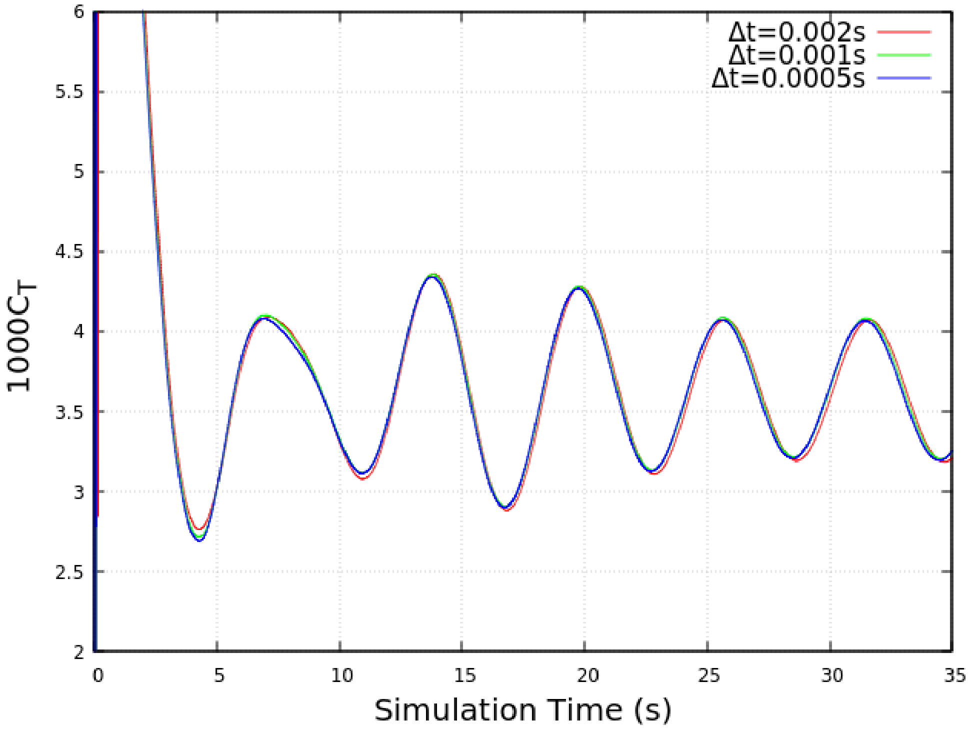

FIGURE 6.10: KCS total resistance coefficient variation with time history for three time steps with Mesh3

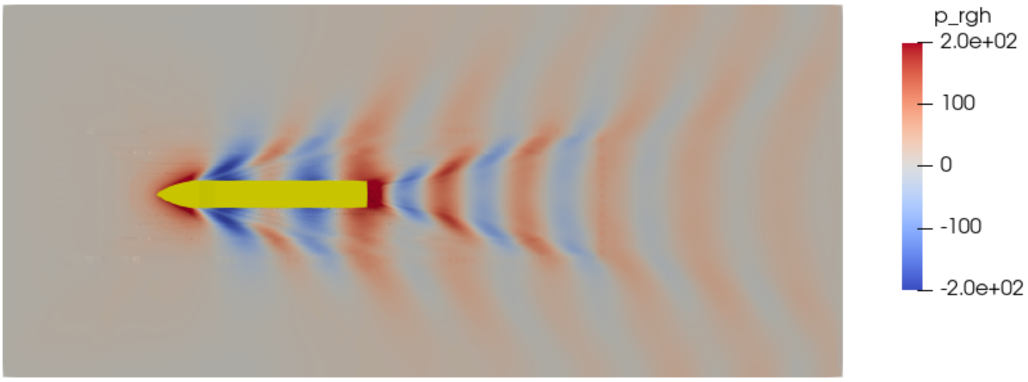

(A) β = 0 °, β_r = 0 °

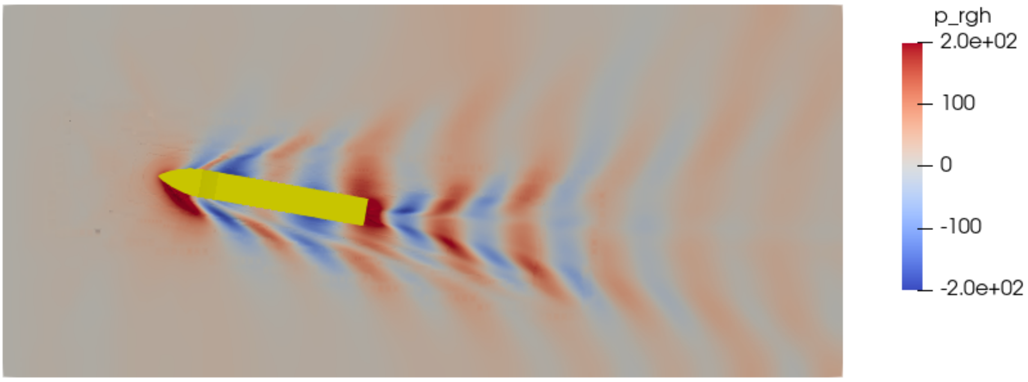

(B) β = +10 °, β_r = 0 °

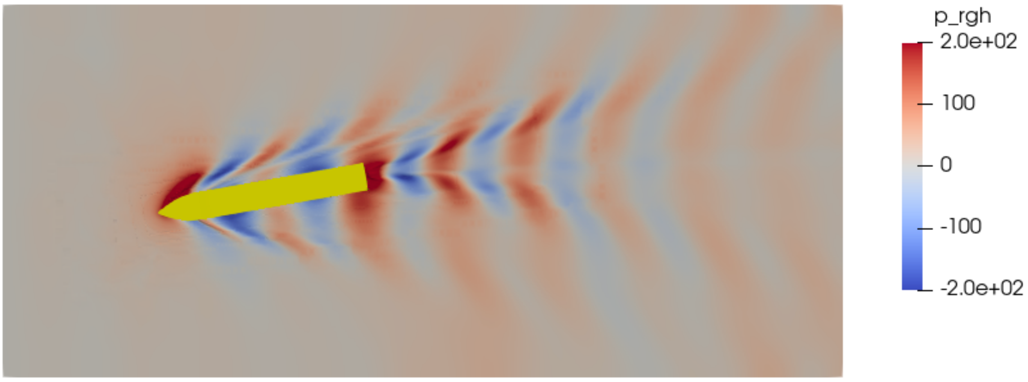

(C) β = -10 °, β_r = 0 °

FIGURE 6.11: Hydrodynamic pressure distribution on the free surface with different drift angles in resistance tests, Fn=0.26

In addition, hydrodynamic pressure distribution on the free surface at three static drift angles of resistance tests is presented in Figure 6.11, demonstrating a good resolution of the adopted mesh density and time step.

6.3 Results and discussion

6.3.1 Hull-rudder interaction

To validate the accuracy of numerical results, the KCS of the Southampton model scale is adopted to perform the calm water resistance test in Boldrewood Towing Tank. The KCS experiments at Southampton are analyzed and post-processed by the author of this thesis. The main particulars of the SOTON KCS model and the tank dimensions are listed in Tables 6.7 and 6.8.

TABLE 6.7: Main particulars of KCS comparison between Tokyo'15 Model and SOTON Model

Parameter	Tokyo'15 Model 1	SOTON Model
Scale ratio	31.60	60.96
Lwl	7.3577 m	3.814 m
Lpp	7.2786 m	3.7729 m
Draft (T)	0.3418 m	0.1772 m
Beam	1.0190 m	0.53 m
Depth	0.6013m	0.282 m
Wetted surface area w/o rudder	9.4379 m^2	2.5359 m^2
Rudder Type	Semi-balanced horn rudder	All movable rudder
Wetted surface area of rudder	0.1152 m^2	0.0310m^2

TABLE 6.8: Dimensions of Boldrewood Towing Tank

Dimension	Value
Length	138 m
Width	6 m
Depth	3.5 m

As the CFD and EFD results are obtained using two different model scales' KCS, thus the standard scaling approach is used to fit and scale the total resistance and side force of the SOTON scale to the Toyko scale using the following equations:

$$\mathrm{Ct}_{\mathrm{Tokyo}} - \mathrm{Cf}_{\mathrm{Tokyo}} = \mathrm{Ct}_{\mathrm{soton}} - \mathrm{Cf}_{\mathrm{soton}} \tag{6.1}$$

$$\mathrm{Fy}_{\mathrm{Tokyo}} = \mathrm{Fy}_{\mathrm{soton}} \tag{6.2}$$

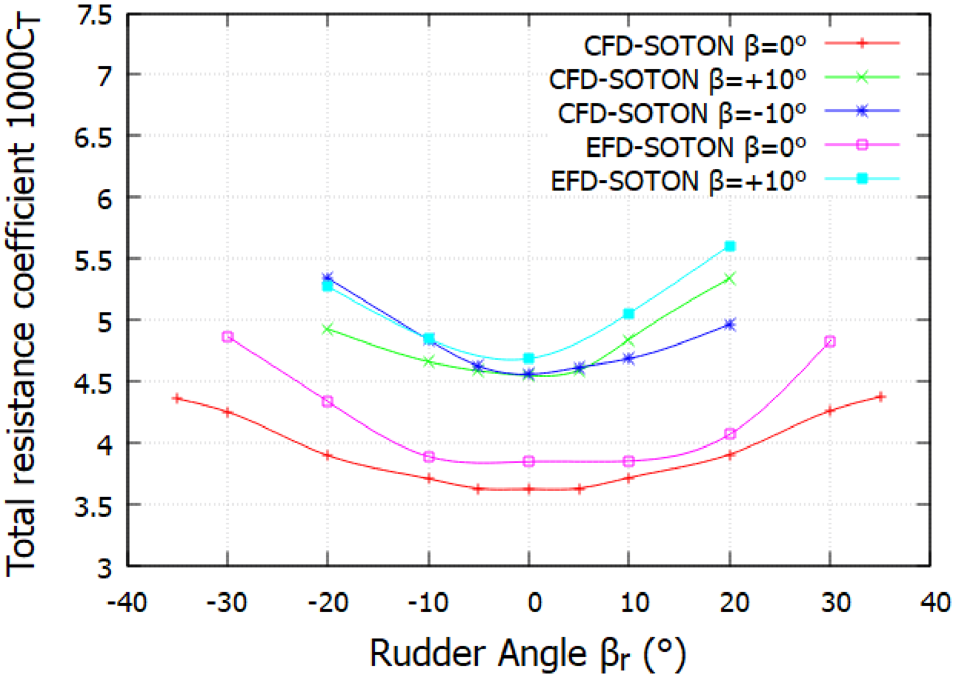

FIGURE 6.12: Comparison of CFD and EFD results for non-dimensional KCS total resistance coefficient C_T

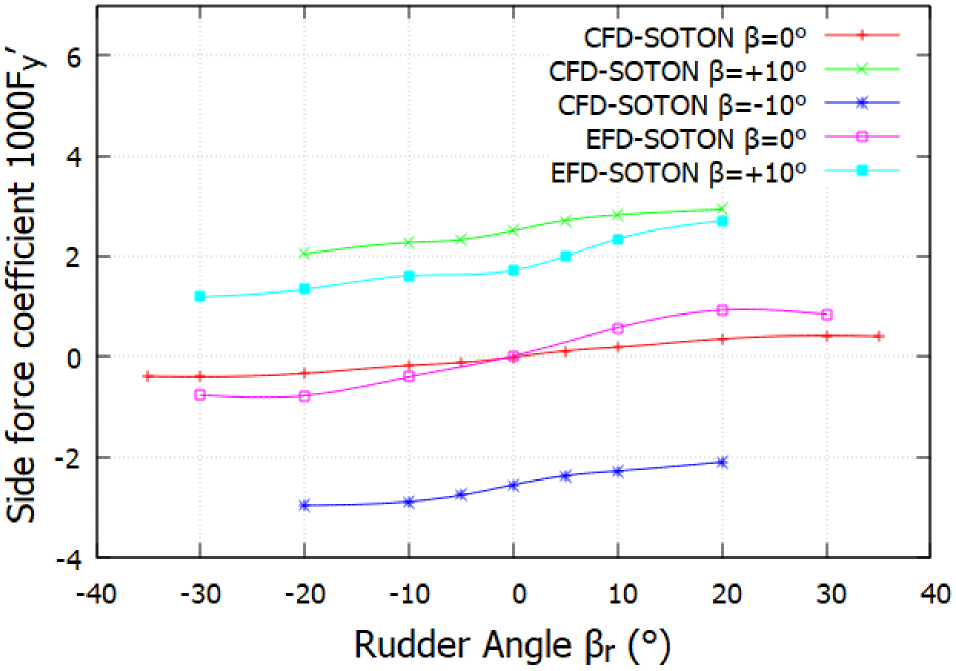

FIGURE 6.13: Comparison of CFD and EFD results for non-dimensional KCS side force coefficient $F_Y^{'}$

Figure 6.12 presents the influences of drift and rudder angles on the KCS total resistance coefficient C_T, which includes the longitudinal drag from the KCS hull and the KCS rudder in calm water at the ship design Froude number of 0.26. Also, the plot of the KCS side force coefficient F_Y' with different drift and rudder angles is shown in Figure 6.13. Overall, both hydrodynamic forces (drag and side forces) present good agreement between EFD and CFD results for all static drift and rudder angles. For zero drift drag force, it increases with the increment of rudder angle magnitude, and the C_T is nearly symmetric about the axis of β_r=0 °, as shown in Figure 6.12. When a non-zero drift angle is applied, the drag force plots of β = -10 °and +10 °shift upwards and the maximum value of C_T occurs at +20 °rudder angle for positive drift angle while it is observed at -20 °rudder angle for negative drift angle. For β=0 °and +10 °, EFD results are slightly higher than CFD results, mainly because the all-movable rudder type is used in the experiment, therefore inducing more rudder drag force compared to CFD results, where only the rudder blade is rotatable. In addition, the bigger deviation between EFD and CFD can be found for larger rudder angles, e.g -30 °and +30 °. The main possible reason is the effect of increased rudder angles, which makes the fluid around the rudder more turbulent and less streamlined. The selection of the turbulence model in RANS may contribute to flow separation, where the fluid detaches from the rudder surface and forms vortices, which makes CFD challenging to capture accurately. Therefore, a more advanced turbulence model may be required for large drift angles and rudder deflection angles.

In terms of the non-dimensional lateral force F_Y' at straight-ahead condition (zero drift angle), the general trend is that the side force increases with the larger absolute value of the rudder angle, and the sign of transverse force is the same as that of rudder angle. Similar to drag force, the side force of EFD at zero drift is slightly larger than CFD results, which can also be attributed to the bigger wetted surface area of the adopted all-movable rudder. When a non-zero drift angle is applied, the lateral force curve slope does not change significantly. However, it is evident that positive and negative drift angles lead to upward and downward shifts, respectively. It is interesting to note that the EFD results are more minor than the CFD results for the +10 °drift condition. A possible explanation is that the actual drift angle in towing tank test is smaller than 10 °, but the overall trends from both EFD and CFD are consistent. In addition, compared to the influence of rudder angle, the effect of drift angle is more notable in lateral force.

Table 6.9 displays the longitudinal force components comprising the total resistance encountered by KCS hull and rudder when operating in straight-ahead condition ($\beta =$ 0 °). The result reveals that the hull pressure drag component decreases as the rudder angle increases while the viscous drag component remains relatively constant. This outcome is due to the non-uniform fluid flow upstream of the rudder when a non-zero rudder angle is applied. As a result, the pressure distribution along the length of the hull is altered, leading to a reduction in the net pressure force.

TABLE 6.9: Drag force components of KCS at 0 °drift with rudder angles (unit: N)

β_r (°)	Hull R_P	Hull R_V	Rudder R_P	Rudder R_V	R_{Hull}	R_{Rudder}	R_T
-35	9.03	65.91	25.05	0.39	74.94	25.44	100.38
-30	10.91	66.08	20.54	0.43	76.99	20.97	97.96
-20	13.35	66.16	9.60	0.68	79.50	10.28	89.79
-10	14.65	66.11	3.90	0.77	80.76	4.67	85.43
-5	15.05	66.16	1.58	0.81	81.21	2.39	83.60
0	15.39	66.20	1.05	0.84	81.59	1.89	83.48
5	15.05	66.11	1.65	0.82	81.15	2.47	83.62
10	14.59	66.50	3.76	0.77	81.09	4.53	85.62
20	13.34	66.11	9.81	0.72	79.45	10.53	89.98
30	10.87	66.01	20.83	0.43	76.88	21.26	98.14
35	8.95	65.97	25.43	0.39	74.92	25.82	100.73

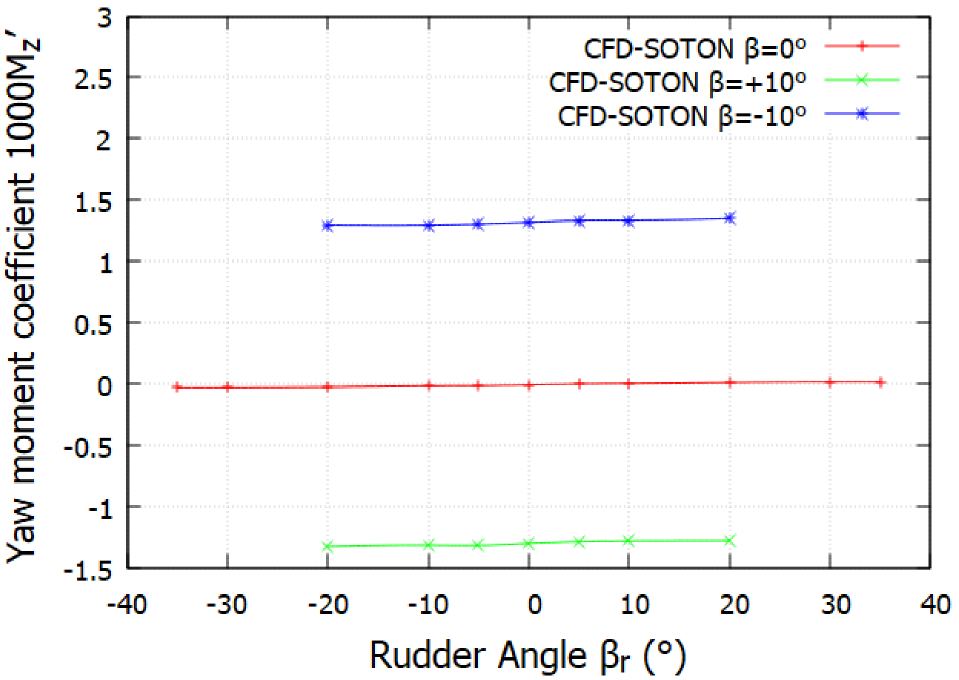

FIGURE 6.14: Influnece of drift and rudder angle on non-dimensional KCS yaw moment coefficient $M_z^{'}$

The effect of drift and rudder angle on the non-dimensional yaw moment $M_z^{'}$ is presented in Figure 6.14. Although $M_z^{'}$ increases slightly as the rudder angle increases, the impact is relatively minor. In contrast, the yaw moment is more significantly affected by changes in the drift angle. It should be noted that the drift angle produces opposite effects on the yaw moment, which contrasts with the influence of the drift angle on the side force. Specifically, positive drift angles result in a downward shift of the yaw moment curve, while negative drift angles cause an upward shift.

The influence of static drift and rudder angle on rudder forces is demonstrated in Figures 6.15 and 6.16. As the rudder angle increases, the rudder force grows owing to the larger angle of attack. When a drift angle is applied, the slope of the rudder drag curve becomes more pronounced than in zero drift cases. In addition, the applied non-zero drift angles result in a vertical shift in the rudder lift curve but have a relatively minor impact on the curve slope.

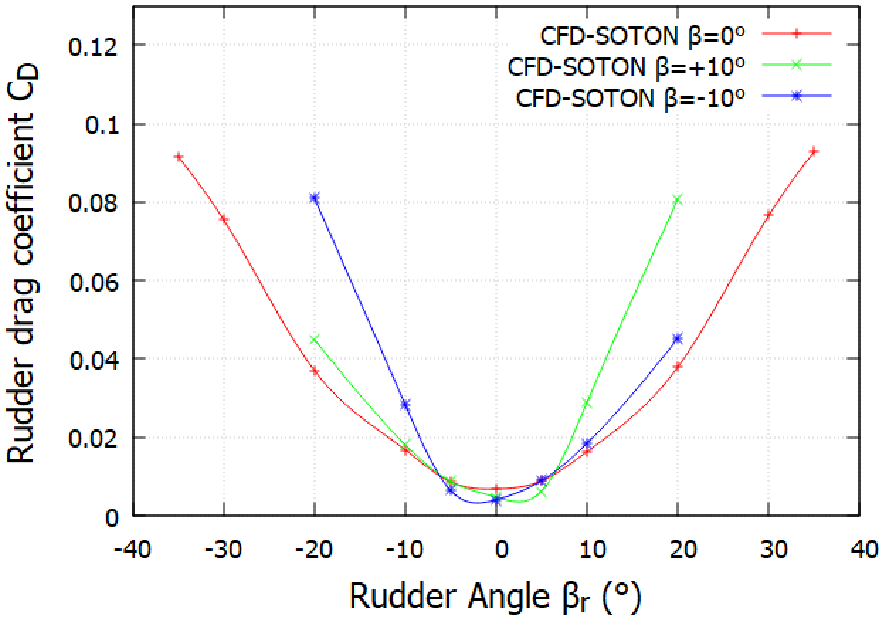

FIGURE 6.15: Effect of drift and rudder angle on rudder drag coefficient C_D

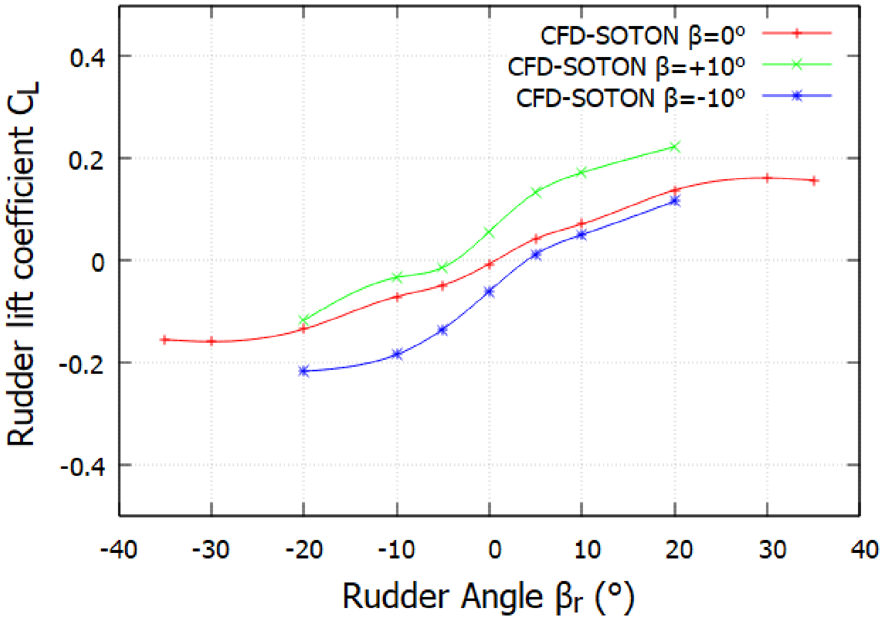

FIGURE 6.16: Effect of drift and rudder angle on rudder lift coefficient C_L

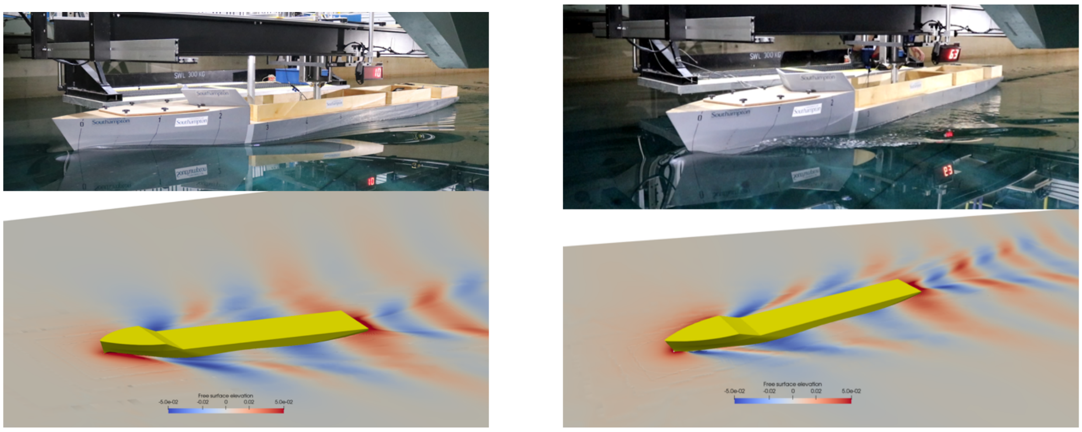

(A) Zero degree drift KCS

(B) Ten-degree drift KCS

FIGURE 6.17: Wave elevation comparison between EFD and CFD for zero and non-zero drift scenarios from side view, *Fn*=0.26

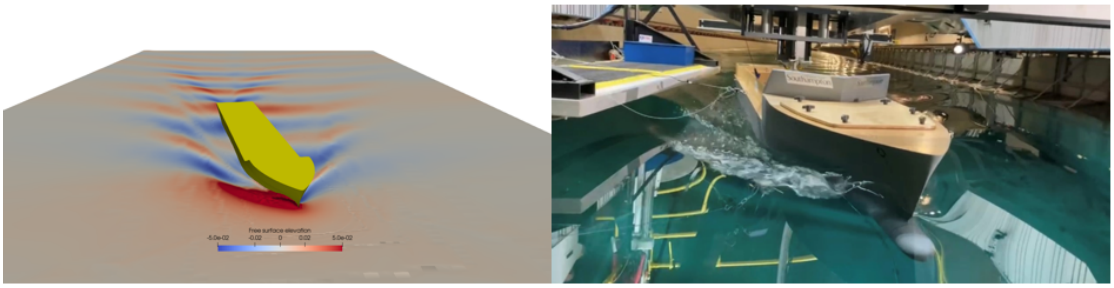

(A) Wave elevation at bow of CFD and experiment for KCS at angle drift of 10 °

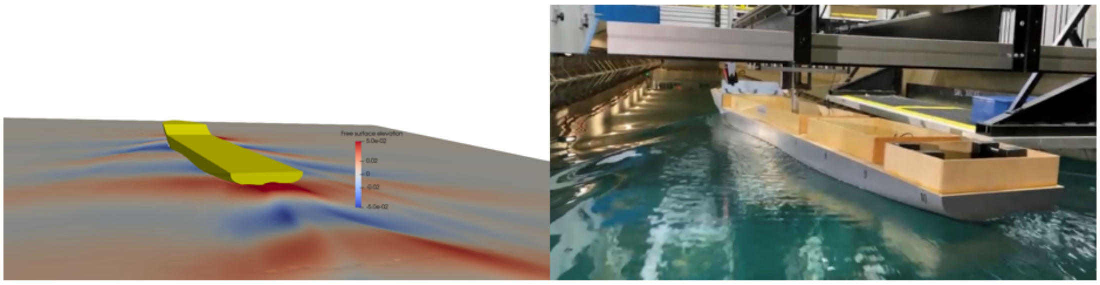

(B) Wave elevation at stern of CFD and experiment for KCS at angle drift of 10 °

FIGURE 6.18: Wave elevation of CFD and experiment for KCS at angle drift of 10 °at bow and stern, *Fn*=0.26

Straight-ahead and 10 °drift KCS wave patterns predicted by CFD and EFD from the side view with *Fn*=0.26 in resistance test are presented in Figure 6.17. It can be found that wave elevations generated by CFD match well with experimental measurement: high elevation occurs at the bow region, followed by a gradual decrease along the hull length, and low elevation can be seen around the amidship. The applied non-zero drift angle not only intensifies the asymmetry of the wave pattern but also develops a tiny high-elevation region near the bow, which is shown in (B) of Figure 6.17. Similarly,

Figure 6.18 illustrates wave elevations of 10 °drift KCS from the bow and stern view: overall very good agreement can be found between EFD and CFD when predicting wave pattern, especially the experiment demonstrating that the applied 10 °drift angle results in an obvious high wave elevation at the starboard of the bow region and CFD can capture this phenomenon accurately, as presented in (A) of Figure 6.18.

6.3.2 Hull-propeller-rudder interaction

6.3.2.1 Influence of drift angle on hull drag

Figure 6.19 illustrates the calculated KCS total resistance coefficients (C_T) in a straight-ahead condition for five different propeller revolution rates using the BEMt and Yamazaki propeller models. Both BEMt and Yamazaki models exhibit a consistent trend in the variation of the KCS total resistance coefficients (C_T): as the rudder angle magnitude increases, the total drag correspondingly rises. Besides, a higher propeller revolution rate leads to an increased total drag, partially resulting from reduced pressure at the hull's rear. Due to the unidirectional rotation of the propeller, a more substantial drag is observed at a negative, non-zero rudder angle compared to its corresponding positive rudder angle. Overall, a good agreement can be found between BEMt and Yamazaki models. However, their discrepancies become more evident as the propeller revolution rate increases.

The KCS total resistance coefficients (C_T) values under non-zero static drifting conditions (β = -10°, +10°) are provided in Table 6.10. To examine the influence of the rudder on KCS total resistance at non-zero drift, a comparison is made between the differences in C_T values (dC_T) for drift conditions and zero drift scenarios, as shown in Figure 6.20. The applied drift angle clearly increases the total ship drag but with an opposite trend for positive and negative drifts: dC_T increases when the rudder angle increases from -20 °to +20 °for +10 °drift angle while the curve of dC_T shows decreasing trend with rudder angles for -10 °drift.

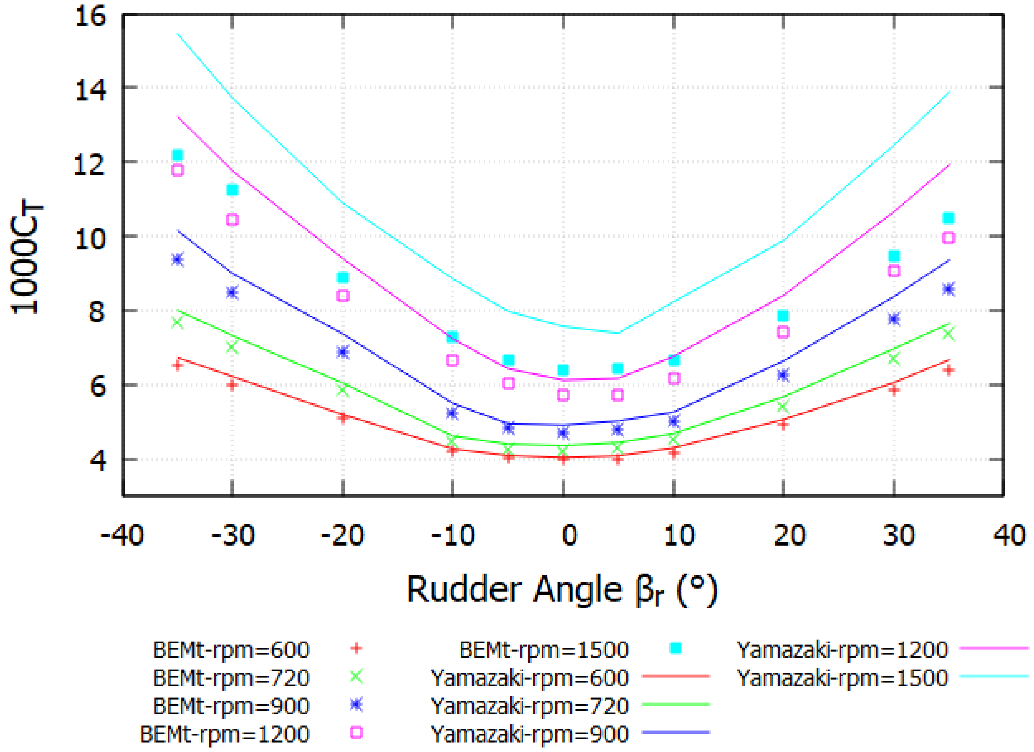

FIGURE 6.19: Zero drift KCS's C_T predicted by BEMt and Yamazaki under five different propeller revolutions' conditions

TABLE 6.10: Total drag coefficient at drift angles +10 °and -10 °, predicted by BEMt and Yamazaki under five different propeller revolutions' conditions

		BEMt					Yamazaki				
	rpm	600	720	900	1200	1500	600	720	900	1200	1500
β_r	β	Ct	Ct	Ct	Ct	Ct	Ct	Ct	Ct	Ct	Ct
-20 °	+10 °	5.394	5.853	6.916	8.517	9.242	5.563	6.121	7.430	9.448	11.103
-10 °	+10 °	4.861	5.151	5.600	6.902	7.730	4.998	5.377	5.987	7.425	9.056
-5 °	+10 °	4.701	4.955	5.347	6.389	7.257	4.840	5.187	5.738	6.871	8.269
0 °	+10 °	4.659	4.895	5.278	6.224	7.015	4.788	5.124	5.647	6.698	7.969
5 °	+10 °	4.728	4.969	5.394	6.458	7.167	4.868	5.197	5.776	6.899	8.085
10 °	+10 °	4.929	5.212	5.749	7.078	7.680	5.063	5.425	6.115	7.272	8.675
20 °	+10 °	5.956	6.487	7.468	8.704	9.151	6.076	6.781	7.875	9.635	11.131
-20°	-10 °	6.403	7.095	8.143°	9.702	9.931	6.434	7.161	8.327	10.208	11.724
-10 °	-10 °	5.367	5.715	6.415	7.606	8.046	5.348	5.712	6.431	7.865	9.223
-5 °	-10 °	4.872	5.187	5.762	6.827	7.373	4.949	5.237	5.769	7.085	8.401
0 °	-10 °	4.623	4.843	5.413	6.356	6.980	4.717	4.923	5.391	6.629	7.927
5 °	-10 °	4.636	4.815	5.185	6.245	6.865	4.729	4.948	5.373	6.492	8.081
10	-10 °	4.816	5.024	5.366	6.433	7.050	4.929	5.172	5.637	6.849	8.426
20 °	-10 °	5.411	5.790	6.314	7.519	7.966	5.522	5.965	6.704	8.163	9.789

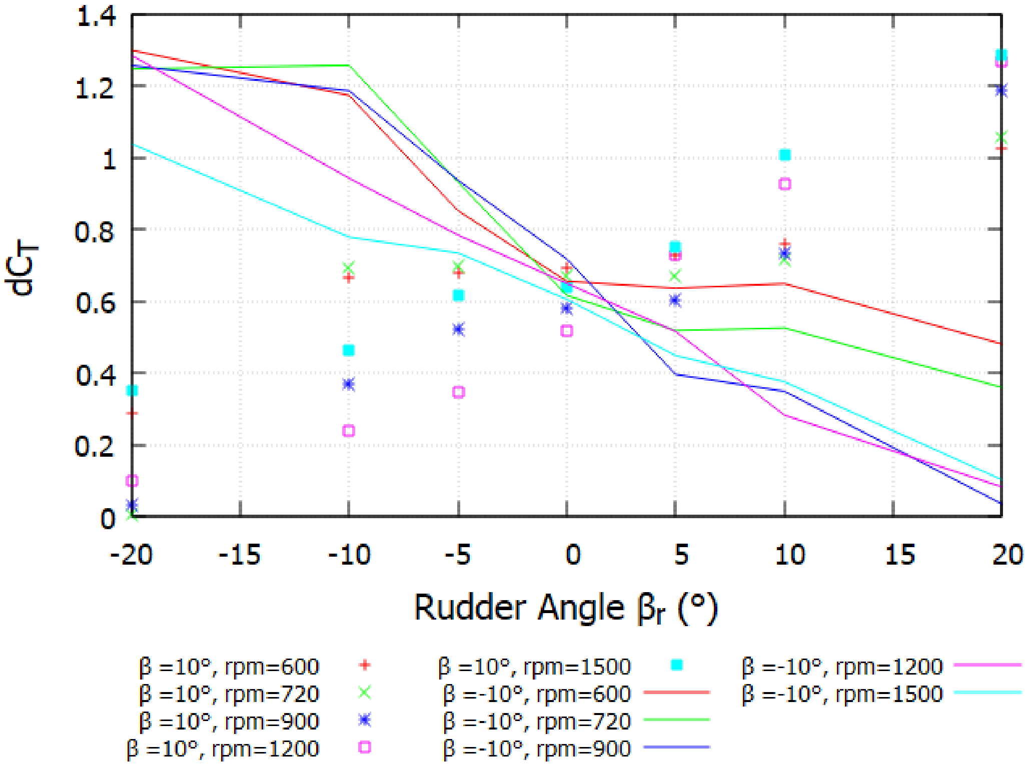

FIGURE 6.20: Effect of drift angle on hull drag augments, predicted by BEMt, under five different propeller revolutions' conditions

6.3.2.2 Drift angle influence on propeller performance

The computed propeller forces (K_T, $10K_Q$) by BEMt and Yamazaki models for three static drift cases at propeller revolution of 600 rpm are shown in Figure 6.21, Figure 6.22 and Figure 6.23. Both body force models can effectively capture the fluctuations in propeller performance under varying static drift and rudder angle conditions. Furthermore, the propeller performance predictions derived from these models demonstrate a similar pattern. A more substantial discrepancy between the two propeller models is observed in the calculated thrust coefficients in comparison to the propeller torque coefficients. This difference can also be found in the open water curves of the KCS propeller presented in Chapter 4. Specifically, the Yamazaki model tends to overestimate the K_T values slightly, whereas the BEMt model exhibits a minor underestimation of the K_T.

Table 6.11 lists the propeller thrust and torque arguments (dK_T, d10K_Q), derived by evaluating the net change in propeller forces between the drift (β=-10 °, +10 °) and zero-drift (β=0 °) scenarios. In comparison to cases with a -10 °drift angle, the propeller performance tends to experience a greater deterioration when subjected to a +10 °drift angle at corresponding rudder angles. A possible explanation is that positive drift angles may induce more flow separation and turbulence around the propeller, resulting in a more negative impact on thrust and torque generated by the propeller. Besides, the propeller operating at a positive drift angle may cause unfavorable flow interaction with the downstream rudder, leading to a more significant decrease in propeller performance.

TABLE 6.11: Propeller thrust and torque augments at drift angles +10 °and -10 °, predicted by BEMt under five different propeller revolutions' conditions

	rpm	600	720	900	1200	1500	600	720	900	1200	1500
β_r	β	dK_T	dK_T	dK_T	dK_T	dK_T	d10K_Q	d10K_Q	d10K_Q	d10K_Q	d10K_Q
-20 °	+10 °	-0.008	-0.006	-0.002	-0.005	-0.005	-0.015	-0.019	-0.018	-0.011	-0.027
-10 °	+10 °	-0.002	-0.001	-0.002	-0.005	-0.005	-0.002	-0.005	-0.014	-0.011	-0.026
-5 °	+10 °	-0.002	-0.001	-0.001	-0.005	-0.005	-0.003	-0.005	-0.013	-0.012	-0.024
0 °	+10 °	-0.002	-0.001	0.000	-0.005	-0.005	-0.003	-0.006	-0.012	-0.011	-0.025
5 °	+10 °	-0.003	-0.001	-0.001	-0.004	-0.005	-0.005	-0.006	-0.013	-0.009	-0.023
10 °	+10 °	-0.004	-0.002	-0.001	-0.004	-0.005	-0.007	-0.005	-0.013	-0.010	-0.021
20 °	+10 °	0.006	0.002	-0.001	-0.005	-0.005	0.010	0.004	-0.009	-0.013	-0.025
-20 °	-10 °	-0.002	-0.004	-0.005	-0.001	0.003	-0.006	-0.009	-0.014	-0.004	0.048
-10 °	-10 °	0.001	-0.001	-0.005	-0.002	0.004	0.001	0.000	-0.009	-0.003	0.047
-5 °	-10 °	-0.002	-0.003	-0.005	-0.002	0.004	-0.002	0.000	-0.009	-0.006	0.048
0 °	-10 °	-0.003	-0.004	-0.005	-0.002	0.004	-0.004	-0.003	-0.008	-0.005	0.051
5 °	-10 °	-0.003	-0.004	-0.006	-0.002	0.004	-0.003	-0.003	-0.012	-0.006	0.051
10 °	-10 °	-0.002	-0.004	-0.007	-0.003	0.004	0.000	0.000	-0.011	-0.008	0.050
20 °	-10 °	-0.005	-0.007	-0.009	-0.003	0.004	-0.004	-0.003	-0.017	-0.011	0.048

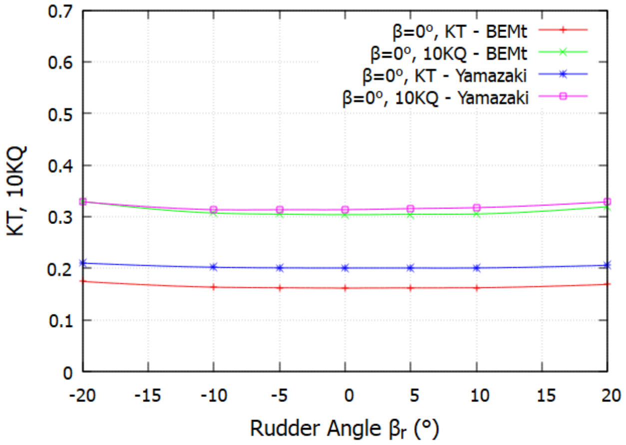

FIGURE 6.21: propeller forces predicted by BEMt and Yamazaki at 0 °drift, 600rpm

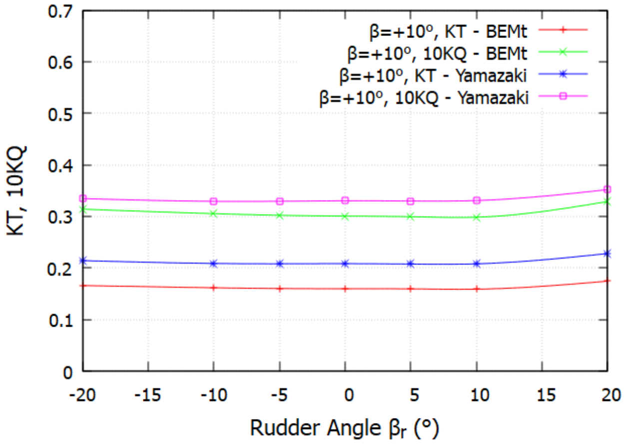

FIGURE 6.22: Propeller forces predicted by BEMt and Yamazaki at +10 °drift, 600rpm

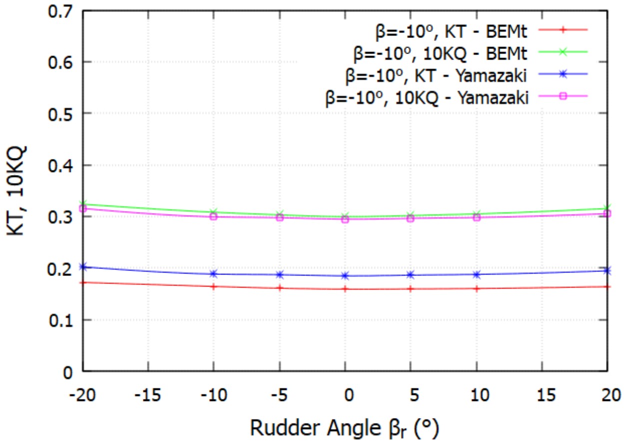

FIGURE 6.23: Propeller forces predicted by BEMt and Yamazaki at -10 °drift, 600rpm

Figure 6.24 presents the axial velocity contours at cross-section x/Lpp=0.9911 in three drift conditions with rpm=600, β_r=0 °, predicted by BEMt and Yamazaki model. Both

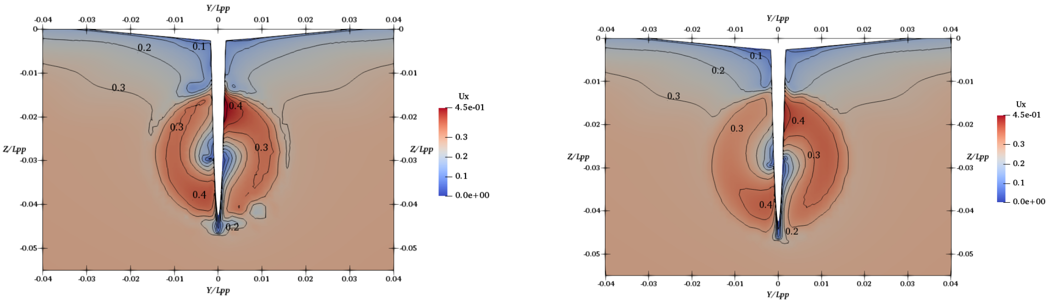

(A) $\beta = 0$ °, BEMt (B) $\beta = 0$ °, Yamazaki

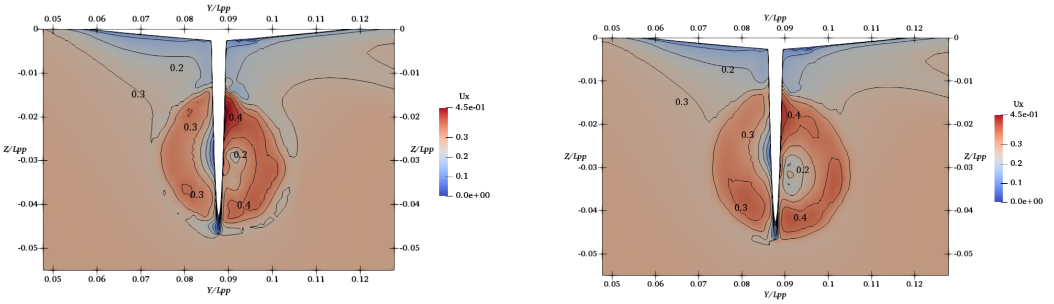

(C) $\beta = +10$ °, BEMt (D) $\beta = +10$ °, Yamazaki

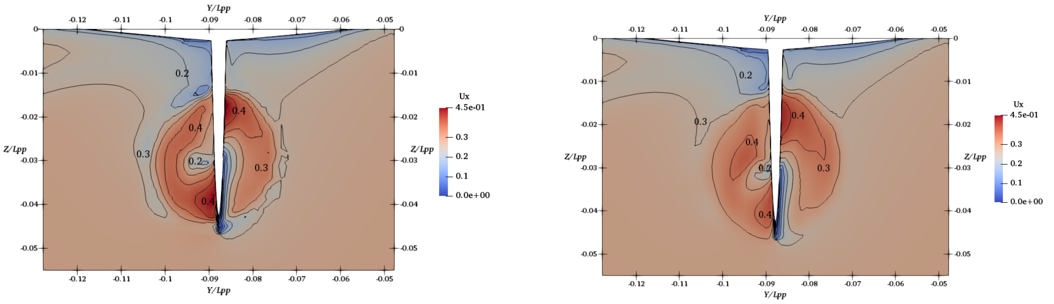

(E) $\beta = -10$ °, BEMt (F) $\beta = -10$ °, Yamazaki

FIGURE 6.24: Local axial flow contours (U_X) behind the KCS propeller at x/Lpp=0.9911 for three drift scenarios with zero rudder angle, predicted by BEMt and Yamazaki models, rpm=600

body force models can accurately capture the influence of drift angle on local axial velocity and the contour's patterns and values show good similarity, although Yamazaki theory models both axial and tangential flow effects while BEMt only includes the axial flow effect of the propeller. In addition, local velocity profiles downstream of the propeller plane x/Lpp=0.9911 at z/Lpp=-0.03 for three drift scenarios predicted by both propeller models are shown in Figure 6.25. All plots are not continuous around the y/L_{pp}=0 due to the presence of the rudder. The distribution of velocities predicted by two body force models shows good agreement, in particular for the straight-ahead case. In non-zero drift conditions, differences are mainly observed for the propeller axial velocities (u plots) near the rudder blade surface region: $0 < y/Lpp < 0.01$ for +10 °drift while $-0.01 < y/Lpp < 0$ for -10 °drift.

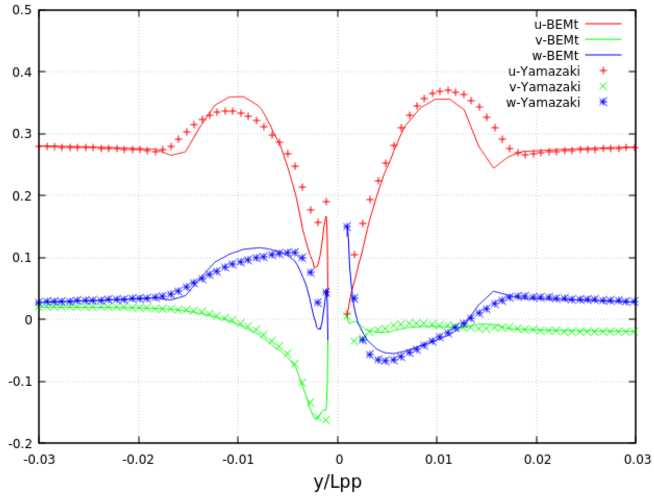

(A) β=0 °, β_r=0 °

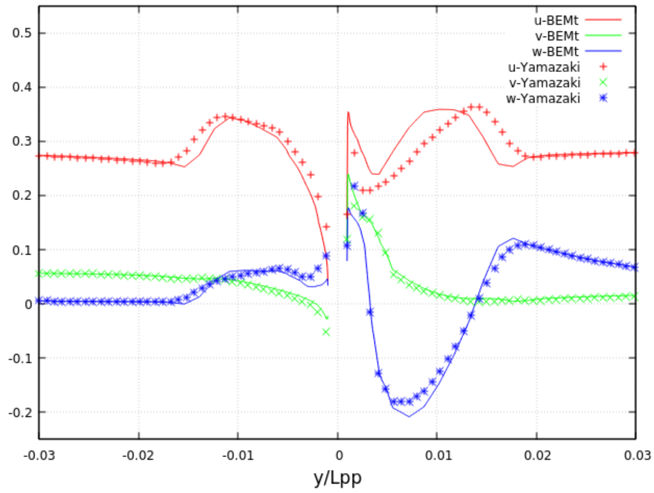

(B) β=+10 °, β_r=0 °

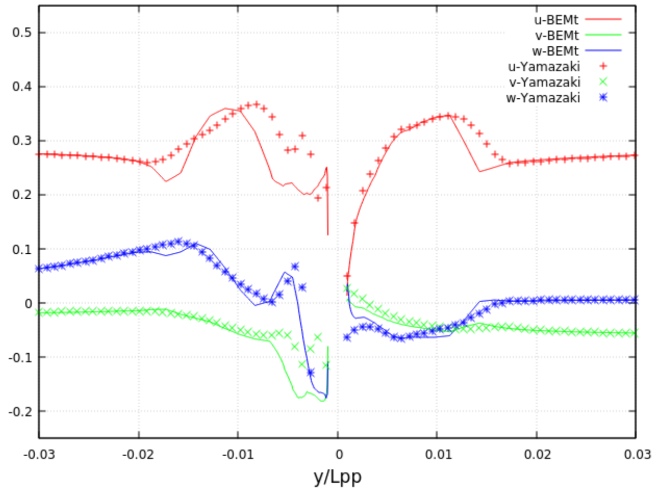

(C) β=-10 °, β_r=0 °

FIGURE 6.25: Influence of drift angle on local velocity profiles at x/Lpp=0.9911, β_r=0 °, rpm=600, predicted by BEMt and Yamazaki models

6.3.2.3 Drift angle influence on rudder force

The impact of drift on rudder force at a propeller revolution rate of 600 rpm is illustrated in Figures 6.26 and 6.27. It is found that the presence of a non-zero drift angle exacerbates the asymmetry of the C_D curve. However, it is noteworthy that the minimum rudder drag value consistently occurs at $\beta_r = 0°$ for all three drift scenarios. Furthermore, the introduction of +10° and -10° drift leads to upward and downward displacements, respectively, in relation to the lift curve with zero drift.

Figures 6.28 to 6.31 display the impact of propeller revolution on rudder performance at both positive and negative drift angles, as predicted by the BEMt and Yamazaki models. In general, the rudder performance calculated by both models demonstrates strong agreement for rudder lift across all scenarios, as well as rudder drag in the majority of cases, except for the highest propeller revolution rate of 1500 rpm. This discrepancy arises due to the Yamazaki model's overestimation of propeller forces in comparison to the BEMt model, which consequently results in an augmented inflow velocity to the rudder and an increased rudder drag.

At +10 °drift angle, the asymmetry of the C_D curves diminishes as the propeller revolution rate increases, which could be attributable to the enhanced flow straightening effects of the propeller. The lift curve C_L slope exhibits an increasing trend as the rpm varies from 600 to 1200. However, the rudder lift declines when the rpm reaches 1500, suggesting that the rudder likely stalls between 1200 and 1500 rpm. In the case of -10 °drift conditions, noticeable higher rudder drag values are observed at negative rudder angles for all propeller revolutions. The lift curves exhibit a variation trend similar to that of the +10 °drift condition. The impact of drift on rudder performance, as explored in this study, demonstrates good concordance with both experimental data from Molland & Turnock (1995) numerical results presented by Badoe et al. (2015), in which the influence of drift on the performance of a rudder situated downstream of three different centreboard configurations is investigated, further validating the findings of this research.

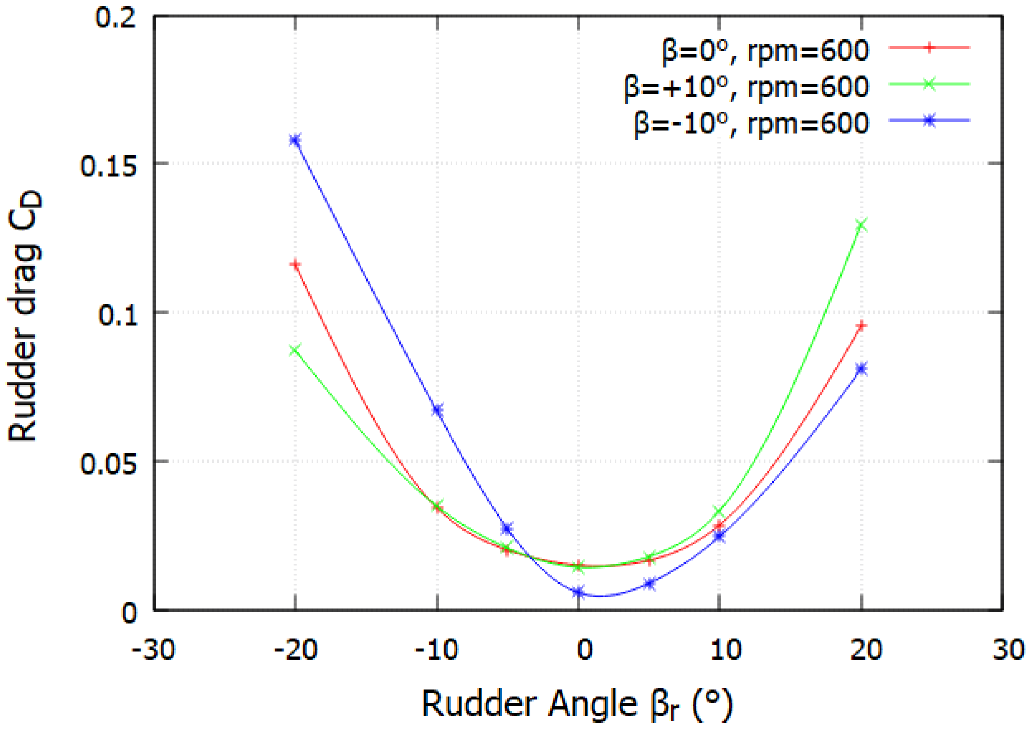

FIGURE 6.26: Rudder drag predicted by BEMt at three drift angle, 600rpm

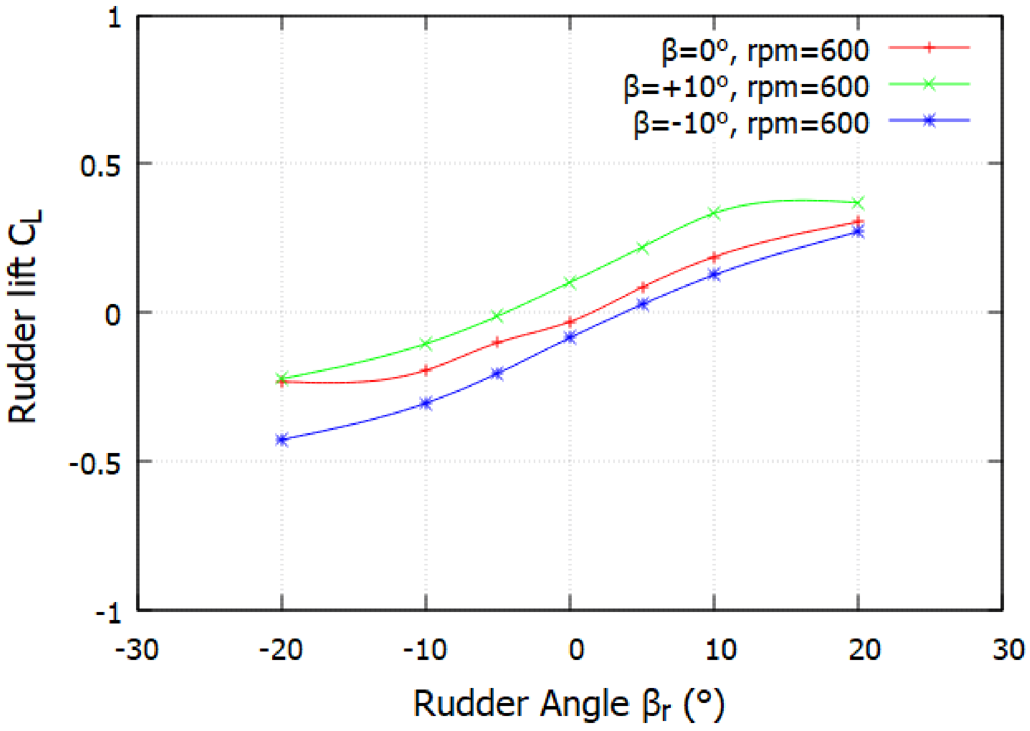

FIGURE 6.27: Rudder lift predicted by BEMt at three drift angle, 600rpm

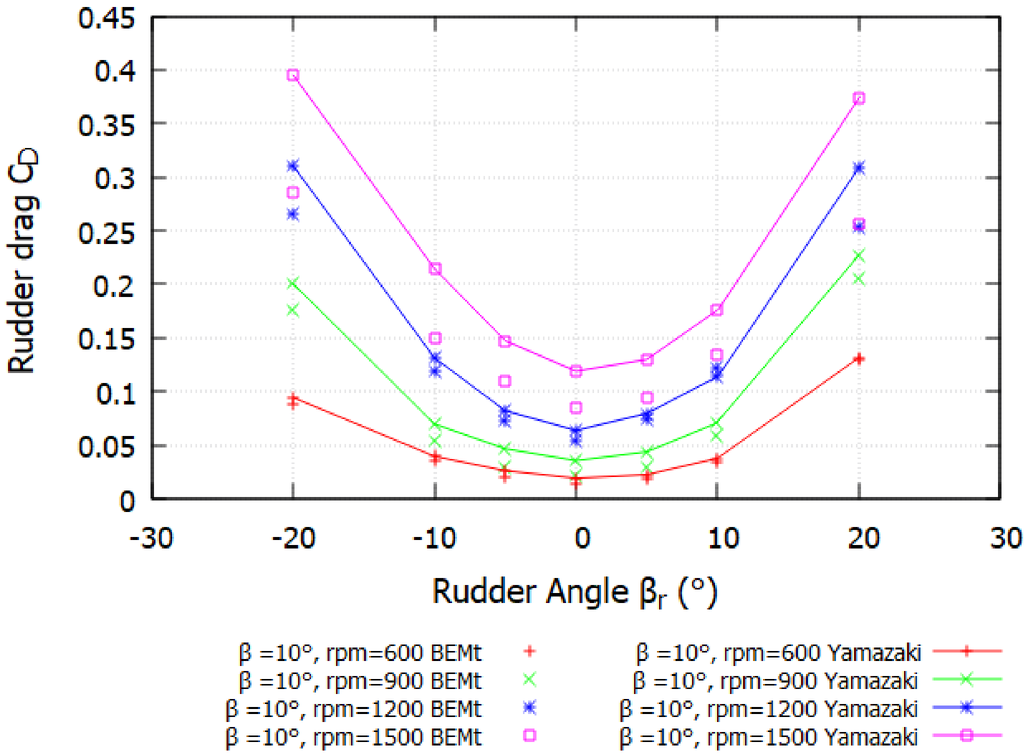

FIGURE 6.28: Effect of propeller revolution on rudder drag predicted by BEMt and Yamazaki at +10 °drift

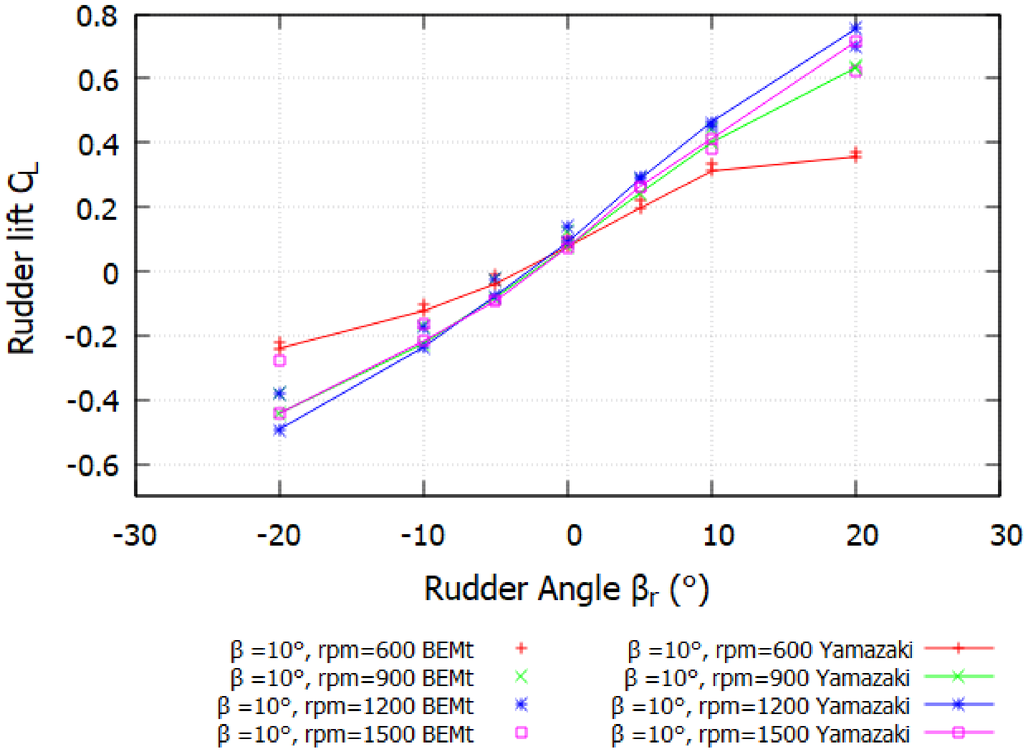

FIGURE 6.29: Effect of propeller revolution on rudder lift predicted by BEMt and Yamazaki at +10 °drift

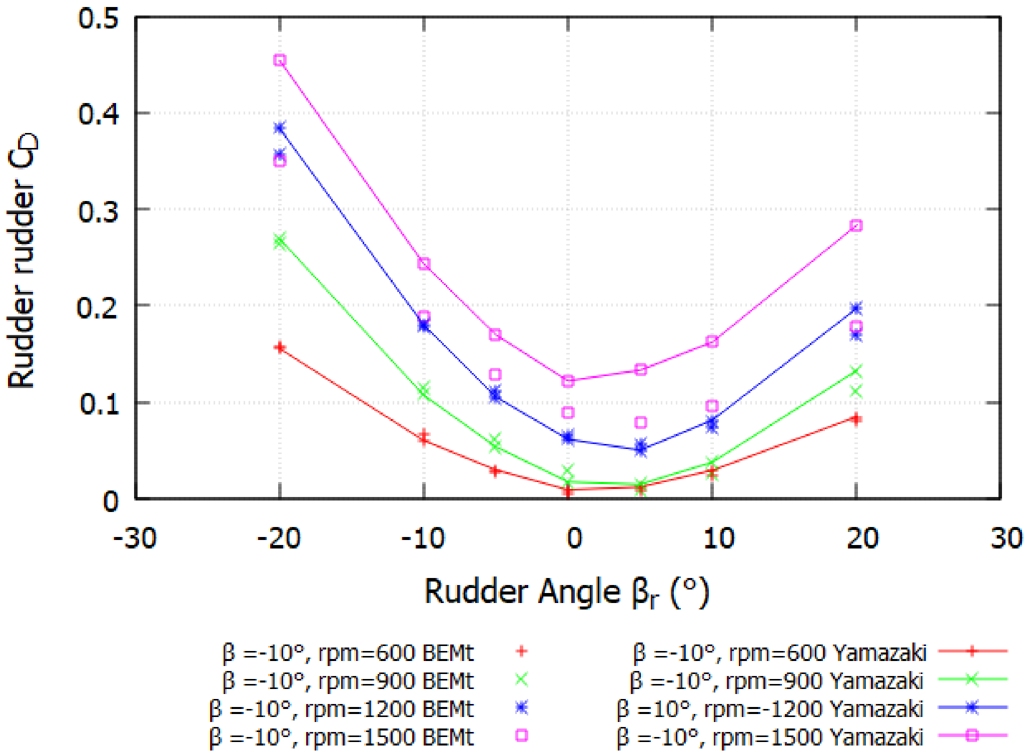

FIGURE 6.30: Effect of propeller revolution on rudder drag predicted by BEMt and Yamazaki at -10 °drift

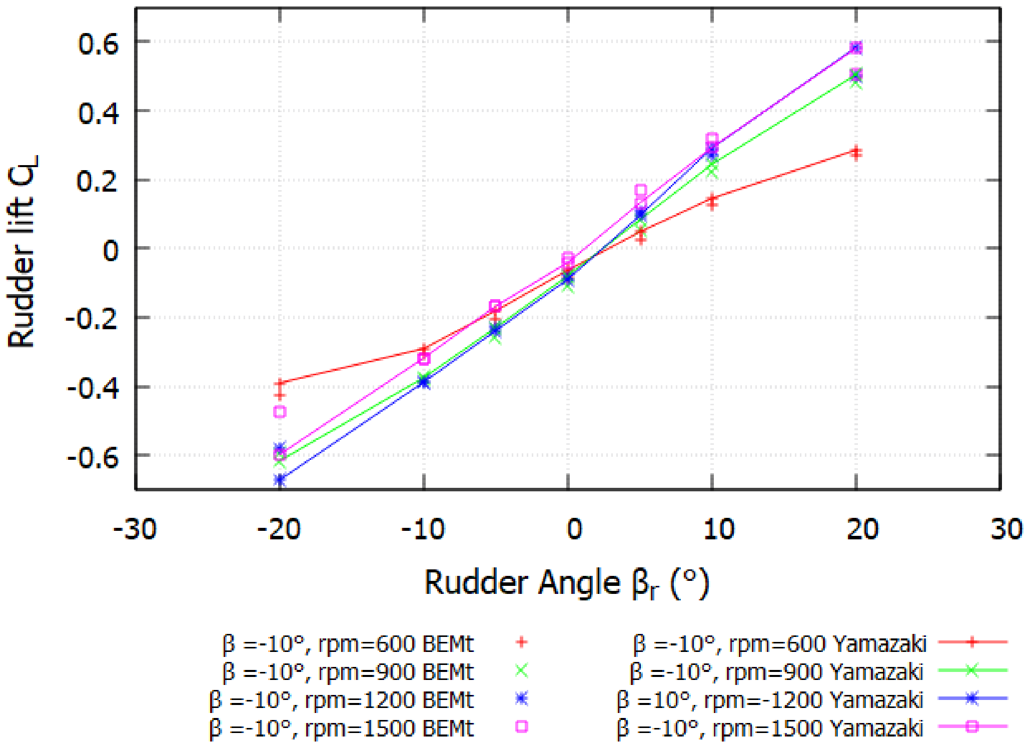

FIGURE 6.31: Effect of propeller revolution on rudder lift predicted by BEMt and Yamazaki at -10 °drift

6.3.2.4 Influence of drift on the hull-propeller-wake interaction

As mentioned in section 2.2.4, thrust deduction t and wake fraction ω_t are two important parameters used to measure the hull-propeller and hull-wake interactions. The hull efficiency η_H is defined as:

$$\eta_H = \frac{1-t}{1-\omega_t} \tag{6.3}$$

Therefore, the interaction effect parameters $1-t$ and $1-\omega_t$ play a vital role in the hull efficiency, subsequently the overall propulsive efficiency of the ship. The computed results are based on the simulations with the use of the BEMt propeller model.

In order to investigate the impact of static drift and rudder angle on the interaction effects between the hull, propeller, and wake, Table 6.12 presents the thrust deduction and wake fraction for all considered cases. The effective wake fraction is derived based on the thrust identity method. In addition, the hull efficiency η_H for three drift scenarios are plotted in Figures 6.32 to 6.34. It is found that the optimal hull efficiency occurs at zero rudder angle (β_r =0 °) for all propeller revolution rates when the drift angle is 0 °and +10 °. Conversely, under -10°drift conditions, the hull efficiency reaches its peak at an approximate rudder angle of +5°.

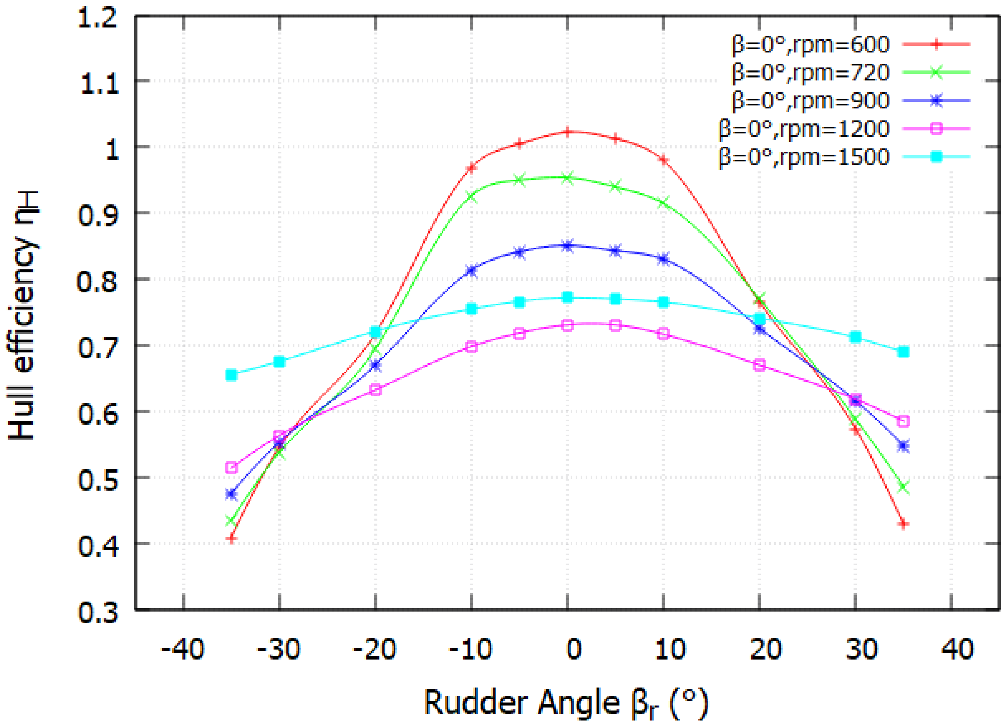

FIGURE 6.32: Hull efficiency η_H at 0 °drift

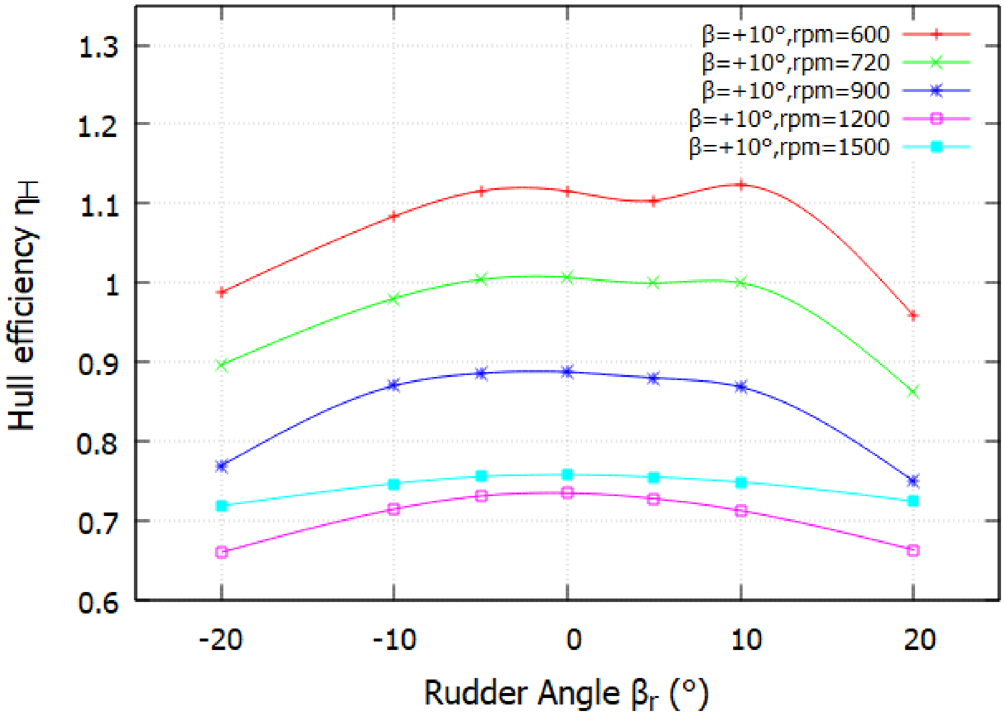

FIGURE 6.33: Hull efficiency η_H at +10 °drift

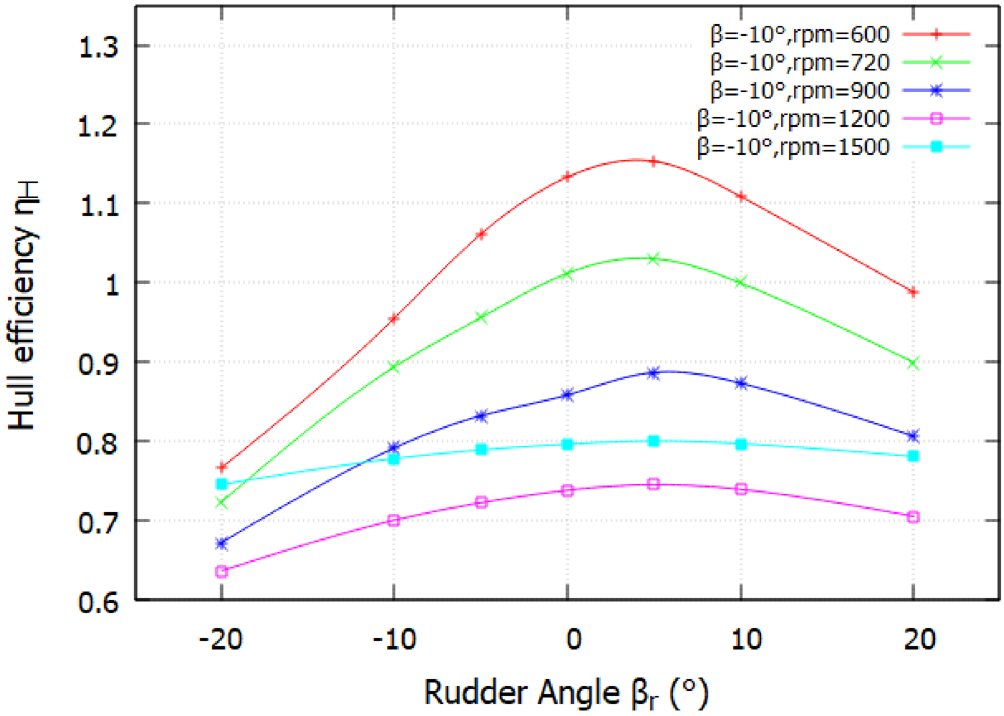

FIGURE 6.34: Hull efficiency η_H at -10 °drift

TABLE 6.12: Thrust deduction and wake fraction in three drift conditions, predicted by BEMt under five different propeller revolutions' conditions

		β=0 °	β=+10 °	β=-10 °	β=0 °	β=+10 °	β=-10 °
	β_r (°)	$1-t$	$1-t$	$1-t$	$1-\omega_t$	$1-\omega_t$	$1-\omega_t$
600rpm	-20	0.593	0.836	0.637	0.826	0.846	0.832
	-10	0.826	0.928	0.812	0.852	0.856	0.850
	-5	0.859	0.959	0.910	0.854	0.859	0.858
	0	0.875	0.960	0.977	0.856	0.860	0.862
	5	0.866	0.950	0.993	0.855	0.861	0.861
	10	0.837	0.969	0.953	0.854	0.862	0.859
	20	0.643	0.792	0.841	0.840	0.826	0.851
720rpm	-20	0.620	0.815	0.653	0.893	0.909	0.903
	-10	0.848	0.901	0.822	0.915	0.919	0.920
	-5	0.873	0.925	0.885	0.918	0.921	0.925
	0	0.877	0.929	0.941	0.919	0.923	0.930
	5	0.864	0.923	0.959	0.919	0.923	0.930
	10	0.841	0.924	0.930	0.919	0.924	0.930
	20	0.697	0.775	0.831	0.905	0.898	0.924
900rpm	-20	0.675	0.782	0.689	1.008	1.017	1.026
	-10	0.832	0.896	0.823	1.023	1.029	1.039
	-5	0.867	0.915	0.871	1.030	1.033	1.047
	0	0.880	0.918	0.902	1.033	1.035	1.051
	5	0.871	0.910	0.935	1.032	1.034	1.054
	10	0.855	0.899	0.922	1.030	1.034	1.056
	20	0.739	0.766	0.846	1.018	1.020	1.049
1200rpm	-20	0.756	0.803	0.764	1.195	1.216	1.201
	-10	0.840	0.876	0.849	1.203	1.226	1.212
	-5	0.869	0.900	0.879	1.208	1.231	1.217
	0	0.886	0.907	0.901	1.212	1.234	1.221
	5	0.885	0.897	0.910	1.211	1.231	1.222
	10	0.867	0.876	0.904	1.209	1.229	1.223
	20	0.808	0.814	0.860	1.206	1.227	1.219
1500rpm	-20	0.856	0.874	0.869	1.186	1.215	1.166
	-10	0.897	0.910	0.908	1.188	1.218	1.167
	-5	0.913	0.922	0.921	1.190	1.219	1.168
	0	0.920	0.927	0.931	1.192	1.223	1.169
	5	0.919	0.924	0.936	1.194	1.223	1.169
	10	0.914	0.916	0.932	1.194	1.224	1.170
	20	0.885	0.888	0.914	1.194	1.225	1.171

6.4 Chapter summary

Accurately predicting the overall propulsive efficiency of the integrated hull-propeller-rudder configuration presents a significant challenge due to the complex fluid hydrodynamics surrounding the vessel's stern region (Badoe et al. 2016). Upon addressing this issue in the context of ship manoeuvres, the introduction of drift and rudder angle parameters further exacerbates the complexity of the problem. Therefore, it is of great significance to study the effect of effective drift and rudder angle on the hull-propeller-rudder interaction.

This chapter mainly provides a methodology for studying the fully-appended KCS subject to static drift angles in conjunction with an array of rudder angles, which can represent quasi-static phases of an actual ship manoeuvre. This innovative approach removes the need for modelling the complete time varying manoeuvre, which greatly reduces the computational expenses and provides a reference for experimental measurement of hull and appendage forces when the angle of drift is applied (Zhang et al. 2022). Compared to Chapter 5, the free surface effect is considered in this chapter, which makes simulation closer to reality in contrast to the double body approach, although the computational cost is considerably increased. The free surface also contributes to wave-making resistance, making the predicted ship resistance better in agreement with EFD data. However, the unsteady flow conditions introduced by the free surface also cause fluctuations in the loading experienced by the hull, propeller and rudder, thereby altering their actual hydrodynamic performance compared to the double body method.

The details of the drift effect on the hull-propeller-rudder-wake interaction are demonstrated from the numerical results derived. When the non-zero drift angle is applied, the drag, and lateral force experienced by the hull increase with the increasing rudder angle magnitude. The presence of the rotating propeller tends to intensify this increasing trend. Meanwhile, the rudder forces are mainly dependent on the upstream propeller performance. Higher propeller loading tends to shift the rudder lift and can delay the rudder stall.

Two body force propeller models are adopted to capture the propeller performance operating in drifting conditions. Overall good agreement of propeller forces is found between the BEMt and the Yamazaki models. However, the propeller thrust discrepancies are more evident at high propeller loading conditions. Body force models are cost-effective methods and can provide a relatively accurate prediction of propeller forces without necessitating the modelling of the actual propeller geometry, thereby significantly reducing the associated computational costs. However, fully discretized propeller modelling remains indispensable when the investigation's emphasis is centred on the local flow characteristics near the stern.

This methodology can be improved by considering other important factors, such as the effect of ship motion, and more thorough verification and validation, particularly for non-zero drift scenarios.

Chapter 7

Influence of drift angle on fully appended KCS in waves

7.1 Introduction

When a ship operates in actual sea states, it encounters various conditions beyond calm waters. These diverse conditions include wave effects, wind conditions, currents, tides, etc. However, one of the most frequent and dominant factors is waves, which could significantly impact the manoeuvring performance of ships. As ship manoeuvring in waves is a complex hydrodynamic problem with the interaction of many factors such as ship resistance, seakeeping, propulsion, and manoeuvrability (Wang & Wan 2018), the understanding of ship manoeuvrability in real sea states is not well developed (ITTC 2021) and manoeuvring prediction capability is still challenging (Sanada et al. 2021). With the rapid development of high-performance computing, studying ship manoeuvring in waves becomes more feasible, as mentioned in section 2.5. However, due to the complex interaction between the hull, propeller, rudder and the surrounding fluid, direct numerical simulation methods are still very costly and time-consuming. Consequently, there remains a great need for a cost-effective approach that enables accurate prediction of ship manoeuvring performance during the early stage of ship design.

From the perspective of green shipping and carbon reduction, it is vital to benefit from wind assistance for ship design when considering the alternative clean fuel source. The use of wind, as one of the most promising ways, can potentially help to realize the goal of decarbonization in the maritime. Therefore, it is essential to gain a full understanding of how the presence of wind assist devices will affect the powering performance of vessels in real seaways. The wind assist system can help reduce the required thrust from the propeller, but meanwhile, it will generate the lateral force on the hull, which results in the ship operating at an angle of drift. The previous two chapters present the influence of static drift and rudder angles on KCS's resistance and propulsion performance in calm water. Based on the experience gained from Chapters 5 and 6, the same methodology is applied in this chapter to investigate the influence of drift angle on fully appended KCS's powering performance in regular waves. The BEMt is chosen for propeller modelling due to its low computational cost requirement compared to a fully discretized propeller and its robustness to capture the non-uniform propeller flow in unsteady conditions, as demonstrated in Windén (2014) and Badoe (2015).

7.2 Numerical setup

This section aims to present the numerical configuration of simulating the fully appended KCS in regular head waves, with a focus on differences between calm water and wave conditions although the overall setup follows the ones presented in section 6.2.

7.2.1 Generalized configurations

The choice of the model scale KCS (L_{pp}=7.2786m) is made for all simulations in this chapter. Mesh generation procedures are the same as the ones presented in section 6.2.5 and the numerical towing tank domain is also generated based on the CFD application guidelines from the ITTC (ITTC 2014). The adopted mesh for each scenario and domain dimensions are the same as that of the previous chapter. In terms of ship motion, the hull is set to free to heave and pitch in resistance tests while fixed in all degrees of freedom for fixed RPM tests.

7.2.2 Wave generation and boundary conditions

The OpenFOAM v7 default wave generator is adopted for wave generation, and the $setWaves$ utility is used to apply specific wave models to the computational domain for case initialisation using level sets for second-order accuracy (OpenFOAM Foundation 2023). In addition, the wave setup in OpenFOAM is achieved using boundary conditions, as shown in Table 7.1, which is almost the same as Table 6.2 but different in U and $alpha$ for the inlet.

Three different lengths of head waves are employed for wave simulations, namely R1, R3 and R5, corresponding to short, medium and long waves. Wavelength and wave amplitude are scaled according to the wave condition of case 2.10 from the 2015 Tokyo workshop (Hino et al. 2020) using the ratio of L_{pp} and details of wave properties are listed in Table 7.2.

TABLE 7.1: Boundary conditions for regular wave simulations

-	Inlet	Outlet	Atmosphere	Hull/Rudder
U	waveVelocity	outletPhaseMeanVelocity	pressureInletOutletVelocity	movingWallVelocity
p	fixedFluxPressure	ZG	totalPressure	fixedFluxPressure
k	FV	inletOutlet	inletOutlet	kqRWallFunction
ω	FV	inletOutlet	inletOutlet	omegaWallFunction
ν_t	FV	ZG	ZG	nutkRoughWallFunction
Fv	FV	FV	FV	FV
alpha	waveAlpha	variableHeightFlowRate	inletOutlet	ZG

TABLE 7.2: Wave properties of three head waves

Parameters	R1	R3	R5
Wave type	Stokes second order wave		
λ/L_{pp}	0.651	1.15	1.951
wavelength (m)	4.735	8.368	14.197
Wave Frequency (Hz)	0.574	0.432	0.332
Wave period (s)	1.741	2.315	3.015
Wave speed (m/s)	2.719	3.615	4.708
Wave number	1.327	0.751	0.443
Amplitude (m)	0.0372	0.0737	0.1175

7.2.3 Simulation conditions

Three sets of simulations are performed on the fully appended model scale KCS in head wave conditions: R1, R3 and R5. The same ranges of drift angle as presented in the previous chapter are applied: β= -10 °, β= 0 °, β= +10 °. In each drift scenario, several static rudder angles are adopted. The wave resistance test (towing condition in head waves) is conducted for all cases (KCS hull with the rudder but without propeller) initially at the ship design speed (F_n=0.26 and ship speed U equals 2.196 m/s. Subsequently, three sets of fixed RPM tests are performed with RPM values = 900, 1200, and 1500 in three head waves using the BEMt propeller modelling approach. The details of the simulation conditions are presented as follows:

- KCS at drift angle, β= 0 °, with five static rudder angles, β_r= -20 °, -10 °, 0 °, 10 °, 20 °.
- KCS at drift angle, β= -10 °, with five static rudder angles, β_r= -20 °, -10 °, 0 °, 10 °, 20 °.
- KCS at drift angle, β= +10 °, with five static rudder angles, β_r= -20 °, -10 °, 0 °, 10 °, 20 °.

7.2.4 Data collection and processing

The introduction of waves during simulations leads to periodic oscillations in computed results, such as the ship resistance, during the converging period. The amplitude of these oscillations varies depending on the wave conditions, as shown in Figure 7.1. Therefore, the simulation results in this chapter are obtained by taking the mean of the signal. In order to ensure the accuracy of the calculated results, a minimum of five complete signal cycles are utilized to derive an averaged outcome. For instance, the wave added resistance R_{AW} is derived by the mean value of the total resistance signal in regular waves and then subtracting the corresponding calm water resistance R_{CW} in the same scenario (applied same drift, rudder angles and ship speed), which is obtained from Chapter 6.

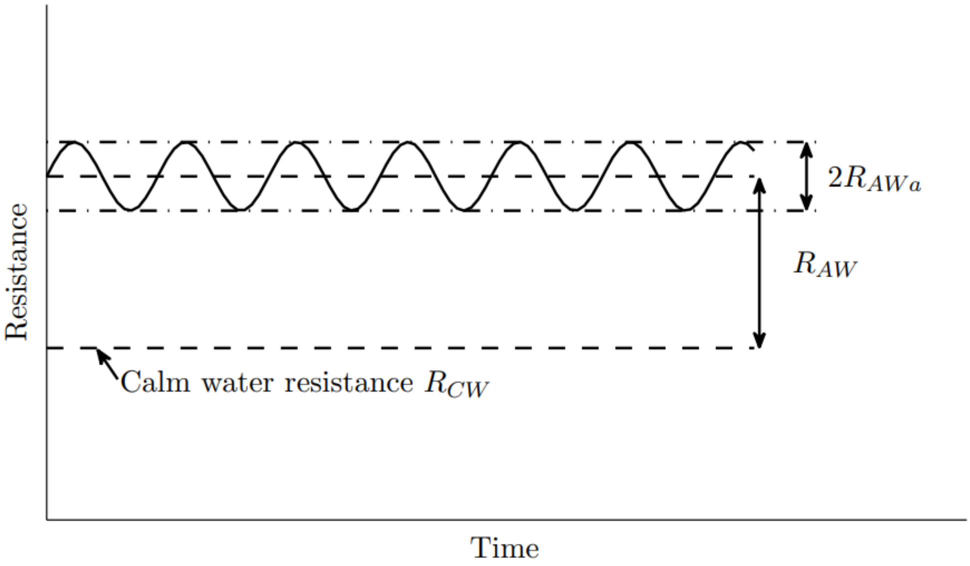

FIGURE 7.1: Definition of measured quantities of added resistance (Windén 2014)

7.3 Results and discussion

7.3.1 Hull-rudder interaction in waves

The plot shown in Figure 7.2 displays the total longitudinal forces of the straight-ahead KCS bare hull, which is the sum of pressure and viscous forces in the x-direction over time for three different regular wave conditions. The mean value is computed by averaging crest or trough values from multiple cycles of converging oscillation periods to determine the total ship resistance in head waves; for instance, the total ship resistance in long wavelength R5 is calculated by taking the mean of the signal from trough values at around t=5s to trough values approximately t=20s, as illustrated on the blue line from Figure 7.2. As the wavelength increases gradually from R1 to R5, the absolute force values also exhibit a dramatically increasing trend.

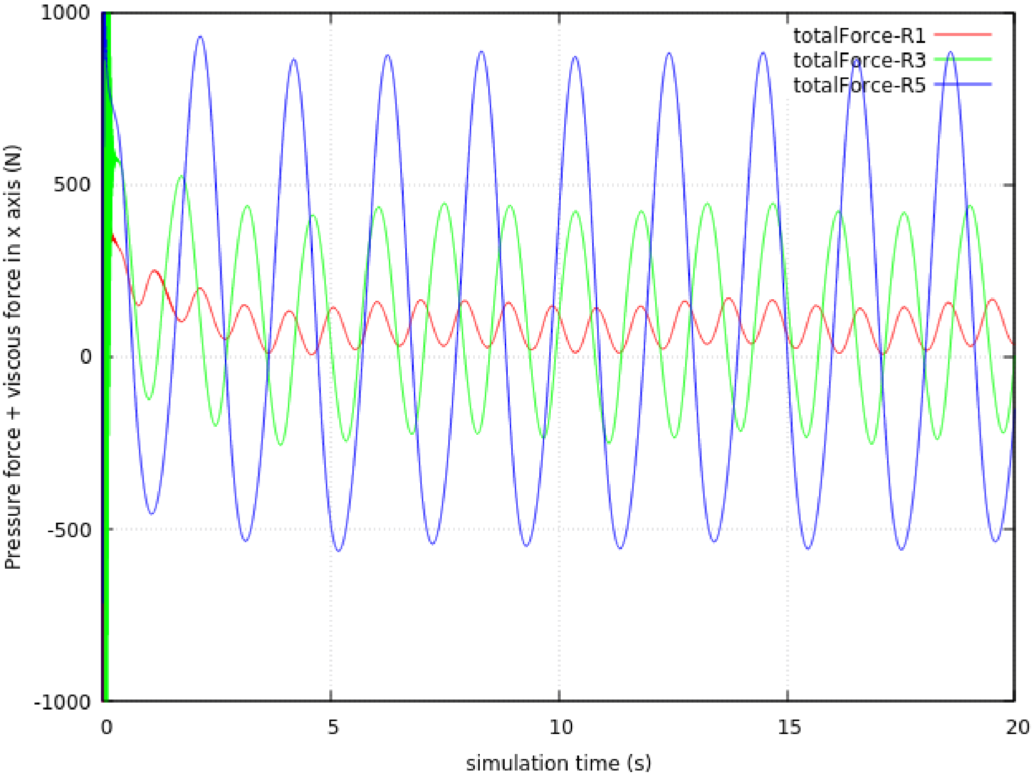

FIGURE 7.2: Time history of zero drift KCS bare hull resistance signals in three regular waves

7.3.1.1 Drift influence on hull forces in waves

- Total resistance, side force and yaw moment

Figure 7.3 displays the total ship resistance C_T of straight-ahead KCS in regular waves, and comparisons are made with EFD data of Southampton model scale KCS. Tests are conducted at Boldrewood Towing Tank of the University of Southampton in September 2022 and the author of this thesis is involved with all experiments and carries out data analysis, which are used for validation and comparison with CFD results. The same scaling approach is used for fitting and scaling, as mentioned in section 6.3.1. Overall, it is evident that ship resistance increases as the wavelength increases. This is due to the higher speed over the hull in scenarios with higher wavelengths, resulting in a higher pressure force component: the values of C_T in R5 are approximately 1.3 times those in R1. CFD calculations exhibit the same variation trend as EFD data, although there are still deviations, especially in medium and long wave cases, approximately 7.3 % and 10.1 % in R3 and R5, respectively, at zero rudder angle. In addition to using an all-movable rudder in EFD, which can produce higher rudder drag in contrast to the fixed rudder skeg in CFD simulations, another possible explanation for the observed discrepancy is that the fluctuating water pressure induced by the wave motion contributes to additional drag force on the rudder, and this effect is likely to be more significant in medium and long wave conditions than short one.

Table 7.3 lists the values of C_T in heading waves for drift KCS. The same phenomena can be found in drift scenarios: longer wavelength leads to higher drag forces. It is interesting to note the applied non-zero drift angles weaken this increasing tendency: the C_T ratio between R5 and R1 is around 1.2, while it is 1.3 in zero drift cases. Overall drift KCS drag trend in the regular waves is similar to that of calm water, as presented in Figure 6.11: the maximum C_T occurs at β_r=+20 °for +10 °drift KCS while at β_r=-20 °when -10 °drift angle is employed.

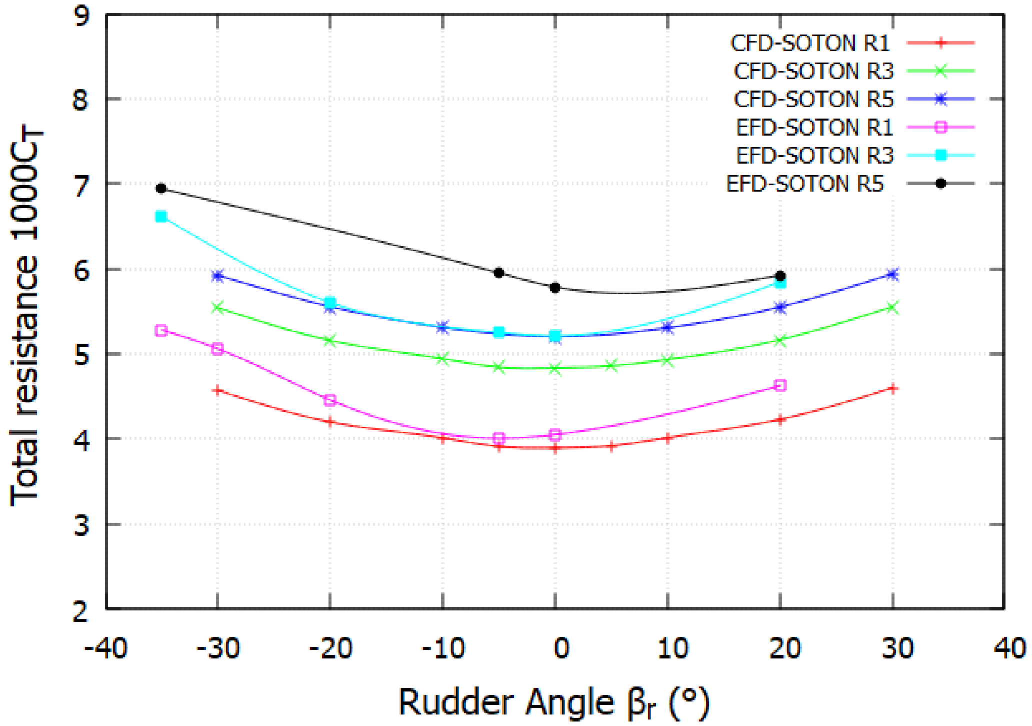

FIGURE 7.3: Comparison of CFD and EFD data for zero drift KCS total resistance coefficient C_T in R1, R3, R5 regular waves

The non-dimensionalized side force coefficients encountered by KCS in three waves are displayed in Table 7.4. In terms of different wave conditions, the highest lateral force is found at medium wave R3 for all drift cases, although differences in F'_Y are relatively tiny for three wavelengths' cases. The employed non-zero drift angle tends to shift the side force curve: a positive drift angle results in an upward shift, while a negative one leads to a downward tendency.

TABLE 7.3: Total ship resistance coefficients $1000C_T$ in head waves R1, R3 and R5 for drift KCS,$\beta = +10$ °, -10 °

$\beta = +10$ °	rudder angle β_r (°)	R1	R3	R5
	-20	5.309	6.078	6.527
	-10	5.040	5.780	6.243
	0	4.906	5.643	6.122
	10	5.186	5.932	6.428
	20	5.707	6.447	6.940
$\beta = -10$ °	rudder angle β_r (°)	R1	R3	R5
	-20	5.710	6.448	6.940
	-10	5.225	5.941	6.458
	0	4.922	5.650	6.142
	10	5.047	5.787	6.271
	20	5.331	6.075	6.547

Table 7.5 demonstrates the non-dimensionalized yaw moment coefficients experienced by drift KCS in waves. In contrast to side force, non-zero drift angles lead to the opposite shift: an ascending displacement of M'_Z curve is observed with a negative drift angle, whereas a positive drift angle leads to a descending trend. In addition, the presence of waves tends to alter the magnitude of the yaw moment coefficient slightly, and the yaw moment increases with the increment of wavelength, which is different from the wavelength influence on the ship's transverse force.

TABLE 7.4: Non-dimensionalized side force coefficients $1000F'_Y$ experienced by the KCS hull in head wave

$\beta = 0$ °	rudder angle β_r (°)	R1	R3	R5
	-30	-0.419	-0.443	-0.433
	-20	-0.351	-0.381	-0.386
	-10	-0.180	-0.197	-0.192
	-5	-0.122	-0.131	-
	0	-0.012	-0.014	-0.007
	5	0.119	0.132	-
	10	0.196	0.207	0.205
	20	0.370	0.393	0.397
	30	0.435	0.453	0.445
$\beta = +10$ °	rudder angle β_r (°)	R1	R3	R5
	-20	2.220	2.558	2.519
	-10	2.459	2.801	2.753
	0	2.705	3.059	2.993
	10	3.017	3.406	3.307
	20	3.140	3.505	3.423
$\beta = -10$ °	rudder angle β_r (°)	R1	R3	R5
	-20	-3.159	-3.485	-3.454
	-10	-3.061	-3.402	-3.338
	0	-2.746	-3.073	-3.025
	10	-2.490	-2.815	-2.774
	20	-2.259	-2.576	-2.554

TABLE 7.5: Non-dimensionalized yaw moment coefficients $1000M'_Z$ encountered by the KCS hull in head wave

$\beta = 0$ °	rudder angle β_r (°)	R1	R3	R5
	-30	-0.0282	-0.0283	-0.0292
	-20	-0.0228	-0.0230	-0.0254
	-10	-0.0138	-0.0133	-0.0156
	-5	-0.0121	-0.0117	-
	0	-0.0053	-0.0042	-0.0060
	5	0.0009	0.0045	-
	10	0.0049	0.0080	0.0061
	20	0.0155	0.0179	0.0167
	30	0.0212	0.0244	0.0201
$\beta = +10$ °	rudder angle β_r (°)	R1	R3	R5
	-20	-1.3331	-1.3699	-1.4337
	-10	-1.3227	-1.3586	-1.4216
	0	-1.3064	-1.3403	-1.4060
	10	-1.2842	-1.3173	-1.3850
	20	-1.2798	-1.3131	-1.3816
$\beta = -10$ °	rudder angle β_r (°)	R1	R3	R5
	-20	1.3024	1.3379	1.3975
	-10	1.3054	1.3378	1.4007
	0	1.3270	1.3620	1.4214
	10	1.3439	1.3754	1.4365
	20	1.3564	1.3906	1.4502

- Added resistance in waves

As shown in Figure 7.1, the added resistance in waves can be obtained by:

$$R_T - R_{CW} = R_{AW} \tag{7.1}$$

Where R_T is the ship total resistance in waves, R_{CW} is the calm water resistance. R_{AW} is the added resistance in waves. A non dimensional added resistance coefficient σ_{AW} can be expressed as:

$$\sigma_{AW} = \frac{R_{AW} L_{PP}}{\rho g \zeta_0^2 B^2} \tag{7.2}$$

Where ζ_0 is the wave amplitude and B is the ship breadth, ρ is the density of water, and g is the gravity acceleration, L_{PP} is the ship length between perpendiculars.

The influence of static rudder angles and wavelength on the non-dimensional added resistance coefficient σ_{AW} of zero drift KCS in three head waves is presented in Figure 7.4. In terms of wave effect, it is found that medium wavelength R3 (λ/L_{PP} = 1.15) induces the highest added resistance while R5 wave (λ/L_{PP} = 1.951) generates the lowest σ_{AW} value. In addition, the effect of the rudder angle on the added resistance is significant, particularly in short wave cases R1. For example, when the rudder angle varies from 0 °to +30 °, the value of σ_{AW} is increased by approximately 27.1 % in R1, while around 6.9% in R3 and 6.3 % in R5. The overall trend is similar for all wave conditions: the applied non-zero rudder angles lead to higher wave-added resistance and the increment depends on the absolute magnitude of the rudder angle.

Figure 7.5 illustrates the effect of drift on added resistance with varying rudder angles in short, medium, and long wave cases. Compared to medium and long waves, more noticeable variation can be found in short wave conditions: the peak of σ_{AW} occurs at β_r = -10 °when the drift angle is -10 °, while the maximum value is at β_r = -20 °for β=+10 °. In contrast to straight-ahead conditions, the influence of wavelength on σ_{AW} does not follow the same trend when the non-zero drift angle is applied: the shorter wavelength tends to induce a higher added resistance coefficient, therefore the highest σ_{AW} can be observed in short wave R1 cases (λ/L_{PP} = 0.651) for both drift scenarios while it happens in medium wave conditions at β= 0 °.

Figure 7.6 presents different model scales of KCS's added resistance coefficient σ_{AW} at straight-ahead conditions from both experimental and numerical results. Experimental results of FORCE, IIHR, and OU are derived from Hino et al. (2020). Overall good consistency is found among all computed results, the maximum σ_{AW} happens at λ/L_{PP}=1.15, which is around the resonance case. Compared to experimental findings from other academic institutions and the computational outcomes from SOTON, there is an evident discrepancy of SOTON experimental data at λ/L_{PP}=1.15 and 1.37, which indicates further repeated tests should be conducted to eliminate experimental uncertainty. However, the numerical analyses from SOTON demonstrate a very good agreement with the experimental datasets presented at the 2015 Tokyo CFD workshop (Hino et al. 2020).

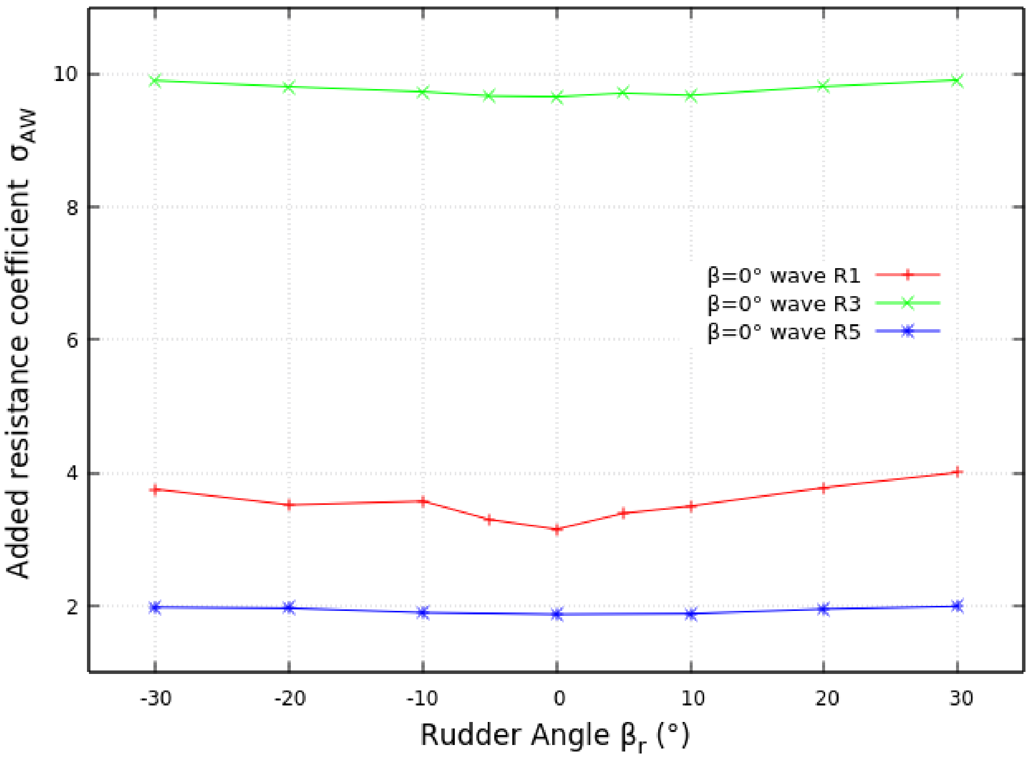

FIGURE 7.4: Influence of static rudder angle on added resistance coefficient σ_{AW} of straight-ahead KCS in three regular waves

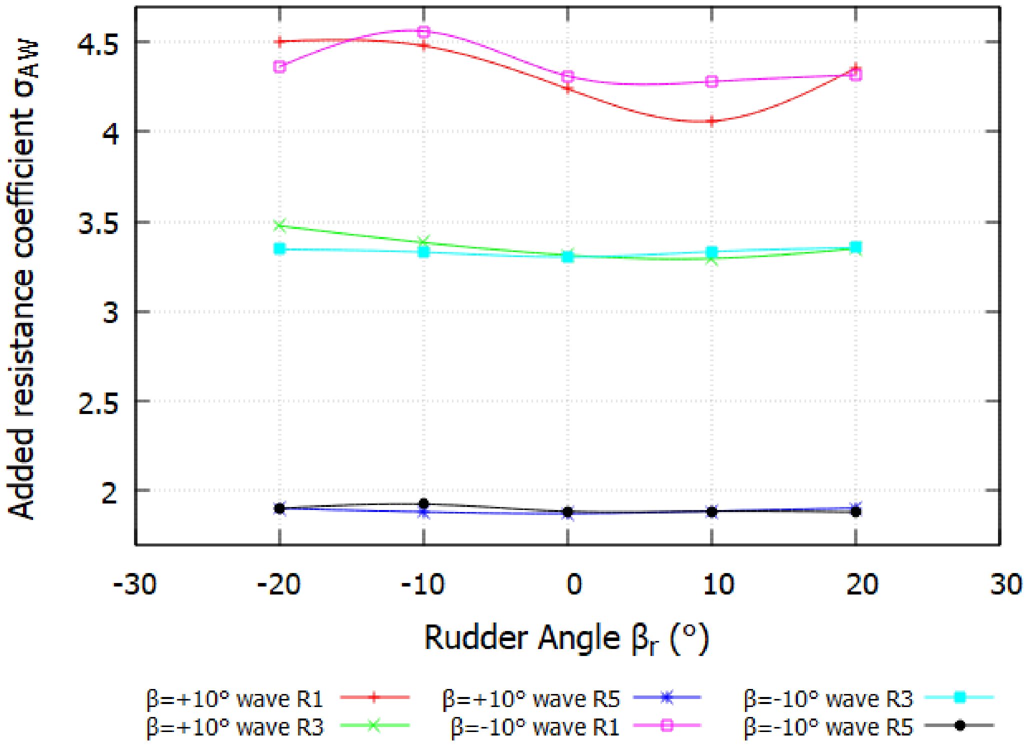

FIGURE 7.5: Influence of drift and rudder angle on added resistance coefficient σ_{AW} of KCS in three different wavelengths' conditions

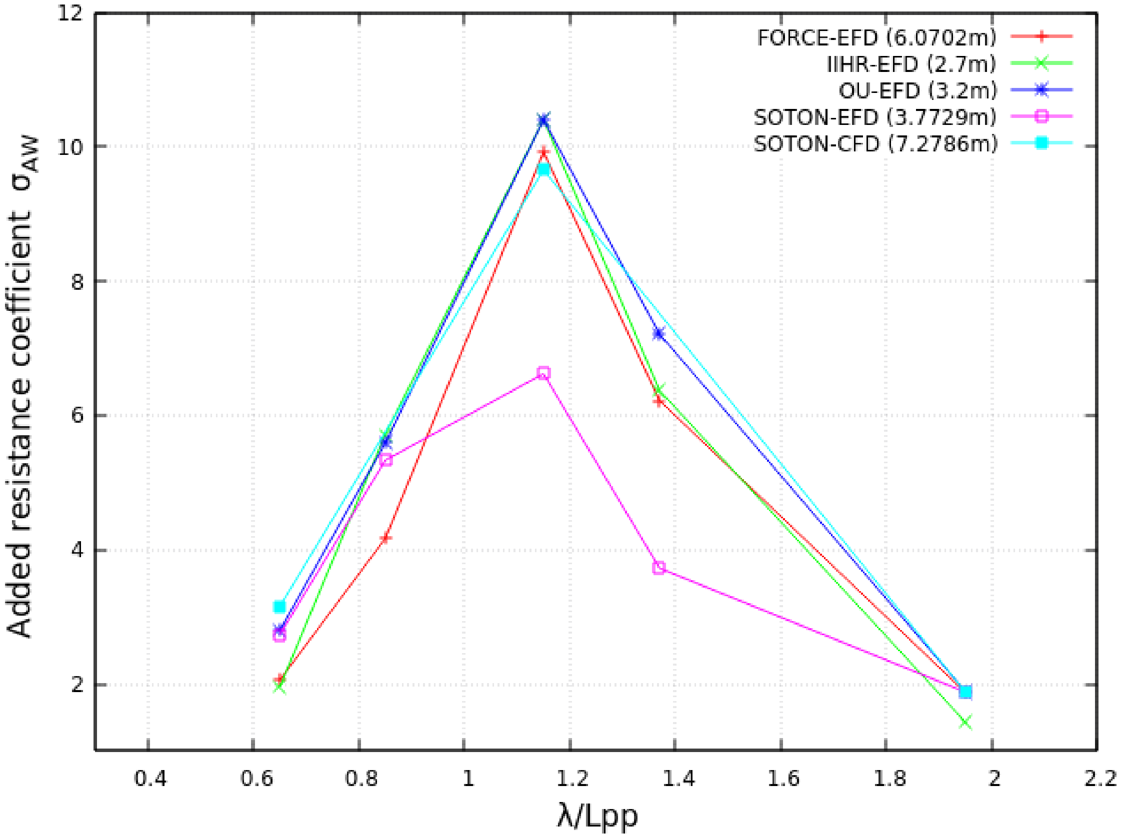

FIGURE 7.6: Comparison between CFD and EFD data for zero drift KCS added resistance coefficient σ_{AW}

7.3.1.2 Influence of drift on rudder forces in waves

The influence of drift angle on rudder forces performance in medium wave R3 is shown in Figures 7.7 and 7.8. Overall rudder forces variation follows the same trend as those in calm water, as shown in Figures 6.14 and 6.15. The presence of head waves leads to the increase of both rudder drag and lift. In terms of drag force, the value of C_D at the largest rudder angle magnitude scenario in R3 is increased by approximately 10.7 %, 13 %, and 4.5% than calm water condition in drift angle of 0 °, +10 °and -10 °, indicating the combination effect of medium wave and positive drift is the most dominant among them. Similarly, the applied drift angle results in the vertical shift of the rudder lift C_L curve and the slope of the curve is steeper in medium wave R3 than that in calm water.

To determine the effect of different wavelengths on rudder forces, rudder drag and lift coefficients in all considered cases are listed in Tables 7.6 and 7.7. It is found that the medium wave R3 condition tends to induce the highest of both C_D and C_L values at most rudder angles for all drift cases though differences between three wave scenarios are quite tiny.

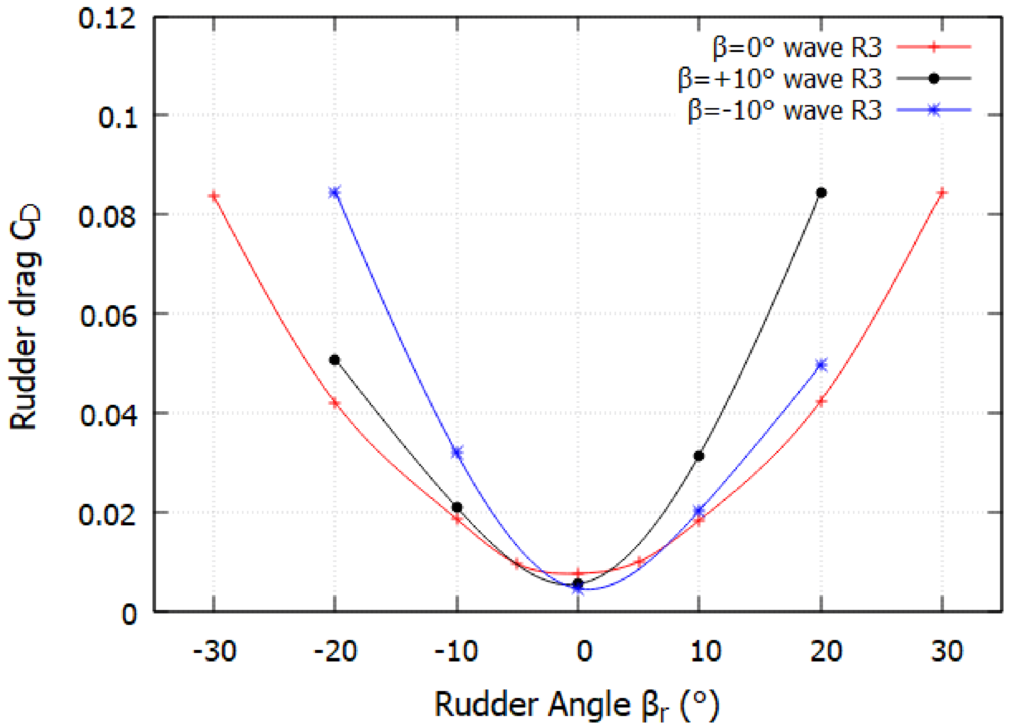

FIGURE 7.7: Effect of drift on rudder drag performance in medium wave R3

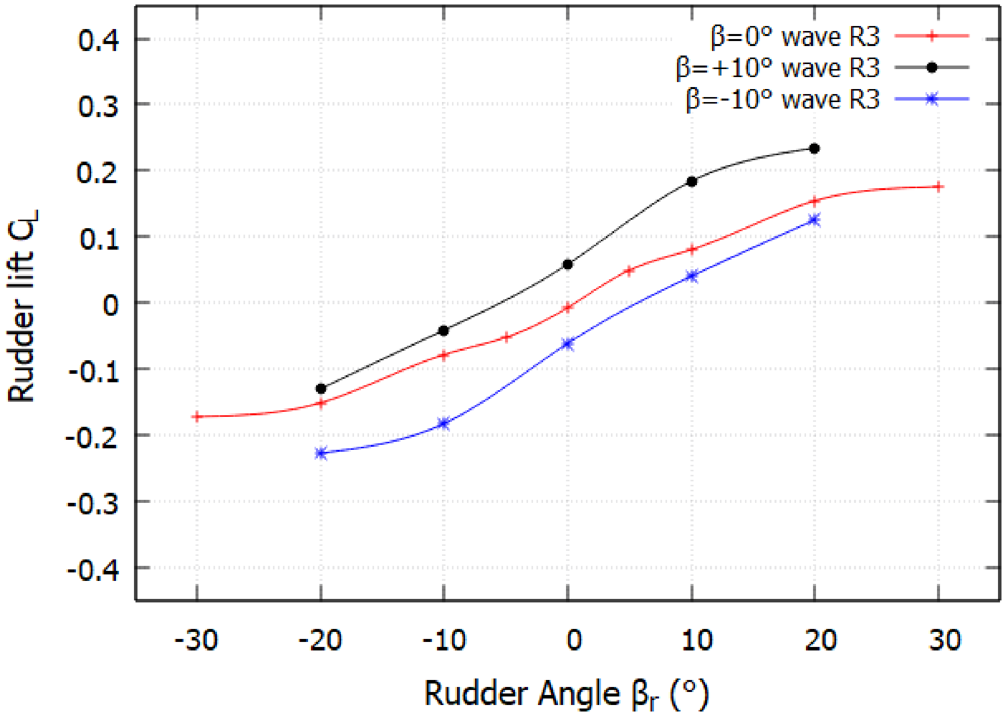

FIGURE 7.8: Effect of drift on rudder lift curve in medium wave R3

TABLE 7.6: Rudder drag coefficients C_D encountered by the KCS rudder in head waves

$\beta = 0$ °	rudder angle β_r (°)	R1	R3	R5
	-30	0.0785	0.0837	0.0831
	-20	0.0386	0.0421	0.0420
	-10	0.0174	0.0187	0.0173
	-5	0.0090	0.0096	-
	0	0.0072	0.0077	0.0066
	5	0.0093	0.0101	-
	10	0.0172	0.0184	0.0171
	20	0.0395	0.0424	0.0419
	30	0.0794	0.0845	0.0838
$\beta = +10$ °	rudder angle β_r (°)	R1	R3	R5
	-20	0.0492	0.0508	0.0478
	-10	0.0202	0.0210	0.0194
	0	0.0052	0.0056	0.0052
	10	0.0319	0.0315	0.0335
	20	0.0844	0.0843	0.0861
$\beta = -10$ °	rudder angle β_r (°)	R1	R3	R5
	-20	0.0848	0.0846	0.0855
	-10	0.0319	0.0319	0.0339
	0	0.0044	0.0046	0.0045
	10	0.0196	0.0203	0.0193
	20	0.0485	0.0496	0.0478

TABLE 7.7: Rudder lift coefficients C_L encountered by the KCS rudder in head waves

$\beta = 0$ °	rudder angle β_r (°)	R1	R3	R5
	-30	-0.1648	-0.1719	-0.1711
	-20	-0.1397	-0.1511	-0.1536
	-10	-0.0725	-0.0782	-0.0766
	-5	-0.0496	-0.0521	-
	0	-0.0071	-0.0071	-0.0050
	5	0.0449	0.0495	-
	10	0.0751	0.0805	0.0776
	20	0.1434	0.1544	0.1545
	30	0.1675	0.1755	0.1728
$\beta = +10$ °	rudder angle β_r (°)	R1	R3	R5
	-20	-0.1247	-0.1299	-0.1216
	-10	-0.0358	-0.0411	-0.0361
	0	0.0606	0.0584	0.0566
	10	0.1746	0.1839	0.1741
	20	0.2314	0.2342	0.2300
$\beta = -10$ °	rudder angle β_r (°)	R1	R3	R5
	-20	-0.2264	-0.2271	-0.2271
	-10	-0.1836	-0.1824	-0.1797
	0	-0.0636	-0.0613	-0.0598
	10	0.0344	0.0403	0.0364
	20	0.1221	0.1256	0.1207

7.3.1.3 Influence of drift on hydrodynamic pressure distribution on free surface

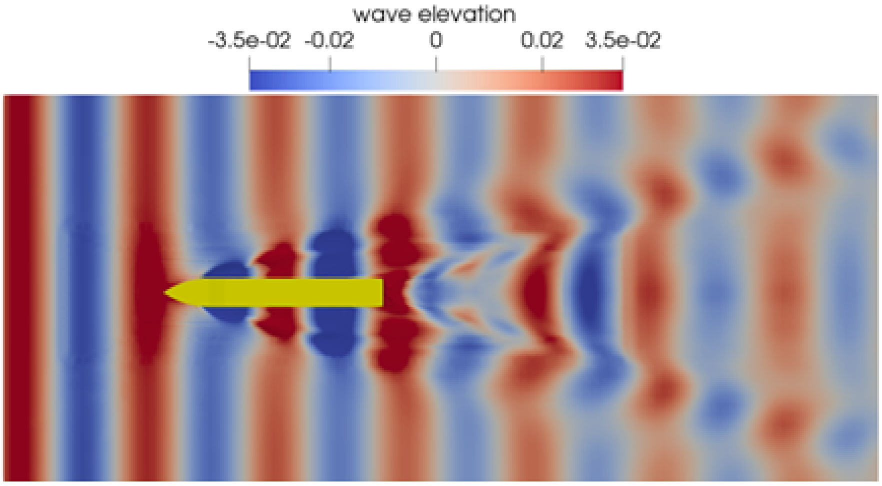

(A) $\beta = 0\,°$, $\beta_r = 0\,°$

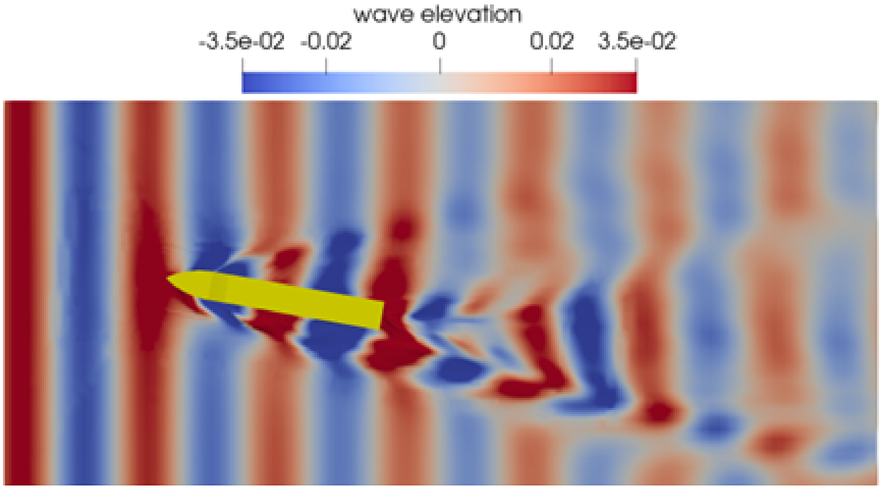

(B) $\beta = +10\,°$, $\beta_r = 0\,°$

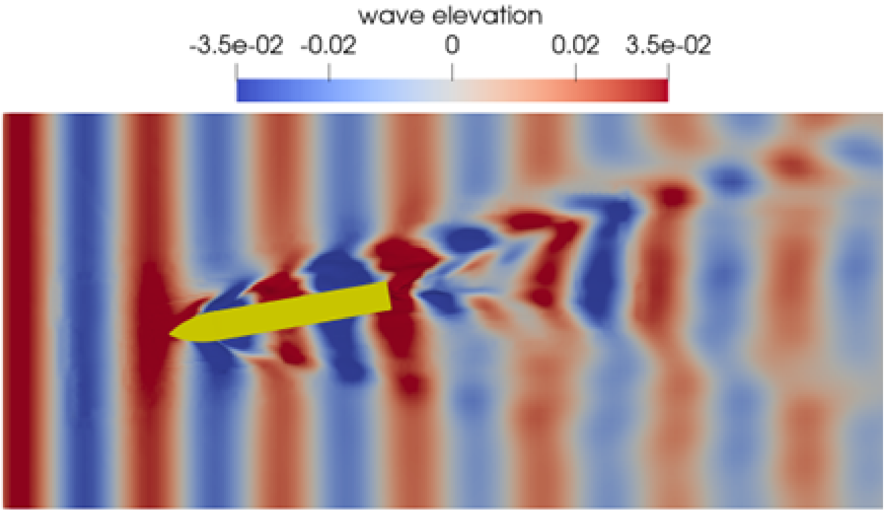

(C) $\beta = -10\,°$, $\beta_r = 0\,°$

FIGURE 7.9: Hydrodynamic pressure distribution on the free surface with different drift angles in short wave R1 (λ/Lpp=0.651) resistance tests, Fn=0.26

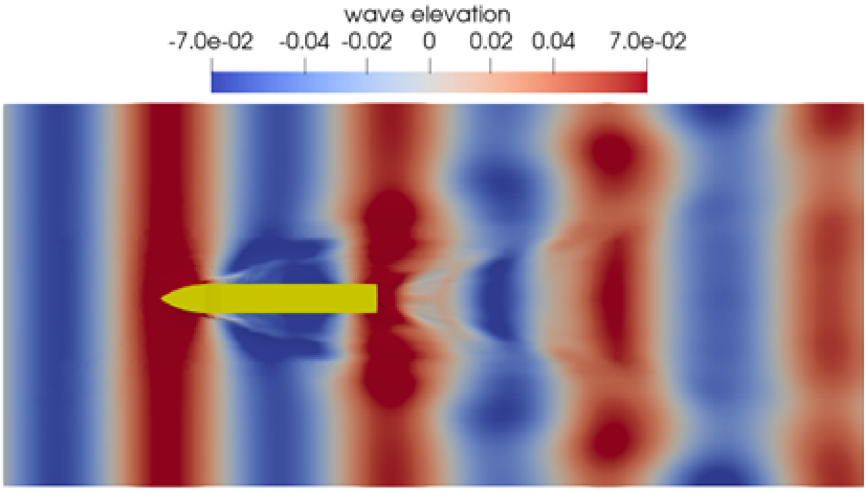

(A) $\beta = 0\,°$, $\beta_r = 0\,°$

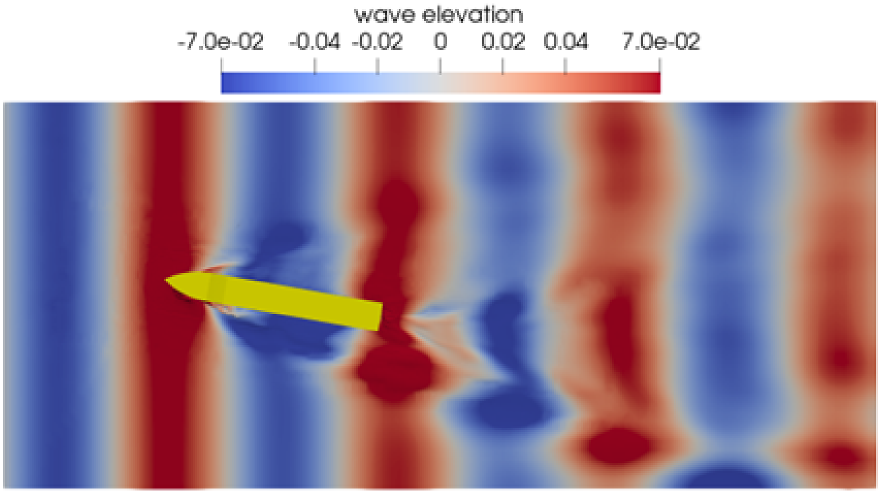

(B) $\beta = +10\,°$, $\beta_r = 0\,°$

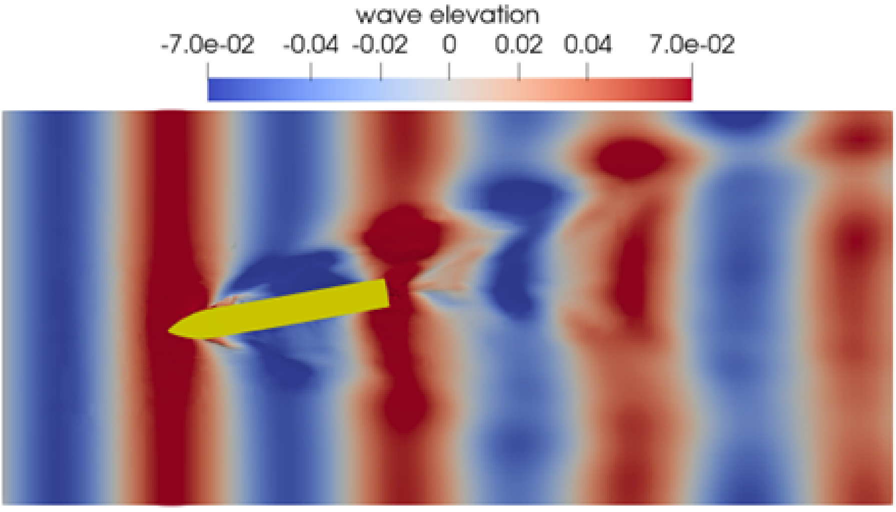

(C) $\beta = -10\,°$, $\beta_r = 0\,°$

FIGURE 7.10: Hydrodynamic pressure distribution on the free surface with different drift angles in medium wave R3 (λ/Lpp=1.15) resistance tests, Fn=0.26

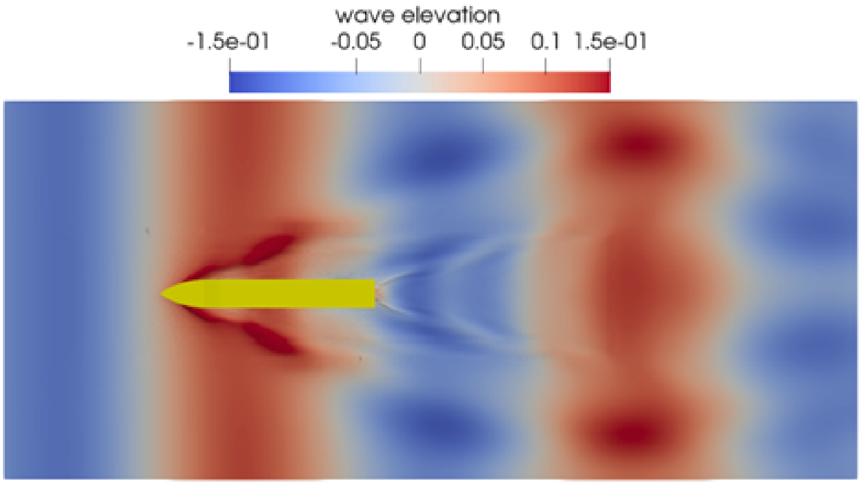

(A) $\beta = 0\,°$, $\beta_r = 0\,°$

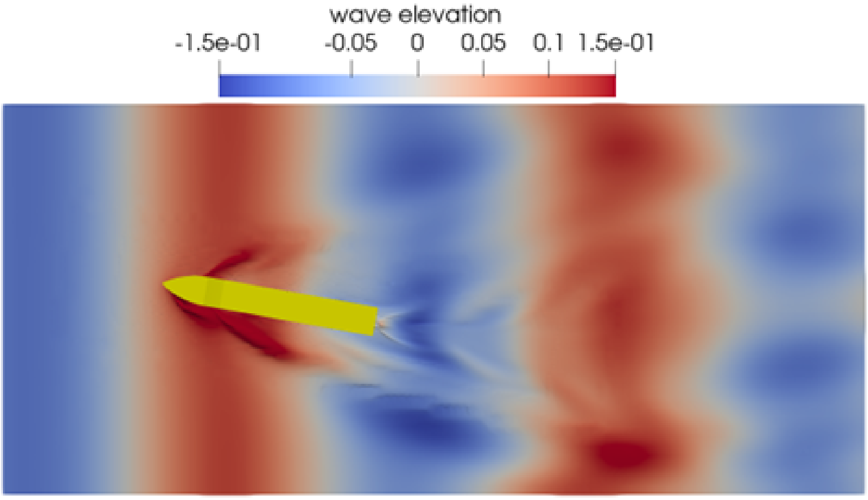

(B) $\beta = +10\,°$, $\beta_r = 0\,°$

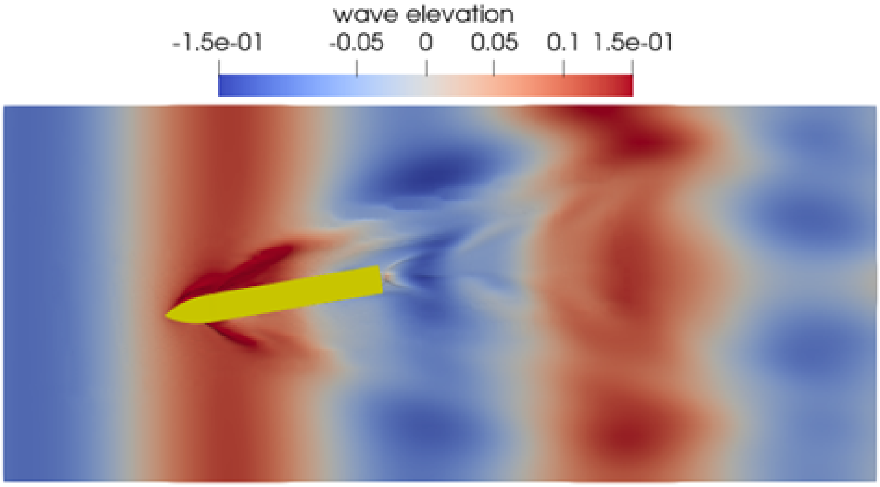

(C) $\beta = -10\,°$, $\beta_r = 0\,°$

FIGURE 7.11: Hydrodynamic pressure distribution on the free surface with different drift angles in long wave R5 (λ/Lpp=1.951) resistance tests, Fn=0.26

7.3.2 Hull-propeller-rudder interaction in waves

The time history of the hull, propeller, and rudder forces in short wave R1 is presented in Figures 7.15 to 7.17. Due to the presence of wave, all the forces oscillate with a certain degree of amplitude but have converged within 5 seconds' simulation time, which corresponds to 75, 100, and 125 propeller revolutions when rpm varying from 900, 1200, to 1500. To ensure to obtain a fully converged solution, the simulation is extended to run for 25 seconds for each rpm value. Compared to forces of the hull and propeller, rudder forces at the high propeller loading, mainly rudder lift, experience more significant oscillation, as shown in Figure 7.17. There are two main possible reasons: 1) High propeller loading induces higher velocity and more swirling flow into the rudder, which can cause irregular pressure distribution and unsteady forces on the rudder; 2) At high thrust loading, the wakefield becomes more asymmetric because of uneven thrust distribution, leading to unsteady forces and oscillation of rudder forces.The studies conducted by Simonsen & Stern (2005), Phillips et al. (2009*b*), and Badoe et al. (2015) emphasize the difficulties in accurately predicting rudder forces, as they involve significant uncertainties and discrepancies between EFD and CFD results. These issues can be mitigated by adopting considerably finer mesh resolutions. Moreover, Date & Turnock (2002) suggests that approximately 5 to 20 million cells are necessary for the complete resolution of rudder forces. By weighing the trade-off between the required calculation accuracy and computational expenses, the mesh resolution implemented in this study can yield relatively accurate predictions of forces associated with ship manoeuvring in wave conditions.

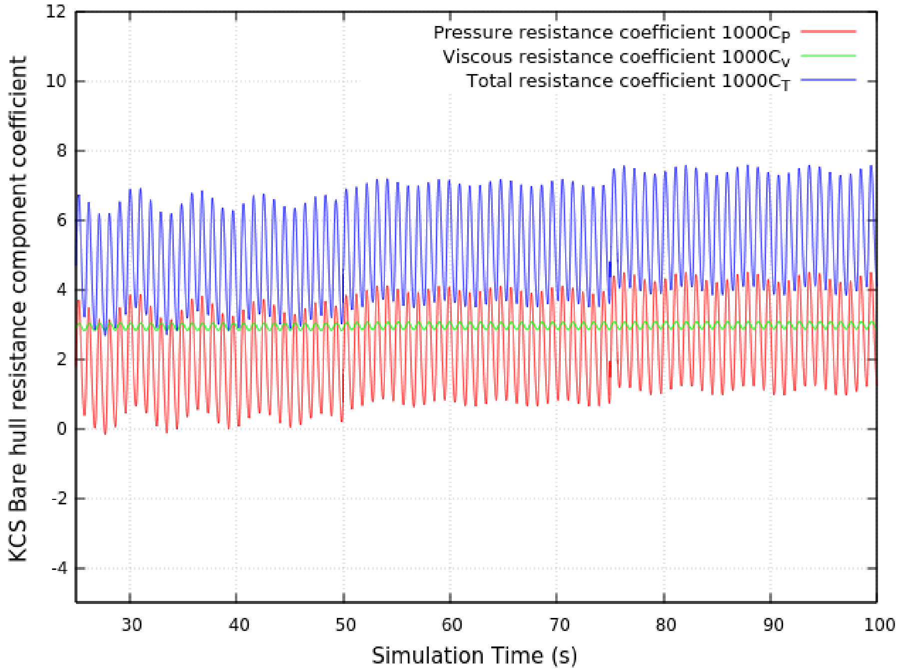

FIGURE 7.12: Time history of hull longitudinal force in short wave R1 with rpm varying from 900, 1200 to 1500, β=0 °and β_r=0 °

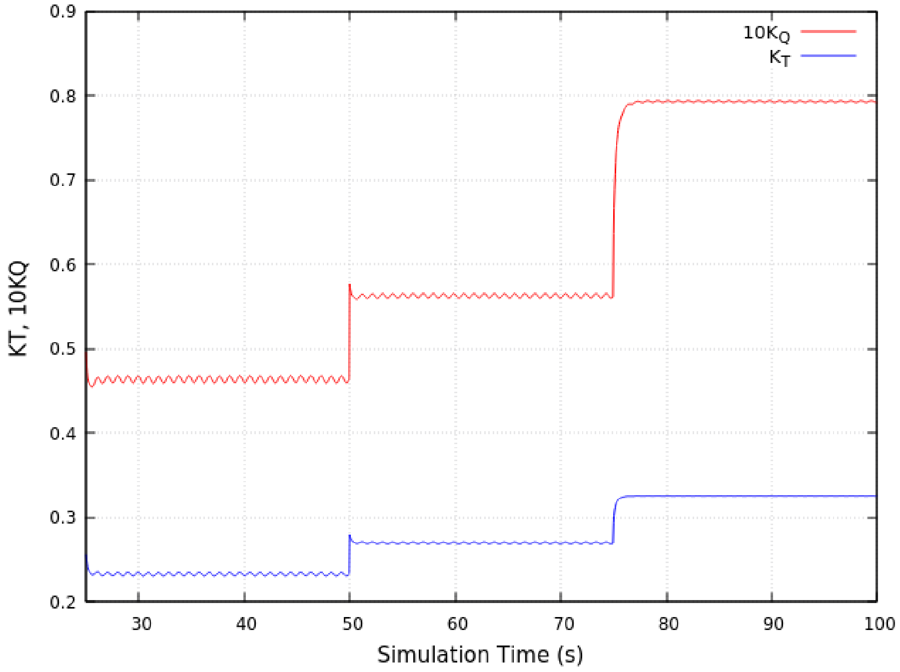

FIGURE 7.13: Time history of propeller forces in short wave R1 with rpm varying from 900, 1200 to 1500, β=0 °and β_r=0 °

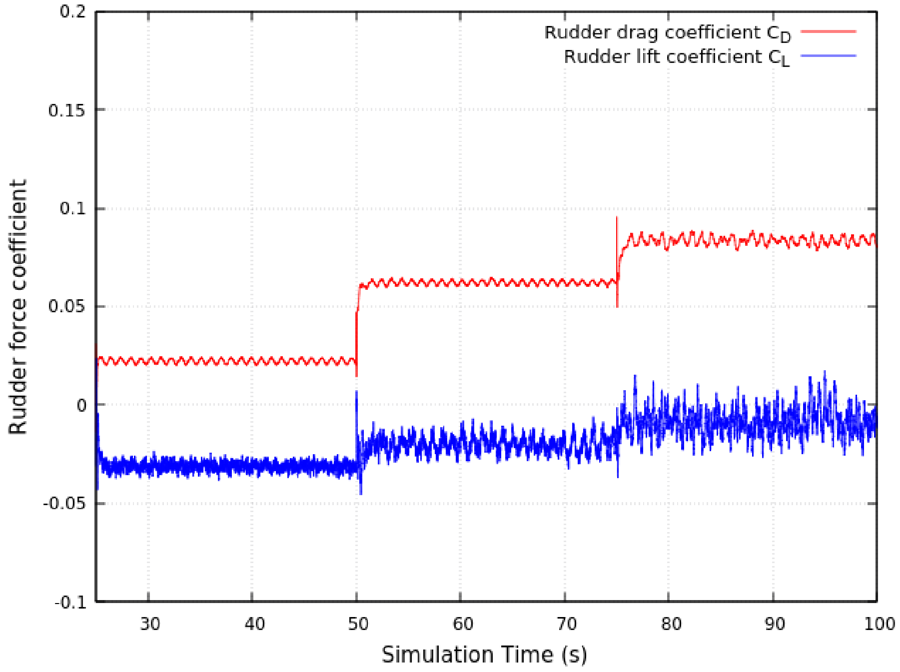

FIGURE 7.14: Time history of rudder forces in short wave R1 with rpm varying from 900, 1200 to 1500, β=0 °and β_r=0 °

7.3.2.1 Influence of drift on hull forces in waves

The effect of drift angle on KCS total resistance coefficients C_T in head waves is presented in Figure 7.15. It is found that the applied non-zero drift angle leads to increases in drag force: the highest C_T occurs at negative rudder angles when a negative drift angle is applied while the maximum happens at positive rudder angles at β=+10 °, although the trend of C_T increasing with rudder angle increments is the same for both drift KCS. However, when the negative static drift is applied, the effect of the rudder angle on drag is more apparent than in positive drift cases. The presence of an operating propeller does not change the influence of wavelength on total drag force: a higher wavelength still induces a higher value of C_T. Figure 7.16 illustrates the effective drift angle influence on the net change of drag forces, benchmarking with zero drift scenarios. Although the applied drift angle results in increments of resistance coefficients in all considered cases: the net change of C_T increases with the ascending of the rudder angle from -20 °to +20 °for β= +10 °while the dC_T decreases with the same variation of the rudder angle for β= -10 °. In addition, different wavelengths also affect the slope of the dC_T curve: for instance, in negative drift cases, the effect of long wave R5 is dominant in the negative rudder angle range while short wave R1 gives the steepest slope. Table 7.8 lists all values of total resistance coefficients in all considered cases and the resistance augments of dC_T benchmarking with calm water scenarios.

In addition to the drag forces, the effect of static drift and rudder angles on KCS lateral force and yaw moment is shown in Table 7.9. Regarding side force encountered by KCS, a non-zero drift angle leads to the vertical shift: upwards for positive drift while downwards for negative drift, the same as the variation trend in calm water scenarios. The presence of waves tends to increase the displacement of the shift, and longer wavelength induces more significant displacement. However, the overall F_Y' curve slope does not change significantly with variations in drift angle and wavelength. When the propeller revolution rates rpm vary from 900 to 1200, the slope of the side force curve in three wave conditions also increases, but the change is very tiny. When the rpm further increases to 1500, the slope exhibits descending trend compared with the 1200rpm case. In terms of the yaw moment on KCS, the influence of drift angle, wavelength and propeller revolution rates on it is similar to side force, but the main difference is positive and negative drift angles lead to downward and upwards shifts, respectively. Compared to the longitudinal forces, it is concluded that the influence of static drift and rudder angle on KCS's transverse forces and yaw moment is less obvious, but it should be bear in mind that these two factors play crucial roles in ship manoeuvring in waves, particularly ship course keeping and turning abilities.

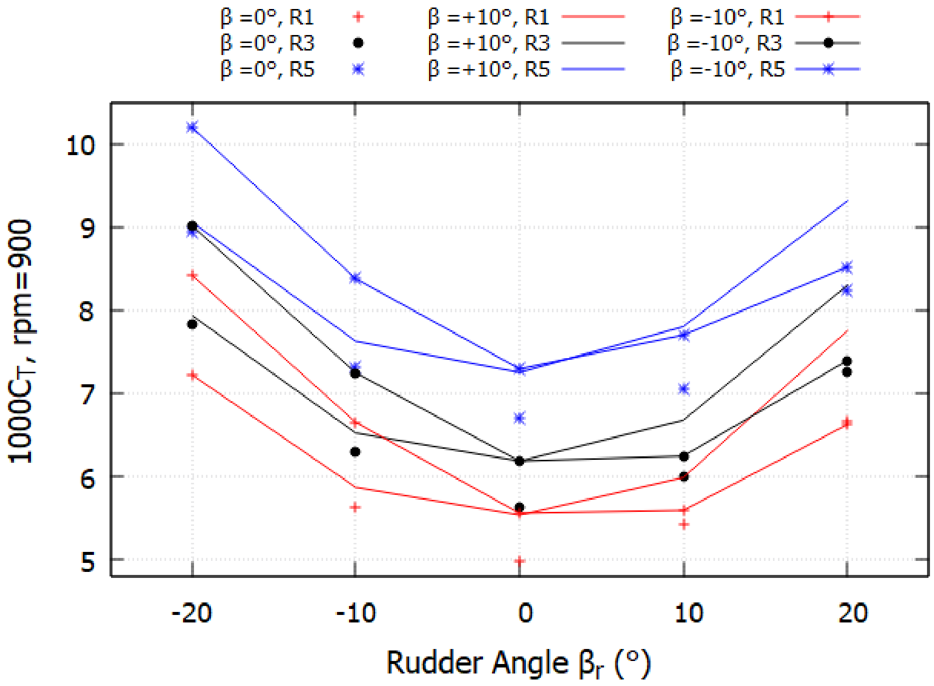

FIGURE 7.15: Influence of drift on KCS resistance in three waves, rpm =900

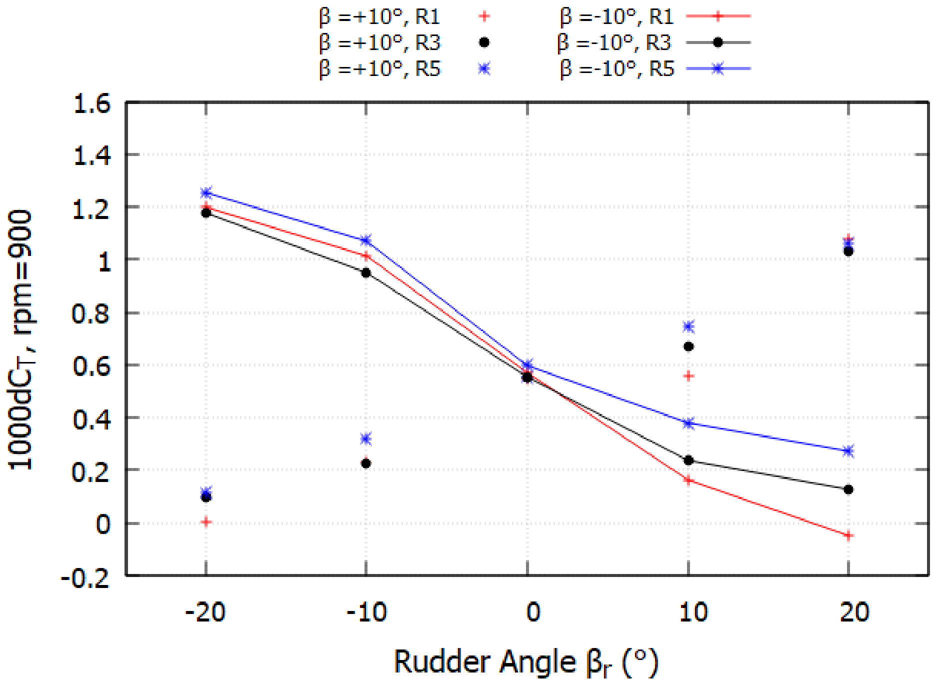

FIGURE 7.16: Influence of drift on KCS resistance augment in three waves, rpm =900, benchmarking with zero drift cases

TABLE 7.8: Total ship resistance coefficients 1000C_T in three waves and augments 1000dC_T benchmarking with calm water scenarios

		β=0 °	β=+10 °	β=-10 °	β=0 °	β=+10 °	β=-10 °
Wave R1	β_r (°)	1000C_T	1000C_T	1000C_T	1000dC_T	1000dC_T	1000dC_T
900rpm	-20	7.220	7.222	8.419	0.334	0.306	0.276
	-10	5.637	5.871	6.651	0.407	0.271	0.235
	0	4.989	5.536	5.560	0.293	0.259	0.147
	10	5.432	5.989	5.595	0.414	0.240	0.229
	20	6.672	7.748	6.624	0.393	0.280	0.310
1200rpm	-20	8.803	8.800	9.935	0.385	0.283	0.233
	-10	7.086	7.145	7.788	0.422	0.243	0.182
	0	5.961	6.449	6.530	0.254	0.225	0.175
	10	6.463	7.323	6.546	0.312	0.245	0.113
	20	7.780	8.963	7.715	0.343	0.259	0.196
1500rpm	-20	9.322	9.432	10.204	0.429	0.190	0.273
	-10	7.701	7.965	8.280	0.433	0.235	0.233
	0	6.613	7.243	7.101	0.238	0.228	0.121
	10	7.002	7.847	7.103	0.327	0.167	0.053
	20	8.109	9.343	8.182	0.245	0.193	0.217
Wave R3							
900rpm	-20	7.838	7.936	9.015	0.951	1.020	0.872
	-10	6.297	6.524	7.247	1.068	0.924	0.832
	0	5.632	6.186	6.186	0.936	0.909	0.773
	10	6.009	6.677	6.247	0.991	0.928	0.880
	20	7.264	8.295	7.392	0.985	0.827	1.078
1200rpm	-20	9.472	9.535	10.560	1.054	1.017	0.858
	-10	7.722	7.823	8.438	1.059	0.921	0.832
	0	6.641	7.106	7.205	0.934	0.882	0.849
	10	7.096	7.971	7.231	0.945	0.892	0.798
	20	8.409	9.568	8.456	0.972	0.864	0.937
1500rpm	-20	9.963	10.167	10.861	1.070	0.925	0.930
	-10	8.323	8.662	8.942	1.054	0.932	0.895
	0	7.274	7.908	7.756	0.898	0.893	0.776
	10	7.647	8.534	7.802	0.972	0.854	0.752
	20	8.759	9.931	8.919	0.895	0.780	0.954
Wave R5							
900rpm	-20	8.942	9.057	10.196	2.056	2.141	2.053
	-10	7.308	7.627	8.378	2.079	2.027	1.963
	0	6.698	7.251	7.294	2.001	1.973	1.881
	10	7.057	7.802	7.700	2.039	2.053	2.330
	20	8.247	9.308	8.518	1.967	1.840	2.205
1200rpm	-20	10.416	10.370	11.666	1.998	1.853	1.963
	-10	8.557	8.712	9.474	1.893	1.811	1.868
	0	7.594	8.010	8.155	1.887	1.786	1.800
	10	8.014	8.782	8.425	1.863	1.704	1.992
	20	9.213	10.440	9.383	1.776	1.736	1.864

TABLE 7.9: KCS side force and yaw moment coefficients $1000F'_Y$ and $1000M'_Z$ in all considered cases

		β=0 °	β=+10 °	β=-10 °	β=0 °	β=+10 °	β=-10 °
Wave R1	β_r (°)	$1000F'_Y$	$1000F'_Y$	$1000F'_Y$	$1000M'_Z$	$1000M'_Z$	$1000M'_Z$
900rpm	-20	-0.952	1.356	-3.858	-0.045	-1.046	0.943
	-10	-0.714	1.900	-3.327	-0.038	-1.010	0.971
	0	-0.077	2.654	-2.668	-0.009	-0.981	1.004
	10	0.816	3.477	-1.814	0.032	-0.936	1.049
	20	1.266	3.950	-1.182	0.056	-0.907	1.078
1200rpm	-20	-0.973	1.410	-3.860	-0.039	-1.028	0.940
	-10	-0.720	1.897	-3.326	-0.030	-1.010	0.974
	0	-0.043	2.686	-2.539	-0.005	-0.971	1.009
	10	0.920	3.525	-1.694	0.040	-0.929	1.051
	20	1.453	4.115	-1.100	0.065	-0.895	1.078
1500rpm	-20	-0.834	1.757	-3.556	-0.024	-0.986	0.964
	-10	-0.577	1.908	-3.137	-0.016	-0.992	0.986
	0	-0.008	2.609	-2.309	-0.001	-0.957	1.018
	10	0.913	3.347	-1.656	0.041	-0.935	1.049
	20	1.338	3.935	-1.070	0.060	-0.887	1.074
Wave R3							
900rpm	-20	-0.946	1.735	-4.230	-0.045	-1.106	0.998
	-10	-0.714	2.272	-3.738	-0.039	-1.081	1.025
	0	-0.073	3.016	-3.045	-0.009	-1.041	1.062
	10	0.813	3.842	-2.185	0.033	-0.998	1.107
	20	1.249	4.348	-1.616	0.056	-0.967	1.137
1200rpm	-20	-0.975	1.773	-4.220	-0.039	-1.091	1.000
	-10	-0.713	2.283	-3.699	-0.031	-1.070	1.032
	0	-0.040	3.059	-2.928	-0.005	-1.033	1.069
	10	0.916	3.885	-2.057	0.041	-0.991	1.112
	20	1.446	4.471	-1.490	0.066	-0.958	1.140
1500rpm	-20	-0.830	2.118	-3.940	-0.024	-1.050	1.025
	-10	-0.573	2.300	-3.520	-0.017	-1.052	1.044
	0	-0.009	2.979	-2.720	0.001	-1.018	1.078
	10	0.900	3.720	-2.026	0.041	-0.981	1.111
	20	1.335	4.288	-1.453	0.060	-0.952	1.137
Wave R5							
900rpm	-20	-0.978	2.027	-4.538	-0.046	-1.222	1.119
	-10	-0.684	2.589	-4.104	-0.036	-1.193	1.143
	0	-0.103	3.332	-3.369	-0.011	-1.157	1.180
	10	0.793	4.157	-2.587	0.030	-1.112	1.211
	20	1.228	4.625	-2.018	0.052	-1.089	1.243
1200rpm	-20	-0.995	2.148	-4.620	-0.039	-1.203	1.116
	-10	-0.642	2.622	-4.077	-0.028	-1.185	1.150
	0	-0.098	3.330	-3.297	-0.006	-1.149	1.185
	10	0.890	4.176	-2.418	0.037	-1.109	1.223
	20	1.407	4.791	-1.852	0.061	-1.077	1.251

7.3.2.2 Drift influence on propeller performance in waves

The presence of the operating propeller accelerates the flow from the upstream hull to the downstream rudder, altering the flow distribution around the rudder. Likewise, when a rudder is positioned behind the propeller, it alters the flow conditions into the propeller plane, changing the actual thrust and torque the propeller induces. The influence of drift angle and rudder angle on the net change of the propeller thrust and torque, dK_T and d10K_Q in regular waves at 900rpm is investigated by comparing the differences in drift and straight-ahead cases, as shown in Figures 7.17 and 7.18.

In terms of propeller thrust augments, the applied drift angle gives rise to the reduction of the thrust coefficient in all considered cases. When the +10 °drift angle is applied, the value of dK_T increases with the rudder angle varying from -20 °to +20 °in three wave conditions. In addition, the wavelength also affects the thrust augment curve: the shorter wavelength tends to have a more negative effect on propeller thrust. In contrast, the negative drift angle leads to the constant descending trend of the dK_T curve when the rudder angle changes from -20 °to +20 °, which indicates the applied negative drift angle has more disadvantageous impacts on propeller thrust coefficients than positive drift conditions. The wavelength effect on the dK_T curve in negative drifting is the same as in positive drift scenarios.

The static drift and rudder angle effect on the propeller torque coefficient is demonstrated in Figure 7.18. In contrast to thrust, the drift effect on torque is more apparent. When the positive drift angle β = +10 °is employed and the rudder angle varies from -20 °to +20 °, the d10K_Q curve exhibits an increasing trend except for the rudder changing from 0 °to +10 °. Besides, the effect of the rudder angle on d10K_Q is almost consistent in three wave conditions: the ratio of d10K_Q values at β_r=-20 °and β_r= +20 °is approximately 1.98, 1.81 and 2.05 in R1, R3 and R5. However, when the negative 10 °drift angle is applied, the d10K_Q exhibits ascending trend when the rudder angle is negative while descending in the positive rudder angle range. The peak of d10K_Q occurs at around -5 °rudder angle. The influence of wavelength on the torque augments is the same as that on thrust augments. Therefore it is indicated that the presence of short wave R1 tends to diminish the performance of propeller forces most in the three considered wave scenarios.

The findings above suggest the possible optimal operation strategy for the ship operating at the angle of drift in regular waves. The values of propeller thrust, torque coefficients in all cases, and their corresponding net changes compared to zero drift are listed in Tables 7.10 and 7.11. It can be concluded that the imposed drift angle adversely impacts propeller performance in head waves to varying extents, which depend on the actual sea states the ship operates in, such as the effective drift angle, geometric rudder angle, wave characteristics, and propeller loading conditions.

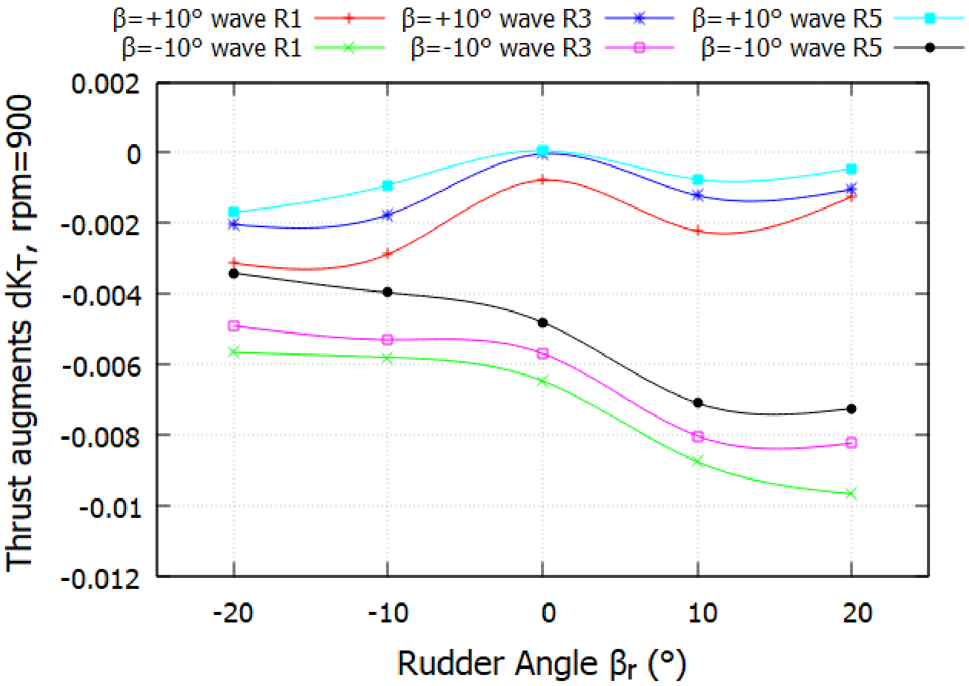

FIGURE 7.17: Effect of drift angle on propeller thrust augments in three waves, rpm =900, benchmarking with zero drift cases

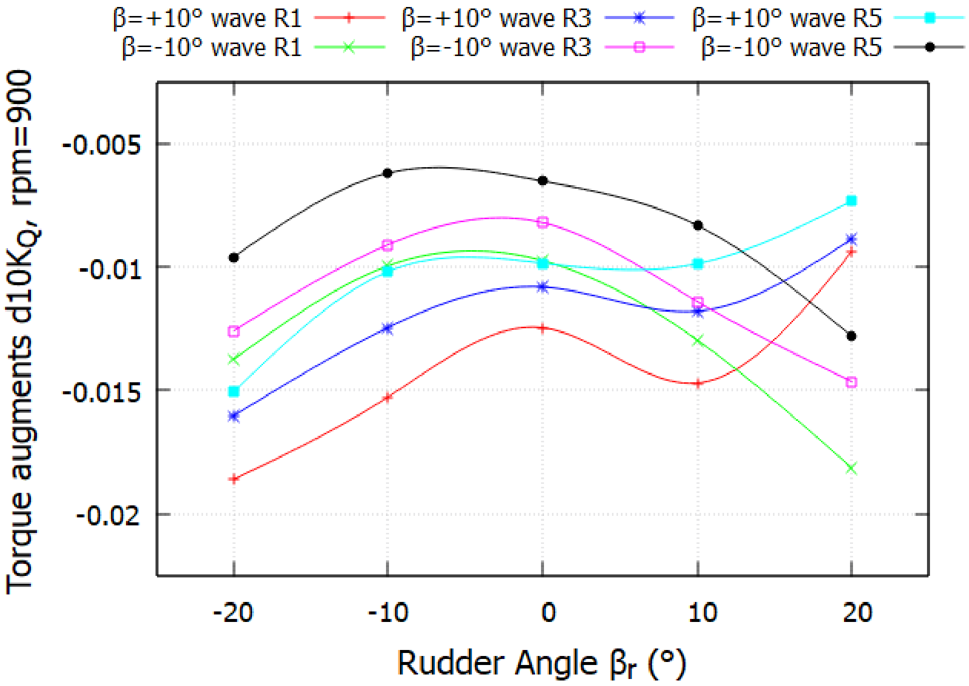

FIGURE 7.18: Effect of drift angle on propeller torque augments in three waves, rpm =900, benchmarking with zero drift cases

TABLE 7.10: Propeller thrust and torque coefficients K_T and $10K_Q$ in all considered cases

		β=0 °	β=+10 °	β=-10 °	β=0 °	β=+10 °	β=-10 °
Wave R1	β_r (°)	K_T	K_T	K_T	$10K_Q$	$10K_Q$	$10K_Q$
900rpm	-20	0.2405	0.2374	0.2349	0.4834	0.4648	0.4696
	-10	0.2365	0.2336	0.2307	0.4708	0.4555	0.4608
	0	0.2331	0.2324	0.2267	0.4637	0.4512	0.4540
	10	0.2346	0.2324	0.2259	0.4665	0.4518	0.4535
	20	0.2377	0.2365	0.2281	0.4742	0.4648	0.4561
1200rpm	-20	0.2736	0.2684	0.2718	0.5754	0.5650	0.5707
	-10	0.2719	0.2663	0.2692	0.5675	0.5566	0.5625
	0	0.2699	0.2651	0.2674	0.5627	0.5524	0.5565
	10	0.2704	0.2660	0.2669	0.5643	0.5556	0.5552
	20	0.2713	0.2665	0.2677	0.5683	0.5560	0.5564
1500rpm	-20	0.3267	0.3217	0.3298	0.8032	0.7779	0.8468
	-10	0.3263	0.3213	0.3294	0.7984	0.7753	0.8419
	0	0.3255	0.3202	0.3291	0.7927	0.7686	0.8385
	10	0.3253	0.3201	0.3289	0.7913	0.7699	0.8361
	20	0.3253	0.3201	0.3288	0.7926	0.7702	0.8355
Wave R3							
900rpm	-20	0.2390	0.2370	0.2341	0.4794	0.4634	0.4668
	-10	0.2348	0.2331	0.2295	0.4665	0.4541	0.4574
	0	0.2316	0.2316	0.2259	0.4601	0.4493	0.4519
	10	0.2331	0.2319	0.2251	0.4626	0.4508	0.4512
	20	0.2363	0.2353	0.2281	0.4707	0.4618	0.4561
1200rpm	-20	0.2729	0.2681	0.2713	0.5734	0.5637	0.5690
	-10	0.2712	0.2662	0.2690	0.5656	0.5555	0.5615
	0	0.2693	0.2645	0.2670	0.5608	0.5503	0.5552
	10	0.2697	0.2655	0.2665	0.5624	0.5537	0.5534
	20	0.2706	0.2661	0.2676	0.5666	0.5551	0.5552
1500rpm	-20	0.3265	0.3220	0.3297	0.8017	0.7787	0.8455
	-10	0.3261	0.3216	0.3294	0.7967	0.7756	0.8406
	0	0.3253	0.3206	0.3290	0.7911	0.7695	0.8373
	10	0.3251	0.3205	0.3289	0.7899	0.7709	0.8353
	20	0.3251	0.3204	0.3288	0.7910	0.7701	0.8356
Wave R5							
900rpm	-20	0.2384	0.2367	0.2350	0.4779	0.4628	0.4683
	-10	0.2339	0.2330	0.2299	0.4637	0.4535	0.4575
	0	0.2311	0.2311	0.2263	0.4580	0.4481	0.4514
	10	0.2326	0.2318	0.2255	0.4608	0.4509	0.4525
	20	0.2358	0.2354	0.2286	0.4691	0.4618	0.4563
1200rpm	-20	0.2724	0.2683	0.2713	0.5719	0.5623	0.5692
	-10	0.2707	0.2662	0.2691	0.5637	0.5542	0.5616
	0	0.2688	0.2646	0.2669	0.5587	0.5493	0.5546
	10	0.2693	0.2654	0.2665	0.5608	0.5515	0.5534
	20	0.2704	0.2664	0.2675	0.5656	0.5550	0.5548

TABLE 7.11: Propeller thrust and torque augments dK_T and d10K_Q benchmarking with zero drift scenarios

		β=+10 °	β=-10 °	β=+10 °	β=-10 °
Wave R1	β_r (°)	dK_T	dK_T	d10K_Q	d10K_Q
900rpm	-20	-0.0031	-0.0057	-0.0186	-0.0137
	-10	-0.0029	-0.0058	-0.0153	-0.0100
	0	-0.0008	-0.0065	-0.0125	-0.0097
	10	-0.0022	-0.0087	-0.0147	-0.0130
	20	-0.0012	-0.0097	-0.0094	-0.0181
1200rpm	-20	-0.0052	-0.0018	-0.0104	-0.0046
	-10	-0.0056	-0.0027	-0.0109	-0.0050
	0	-0.0049	-0.0026	-0.0102	-0.0062
	10	-0.0044	-0.0035	-0.0087	-0.0091
	20	-0.0048	-0.0036	-0.0123	-0.0119
1500rpm	-20	-0.0050	0.0031	-0.0253	0.0436
	-10	-0.0049	0.0032	-0.0231	0.0435
	0	-0.0053	0.0036	-0.0241	0.0458
	10	-0.0052	0.0037	-0.0215	0.0448
	20	-0.0052	0.0035	-0.0223	0.0429
Wave R3					
900rpm	-20	-0.0020	-0.0049	-0.0160	-0.0126
	-10	-0.0018	-0.0053	-0.0125	-0.0091
	0	0.0000	-0.0057	-0.0108	-0.0082
	10	-0.0012	-0.0080	-0.0118	-0.0114
	20	-0.0010	-0.0082	-0.0089	-0.0146
1200rpm	-20	-0.0048	-0.0016	-0.0097	-0.0045
	-10	-0.0051	-0.0023	-0.0101	-0.0041
	0	-0.0047	-0.0023	-0.0105	-0.0056
	10	-0.0042	-0.0032	-0.0087	-0.0090
	20	-0.0045	-0.0031	-0.0115	-0.0114
1500rpm	-20	-0.0045	0.0032	-0.0230	0.0438
	-10	-0.0045	0.0033	-0.0211	0.0439
	0	-0.0048	0.0037	-0.0216	0.0462
	10	-0.0046	0.0038	-0.0190	0.0454
	20	-0.0047	0.0037	-0.0209	0.0446
Wave R5					
900rpm	-20	-0.0017	-0.0034	-0.0151	-0.0096
	-10	-0.0009	-0.0040	-0.0102	-0.0062
	0	0.0001	-0.0048	-0.0098	-0.0065
	10	-0.0008	-0.0071	-0.0099	-0.0083
	20	-0.0004	-0.0072	-0.0073	-0.0128
1200rpm	-20	-0.0042	-0.0011	-0.0096	-0.0026
	-10	-0.0045	-0.0015	-0.0096	-0.0021
	0	-0.0041	-0.0018	-0.0094	-0.0041
	10	-0.0039	-0.0028	-0.0093	-0.0074
	20	-0.0040	-0.0028	-0.0106	-0.0109

7.3.2.3 The drift effect on rudder forces in waves

Accurate assessment of rudder forces when a ship operates in waves is essential for comprehensively understanding ship manoeuvrability and course-keeping capabilities in real seaways. The ship operator has to continuously fine-tune the rudder angle to maintain optimal navigation and performance throughout the vessel's journey. Figures 7.19 and 7.20 present the influence of different rudder angles on rudder force performance when the ship operates at two static drift angles: -10 °and +10 °with propeller revolution rate rpm 900, in three different regular wave conditions.

The varying rudder angles' effect on the rudder drag is studied by comparing the differences in the net drag dC_D of the rudder in two drift conditions (β = +10 °and -10 °), benchmarking with straight-ahead cases (β = 0 °). When the KCS is applied with a positive drift angle, the dC_D curve varies with the increasing trend when the rudder angle changes from -20 °to +20 °. The same tendency can be observed for different wavelength cases, although different wavelengths have a slight effect on the dC_D curve. However, when KCS sails with a negative angle of drift, the varying rudder angles have the opposite effect on rudder drag augments: dC_D shows a descending variation with the rudder angle increasing from -20 °to +20 °. The overall trend for both drift angles is the dC_D curve exhibits central symmetry at the origin point, and the wave effect on rudder drag augments is relatively minor.

Likewise, the effect of drift angle on rudder lift augments in head waves is illustrated in Figure 7.20. The positive and negative drift angles yield corresponding positive and negative values of dC_L, respectively, but the overall variation trend of the lift augment curve is the same for both drifts: dC_L increases when the rudder varying from -20 °to 0 °, then shows the slightly descending and ascending trends when β_r changes from 0 °to +20 °. In addition, the presence of shorter wavelengths leads to higher absolute values of dC_L, although dC_L differences in the three waves are not significant.

All values of rudder forces, C_D and C_L and their corresponding augments dC_D and dC_L are listed in Tables 7.12 and 7.13. These values offer an initial estimation of rudder force performance when a ship operates with a drift angle in waves, potentially contributing to more accurate approaches for assessing ship manoeuvring rudder performance in real sea states.

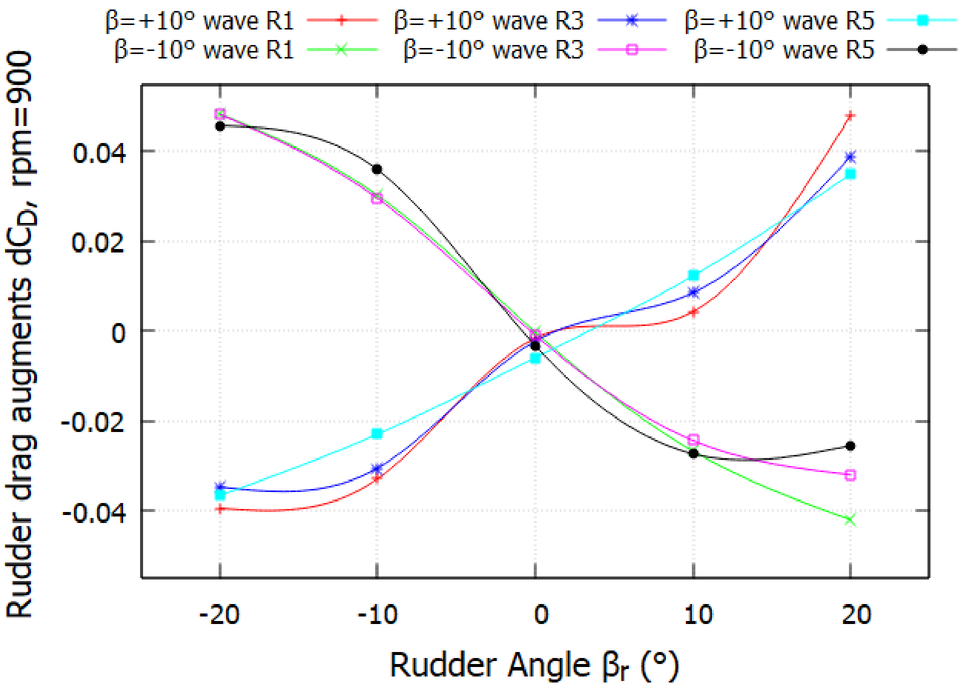

FIGURE 7.19: Effect of drift angle on rudder drag augments in three waves, rpm =900, benchmarking with zero drift cases

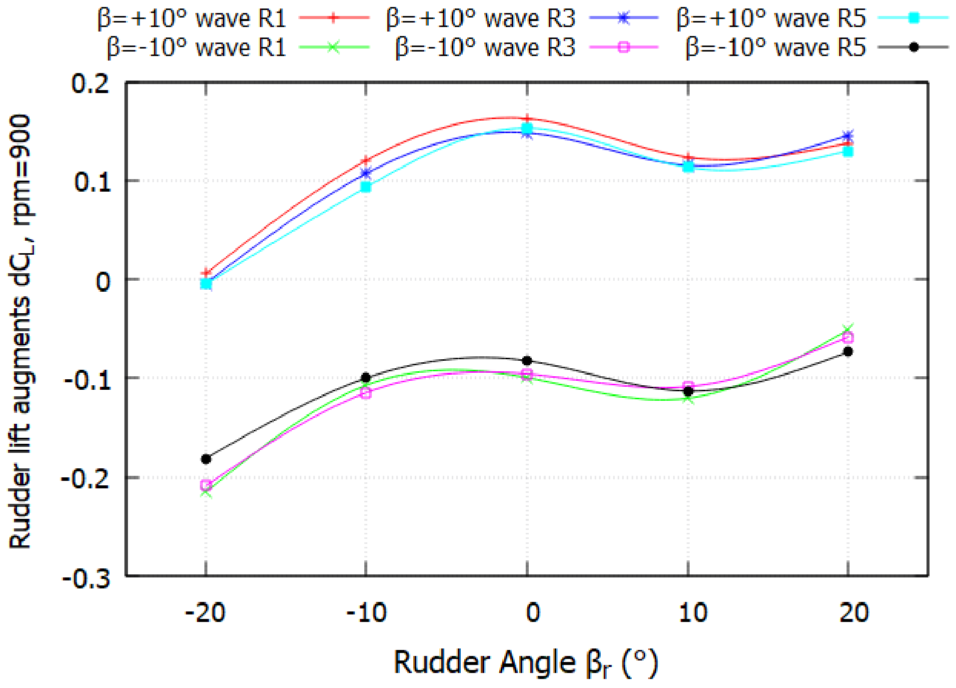

FIGURE 7.20: Effect of drift angle on rudder lift augments in three waves, rpm =900, benchmarking with zero drift cases

TABLE 7.12: Rudder drag and lift coefficients C_D and C_L in all considered cases

		β=0 °	β=+10 °	β=-10 °	β=0 °	β=+10 °	β=-10 °
Wave R1	β_r (°)	C_D	C_D	C_D	C_L	C_L	C_L
900rpm	-20	0.2191	0.1797	0.2675	-0.3892	-0.3835	-0.6044
	-10	0.0857	0.0527	0.1158	-0.2877	-0.1675	-0.3948
	0	0.0223	0.0207	0.0221	-0.0311	0.1314	-0.1305
	10	0.0528	0.0571	0.0261	0.3293	0.4528	0.2090
	20	0.1596	0.2075	0.1176	0.5089	0.6466	0.4580
1200rpm	-20	0.3106	0.2705	0.3617	-0.4061	-0.3755	-0.6045
	-10	0.1575	0.1185	0.1793	-0.2993	-0.1795	-0.3995
	0	0.0621	0.0535	0.0656	-0.0200	0.1399	-0.0793
	10	0.0970	0.1242	0.0658	0.3687	0.4729	0.2584
	20	0.2114	0.2546	0.1692	0.5845	0.7115	0.4944
1500rpm	-20	0.3262	0.2830	0.3580	-0.3588	-0.2601	-0.4930
	-10	0.1800	0.1503	0.1912	-0.2503	-0.1915	-0.3283
	0	0.0835	0.0830	0.0845	-0.0085	0.0952	0.0123
	10	0.1140	0.1310	0.0827	0.3657	0.3872	0.2761
	20	0.2105	0.2525	0.1790	0.5383	0.6246	0.5108
Wave R3							
900rpm	-20	0.2184	0.1837	0.2666	-0.3859	-0.3900	-0.5948
	-10	0.0850	0.0545	0.1146	-0.2866	-0.1797	-0.4013
	0	0.0229	0.0206	0.0220	-0.0294	0.1187	-0.1250
	10	0.0519	0.0604	0.0276	0.3274	0.4427	0.2188
	20	0.1599	0.1986	0.1279	0.5027	0.6483	0.4445
1200rpm	-20	0.3111	0.2749	0.3576	-0.4062	-0.3862	-0.5919
	-10	0.1577	0.1195	0.1788	-0.2953	-0.1847	-0.3909
	0	0.0636	0.0524	0.0660	-0.0201	0.1328	-0.0808
	10	0.0986	0.1217	0.0686	0.3665	0.4596	0.2691
	20	0.2130	0.2515	0.1751	0.5817	0.6980	0.4975
1500rpm	-20	0.3258	0.2878	0.3575	-0.3574	-0.2737	-0.4906
	-10	0.1794	0.1535	0.1925	-0.2476	-0.1948	-0.3243
	0	0.0845	0.0837	0.0835	-0.0109	0.0844	0.0030
	10	0.1140	0.1309	0.0868	0.3596	0.3766	0.2830
	20	0.2120	0.2494	0.1854	0.5372	0.6099	0.5156
Wave R5							
900rpm	-20	0.2239	0.1873	0.2696	-0.3999	-0.4049	-0.5810
	-10	0.0814	0.0584	0.1173	-0.2761	-0.1831	-0.4165
	0	0.0251	0.0192	0.0219	-0.0418	0.1112	-0.1240
	10	0.0542	0.0665	0.0269	0.3210	0.4341	0.2080
	20	0.1587	0.1936	0.1332	0.4962	0.6262	0.4227
1200rpm	-20	0.3140	0.2683	0.3715	-0.4164	-0.3656	-0.6224
	-10	0.1502	0.1170	0.1832	-0.2660	-0.1788	-0.4087
	0	0.0661	0.0521	0.0668	-0.0446	0.1079	-0.0994
	10	0.0992	0.1149	0.0821	0.3580	0.4402	0.2592
	20	0.2076	0.2511	0.1772	0.5683	0.6924	0.4872

TABLE 7.13: Rudder drag and lift augments dC_D and dC_L benchmarking with zero drift scenarios

		β=+10 °	β=-10 °	β=+10 °	β=-10 °
Wave R1	β_r (°)	dC_D	dC_D	dC_L	dC_L
900rpm	-20	-0.0394	0.0484	0.0058	-0.2152
	-10	-0.0329	0.0302	0.1202	-0.1071
	0	-0.0016	-0.0002	0.1625	-0.0994
	10	0.0043	-0.0267	0.1235	-0.1202
	20	0.0479	-0.0420	0.1377	-0.0509
1200rpm	-20	-0.0400	0.0512	0.0306	-0.1984
	-10	-0.0390	0.0218	0.1198	-0.1002
	0	-0.0086	0.0034	0.1599	-0.0593
	10	0.0272	-0.0311	0.1042	-0.1103
	20	0.0432	-0.0422	0.1269	-0.0902
1500rpm	-20	-0.0432	0.0318	0.0987	-0.1342
	-10	-0.0296	0.0113	0.0588	-0.0779
	0	-0.0005	0.0011	0.1037	0.0208
	10	0.0170	-0.0313	0.0215	-0.0896
	20	0.0420	-0.0315	0.0863	-0.0274
Wave R3					
900rpm	-20	-0.0347	0.0483	-0.0041	-0.2089
	-10	-0.0305	0.0295	0.1070	-0.1147
	0	-0.0023	-0.0009	0.1481	-0.0956
	10	0.0085	-0.0243	0.1153	-0.1087
	20	0.0387	-0.0320	0.1456	-0.0582
1200rpm	-20	-0.0361	0.0466	0.0200	-0.1856
	-10	-0.0382	0.0210	0.1106	-0.0956
	0	-0.0112	0.0024	0.1529	-0.0607
	10	0.0231	-0.0300	0.0930	-0.0974
	20	0.0384	-0.0379	0.1164	-0.0842
1500rpm	-20	-0.0380	0.0317	0.0837	-0.1332
	-10	-0.0259	0.0131	0.0528	-0.0767
	0	-0.0008	-0.0010	0.0954	0.0139
	10	0.0169	-0.0272	0.0170	-0.0766
	20	0.0373	-0.0266	0.0727	-0.0216
Wave R5					
900rpm	-20	-0.0366	0.0458	-0.0049	-0.1811
	-10	-0.0230	0.0359	0.0931	-0.1404
	0	-0.0059	-0.0032	0.1530	-0.0822
	10	0.0123	-0.0273	0.1132	-0.1130
	20	0.0349	-0.0255	0.1300	-0.0735
1200rpm	-20	-0.0457	0.0575	0.0508	-0.2060
	-10	-0.0332	0.0330	0.0872	-0.1428
	0	-0.0140	0.0007	0.1525	-0.0548
	10	0.0157	-0.0171	0.0821	-0.0988
	20	0.0435	-0.0304	0.1241	-0.0811

7.3.2.4 Influence of drift on the hull-propeller-wake interaction in waves

- $(1-t)$ and $(1-\omega_t)$

Thrust deduction t and wake fraction ω_t are two critical parameters in assessing a vessel's propulsion efficiency and overall powering performance. To accurately predict the hull efficiency, it is necessary to obtain good estimates of interaction effects $(1-t)$ and $(1-\omega_t)$. Therefore, deriving the optimal hull efficiency requires the knowledge of how to maximize $(1-t)$ and minimize $(1-\omega_t)$ based on equation 6.3. The influence of drift angle on the net change of $(1-t)$ and $(1-\omega_t)$ in waves, benchmarking with straight-ahead KCS, is presented in Figures 7.21 and 7.22. For +10 °drift cases, the $(1-t)$ augments decrease with the varying rudder angle from -20 °to +20 °while this trend is opposite when -10 °'drift angle is applied. Regarding wave influence on the $\mathrm{d}(1-t)$ curve, short wave R1 results in the largest values of $\mathrm{d}(1-t)$ at all rudder angles for both +10 °and -10 °drift angles, while medium wave R3 leads to the smallest values of $(1-t)$ augments. In terms of the drift influence on $(1-\omega_t)$ augments shown in Figure 7.22, +10 °and -10 °drift angle lead to decreasing and increasing trend with the rudder variation from -20 °to +20 °. Regarding the wavelength effect on $\mathrm{d}(1-\omega_t)$, the shortest wave R1 generates the highest $(1-\omega_t)$ augment, and the longest wave R5 induces the lowest value. The values of $(1-t)$, $(1-\omega_t)$ and $\mathrm{d}(1-t)$, $\mathrm{d}(1-\omega_t)$ in all considered cases are listed in Table 7.14 and 7.15.

- Hull efficiency η_H

The influences of different waves and propeller revolution rates on the hull efficiency η_H for three applied drift angles (0 °, +10 °and -10 °) are presented in Figures 7.23 to 7.25. For 0 °and +10 °drift cases, it is found that the optimal hull efficiency occurs at around zero rudder angle while the peak of η_H is located around +5 °rudder angle for -10 °drift cases, which is consistent with the calm water findings presented in section 6.3.2.4. In terms of the propeller revolution rates effect on η_H, the maximum hull efficiency can be found at rpm=900 while the minimum is at rpm=1200. In addition, different wavelengths also impact the distribution of hull efficiency: in all considered cases, the hull efficiency is the best in medium wave R3 conditions, while the worst is found in long wave R5 scenarios. Table 7.16 lists the hull efficiency η_H in all associated cases.

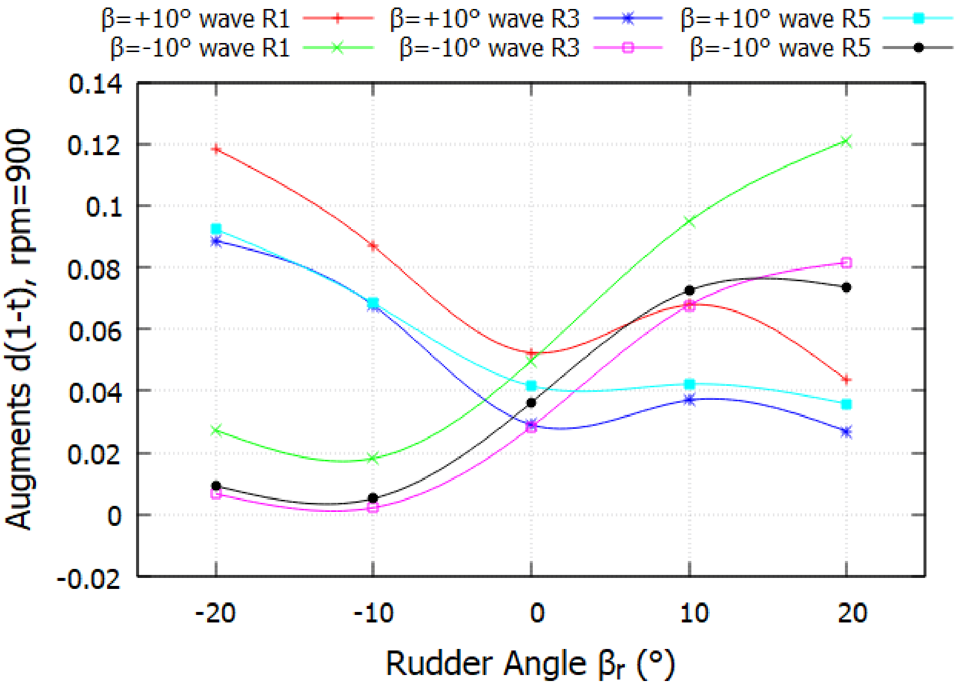

FIGURE 7.21: Effect of drift angle on $1-t$ augments in three waves, rpm =900, benchmarking with zero drift cases

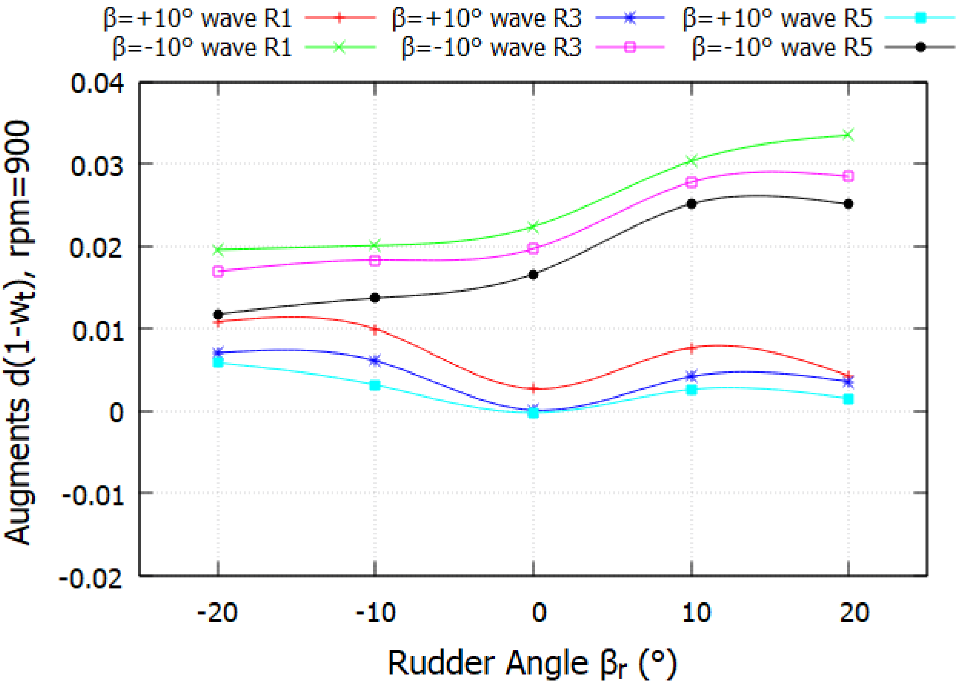

FIGURE 7.22: Effect of drift angle on $1-\omega_t$ augments in three waves, rpm =900, benchmarking with zero drift cases

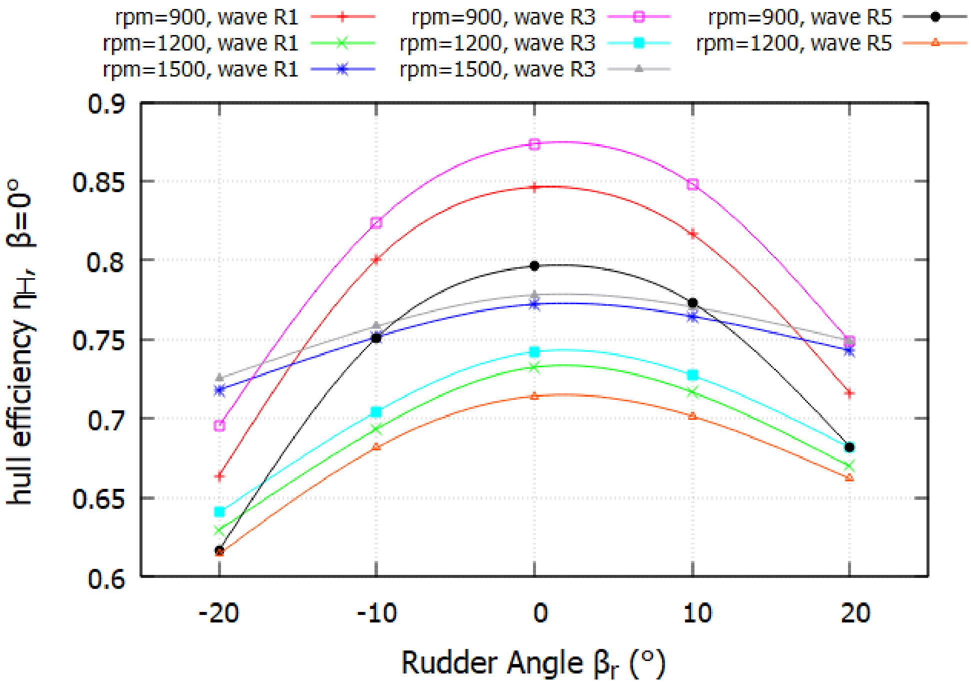

FIGURE 7.23: Effect of rudder angle and propeller revolution rate on hull efficiency η_H in waves, β= 0 °

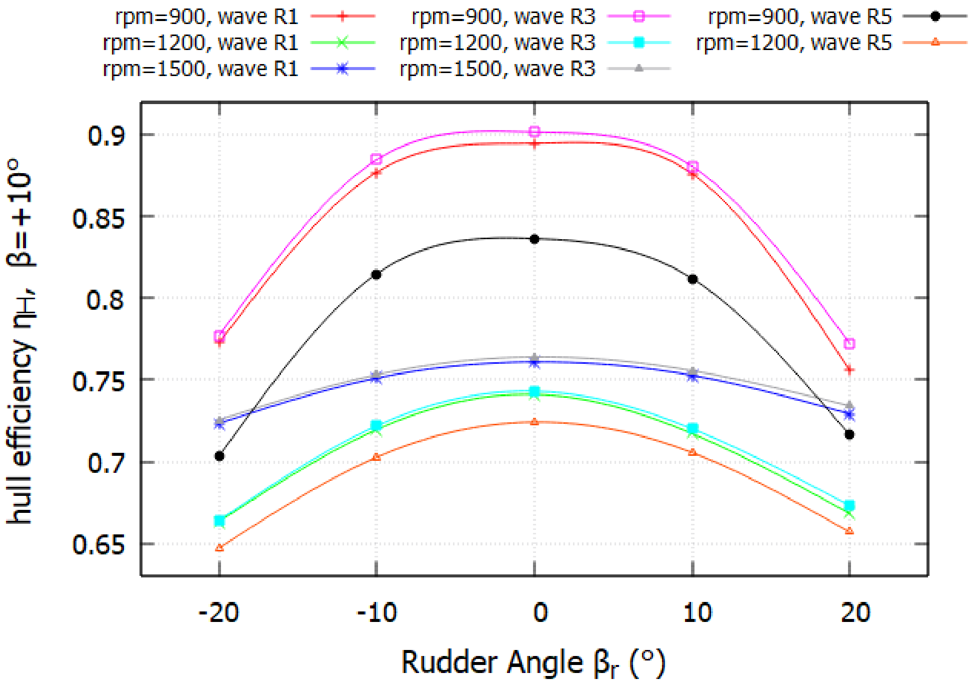

FIGURE 7.24: Effect of rudder angle and propeller revolution rate on hull efficiency η_H in waves, β= +10 °

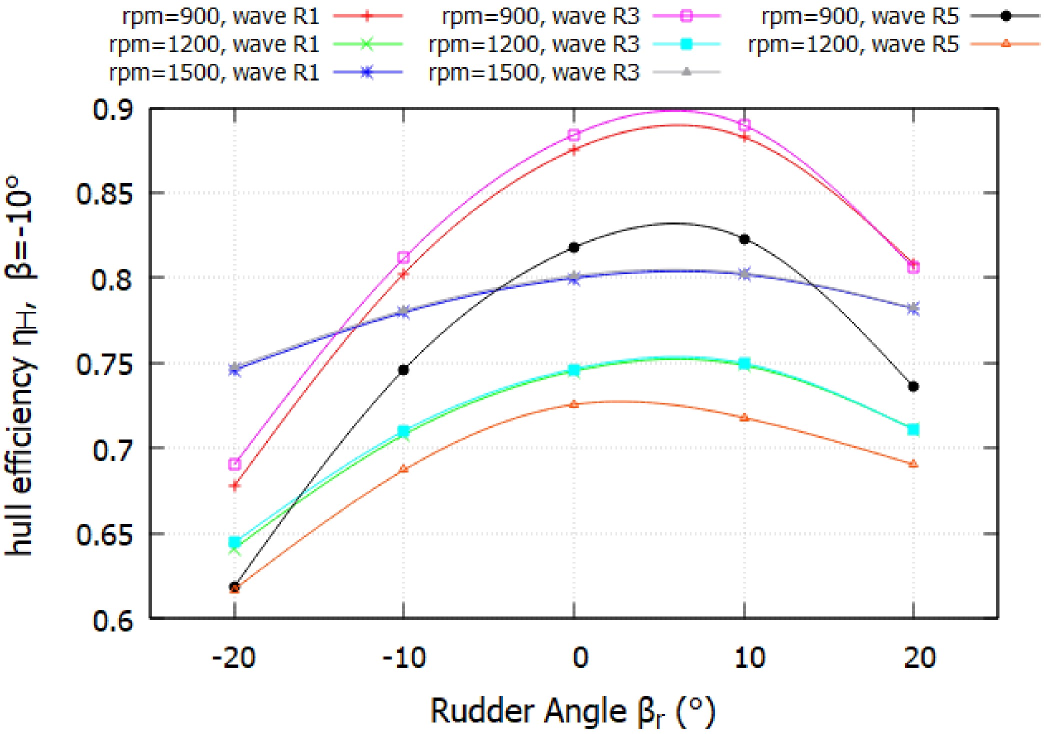

FIGURE 7.25: Effect of rudder angle and propeller revolution rate on hull efficiency η_H in waves, β= -10 °

TABLE 7.14: Thrust deduction and wake fraction 1-t and 1-ω_t in all considered cases

		β=0 °	β=+10 °	β=-10 °	β=0 °	β=+10 °	β=-10 °
Wave R1	β_r (°)	1-t	1-t	1-t	1-ω_t	1-ω_t	1-ω_t
900rpm	-20	0.671	0.789	0.698	1.010	1.021	1.030
	-10	0.820	0.907	0.838	1.024	1.034	1.044
	0	0.877	0.929	0.926	1.036	1.039	1.058
	10	0.842	0.910	0.936	1.031	1.038	1.061
	20	0.730	0.774	0.851	1.020	1.024	1.053
1200rpm	-20	0.752	0.808	0.771	1.194	1.219	1.203
	-10	0.833	0.884	0.860	1.202	1.228	1.215
	0	0.887	0.914	0.911	1.211	1.234	1.223
	10	0.866	0.882	0.917	1.209	1.229	1.225
	20	0.807	0.820	0.869	1.205	1.227	1.222
1500rpm	-20	0.852	0.879	0.871	1.187	1.215	1.168
	-10	0.893	0.914	0.913	1.189	1.217	1.170
	0	0.921	0.931	0.938	1.193	1.224	1.172
	10	0.913	0.922	0.941	1.195	1.224	1.173
	20	0.887	0.893	0.918	1.194	1.225	1.174
Wave R3							
900rpm	-20	0.706	0.795	0.713	1.016	1.023	1.033
	-10	0.849	0.916	0.851	1.030	1.036	1.048
	0	0.910	0.939	0.938	1.041	1.041	1.061
	10	0.879	0.916	0.947	1.036	1.040	1.064
	20	0.767	0.794	0.849	1.025	1.029	1.053
1200rpm	-20	0.767	0.810	0.777	1.197	1.220	1.205
	-10	0.849	0.887	0.863	1.205	1.229	1.216
	0	0.901	0.919	0.914	1.214	1.236	1.225
	10	0.882	0.887	0.920	1.212	1.232	1.227
	20	0.823	0.827	0.869	1.208	1.229	1.222
1500rpm	-20	0.861	0.880	0.874	1.187	1.213	1.169
	-10	0.902	0.915	0.914	1.190	1.216	1.171
	0	0.929	0.933	0.940	1.194	1.222	1.173
	10	0.921	0.923	0.942	1.196	1.222	1.174
	20	0.896	0.897	0.918	1.195	1.223	1.174
Wave R5							
900rpm	-20	0.628	0.720	0.637	1.018	1.024	1.030
	-10	0.776	0.844	0.781	1.033	1.037	1.047
	0	0.830	0.872	0.867	1.043	1.043	1.060
	10	0.803	0.845	0.875	1.038	1.040	1.063
	20	0.700	0.736	0.774	1.027	1.028	1.052
1200rpm	-20	0.737	0.789	0.743	1.200	1.219	1.205
	-10	0.823	0.863	0.835	1.208	1.229	1.215
	0	0.869	0.895	0.889	1.217	1.236	1.225
	10	0.852	0.869	0.881	1.214	1.232	1.227
	20	0.800	0.806	0.844	1.209	1.228	1.222

TABLE 7.15: Thrust deduction and wake fraction augments d$(1-t)$ and d$(1-\omega_t)$ benchmarking with zero drift scenarios

		β=+10 °	β=-10 °	β=+10 °	β=-10 °
Wave R1	β_r (°)	d$(1-t)$	d$(1-t)$	d$(1-\omega_t)$	d$(1-\omega_t)$
900rpm	-20	0.1183	0.0273	0.0109	0.0196
	-10	0.0869	0.0182	0.0100	0.0201
	0	0.0524	0.0497	0.0027	0.0224
	10	0.0679	0.0948	0.0077	0.0303
	20	0.0436	0.1211	0.0043	0.0335
1200rpm	-20	0.0565	0.0191	0.0241	0.0082
	-10	0.0502	0.0263	0.0259	0.0125
	0	0.0272	0.0244	0.0226	0.0119
	10	0.0151	0.0508	0.0203	0.0161
	20	0.0130	0.0618	0.0222	0.0166
1500rpm	-20	0.0271	0.0195	0.0288	-0.0182
	-10	0.0208	0.0192	0.0285	-0.0184
	0	0.0101	0.0164	0.0308	-0.0209
	10	0.0083	0.0277	0.0298	-0.0212
	20	0.0055	0.0308	0.0301	-0.0203
Wave R3					
900rpm	-20	0.0886	0.0067	0.0071	0.0170
	-10	0.0677	0.0023	0.0061	0.0183
	0	0.0291	0.0284	0.0001	0.0197
	10	0.0370	0.0677	0.0042	0.0278
	20	0.0270	0.0816	0.0036	0.0285
1200rpm	-20	0.0431	0.0097	0.0222	0.0075
	-10	0.0380	0.0143	0.0235	0.0105
	0	0.0175	0.0132	0.0219	0.0104
	10	0.0052	0.0385	0.0194	0.0150
	20	0.0038	0.0455	0.0209	0.0142
1500rpm	-20	0.0191	0.0126	0.0259	-0.0186
	-10	0.0133	0.0119	0.0259	-0.0192
	0	0.0042	0.0104	0.0276	-0.0214
	10	0.0022	0.0210	0.0267	-0.0218
	20	0.0017	0.0227	0.0273	-0.0216
Wave R5					
900rpm	-20	0.0924	0.0093	0.0059	0.0118
	-10	0.0684	0.0052	0.0032	0.0137
	0	0.0417	0.0363	-0.0002	0.0166
	10	0.0422	0.0725	0.0026	0.0251
	20	0.0359	0.0736	0.0016	0.0251
1200rpm	-20	0.0519	0.0064	0.0192	0.0050
	-10	0.0401	0.0117	0.0208	0.0071
	0	0.0261	0.0201	0.0191	0.0084
	10	0.0177	0.0292	0.0180	0.0128
	20	0.0060	0.0434	0.0184	0.0131

TABLE 7.16: Hull efficiency η_H in all considered cases

		β=0 °	β=+10 °	β=-10 °
Wave R1	β_r (°)	η_H	η_H	η_H
900rpm	-20	0.6637	0.7725	0.6776
	-10	0.8005	0.8768	0.8026
	0	0.8462	0.8945	0.8753
	10	0.8165	0.8759	0.8826
	20	0.7161	0.7556	0.8083
1200rpm	-20	0.6294	0.6633	0.6410
	-10	0.6933	0.7195	0.7078
	0	0.7323	0.7410	0.7452
	10	0.7166	0.7171	0.7486
	20	0.6697	0.6682	0.7112
1500rpm	-20	0.7180	0.7234	0.7459
	-10	0.7514	0.7510	0.7796
	0	0.7721	0.7609	0.7999
	10	0.7645	0.7526	0.8020
	20	0.7429	0.7291	0.7820
Wave R3				
900rpm	-20	0.6951	0.7770	0.6902
	-10	0.8239	0.8844	0.8116
	0	0.8735	0.9014	0.8840
	10	0.8482	0.8804	0.8897
	20	0.7485	0.7722	0.8057
1200rpm	-20	0.6404	0.6641	0.6445
	-10	0.7043	0.7218	0.7100
	0	0.7419	0.7430	0.7464
	10	0.7273	0.7200	0.7498
	20	0.6816	0.6731	0.7109
1500rpm	-20	0.7252	0.7254	0.7475
	-10	0.7582	0.7530	0.7808
	0	0.7781	0.7640	0.8012
	10	0.7705	0.7555	0.8027
	20	0.7493	0.7339	0.7824
Wave R5				
900rpm	-20	0.6165	0.7032	0.6185
	-10	0.7510	0.8147	0.7461
	0	0.7961	0.8362	0.8178
	10	0.7732	0.8119	0.8231
	20	0.6822	0.7161	0.7359
1200rpm	-20	0.6142	0.6472	0.6170
	-10	0.6815	0.7026	0.6871
	0	0.7140	0.7241	0.7255
	10	0.7014	0.7054	0.7179
	20	0.6619	0.6568	0.6903

7.4 Chapter summary

Accurate estimation of the forces exerted on the hull, propeller, and rudder, as well as interaction effects among these components in wave conditions, is essential for assessing a ship's manoeuvring performance in actual maritime environments. This chapter applies the same methodology as the previous chapter to investigate the influence of static drift and rudder angles on the fully appended KCS in regular head waves. In waves, the unsteady flow results in varying distributions of the associated forces, propulsion coefficients, and these oscillations depend on different amplitudes of adopted wave conditions. All presented simulation results are obtained by taking the mean of the unsteady oscillation signals, as illustrated in section 7.2.4.

Chapter 7 starts with the hull-rudder interaction towing in three different head waves, whose wavelengths and wave amplitudes are scaled based on the wave conditions (C1, C3, C5) of KCS case 2.10 from the 2015 Tokyo workshop. The main computed results include longitudinal and transverse forces, yaw moment on the hull, wave added resistance coefficients, drag and lift forces experienced by the KCS rudder. In terms of hull forces, longer wavelength results in an increasing trend of KCS drag force for all drift scenarios but the applied non-zero drift tends to weaken this ascending tendency. The applied drift angle vertically shifts the curves of side force and yaw moment on the hull but does not change their slope significantly. In addition, different wave conditions also influence F_Y' and M_Z': the highest lateral force is found at the medium wave R3 for all drift cases while the yaw moment coefficient is found to increase with the increment of wavelength. EFD data of C_T from the Southampton scale KCS model is compared with the CFD results at the straight-ahead conditions for three head waves: overall good agreement is found but the usage of different types of the rudder and different wave motions result in some discrepancies, which are more obvious in medium and long wave conditions. The highest added resistance coefficient is found in medium wave for zero drift KCS while it decreases with the wavelength increment when non-zero drift is applied. The rudder forces in waves follow a similar trend as those in calm water but the presence of wave results in steeper slopes of both C_D and C_L curves.

Section 7.3.2 demonstrates the drift angle effect on the fully appended KCS in head waves with the propeller operating at a series of fixed rpm rates. To examine the net effect of drift angle on powering performance, both actual values and corresponding augments benchmarking with zero drift scenario results are presented. It is found that the presence of waves intensifies the variation trends compared to calm water conditions, also making the augment more apparent. However, these variations also depend on different wave properties. For example, the short wave R1 tends to diminish propeller performance most compared to medium and long wave conditions. The applied drift angle also varies hull-propeller-wake interaction effects, which are presented using $(1 - t)$ and $(1 - \omega_t)$ parameters. Effect of different waves and propeller revolution rates on the hull efficiency η_H provides some valuable insights into the optimal η_H in different drift cases, subsequently suggesting potential optimal navigation strategy for ship operators when ships manoeuvre in waves. The tables presented, which encompass both actual values and augments of relevant parameters, have the potential to offer preliminary estimations of the forces acting on the hull, propeller, and rudder, as well as their interactions, taking into account the influence of drift angle and wave conditions. This information may prove valuable for enhancing the assessment methodologies employed in evaluating ship manouvering and powering performance in real sea states.

Chapter 8

Concluding remarks

8.1 Conclusions

Accurately predicting the manoeuvring performance of a vessel when operating in waves is of high importance to improve ship design, which is also closely related to ship navigation safety, reliability and efficiency. This is especially true when a ship sails in the actual sea states. The Specialist Committee on Manoeuvring in Waves of the International Towing Tank Conference (ITTC) admits that the comprehension of ship manoeuvrability in actual sea states remains underdeveloped (ITTC 2021). Compared to resistance, propulsion, and seakeeping aspects, the ability to accurately predict manoeuvring performance still remains a significant challenge due to the complex fluid-structure interaction between the hull, rudder propeller and their surrounding fluids. (Sanada et al. 2021).

Traditional experimental approaches for evaluating ship manoeuvring performance are very costly and have high requirements for test facilities and ship models. In comparison, the CFD approach is a more cost-efficient alternative for determining the ship's manoeuvring performance in waves with rapid development in high-performance computers and numerical techniques. However, conventional dynamic manoeuvring calculations still remain computationally expensive due to the extensive computing resource needed for resolving interactions among ship motion, wakefield and the hydrodynamic forces acting on the vessel and its appendages. One key challenge related to these calculations is the process of validation. Guaranteeing the accuracy of these simulations requires dependable and accurate experimental data, the acquisition of which, unfortunately, is very difficult and costly. This thesis outlines a more cost-effective numerical methodology capable of assessing the resistance and powering performance of a fully appended ship in waves under static drift, static rudder and combined drift rudder conditions, which represents quasi-static phases of an actual ship manoeuvre in waves. This methodology adopts both steady and unsteady CFD analysis approaches and allows for the direct validation of some drift simulations, contributing to the future validation of the actual manoeuvring models or simulations and providing a reference for experimental measurement of hull and appendage forces when drift angle is applied. This methodology has the potential to give some insights into the optimal design and operation of wind assist vessels, helping to identify cost-effective and practical solutions that can be efficiently implemented for maritime decarbonization purposes.

Chapter 1 of this work presents the motivation and need to improve the powering and manoeuvring performance of vessels in real sea states. The subject of ship manoeuvring in waves still requires a better understanding and an accurate and cost-effective numerical method to model hydrodynamic behaviours and interaction effects between the hull, propeller, rudder and surrounding fluid. However, this is not an easy task because of several main factors that contribute to the complexity of this problem:

- Complex geometry: Ships have complex geometries, including varying shape hull forms, the rotating propeller and the rudder, that can influence ships' hydrodynamic performance in real sea states. Accurate representation of these geometries in numerical simulations is challenging, as it requires fine enough mesh revolutions to capture the shape of each component and efficient computational techniques to handle these intricate geometries.
- Non-linearity: when modelling the ship manoeuvring, the presence of waves and ship motions is highly nonlinear, which also induces nonlinear forces and moments on the hull, propeller, and rudder. This can significantly impact the ship's manoeuvrability.
- Fluid-structure interaction: When the ship travels in waves, the hull will alter the inflow into the propeller plane. The rotating propeller also accelerates the flow, changing the flow onto the downstream rudder and pressure distribution of the upstream hull. Meanwhile, the presence of the rudder blocks and varies the fluid onto the upstream propeller, affecting the actual propeller performance.
- Multi-physics coupling: When a ship manoeuvres in waves, it involves various aspects such as resistance, propulsion, seakeeping, manoeuvring and etc. For example, the motion of a ship induced by waves interacts with the vessel's manoeuvring motion, resulting in a significant impact on hydrodynamic forces. This interaction can, in turn, alter the ship's manoeuvring behaviour, and conversely, the manoeuvring behaviour can impact the wave-induced motions (ITTC 2021).
- Computational expenses: direct simulation of dynamic ship manoeuvring in waves requires high-resolution spatial and temporal discretizations, leading to huge computational resources. This makes it difficult and costly to perform real-time or large-scale simulations.

- Validation: The validation process of numerical simulations is of high importance for their credibility and practical use. However, deriving accurate and relevant experimental data for validation purposes is very challenging as it is costly, time-consuming and requires high-accuracy measurements and well-trained technicians.

Consequently, there is a persistent demand for a more economically viable numerical methodology to accurately simulate the ship's resistance, propulsion and manoeuvring capabilities in wave conditions.

A detailed literature review of ship hydrodynamic behaviours in waves is presented in Chapter 2. Both experimental model testing and numerical methods can contribute to a better prediction of ship powering and manoeuvring performance in real seaways. As high-performance computing and numerical methods continue to advance rapidly, the utilization of Computational Fluid Dynamics (CFD) based numerical approaches has emerged as the preferred choice. Due to the fact that conventional direct manoeuvring simulations remain expensive and difficult to validate, the focus of this study is to present a more cost-efficient numerical approach for estimating the resistance, propulsion and manoeuvring performance of a fully appended benchmark KRISO Container Ship (KCS) under static drift angles combined with a series of rudder angles. This kind of numerical configuration represents quasi-static phases of an actual ship manoeuvre, which can significantly reduce the computational costs and make them feasible to be directly validated.

Chapter 3 demonstrates the mathematical formulations and numerical techniques used for developing this cost-effective methodology. A RAN-based analysis method is used for modelling the flow around the fully appended KCS in steady and unsteady conditions. OpenFOAM is selected as the RANS solver due to its flexibility and the relative ease with which additional functions can be included especially propeller numerical modelling. To facilitate the implementation of this method, a stepwise study procedure is used, as shown in section 3.1.

Chapter 4 discusses the numerical framework for simulating ships with the angle of drift and the used numerical propeller modelling approaches. Ship axis and domain axis coordinate systems are explained, and a transformation matrix is used for resolving forces and moments in the ship axis. As this study does not concentrate on the propeller itself and the local flow characteristics are not the focus, body force propeller models are used for their lower computational requirements and relatively accurate prediction compared to the fully discretized propeller modelling. To capture the non-uniform wake resulting from the applied drift angles, rudder angles and propeller unidirectional rotation, a sectorial approach is applied to the Blade element momentum theory (BEMt) code. The BEMt can accurately predict the KCS propeller open water curve and shows good agreement with the experimental data. To guarantee the accuracy and reliability of the BEMt, another body force model, the Yamazaki model, is also employed to verify BEMt's numerical results.

Chapter 5 studies the influence of drift angle on the self-propelled KCS using the steady RANS simulations of double body flow in calm water conditions. Seven drift angles are applied to the KCS without the rudder, as shown in section 5.2. All simulations start with the resistance test and then the self-propulsion test. The detailed resistance components are presented, showing the total resistance encountered by the KCS increases with the increment of drift angle magnitude. The transverse force and yaw moment variations with drift angles exhibit a nearly linear trend, and results are also compared with available EFD and CFD results, demonstrating good consistency, but overall results are underpredicted due to the absence of free surface modelling. The computed velocity profiles and propulsion coefficients of self-propelled KCS at straight-ahead conditions (β=0 °) are compared with EFD data from the 2015 Tokyo CFD workshop and four numerical submissions of the Tokyo workshop, which all include the free surface modelling in their simulations. The overall good agreement indicates that the double body method combined with the body force model is able to predict the self-propulsion characteristics, even the local flow details and can provide a reasonably accurate evaluation of the hull-propeller interaction using affordable computational costs. Based on the experience gained from the previous section, section 5.3 includes the action of an all-movable rudder in double body simulation. The impact of rudder angles on the performance of the hull, the propeller and their interaction is discussed. It is found that the applied drift angle intensifies the variation trend of most parameters and also alters rudder force curves. In addition, the effect of rudder angles on velocity profiles downstream of the propeller plane is also discussed, suggesting rudder angles mainly change velocity distribution near the rudder boundary layer, which needs to be modelled and captured at a reasonable accuracy level to ensure precise estimation of rudder forces and the interaction effect between the hull, propeller and rudder during ship manoeuvring assessment.

In the selected KCS hull form, combined with a design speed of Froude number (Fn) of 0.26, the wave-making resistance experienced by the KCS is considerably high (Ali 2020, Windén 2021*c*). As a result, it is necessary to include the free surface modelling to accurately represent these hydrodynamic interactions. Chapter 6 provides the numerical methodology for modelling the fully-appended KCS under three different drift angles combined with a series of rudder angles in calm water conditions, taking into account of free surface effect, which is more closely related to actual ship manoeuvring performance in reality in contrast to the double body approach. The chapter starts with the numerical configurations, focusing on the differences from the double model's setup. The same benchmarking KCS hull is selected and the KCS forecastle part is included compared to the double body. The semi-balanced horn rudder is used, comprising the rudder blade and rudder skeg. The rudder skeg is fixed to the hull while the rudder blade segment can be rotated corresponding to the applied non-zero rudder angle. In terms of mesh generation, the OpenFOAM mesh utilities blockMesh and snappyHexMesh are utilized. The mesh refinement around the free surface is achieved through blockMesh. Four refinement boxes are created to realize the local mesh refinement around the hull and rudder. Another smaller refinement region is conducted at the aft of the hull, further refining the mesh around the stern and the rudder. These refinement boxes are rotated according to the applied drift angle, making sure they align with the hull's longitudinal axis. This can save a considerable number of cells and thereby computational costs compared to the mesh generation method in Chapter 5. The mesh size of the generated grid for all drift and rudder angles' scenarios is approximately 15M. The grids used in Chapter 6 are also applied to Chapter 7, demonstrating the mesh is fine enough for both calm water and wave cases. All considered cases start with the resistance test and then five sets of fixed RPM tests are conducted with RPM values ranging from 600 to 1500, which covers most operating conditions of vessels. The computed longitudinal and lateral hull forces from resistance tests are compared with experimental data obtained from the Southampton Boldrewood towing tank, showing an overall good agreement and validation. Due to the use of different rudder types and model scales, there are some discrepancies found particularly for cases with large rudder angles ($\beta_r > 20$ °). The influence of drift and rudder angles on rudder drag and lift is also discussed. The applied non-zero drift results in horizontal and vertical shifts on the rudder and lift curves but have a minor effect on the curve slope. For the fixed RPM tests, the action of the propeller is modelled using two body force models, the BEMt and Yamazaki models. Good agreement is found between the numerical results obtained from both, but their discrepancies are more notable at high propeller loading. The possible reason may be certain assumptions made in the momentum theory make the BEMt code more challenging to deduce the propeller-induced velocities. And BEMt model performs less well with the tangential wake effects and this is not significant in considered drift angle scenarios, but tangential wake correction should be taken into account when large drift angles are applied. To determine the net effect of drift angle, augments of the hull, propeller, and rudder forces are presented with varying rudder angles, benchmarking with corresponding straight-ahead cases' results. The influence of drift angle on the hull-propeller-wake interaction is also presented using the thrust deduction and wake fraction parameters, thereby finding that the optimal hull efficiency occurs at zero rudder angle condition when drift angle is 0 °and +10 °while the η_H reaches its peak at around +5 °rudder angle when -10 °drift is applied. Compared to the double model approach, the computational costs of the unsteady RANS method with BEMt code are increased significantly: it takes approximately 50 hours (wall clock time) for one single case with one drift angle, one rudder angle, one propeller revolution rate to run 50 seconds of simulation time to obtain converging results, using two full compute nodes on High-Performance Computing Cluster iridis5 with each compute node has 40 CPUs per node with 192 GB of DDR4 memory. If the Yamzaki model is used, it takes around 55-60 hours to complete the same case. Therefore, the BEMt code is used for the primary propeller modelling method after balancing the trade-off between computational costs and simulation accuracy.

Chapter 7 make use of the numerical methodology and experience gained from Chapter 5 and 6 to study the influence of drift angle on the fully appended KCS's powering performance in regular waves. Three wave conditions are chosen, and wave properties are scaled based on the wave condition of KCS case 2.10 from the 2015 Tokyo workshop. In terms of hull-rudder interaction in head waves, the ship total resistance increases with the increasing wavelength for all drift cases, but the non-zero drift weakens this increasing trend. The applied drift results in the vertical shift of both side force and yaw moment curves experienced by KCS but has little effect on the curves' slope. EFD data from Southampton scale KCS is compared with numerical results of zero drift, and comparison shows overall good agreement although there are some discrepancies in medium and long wave scenarios. The effect of drift on rudder forces follows a similar trend as in calm water conditions, but waves result in steeper slopes of drag and lift curves. To determine the drift effect on the fully appended KCS in waves, the forces of the hull, propeller, and rudder, and their corresponding augments benchmarking with zero drift case are presented. The presence of waves makes the augment more obvious and intensifies the variation trend compared to calm water. The drift angle influence on hull-propeller-wake interaction in waves is presented using $(1-t)$ and $(1-\omega_t)$ parameters and, thereby, the hull efficiency. The computed tables provide an initial prediction of the forces exerted on the hull, appendages and their interaction effects, and the net effect of drift angle and rudder angles on ship powering and manoeuvring performance in wave conditions.

This investigation makes it possible to provide some good insights into better ship design assessment due to ship manoeuvring in waves and operations of wind-assist vessels. More specifically, conclusions drawn from the drift influence on hydrodynamic forces on the hull, propulsor, rudder, and the three-way interaction between them, can lead to improvement in hull form, the choice of propeller rotating rates, the optimal rudder angle when ship manoeuvres in real seaways so that to minimize the negative effects of maritime environmental forces on the ship's manoeurability and course-keeping ability. The obtained results from this thesis can be further used to reduce the power requirements (or resistance) of ships and improve ship propulsive energy efficiency in real sea states by investigating complex interaction at the vessel stern between its propulsors, manoeuvring devices and wake flow, and this could optimize the process of ship design and ship operation. This is also closely related to the ship's stability and safety, which can help identify optimal operational profiles such as ship speed, and heading angle combined with rudder angle to maintain course while mitigating the risk of a ship capsizing or exceeding rolling in rough sea states. Typically, an inward propeller rotation is preferred, but the optimal propulsive performance is not solely determined by the rotation direction. Factors such as different drift conditions, propeller rotating rates, and the influence of wind and waves also should be taken into account. Consequently, this study also contributes to a better understanding of selecting the optimal propeller rotation rate and direction when a ship manoeuvres in actual voyages, thereby reducing travelling times and fuel consumption. In terms of operating wind-assist vessels, the drift angle effect analysis allows for the successful integration of wind propulsion devices such as wing sails on conventional commercial vessels and it ensures that wind-assisted devices can generate thrust efficiently and help to maintain the desired course of vessels, contributing to the zero-carbon ambition of the maritime sector.

8.2 Recommendations for future work

Based on the work conducted and experience gained from this study, suggestions for future work that can build from or improve on this one are outlined below:

- To investigate the combined drift and rudder angles effect on the fully appended vessels, the hull is set to free to heave and pitch only in resistance tests (without propeller) while the hull is fixed in all degrees of freedom when studying the hull-propeller-rudder interaction. The effect of trim and sinkage should be included to give a better prediction of the associated resistance, propulsion, and manoeuvring performance in drift conditions.
- For validation, longitudinal and lateral forces on the hull in some drift computations are validated with experimental data of the Southampton model scale KCS in calm water and regular waves. However, more validation studies should be carried out for propeller and rudder forces in drift scenarios to gain more confidence in the reliability and accuracy of numerical simulations.
- When a propeller operates at significant drift angles due to oblique flow or wave-induced loads, the correction of tangential wake effects should be included in the Blade element momentum theory (BEMt) code to better capture the propeller performance in large drift conditions, which also contributes to more accurate prediction of the downstream rudder forces.

- For wind-assist ships, the computed results in this study make it possible to apply the presented numerical methodology in integrating wind-assist devices onto traditional commercial ships and predicting the interactions between wind propulsion systems and the ship's hydrodynamics, enabling better predictions of wind-assist vessels' resistance and powering performance.

References

Aalbers, A. & Gent, W. (1985), Unsteady wake velocities due to waves and Motions measured on a ship model in head waves, *in* 'Proceedings of 15th symposium on naval hydrodynamics', pp. 69–81.

Ali, M. A. (2020), Effect of ship motions on propeller-hull interaction, PhD thesis, Memorial University of Newfoundland.

Amini, H. & Steen, S. (2011), 'Experimental and theoretical analysis of propeller shaft loads in oblique inflow', *Journal of Ship Research* **55**(04), 268–288.

Arribas, F. P. (2007), 'Some methods to obtain the added resistance of a ship advancing in waves', *Ocean Engineering* .

Atsavapranee, P., Miller, R., Dai, C., Klamo, J. & Fry, D. (2010), Steady-turning experiments and rans simulations on a surface combatant hull form (model# 5617), *in* '28th Symposium on Naval Hydrodynamics, Pasadena', : Office of Naval ResearchAssociates, Inc Arlington, VirginiaRed Hook, NY . . . , pp. 12–17.

Badoe, C. E. (2015), Design practice for the stern hull of a future twin-skeg ship using a high fidwlity numerical approach, Phd thesis, University of Southampton.
URL: *http://eprints.soton.ac.uk/158357/*

Badoe, C. E., Phillips, A. B. & Turnock, S. R. (2015), 'Influence of drift angle on the computation of hull–propeller–rudder interaction', *Ocean engineering* **103**, 64–77.

Badoe, C., Phillips, A. & Turnock, S. (2014), Ship wake field analysis using a coupled BEMt-RANS approach, *in* 'NuTTS '14: 17th Numerical Towing Tank Symposium,', Chalmers University of Technology, Marstrand, Sweden.

Badoe, C., Turnock, S. & Phillips, A. (2016), Impact of hull propeller rudder interaction on ship powering assessment, *in* 'Hull Performance and Insight Conference'.

Balaras, E., Schroeder, S. & Posa, A. (2015), 'Large-eddy simulations of submarine propellers', *Journal of Ship Research* **59**(04), 227–237.

Baltazar, J., Falcão de Campos, J. & Bosschers, J. (2012), 'Open-water thrust and torque predictions of a ducted propeller system with a panel method', *International Journal of Rotating Machinery* **2012**.

Benini (2004), 'Significance ofblade element theory in performance prediction of marine propellers', *Ocean Engineering* **31**, 957–974.

Bensow, R. E. & Bark, G. (2010), Simulating cavitating flows with les in openfoam, *in* 'V European conference on computational fluid dynamics', pp. 14–17.

Bertram, V. (2000), 'Practical Ship Hydrodynamics', *Practical Ship Hydrodynamics* .

Bertram, V. (2012), *Practical Ship Hydrodynamics*.

Broglia, R., Dubbioso, G., Durante, D. & Di Mascio, A. (2015), 'Turning ability analysis of a fully appended twin screw vessel by cfd. part i: Single rudder configuration', *Ocean engineering* **105**, 275–286.

Burrill, L. (1944), 'Calculation of marine propeller performance characteristics', *Transactions of NECIES.* **60**.

Califano, A. & Steen, S. (2011), 'Numerical simulations of a fully submerged propeller subject to ventilation', *Ocean engineering* **38**(14-15), 1582–1599.

Cao, M. (1988), 'The open-water characteristics of a propeller with varying depth of shaft and in waves', *Journal of Shang-hai Jiao Tong University* **22**(3), 27–35.

Caribbean, R. (2017), 'Turnaround day: Watch behind the scenes of the ultimate pit stop'. Accessed: 2023-04-26.
URL: *https://www.royalcaribbean.com/blog/turnaround-day-watch-behind-the-scenes-of-the-ultimate-pit-stop/*

Carlton, J. S. (2018), *Marine propellers and propulsion*.

Carrica, P. M., Castro, A. M. & Stern, F. (2010), 'Self-propulsion computations using a speed controller and a discretized propeller with dynamic overset grids', *Journal of Marine Science and Technology* **15**, 316–330.

Choi, J., Min, K.-S., Kim, J., Lee, S. & Seo, H. (2010), 'Resistance and propulsion characteristics of various commercial ships based on cfd results', *Ocean engineering* **37**(7), 549–566.

Date, J. C. & Turnock, S. R. (2002), 'Computational evaluation of the periodic performance of a NACA 0012 fitted with a gurney flap', *Journal of Fluids Engineering, Transactions of the ASME* **124**(1).

Dubbioso, G., Mauro, S., Ortolani, F., Martelli, M., Nataletti, M., Villa, D. & Viviani, M. (2015), Experimental and numerical investigation of asymmetrical behaviour of rudder/propeller for twin screw ships, *in* 'International Conference on Marine Simulation and Ship Maneuverability (MARSIM'15)'.

Durasević, S., Gatin, I., Uroić, T. & Jasak, H. (2022), 'Numerical analysis of self-propulsion flow characteristics in model scale', *Ocean Engineering* **259**, 111885.

El Moctar, O. (2001), 'Numerical computations of flow forces in ship manoeuvring', *Ship Technology Research* **48**(3), 98–123.

Eom, M.-J., Jang, Y.-H. & Paik, K.-J. (2021), 'A study on the propeller open water performance due to immersion depth and regular wave', *Ocean Engineering* **219**, 108265.

Eom, M.-J., Paik, K.-J., Jang, Y.-H., Ha, J.-Y. & Park, D.-W. (2021), 'A method for predicting propeller performance considering ship motion in regular waves', *Ocean Engineering* **232**, 109135.

Epps, B., Ketcham, J. & Chryssostomidis, C. (2010), *Propeller blade stress estimates using lifting line theory*, Association for Computing Machinery.

Faltinsen, O. M., Minsaas, K. J., Liapis, N. & Skjordal, S. O. (1980), PREDICTION OF RESISTANCE AND PROPULSION OF A SHIP IN A SEAWAY.

Feng, D., Yu, J., He, R., Zhang, Z. & Wang, X. (2020*a*), 'Free running computations of kcs with different propulsion models', *Ocean Engineering* **214**, 107563.

Feng, D., Yu, J., He, R., Zhang, Z. & Wang, X. (2020*b*), 'Improved body force propulsion model for ship propeller simulation', *Applied Ocean Research* **104**, 102328.

Ferziger, J. H., Perić, M. & Street, R. L. (2002), *Computational methods for fluid dynamics*, Vol. 3, Springer.

Flood, K. M. (2009), Propeller performance analysis using lifting line theory, Technical report, MASSACHUSETTS INST OF TECH CAMBRIDGE.

Fujii, H. & Takahashi, T. (1975), 'Experimental Study on the Resistance Increase of a Large Full Ship in Regular Oblique Waves', *Journal of the Society of Naval Architects of Japan* .

Gaggero, S., Villa, D. & Viviani, M. (2017), 'An extensive analysis of numerical ship self-propulsion prediction via a coupled bem/rans approach', *Applied Ocean Research* **66**, 55–78.

Gatin, I., Vukcevic, V., Jasak, H. & Lalovic, I. (2018), Manoeuvring simulations using the overset grid technology in foam-extend, *in* '32nd Symposium on Naval Hydrodynamics'.

Gerritsma, J. & Beukelman, W. (1972), 'ANALYSIS OF THE RESISTANCE INCREASE IN WAVES OF A FAST CARGO SHIP.', *International Shipbuilding Progress* .

Goldstein, S. (1929), 'On the vortex theory of screw propellers', *Proceedings of the Royal Society of London. Series A, Containing Papers of a Mathematical and Physical Character* **123**(792).

Greenshields, C. & Weller, H. (2022), *Notes on Computational Fluid Dynamics: General Principles*, CFD Direct Ltd, Reading, UK.

Guo, B., Steen, S. & Deng, G. (2012), 'Seakeeping prediction of kvlcc2 in head waves with rans', *Applied Ocean Research* **35**, 56–67.

Guo, C., Wang, X., Wang, C., Zhao, Q. & Zhang, H. (2020), 'Research on calculation methods of ship model self-propulsion prediction', *Ocean Engineering* **203**, 107232.

Guo, C., Zhao, D., Wang, C. & Chang, X. (2012), 'Experimental research on hydrodynamic characteristics of propeller in waves', *Journal of Ship Mechanics* **16**(9), 1005–1014.

Hino, T., Larsson, L., Stern, F., Visonneau, M., Hirata, N. & Kim, J. (2020), *Numerical Ship Hydrodynamics: An Assessment of the Tokyo 2015 Workshop*, Springer.

Hizir, O., Kim, M., Turan, O., Day, A., Incecik, A. & Lee, Y. (2019), 'Numerical studies on non-linearity of added resistance and ship motions of KVLCC2 in short and long waves', *International Journal of Naval Architecture and Ocean Engineering* .

Hough, G. & Ordway, D. (1964), The generalized actuator disk, Technical report, Therm Advanced Research Inc Ithaca Ny.

International Maritime Organization (2002), 'RESOLUTION MSC. 137(76) STANDARDS FOR SHIP MANOEUVRABILITY'.

Islam, H. & Soares, C. G. (2018), A CFD study of a ship moving with constant drift angle in calm water and waves, *in* 'Progress in Maritime Technology and Engineering - Proceedings of the 4th International Conference on Maritime Technology and Engineering, MARTECH 2018'.

Islam, H. & Soares, C. G. (2019), 'Uncertainty analysis in ship resistance prediction using openfoam', *Ocean Engineering* **191**, 105805.

Issa, R. I. (1986), 'Solution of the implicitly discretised fluid flow equations by operator-splitting', *Journal of computational physics* **62**(1), 40–65.

ITTC (2002), The Resistance Committee, *in* 'Final Report and Recommendations to the 23rd ITTC'.

ITTC (2014), 'Ittc–recommended procedures and guidelines-practical guidelines for ship cfd applications. 7.5-03-02-03 (revision 01)', *ITTC-Recomm. Proced. Guidel.* p. 19.

ITTC (2017*a*), 'Calculation of the weather factor fw for decrease of ship speed in waves', *International Towing Tank Confterence – Recommended Procedures and Guidelines* **00**.

ITTC (2017*b*), 'Recommended procedures and guidelines, 7.5-03-01-01, uncertainty analysis in cfd verification and validation methodology and procedures'.

ITTC (2021), The Specialist Committee on Manoeuvring in Waves - Final Report and Recommendations to the 29th ITTC, Technical report.

Jamali, A. (2011), 'Investigation of propeller characteristics with different locations of the rudder'.

Jasak, H. (1996), 'Error analysis and estimation for the finite volume method with applications to fluid flows.'.

Jasak, H., Jemcov, A., Tukovic, Z. et al. (2007), Openfoam: A c++ library for complex physics simulations, *in* 'International workshop on coupled methods in numerical dynamics', Vol. 1000, pp. 1–20.

Jiang, L., Yao, J. & Liu, Z. (2022), 'Comparison between the rans simulations of double-body flow and water–air flow around a ship in static drift and circle motions', *Journal of Marine Science and Engineering* **10**(7), 970.

Jin, Y., Duffy, J., Chai, S. & Magee, A. R. (2019), 'Dtmb 5415m dynamic manoeuvres with urans computation using body-force and discretised propeller models', *Ocean Engineering* **182**, 305–317.

Journee, J. (1992), Experiments and calculations on 4 Wigley hull forms in head waves, Technical report.

Kashiwagi, M. (1992), 'Added resistance, wave-induced steady sway force and yaw moment on an advancing ship', *Ship Technology Research (Schiffstechnik)* **39**(1), 3–16.

Kawamura, T., Miyata, H. & Mashimo, K. (1997), 'Numerical simulation of the flow about self-propelling tanker models', *Journal of marine science and technology* **2**, 245–256.

Kerwin, J. E., Kinnas, S. A., Lee, J.-T. & Shih, W.-Z. (1987), A surface panel method for the hydrodynamic analysis of ducted propellers, Technical report, Massachusetts Inst of Tech Cambridge Dept of Ocean Engineering.

Kerwin, J. E. & Lee, C.-S. (1978), Prediction of steady and unsteady marine propeller performance by numerical lifting-surface theory, Technical report.

Khanfir, S., Hasegawa, K., Nagarajan, V., Shouji, K. & Lee, S. K. (2011), 'Manoeuvring characteristics of twin-rudder systems: rudder-hull interaction effect on the manoeuvrability of twin-rudder ships', *Journal of marine science and technology* **16**, 472–490.

Kim, D. J., Yun, K., Park, J.-Y., Yeo, D. J. & Kim, Y. G. (2019), 'Experimental investigation on turning characteristics of kvlcc2 tanker in regular waves', *Ocean Engineering* **175**, 197–206.

Kim, D., Song, S. & Tezdogan, T. (2021), 'Free running cfd simulations to investigate ship manoeuvrability in waves', *Ocean Engineering* **236**, 109567.

Kim, H., Akimoto, H. & Islam, H. (2015), 'Estimation of the hydrodynamic derivatives by RaNS simulation of planar motion mechanism test', *Ocean Engineering* **108**.

Kim, K. H. & Kim, Y. (2011), 'Numerical study on added resistance of ships by using a time-domain Rankine panel method', *Ocean Engineering* .

Kim, M., Hizir, O., Turan, O. & Incecik, A. (2017), 'Numerical studies on added resistance and motions of KVLCC2 in head seas for various ship speeds', *Ocean Engineering* **140**.

Kim, Y., Seo, M. G., Park, D., Lee, J. & Yang, K. (2014), Numerical and Experimental Analyses of Added Resistance in Waves, *in* '29th International Workshop on Water Waves and Floating Bodies', Osaka, Japan.

Krasilnikov, V., Ponkratov, D. & Crepier, P. (2011), A numerical study on the characteristics of the system propeller and rudder at low speed operation, *in* 'Second International Symposium on Marine Propulsors', Vol. 2, p. 12.

Kumar, P. & Mahesh, K. (2017), 'Large eddy simulation of propeller wake instabilities', *Journal of Fluid Mechanics* **814**, 361–396.

Kundu, P. K., Cohen, I. M. & Dowling, D. R. (2015), *Fluid mechanics*, Academic press.

Larsson, L., Patel, V. & Dyne, G. (1991), 'Proceedings of 1990 sspa-cth-iihr workshop on ship viscous flow', *Flowtech International, Gothenburg, Sweden, Report* (2).

Larsson, L., Stern, F. & Visonneau, M. (2013), *Numerical Ship Hydrodynamics - An assessment of the Gothenburg 2010 Workshop*, Springer Science & Business Media.

Larsson, L., Stern, F., Visonneau, M., Hino, T., Hirata, N. & Kim, J. (2015), Proceedings, Tokyo 2015 Workshop on CFD in Ship Hydrodynamics, *in* 'Tokyo CFD Workshop'.

Launder, B. E. & Sharma, B. I. (1974), 'Application of the energy-dissipation model of turbulence to the calculation of flow near a spinning disc', *Letters in heat and mass transfer* **1**(2), 131–137.

Lee, C. (1983), 'Propeller in waves–state of the art'.

Lee, J., Park, D. M. & Kim, Y. (2017), 'Experimental investigation on the added resistance of modified KVLCC2 hull forms with different bow shapes', *Proceedings of the Institution of Mechanical Engineers Part M: Journal of Engineering for the Maritime Environment* **231**(2).

Lee, S.-K., Yu, K., Chen, H.-C. & Tseng, R. K.-C. (2010), Cfd simulation for propeller performance under seaway wave condition, *in* 'The Twentieth International Offshore and Polar Engineering Conference', OnePetro.

Lee, Y.-G., Yu, J.-W., Kang, B.-H. & Pak, K.-R. (2008), 'A numerical study on the flow around a rudder behind low speed full ship', *Journal of Ship and Ocean technology* **12**(2), 41–52.

Ley, J., Sigmund, S. & El Moctar, O. (2014), Numerical prediction of the added resistance of ships in waves, *in* 'Proceedings of the International Conference on Offshore Mechanics and Arctic Engineering - OMAE', Vol. 2.

Liu, F. (2016), 'A thorough description of how wall functions are implemented in openfoam', *Proceedings of CFD with OpenSource Software* **34**.

Liu, J., Quadvlieg, F. & Hekkenberg, R. (2015), 'Impacts of rudder profiles on ship manoeuvrability'.

Liu, S. & Papanikolaou, A. (2016), 'Fast approach to the estimation of the added resistance of ships in head waves', *Ocean Engineering* .

Longo, J. & Stern, F. (2002), 'Effects of drift angle on model ship flow', *Experiments in fluids* **32**(5), 558–569.

Lungu, A. (2020), 'Overall performances of a propeller operating near the free surface', *IOP Conference Series: Materials Science and Engineering* **916**(1).

Lyu, W. & el Moctar, O. (2017), 'Numerical and experimental investigations of wave-induced second order hydrodynamic loads'.

McCarthy, J., Norley, W. & Ober, G. (1961), The Performance of a Submerged Propeller in Regular Wave, Technical report, David Taylor Model Basin, Washington DC, USA.

Menter, F. R. (1994), 'Two-equation eddy-viscosity turbulence models for engineering applications', *AIAA Journal* .

Menter, F. R., Kuntz, M. & Langtry, R. (2003), 'Ten Years of Industrial Experience with the SST Turbulence Model Turbulence heat and mass transfer', *Cfd.Spbstu.Ru* **4**(July 2014).

MEPC72, I. (2018), 'Resolution mepc. 304 (72)', *Initial IMO Strategy on Reduction of GHG Emissions from Ships* .

Moctar, O. e., Sigmund, S., Ley, J. & Schellin, T. E. (2017), 'Numerical and experimental analysis of added resistance of ships in waves', *Journal of Offshore Mechanics and Arctic Engineering* **139**(1).

Mofidi, A. & Carrica, P. M. (2014), 'Simulations of zigzag maneuvers for a container ship with direct moving rudder and propeller', *Computers & fluids* **96**, 191–203.

Molland, A. F., Turnock, S. R. & Hudson, D. A. (2017), *Ship resistance and propulsion.*
URL: *https://linkinghub.elsevier.com/retrieve/pii/B9780750681506500140*

Molland, A. & Turnock, S. (1992), 'Further wind tunnel tests on the influence of propeller loading on ship rudder performance'.

Molland, A. & Turnock, S. (1995), 'Wind tunnel tests on the effect of a ship hull on rudder-propeller performance at different angles of drift'.

Molland, A. & Turnock, S. (2002), 'Flow straightening effects on a ship rudder due to upstream propeller and hull', *International shipbuilding progress* **49**(3), 195–214.

Molland, A. & Turnock, S. (2007), *Marine Rudders and Control Surfaces*.

Monroy, C. & Seng, S. (2017), Time-stepping schemes for seakeeping in openfoam, *in* 'Proceedings of the 10th International Workshop on Ship and Marine Hydrodynamics'.

Moriyama, F. (1979), 'On an approximate numerical method for estimating the performance of marine propellers', *Papers of Ship Research Institute* **16**(6), 361–376.

Moukalled, F., Mangani, L., Darwish, M., Moukalled, F., Mangani, L. & Darwish, M. (2016), *The finite volume method*, Springer.

Muscari, R., Dubbioso, G., Viviani, M. & Di Mascio, A. (2017), 'Analysis of the asymmetric behavior of propeller–rudder system of twin screw ships by cfd', *Ocean Engineering* **143**, 269–281.

Nakamura S, Hosoda R, Naito S, I. M. (1975), 'Propulsive performance of a container ship in waves (4th Report)', *J Kansai Soc Naval Archit Japan* **159**, 29–39.

Nakamura, S. & Naito, S. (1975), 'Propulsive performance of a container ship in waves', *Journal of the Society of Naval Architects of Japan* **15**, 22–47.

Nakamura, S., Naito, S. & Inoue, R. (1975), 'Open-water characteristics and load fluctuations of propeller in waves', *J Kansai Soc Naval Archit Japan* **159**, 41–55.

Nakamura, S. & Natio, S. (1977), 'Propulsive performance of a container ship in waves', *Journal of the Society of Naval Architects of Japan* .

Natio, S. & Nakamura, S. (1979), 'Open-water characteristics and load fluctuations of propeller at racing conditions in waves', *Journal of Kansai Society of Naval Architects* pp. 51–63.

Navier, C. (1823), 'Memory on the laws of fluid motion', *Memories of the Royal Academy of Sciences of the Institut de France* **6**(1823), 389–440.

Newman, J. N. (1967), 'The Drift Force and Moment on Ships in Waves', *Journal of Ship Research* **11**(01), 51–60.

Ohashi, K., Kobayashi, H. & Hino, T. (2018), 'Numerical simulation of the free-running of a ship using the propeller model and dynamic overset grid method', *Ship Technology Research* **65**(3), 153–162.

OpenFOAM Foundation (2023), 'Openfoam', `https://openfoam.org/`.

OpenFOAMFoundation (2019), 'OpenFOAM version 7'.
URL: *https://openfoam.org/download/7-source/*

Ozdemir, Y. H. & Barlas, B. (2017), 'Numerical study of ship motions and added resistance in regular incident waves of KVLCC2 model', *International Journal of Naval Architecture and Ocean Engineering* .

Paik, B. G., Lee, C. M. & Lee, S. J. (2005), 'Comparative measurements on the flow structure of a marine propeller wake between an open free surface and closed surface flows', *Journal of marine science and technology* **10**, 123–130.

Papanikolaou, A. & Zaraphonitis, G. (1987), 'On an Improved Method for the Evaluation of Second-Order Motions and Loads on 3D Floating Bodies in Waves', *Journal Schiffstechnik-Ship Technology Research* **34**, 170–211.

Park, D. M., Lee, J. H., Jung, Y. W., Lee, J., Kim, Y. & Gerhardt, F. (2019), 'Experimental and numerical studies on added resistance of ship in oblique sea conditions', *Ocean Engineering* **186**.

Patankar, S. V. & Spalding, D. B. (1983), A calculation procedure for heat, mass and momentum transfer in three-dimensional parabolic flows, *in* 'Numerical prediction of flow, heat transfer, turbulence and combustion', Elsevier, pp. 54–73.

Phillips, A. B., Turnock, S. R. & Furlong, M. (2009*a*), 'Evaluation of manoeuvring coefficients of a self-propelled ship using a blade element momentum propeller model coupled to a Reynolds averaged Navier Stokes flow solver', *Ocean Engineering* **36**(15-16).

Phillips, A. B., Turnock, S. R. & Furlong, M. (2009*b*), 'Evaluation of manoeuvring coefficients of a self-propelled ship using a blade element momentum propeller model coupled to a reynolds averaged navier stokes flow solver', *Ocean Engineering* **36**(15-16), 1217–1225.

Phillips, A. B., Turnock, S. R. & Furlong, M. (2010), 'Accurate capture of propeller-rudder interaction using a coupled blade element momentum-RANS approach', *Ship Technology Research* **57**(2).

Phillips, W. F. (2002), 'Propeller momentum theory with slipstream rotation', *Journal of aircraft* **39**(1), 184–187.

Pien, P. C. (1961), 'The calculation of marine propellers based on lifting-surface theory', *Journal of Ship Research* **5**(03), 1–14.

Pinkster, J. A. (1979), 'Mean and low frequency wave drifting forces on floating structures', *Ocean Engineering* **6**(6).

Procedures, I. & Guidelines (2008), Uncertainty analysis in cfd verification and validation methodology and procedures.

Rankine, W. J. M. (1865), 'On the mechanical principles of the action of propellers', *Transactions of the Institution of Naval Architects* **6**.

Riesner, M. & el Moctar, O. (2018), 'A time domain boundary element method for wave added resistance of ships taking into account viscous effects', *Ocean Engineering* .

Rusche, H. (2003), Computational fluid dynamics of dispersed two-phase flows at high phase fractions, PhD thesis, Imperial College London (University of London).

Saettone, S., Taskar, B., Regener, P. B., Steen, S. & Andersen, P. (2020), 'A comparison between fully-unsteady and quasi-steady approach for the prediction of the propeller performance in waves', *Applied Ocean Research* **99**, 102011.

Salvesen, N. (1975), 'SECOND-ORDER STEADY-STATE FORCES AND MOMENTS ON SURFACE SHIPS IN OBLIQUE REGULAR WAVES.', ((1975)).

Sanada, Y., Elshiekh, H., Toda, Y. & Stern, F. (2019), 'Onr tumblehome course keeping and maneuvering in calm water and waves', *Journal of Marine Science and Technology* **24**, 948–967.

Sanada, Y., Ito, S., Toda, Y. & Stern, F. (2017), Added Powering Measurements of KRISO Container Ship Maneuvering in Regular Variable Heading Waves, *in* 'SNAME 30th American Towing Tank Conference, ATTC 2017'.

Sanada, Y., Park, S., Kim, D.-H., Wang, Z., Stern, F. & Yasukawa, H. (2021), 'Experimental and computational study of hull–propeller–rudder interaction for steady turning circles', *Physics of Fluids* **33**(12), 127117.

Sánchez-Caja, A., Martio, J., Saisto, I. & Siikonen, T. (2015), 'On the enhancement of coupling potential flow models to rans solvers for the prediction of propeller effective wakes', *Journal of Marine Science and Technology* **20**, 104–117.

Schulten, J. B. (1996), 'Advanced propeller performance calculation by a lifting surface method', *Journal of propulsion and power* **12**(3), 477–485.

Senjanović, I., Katavić, J., Vukčević, V., Vladimir, N. & Jasak, H. (2020), 'Launching of ships from horizontal berth by tipping tables–cfd simulation of wave generation', *Engineering Structures* **210**, 110343.

Seo, J. H., Seol, D. M., Lee, J. H. & Rhee, S. H. (2010), 'Flexible cfd meshing strategy for prediction of ship resistance and propulsion performance', *International Journal of Naval Architecture and Ocean Engineering* **2**(3), 139–145.

Seo, M. G., Park, D. M., Yang, K. K. & Kim, Y. (2013), 'Comparative study on computation of ship added resistance in waves', *Ocean Engineering* .

Seol, H., Jung, B., Suh, J.-C. & Lee, S. (2002), 'Prediction of non-cavitating underwater propeller noise', *Journal of sound and vibration* **257**(1), 131–156.

Shen, Z., Wan, D. & Carrica, P. M. (2015), 'Dynamic overset grids in OpenFOAM with application to KCS self-propulsion and maneuvering', *Ocean Engineering* .

Shipping, S. G. (2023), 'Case study'. Accessed: 2023-04-26.
URL: *https://smartgreenshipping.com/casestudy*

Sigmund, S. & El Moctar, O. (2018), 'Numerical and experimental investigation of added resistance of different ship types in short and long waves', *Ocean Engineering* **147**, 51–67.

Simonsen, C. D. & Stern, F. (2005), 'RANS maneuvering simulation of Esso Osaka with rudder and a body-force propeller', *Journal of Ship Research* **49**(2).

Sluijs, M. (1972), Performance and propeller load fluctuations of a ship in waves, Technical report.

Söding, H., Shigunov, V., Schellin, T. E. & El Moctar, O. (2014), 'A rankine panel method for added resistance of ships in waves', *Journal of Offshore Mechanics and Arctic Engineering* **136**(3).

Stanier, M. (1998), 'Investigation into propeller skew using a 'rans' code part 2: Scale effects', *International Shipbuilding Progress* **45**.

Stern, F., Wilson, R. V., Coleman, H. W. & Paterson, E. G. (2001), 'Comprehensive approach to verification and validation of cfd simulations—part 1: methodology and procedures', *J. Fluids Eng.* **123**(4), 793–802.

Stocker, M. R. (2016), Surge free added resistance tests in oblique wave headings for the KRISO container ship model, PhD thesis.

Stokes, G. G. et al. (1851), 'On the effect of the internal friction of fluids on the motion of pendulums'.

Storm-Tejsen, J. (1973), 'Added resistance in waves', *Trans SNAME* **81**, 250–279.

Sumislawski, P., Sahab, A. & Shevchuk, I. (2022), 'Numerical investigation of the jbc hull and propeller interaction under static drift condition', *34th Symposium on Naval Hydrodynamics, Washington, United States, 26th June - 01 July 2022* .

Sun, S., Li, L., Wang, C. & Zhang, H. (2018), 'Numerical prediction analysis of propeller exciting force for hull–propeller–rudder system in oblique flow', *International Journal of Naval Architecture and Ocean Engineering* **10**(1).

Taniguchi, K. (1961), 'Propulsion performance in waves', *Bull Soc Naval Archit Japan* **383**, 315–328.

Tao, Y. & Zhang, C. (1991), 'A study on propeller thrust and torque increase in regular waves'.

Tasaki, R. (1957), 'On the characteristics of the driving machine in the self-propulsion test among waves', *Journal of Zosen Kiokai* **1957**(101), 25–32.

Taskar, B., Steen, S., Bensow, R. E. & Schröder, B. (2016), 'Effect of waves on cavitation and pressure pulses', *Applied ocean research* **60**, 61–74.

Taskar, B., Steen, S. & Eriksson, J. (2017), 'Effect of waves on cavitation and pressure pulses of a tanker with twin podded propulsion', *Applied Ocean Research* **65**, 206–218.

Taskar, B., Yum, K. K., Steen, S. & Pedersen, E. (2016), 'The effect of waves on engine-propeller dynamics and propulsion performance of ships', *Ocean Engineering* .

Tezdogan, T., Demirel, Y. K., Kellett, P., Khorasanchi, M., Incecik, A. & Turan, O. (2015), 'Full-scale unsteady rans cfd simulations of ship behaviour and performance in head seas due to slow steaming', *Ocean Engineering* **97**, 186–206.

Tokgoz, E. (2015), 'A cfd study on the propeller-hull interaction flow in waves using body-force distribution model'.

Tsukada, Y., Hinatsu, M. & Hasegawa, J. (1977), 'Measurement of unsteady ship wakes in waves', *J Kansai Soc Naval Archi Japan* **228**, 15–20.

Tu, J., Yeoh, G. H. & Liu, C. (2018), *Computational fluid dynamics: a practical approach*, Butterworth-Heinemann.

Turnock, S. R., Phillips, A. B. & Furlong, M. (2008), URANS SIMULATIONS OF STATIC DRAFT AND DYNAMIC MANEUVERS OF THE KVLCC2 TANKER, *in* 'Workshop on Verification and Validation of Ship Maneuvering Simulation Methods-SIMMAN 2008', Force Technology, Copenhagen, Denmark.

Ubbink, O. & Issa, R. (1999), 'A method for capturing sharp fluid interfaces on arbitrary meshes', *Journal of computational physics* **153**(1), 26–50.

Ueno, M., Tsukada, Y. & Tanizawa, K. (2013), 'Estimation and prediction of effective inflow velocity to propeller in waves', *Journal of Marine Science and Technology (Japan)* **18**(3), 339–348.

Valanto, P. & Hong, Y. P. (2015), Experimental investigation on ship wave added resistance in regular head, oblique, beam, and following waves, *in* 'Proceedings of the International Offshore and Polar Engineering Conference', Vol. 2015-Janua.

Van Doormaal, J. P. & Raithby, G. D. (1984), 'Enhancements of the simple method for predicting incompressible fluid flows', *Numerical heat transfer* **7**(2), 147–163.

Vaz, G. & Bosschers, J. (2006), Modelling three dimensional sheet cavitation on marine propellers using a boundary element method, *in* 'Sixth International Symposium on Cavitation CAV2006, Wageningen, The Netherlands'.

Versteeg, H. K. & Malalasekera, W. (2007), *An introduction to computational fluid dynamics: the finite volume method*, Pearson education.

Villa, D., Gaggero, S. & Brizzolara, S. (2012), Ship self propulsion with different cfd methods: from actuator disk to viscous inviscid unsteady coupled solvers, *in* '10th International Conference on Hydrodynamics, St. Petersburg, Russia'.

Villa, D., Gaggero, S., Gaggero, T., Tani, G., Vernengo, G. & Viviani, M. (2019), 'An efficient and robust approach to predict ship self-propulsion coefficients', *Applied Ocean Research* **92**, 101862.

Wang, G. & Jia, D. (1989), 'Influence of free surface on propeller characteristics', *Shipbuilding of China* **1**, 1–8.

Wang, J. & Wan, D. (2018), 'Cfd investigations of ship maneuvering in waves using naoe-foam-sjtu solver', *Journal of Marine Science and Application* **17**(3), 443–458.

Wang, J., Zou, L. & Wan, D. (2017), 'Cfd simulations of free running ship under course keeping control', *Ocean engineering* **141**, 450–464.

Wilcox, D. C. (1988), 'Reassessment of the scale-determining equation for advanced turbulence models', *AIAA journal* **26**(11), 1299–1310.

Wilson, R., Shao, J. & Stern, F. (2004), 'Discussion: Criticisms of the "correction factor" verification method', *J. Fluids Eng.* **126**(4), 704–706.

Wilson, R. & Stern, F. (2002), Verification and validation for rans simulation of a naval surface combatant, *in* '40th AIAA Aerospace Sciences Meeting & Exhibit', p. 904.

Windén, B. (2014), Powering Performance of a Self Propelled Ship in Waves, Phd thesis, University of Southampton.
URL: *https://eprints.soton.ac.uk/365546*

Windén, B. (2021*a*), An Open-Source Framework for Ship Performance CFD.

Winden, B. (2021*b*), An open-source framework for ship performance cfd, *in* 'SNAME 26th Offshore Symposium', OnePetro.

Windén, B. (2021*c*), Predicting the powering performance of different vessel types using an open-source CFD propulsion framework, *in* 'SNAME Maritime Convention 2021, SMC 2021'.

Windén, B., Turnock, S. & Hudson, D. (2014), 'A rans modelling approach for predicting powering performance of ships in waves', *International Journal of Naval Architecture and Ocean Engineering* **6**(2), 418–430.

Wöckner-Kluwe, K. (2013), *Evaluation of the Unsteady Propeller Performance behind Ships in Waves*.

Woeste, J. T., O'Reilly, C. M., Gouveia, R. K. & Young, Y. L. (2022), 'Propeller–hull interactions and added power in head seas', *Ocean Engineering* **247**, 110630.

Yamazaki, R. (1968), 'On the propulsion theory of ships on still water-introduction-.', *Memoirs of the Faculty of Engineering, Kyushu University* **27**(4).

Yamazaki, R. (1977), 'On the propulsion theory of ships on still water–improved theoretical method', *Memoirs of the Faculty of Engineering* **37**(1).

Yamazaki, R. (1998), 'Deduction of the simplified propeller theory', *TRANSACTIONS-WEST JAPAN SOCIETY OF NAVAL ARCHITECTS* pp. 251–272.

Yang, K. K., Kim, Y. & Jung, Y. W. (2018), 'Enhancement of asymptotic formula for added resistance of ships in short waves', *Ocean Engineering* .

Yang, K. K., Kim, Y. & Nam, B. W. (2015), 'Cartesian-grid-based computational analysis for added resistance in waves', *Journal of Marine Science and Technology (Japan)* .

Yasukawa, H., Hasnan, M. & Matsuda, A. (2021), 'Validation of 6-dof motion simulations for ship turning in regular waves', *Journal of Marine Science and Technology* pp. 1–16.

Yumuro, A. (1974), 'An experimental studies on incoming flow-direction to the rudder of a ship sailing obliquely on rudder performance', *Ishikawajima-Harima Engineering Review* **3**(4).

Yumuro, A. (1975), 'A model experiment on incoming-flow direction to the rudder of a ship sailing obliquely'.

Yumuro, A. (1978), An experimental study on inflow direction and inflow velocity to the rudder of a ship in manoeuvring motion, *in* 'Ishikawajima-Harima Heavy Industries Co. Ltd, Proceedings of the Conference on Ship Manoeuvrability and Handling, Varna, Bulgaria, Paper 11, Paper: 1978-3 Proceedings.'.

Zhang, Y., Hudson, D., Windén, B. & Turnock, S. (2021), Evaluating the effects of drift angle on the self-propelled ship using blade element momentum theory, *in* '23rd Numerical Towing Tank Symposium', NUTTS Committee, Mülheim an der Ruhr, Germany, 11th – 13th October 2021.

Zhang, Y., Windén, B., Hudson, D. & Turnock, S. (2022), Hydrodynamic performance of a self-propelled kcs at angle of drift including rudder forces, *in* '24th Numerical Towing Tank Symposium', NUTTS Committee, Zagreb Croatia, 16 – 18 October 2022.

Zhao, Q., Guo, C., Su, Y., Liu, T. & Meng, X. (2017), 'Study on unsteady hydrodynamic performance of propeller in waves', *Journal of Marine Science and Application* **16**(3), 305–312.

Appendix A

Example code

snappyHexMesh code for VOF calculations:

```
/*--------------------------------*- C++ -*-----------------------------------*\
| =========                 |                                                  |
| \\      /  F ield         | OpenFOAM: The Open Source CFD Toolbox           |
|  \\    /   O peration     | Version:  7                                   |
|   \\  /    A nd           | Web:      www.OpenFOAM.org                      |
|    \\/     M anipulation  |                                                  |
\*----------------------------------------------------------------------------*/
FoamFile
{
    version     2.0;
    format      ascii;
    class       dictionary;
    object      snappyHexMeshDict;
}

// * * * * * * * * * * * * * * * * * * * * * * * * * * * * * * * * * * * * * //

// Which of the steps to run
castellatedMesh true;
snap            true;
addLayers       true;



// Geometry. Definition of all surfaces. All surfaces are of class
// searchableSurface.
// Surfaces are used
// - to specify refinement for any mesh cell intersecting it
// - to specify refinement for any mesh cell inside/outside/near
// - to 'snap' the mesh boundary to the surface
geometry
{
        hull.stl // ship
    {
        type triSurfaceMesh;
        name hull;
    }
        rudder.stl // rudder
```

```
    {
        type triSurfaceMesh;
        name rudder;
    }

        skeg.stl // skeg
    {
        type triSurfaceMesh;
        name skeg;
    }

    big  // User defined region name
  {
    type    searchableBox;      // region defined by bounding box
    min     (5.7 -0.7  -0.4);
    max     (7.7 0.7  0.4);
  }

 /** small  // User defined region name
  {
    type    searchableBox;      // region defined by bounding box
    min     (6.35 -0.6  0.25);
    max     (7.55  0.6  0.35);
  }*/

};



// Settings for the castellatedMesh generation.
castellatedMeshControls
{
  #include "CM"
}



// Settings for the snapping.
snapControls
{
  #include "snapMeshDict"
}



// Settings for the layer addition.
addLayersControls
{
  #include "BL"
}



// Generic mesh quality settings. At any undoable phase these determine
// where to undo.
meshQualityControls
{
    #include "meshQualityDict"
}
```

```
// Advanced

// Flags for optional output
// 0 : only write final meshes
// 1 : write intermediate meshes
// 2 : write volScalarField with cellLevel for postprocessing
// 4 : write current intersections as .obj files
debug 0;

writeFlags
(
        scalarLevels
        layerFields
);


// Merge tolerance. Is fraction of overall bounding box of initial mesh.
// Note: the write tolerance needs to be higher than this.
mergeTolerance 1E-6;


// ************************************************************************* //
```

LISTING A.1: snappHexMeshDict code

```
/*--------------------------------*- C++ -*----------------------------------*\
| =========                 |                                                 |
| \\      /  F ield         | OpenFOAM: The Open Source CFD Toolbox           |
|  \\    /   O peration     | Version:  7                                   |
|   \\  /    A nd           | Web:      www.OpenFOAM.org                      |
|    \\/     M anipulation  |                                                 |
\*---------------------------------------------------------------------------*/
FoamFile
{
    version     2.0;
    format      ascii;
    class       dictionary;
    object      castellatedMeshDict;
}

// * * * * * * * * * * * * * * * * * * * * * * * * * * * * * * * * * * * * * //


// Refinement parameters
// ~~~~~~~~~~~~~~~~~~~~~

// If local number of cells is >= maxLocalCells on any processor
// switches from from refinement followed by balancing
// (current method) to (weighted) balancing before refinement.
maxLocalCells 40000000;

// Overall cell limit (approximately). Refinement will stop immediately
// upon reaching this number so a refinement level might not complete.
// Note that this is the number of cells before removing the part which
// is not 'visible' from the keepPoint. The final number of cells might
// actually be a lot less.
maxGlobalCells 300000000;
```

```
// The surface refinement loop might spend lots of iterations refining just a
// few cells. This setting will cause refinement to stop if <= minimumRefine
// are selected for refinement. Note: it will at least do one iteration
// (unless the number of cells to refine is 0)
minRefinementCells 20;

// Number of buffer layers between different levels.
// 1 means normal 2:1 refinement restriction, larger means slower
// refinement.
nCellsBetweenLevels 1;



// Explicit feature edge refinement
// ~~~~~~~~~~~~~~~~~~~~~~~~~~~~~~~~

// Specifies a level for any cell intersected by its edges.
// This is a featureEdgeMesh, read from constant/triSurface for now.
features
(
        {
            file        "hull.eMesh";
            level      1;//was 2
        }
        {
            file        "rudder.eMesh";
            level      1;//was 2
        }
        {
            file        "skeg.eMesh";
            level      1;//was 2
        }


);



// Surface based refinement
// ~~~~~~~~~~~~~~~~~~~~~~~~

// Specifies two levels for every surface. The first is the minimum level,
// every cell intersecting a surface gets refined up to the minimum level.
// The second level is the maximum level. Cells that 'see' multiple
// intersections where the intersections make an
// angle > resolveFeatureAngle get refined up to the maximum level.

refinementSurfaces
{
    hull
    {
        // Surface-wise min and max refinement level
        level (1 1);//was 5 5
    }


    rudder
    {
```

```
        // Surface-wise min and max refinement level
        level (3 3);//was 5 5
    }

    skeg
    {
        // Surface-wise min and max refinement level
        level (3 3);//was 5 5
    }
}

resolveFeatureAngle 30; // was 30


// Region-wise refinement
// ~~~~~~~~~~~~~~~~~~~~~~

// Specifies refinement level for cells in relation to a surface. One of
// three modes
// - distance. 'levels' specifies per distance to the surface the
//   wanted refinement level. The distances need to be specified in
//   descending order.
// - inside. 'levels' is only one entry and only the level is used. All
//   cells inside the surface get refined up to the level. The surface
//   needs to be closed for this to be possible.
// - outside. Same but cells outside.

refinementRegions
{
 /* hull
  {
    mode distance;
    levels
    (
        (0.01 1) //was 5
    );
 }
  rudder
  {
    mode distance;
    levels
    (
        (0.01 1) //was 5
    );
   }*/


     big
  {
    mode inside;
    levels ((100000 0));
    levelIncrement  (0 5 (1 1 0));
  }

 /* small
  {
    mode inside;
    levels ((100000 0));
    levelIncrement  (0 5 (1 1 0));
```

```
  }*/
}


// Mesh selection
// ~~~~~~~~~~~~~~

// After refinement patches get added for all refinementSurfaces and
// all cells intersecting the surfaces get put into these patches. The
// section reachable from the locationInMesh is kept.
// NOTE: This point should never be on a face, always inside a cell, even
// after refinement.
locationInMesh (24 0 0);


// Whether any faceZones (as specified in the refinementSurfaces)
// are only on the boundary of corresponding cellZones or also allow
// free-standing zone faces. Not used if there are no faceZones.
allowFreeStandingZoneFaces false;


// ************************************************************************* //
```

LISTING A.2: castellatedMeshDict code

```
/*--------------------------------*- C++ -*----------------------------------*\
| =========                 |                                                 |
| \\      /  F ield         | OpenFOAM: The Open Source CFD Toolbox           |
|  \\    /   O peration     | Version:  7                                   |
|   \\  /    A nd           | Web:      www.OpenFOAM.org                      |
|    \\/     M anipulation  |                                                 |
\*---------------------------------------------------------------------------*/
FoamFile
{
    version     2.0;
    format      ascii;
    class       dictionary;
    object      snapMeshDict;
}

// * * * * * * * * * * * * * * * * * * * * * * * * * * * * * * * * * * * * * //




//- Number of patch smoothing iterations before finding correspondence
//  to surface
nSmoothPatch 10; //WAS 5

//- Relative distance for points to be attracted by surface feature point
//  or edge. True distance is this factor times local
//  maximum edge length.
//    tolerance 4.0;
tolerance 1; //was 4

//- Number of mesh displacement relaxation iterations.
nSolveIter 300;

//- Maximum number of snapping relaxation iterations. Should stop
```

```
//  before upon reaching a correct mesh.
nRelaxIter 30;

// Feaature snapping
//
    // Number of feature edge snapping iterations
    // Leave out all together to disable
    nFeatureSnapIter 25;

    //- Detect (geometric Only) features by sampling the surface
    //  (default=false)
    implicitFeatureSnap true;

    //- Use castellatedMeshControls::features (default=yes)
    explicitFeatureSnap false;

    //- Detect points on jultiple surfaces (only for explicitFeatureSnap)
    multiRegionFeatureSnap false;

// ************************************************************************* //
```

LISTING A.3: snapMeshDict code

```
/*--------------------------------*- C++ -*----------------------------------*\
| =========                 |                                                 |
| \\      /  F ield         | OpenFOAM: The Open Source CFD Toolbox           |
|  \\    /   O peration     | Version:  7                                   |
|   \\  /    A nd           | Web:      www.OpenFOAM.org                      |
|    \\/     M anipulation  |                                                 |
\*---------------------------------------------------------------------------*/
FoamFile
{
    version     2.0;
    format      ascii;
    class       dictionary;
    object      layersMeshDict;
}

// * * * * * * * * * * * * * * * * * * * * * * * * * * * * * * * * * * * * * //

// Are the thickness parameters below relative to the undistorted
// size of the refined cell outside layer (true) or absolute sizes (false).
relativeSizes true;

// Per final patch (so not geometry!) the layer information
layers
{
hull
    {
        nSurfaceLayers 8; // was 3

    }
rudder
    {
        nSurfaceLayers 8; // was 3

    }
skeg
    {
```

```
        nSurfaceLayers 8; // was 3

    }
}

// Expansion factor for layer mesh
expansionRatio 1.2;


// Wanted thickness of final added cell layer. If multiple layers
// is the thickness of the layer furthest away from the wall.
// Relative to undistorted size of cell outside layer.
// See relativeSizes parameter.
finalLayerThickness 0.5;
//finalLayerThickness 0.03;

// Minimum thickness of cell layer. If for any reason layer
// cannot be above minThickness do not add layer.
// See relativeSizes parameter.
minThickness 0.02;
//minThickness 0.0082;

// If points get not extruded do nGrow layers of connected faces that are
// also not grown. This helps convergence of the layer addition process
// close to features.
// Note: changed(corrected) w.r.t 17x! (didn't do anything in 17x)
nGrow 0;


// Advanced settings

// When not to extrude surface. 0 is flat surface, 90 is when two faces
// are perpendicular
featureAngle 180; // was 180

// Maximum number of snapping relaxation iterations. Should stop
// before upon reaching a correct mesh.
nRelaxIter 50;

// Number of smoothing iterations of surface normals
nSmoothSurfaceNormals 20; // was 1

// Number of smoothing iterations of interior mesh movement direction
nSmoothNormals 10;

// Smooth layer thickness over surface patches
nSmoothThickness 20;

// Stop layer growth on highly warped cells
maxFaceThicknessRatio 0.5; // was 0.5

// Reduce layer growth where ratio thickness to medial
// distance is large
maxThicknessToMedialRatio 0.3;

// Angle used to pick up medial axis points
// Note: changed(corrected) w.r.t 17x! 90 degrees corresponds to 130 in 17x.
minMedialAxisAngle 90;
```

```
// Create buffer region for new layer terminations
nBufferCellsNoExtrude 0;


// Overall max number of layer addition iterations. The mesher will exit
// if it reaches this number of iterations; possibly with an illegal
// mesh.
nLayerIter 50;

// Max number of iterations after which relaxed meshQuality controls
// get used. Up to nRelaxIter it uses the settings in meshQualityControls,
// after nRelaxIter it uses the values in meshQualityControls::relaxed.
nRelaxedIter 20;

// ************************************************************************* //
```

LISTING A.4: layersMeshDict code

PropllerDict code for BEMt and Yamazaki propeller modelling:

```
/*---------------------------------*- C++ -*-----------------------------------*\
| =========                 |                                                 |
| \\      /  F ield         | OpenFOAM: The Open Source CFD Toolbox           |
|  \\    /   O peration     | Version:  7                                 |
|   \\  /    A nd           | Web:      www.OpenFOAM.org                      |
|    \\/     M anipulation  |                                                 |
\*---------------------------------------------------------------------------*/
FoamFile
{
    version     2.0;
    format      ascii;
    class       dictionary;
    location    "system";
    object      propellerDict;
}
// * * * * * * * * * * * * * * * * * * * * * * * * * * * * * * * * * * * * * //


/////////////////////
//Limiters and controls
applyRPMincreaseLimiter true;
RPMincreaseLimitValue 10;
applyMaxRPM true;
maxRPM  1440.00000000000000000000;
startRPM 720.00000000000000000000;
allowExplicitRPM false;
U0 2.196;

applyModelEvery 50;

g (0 0 -9.81);

//Density of fluid that propeller is working in
rhoProp 999.1026;



//Propeller shaft orientation in initial state. Will determine direction of propeller force on the hull
propShaftOrientation    (-1 0 0);

//Centre of propeller, used to define propeller location in initial state.
propOrigin      (7.1512245 0 -0.212025618);


//Propeller model
propellerModel BEMt;
propellerControl fixedRPM;
controlStyle "forced";

fixedRPMCoeffs
{
        RPM     720.00000000000000000000;
}

BEMtCoeffs
{
        radius  0.125; //0.124999765
        hubRadius 0.0225; //0.02249995769
```

```
        thickness 0.025;  //0.02499995299

        Z 5;

        nRefRads        11;

        rR       ( .18 .25 .3 .4 .5 .6 .7 .8 .9 .95 1);
        P_D     ( .8347 .8912 .9269 .9783 1.0079 1.013 .9967 .9566 .9006 .8683 .8331);
        C_D     ( .2313 .2618 .2809 .3138 .3403 .3573 .359 .3376 .2797 .2225 .0001);
        T_C     ( .04585 .04071 .03712 .03047 .02459 .01947 .01492 .01073 .00693 .00528 .00369);


        BARatio .8;

        rotDir  1;

        //Number of panels
        nSectors 36;
        nRad    10;

        mapOrder 2;



}




probeCoeffs
{

        maxIterations 1000;

        probedCONCMeshFields
        {

                Ulocalmid
                {
                        interpolationVariable
                        {
                                U cellPoint;
                        }
                        location centrePlane;
                        //2%D Downstream shift
                        offset -.005; //0.00058;
                }
        }


}

// ************************************************************************* //
```

LISTING A.5: propellerDict code

waveProperties code for regular wave generation:

```
/*--------------------------------*- C++ -*----------------------------------*\
  =========                 |
  \\      /  F ield         | OpenFOAM: The Open Source CFD Toolbox
   \\    /   O peration     | Website:  https://openfoam.org
    \\  /    A nd           | Version:  7
     \\/     M anipulation  |
\*---------------------------------------------------------------------------*/
FoamFile
{
    version     2.0;
    format      ascii;
    class       dictionary;
    location    "constant";
    object      waveProperties;
}
// * * * * * * * * * * * * * * * * * * * * * * * * * * * * * * * * * * * * //

origin          (0 0 0);

direction       (1 0 0);

waves
(
    Stokes2
    {
        length      14.197; // scale from 2015 Tokyko workshop using Lpp
        amplitude   0.1175; // scale from 2015 Tokyko workshop using Lpp
        phase       0;
        angle       0;
    }
);

UxMean          2.196;

UMean           ($UxMean 0 0);

scale           table ((2 1) (12 0));


// ************************************************************************* //
```

LISTING A.6: Waveproperties code